Study of Optical Beam-Shifts Phenomena Using Different Beam Profiles

Thesis submitted for the degree of

Doctor of Philosophy (Science)

in

Physics (Experimental)

by

Soumen Mandal

Department of Physics

University of Calcutta

2025

Dedicated to my Family and Teachers...

Acknowledgement

After seven exciting years of my significant academic adventure at S. N. Bose National Centre for Basic Sciences - two years of M. Sc. and five years of Ph. D. - I am finally ready to wrap up my Ph. D. thesis. Although I was never alone on this journey, I would like to take a moment to express my gratitude to all those who made this thesis possible.

First and foremost, I would like to sincerely thank Prof. Manik Pradhan, my thesis supervisor, for his unwavering support, encouraging words, and insightful research directions. His encouragement and support got me through all the highs and lows of these years, pushing me to go past one obstacle after another. His insightful suggestions regarding studies and other facets of life have immensely enriched me, increasing my self-confidence and optimism about life in general. Additionally, I would like to express my gratitude to Professors Akhlesh Lakhtakia and Mark Horn of Pennsylvania State University (USA) for their long-term collaboration and guiding me towards a new direction in my research objectives. I also thank Prof. Ranjit Biswas and Prof. Suman Chakraborty for being in the thesis committee and offering useful feedback throughout the annual evaluations.

My science teachers from the beginning are perhaps the people I owe the most. Having science teachers like Chotu Sir (Jamini Manna), Dipankar Dinda Sir, Madan Sir (Madan Jana), Palash Sir (Palash Chatterjee) in my early school years was a blessing since they not only sparked my interest in science but also taught me the fundamentals of morality and ethics which helped me a lot to pursue research in several ways. Additionally, I would like to express my gratitude to our college professors, S. D. C. Sir (Somdeb Chakraborty), A. D. Sir (Abhisek Dey), and A. G. Sir (Amitava Ghorai), who patiently answered all of our questions, clearly explained the complex concepts of various physics courses, and encouraged me to pursue further studies in physics. I also want to thank all of the professors at SNBNCBS who patiently and carefully taught us during our master's program. I have to admit that having such wonderful teachers during my academic career has been a true blessing. I'm not brave enough to thank them or pay back their debts. However, these enduring recollections propelled me to strive to become a pupil deserving of such exceptional instructors.

I am lucky to have had seniors like Akash Das, Ardhendu Pal, Biswajit Panda, Jayita Banerjee, and Puspendu Barik during my Ph.D. tenure. They have taught me a lot about academic research and have always made the lab feel homely. More precisely, throughout the

first two years, Akash da taught me experimental methods and manuscript preparation. I should add separately that I had a special bond with Ardhendu da and Biswajit da, who constantly pushed me to try new things in research, culture, and sports. This helped me get over my stage fright and gave me more confidence. I'm grateful to my junior lab mates Soumyadipta, Indrayani, Dinesh, Anuradha, and Arup for keeping this group alive and making the work engaging.

Aside from my lab mates, I've had a lovely seven-year adventure at SNBNCBS with many loving and caring friends, without whom life would have been drab and monotonous. First and foremost, I'd like to thank the "chicken dinner" group, which included Anirban, Animesh, Avik, Koushik, Sudipto, Soham, Rajdeep, Ishita, and Shinjini, for their invaluable assistance throughout the years. The annual trip, cooking in various events, 'adda' in the cafeteria, and night walks with all types of chats with these folks really freed up my mind at the end of the arduous days and never made me feel alone on this voyage. I can't forget my other buddies Shubham, Gaurav, Ankita, and Varsha from M.Sc. I am also grateful to many other persons on campus, such as Shashank, Sidhhartha (Biswas) Da, Anish (Das) Da, Shubham (Purwar) Da, Pritam, Sayan, and Sudip (Pramanik) for accompanying me on this journey via various facets. I'd also like to thank everyone with whom I've spent time at SNBNCBS when playing cricket, badminton, or participating in other social or sporting activities.

I am fortunate to have many charming childhood buddies. I must thank my college pals Sayak, Rohan, Debayudh, Surajit, and Haider, with whom I still have a very unique bond. I remember having a group discussion with Sayak and Rohan in college, which helped me a lot in covering the vast subject and preparing for competitive exams. I would like to thank some of my close and old schoolmates, Satyajit (Pandit), Subhojit (Mondal), Poulomi, Robijyoti, Soham, Swarnil, Aritra, Suvam, Promit, Soumendu, Rohan (Singh), Sourav, and Soujit, for providing me with memorable moments and enriching my life with fulfillment and happiness. I still have very close connections with several of them. Thank you for a great time together. It is impossible to communicate my heartfelt gratitude and appreciation to all of you.

As I enjoy reading and, more recently, listening to audio stories books, some of which not only provided a positive vibe but also changed my perspective on life. I particularly think of 'The Stories of Mahabharata by Sudipta Bhawmik (Amazon music)', 'Times of Puran', Talks by Premananda Ji Maharaj and numerous episodes of Sunday Suspense and other audio story

channels available on YouTube, which helped me spend quality time. Among other things, I'd like to highlight that watching web series, movies, and various sports such as cricket, football, badminton, and others has become another approach to unwind my thoughts. Overall, these journeys would not have gone as smoothly without the much-needed amusement indicated above.

I consider myself extremely fortunate to have been born into such a loving and supporting family. No words can express the impact of my 'guardian angels' - my parents and older brother. All of my accomplishments are the result of my family's hard work and unwavering sacrifices to shape me into the person I am. Special mention to my brother, who constantly emphasizes the road that will benefit me. I also want to thank all of my cousin brothers, sisters, and maternal uncle for the fun times we've had together. I must mention Jagadish da and Khokan Da for being the motivation for higher studies. I am also thankful to my grandparents for getting never-ending support, love, care and blessings from them.

I am extremely thankful to the S. N. Bose National Centre for Basic Sciences for offering me the PhD fellowship, as well as all of the experimental and computational resources and a lovely, green campus. I thank the students' mess (SNB Mess), the institute canteen, the kitchen crew, the library staff, all of the group D staff, and the security staff for their unappreciated efforts to make campus a secure, healthy place to live every day.

Finally, I want to thank the Almighty God for holding my hand through various ups and downs in my life throughout this journey.

Abstract

The problem of reflection and refraction at an optical interface is well described by the Snell's law and Fresnel formulations considering the incident light as plane wave. However, a real laser beam that consists of an infinite number of plane waves with slightly different wave vectors doesn't exactly follows the laws of geometrical optics. During the interactions, the beam centroid position is displaced by a sub-wavelength distance either in-plane or out of the plane of incidence, known as optical beam shift. While the out-of-plane shift is referred to as the Imbert-Fedorov (IF) shift or the photonic spin Hall effect (PSHE), which results from photonic spin-orbit interactions, the in-plane shift is known as the Goos-Hänchen (GH) shift, which arises from the dispersion of reflection coefficients. The fundamental significance of these sub-wavelength scale phenomena, along with their enormous potential for use in advanced optoelectronics and photonic sensors, have made them a focus of active research in recent decades. Therefore, it is increasingly clear that the intricacies of this light-matter interaction and its regulating characteristics need to be studied in detail. However, detecting this minuscule effect is problematic due to its small size (spatial shift ~ nanometer, angular shift ~ nanoradian). As a result, the weak value amplification (WVA) approach is used, enhancing the wavelength-scale optical beam shift to the beam width scale.

In this thesis, we have investigated how the polarization states and angle of incidences can control the Goos-Hänchen (GH) shift in the vicinity of critical angle of incidences in total internal reflection condition. A general theoretical model using Jones matrix formalism is developed. The application idea of tunable GH shift values in bio-sensor or polarization-controlled devices is also discussed in detail. Next, the interaction surface dependent variation of GH shifts is investigated considering mono layered (ML) tungsten di-selenide (WSe_2) placed on SiO_2-Si substrate. It is observed that the critical angle of incidence is drastically shifted as compared to the glass-air interface which is also predicted from reflection coefficients that are calculated using transfer matrix method (TMM). Further, to investigate how the beam shape can affect the magnitude of GH shifts near the critical angle, two orthogonal first order Hermite-Gauss (HG) light beam, HG_{10} and HG_{01} are created using phase only spatial light modulator (SLM) and employed in WVA setup. The experimental data presents angular dependence of GH shifts in TIR region for both the modes. A comparison of shift values for HG modes with the case simple Gaussian light beam (TEM_{00}) clearly dictate the advantage of using higher order light beams over Gaussian beam.

Next, the study of photonic spin splitting (PSS) in transverse as well as longitudinal direction is investigated using p- and s-polarized Gaussian light beam. The investigation is focused near the Brewster angle of incidence during the partial reflection at ML WSe_2/SiO_2-Si interface. Finally, employing a vortex light beam, how the generalized PSS get modified by the azimuthal index (l), post-selection angle and polarization states at different angle of incidences are investigated at air-glass interface. As the conventional WVA formalism is restricted at the strong coupling regime and very close to orthogonal pre- and post-selection states, an improved weak measurement model is developed using wave vector formalism to support the experimentally obtained results. The developed generalized theoretical model is valid for external as well as internal reflection from absorptive material interaction surface irrespective of the above-mentioned limitations. Even the optimum overlap of pre- and post-selection states to get maximum amplified PSS is also elaborated. The important findings of this thesis will enrich the understanding of optical beam shifts and open up the different application possibilities in wavefront manipulation, determination of optical parameters, optical sensing, and nano-photonics.

সারাংশ

অপটিক্যাল ইন্টারফেসে প্রতিফলন এবং প্রতিসরণ সমস্যাটি স্নেলের সূত্র এবং ফ্রেসনেল সূত্র দ্বারা সুন্দরভাবে বর্ণনা করা হয়েছে, যা আপতিত আলোকে সমতল তরঙ্গ হিসেবে বিবেচনা করে। তবে, একটি বাস্তব লেজার রশ্মি যা অসীম সংখ্যক সমতল তরঙ্গ নিয়ে গঠিত এবং সামান্য ভিন্ন তরঙ্গ ভেক্টর ধারণ করে, তা জ্যামিতিক আলোকবিদ্যার নিয়মগুলি ঠিক অনুসরণ করে না। মিথস্ক্রিয়া চলাকালীন, রশ্মি কেন্দ্রবিন্দু অবস্থানটি সমতলের অভ্যন্তরে বা আপতন সমতলের বাইরে একটি উপ-তরঙ্গদৈর্ঘ্য দূরত্ব দ্বারা স্থানচ্যুত হয়, যা অপটিক্যাল রশ্মি স্থানান্তর নামে পরিচিত। যদিও সমতলের বাইরে স্থানান্তরকে *ইম্বার্ট-ফেডোরভ স্থানান্তর* বা *ফোটোনিক স্পিন হল প্রভাব* বলা হয়, যা ফোটোনিক স্পিন-অরবিট মিথস্ক্রিয়া থেকে উদ্ভূত হয়, তবে সমতলের ভিতরে স্থানান্তরকে গুস-হ্যানচেন স্থানান্তর বলা হয়, যা প্রতিফলন সহগের বিচ্ছুরণ থেকে উদ্ভূত হয়। এই উপ-তরঙ্গদৈর্ঘ্য স্কেল ঘটনার মৌলিক তাৎপর্য, উন্নত অপটোইলেক্ট্রনিক্স এবং ফোটোনিক সেন্সরগুলিতে ব্যবহারের জন্য তাদের বিশাল সম্ভাবনা সহ, সাম্প্রতিক দশকগুলিতে এগুলিকে সক্রিয় গবেষণার কেন্দ্রবিন্দুতে পরিণত করেছে। অতএব, এটি ক্রমশ স্পষ্ট হয়ে উঠছে যে এই আলোক-পদার্থের মিথস্ক্রিয়ার জটিলতা এবং এর নিয়ন্ত্রণকারী বৈশিষ্ট্যগুলি বিস্তারিতভাবে অধ্যয়ন করা প্রয়োজন। তবে, এই ক্ষুদ্র প্রভাব সনাক্তকরণ সমস্যাযুক্ত কারণ এর আকার ছোট (স্থানিক স্থানান্তর ~ ন্যানোমিটার, কৌণিক স্থানান্তর ~ ন্যানোরেডিয়ান)। ফলস্বরূপ, দুর্বল মান পরিবর্ধন পদ্ধতি ব্যবহার করা হয়, যা তরঙ্গদৈর্ঘ্য-স্কেল অপটিক্যাল বিম স্থানান্তরকে বিম প্রস্থ স্কেলে বৃদ্ধি করে।

এই থিসিসে, আমরা তদন্ত করেছি যে কীভাবে মেরুকরণ অবস্থা এবং আপতন কোণ অভ্যন্তরীণ পূর্ণপ্রতিফলন অবস্থায় সংকট আপতন কোণের আশেপাশে গুস-হ্যানচেন স্থানান্তরকে নিয়ন্ত্রণ করতে পারে। জোন্স ম্যাট্রিক্স ফর্মালিজম ব্যবহার করে একটি সাধারণ তাত্ত্বিক মডেল তৈরি করা হয়েছে। জৈব-সেন্সর বা পোলারাইজেশন-নিয়ন্ত্রিত ডিভাইসগুলিতে টিউনেবল গুস-হ্যানচেন শিফট মানগুলির প্রয়োগ ধারণাটিও বিশদভাবে আলোচনা করা হয়েছে। এরপর, সিলিকন ডাই অক্সাইড - সিলিকন সাবস্ট্রেটে স্থাপন করা একস্তর টাংস্টেন ডাই-সেলেনাইড বিবেচনা করে গুস-হ্যানচেন শিফটের মিথস্ক্রিয়া পৃষ্ঠ-নির্ভর প্রকরণ তদন্ত করা হয়। দেখা গেছে যে, কাচ-বাতাসের ইন্টারফেসের তুলনায় সংকট আপতন কোণটি ব্যাপকভাবে স্থানান্তরিত হয়, যা ট্রান্সফার ম্যাট্রিক্স পদ্ধতি ব্যবহার করে গণনা করা প্রতিফলন সহগ থেকেও পূর্বাভাস দেওয়া হয়। অধিকন্তু, সংকট কোণের কাছাকাছি গুস-হ্যানচেন

স্থানান্তরের মাত্রাকে রশ্মির আকৃতি কীভাবে প্রভাবিত করতে পারে তা তদন্ত করার জন্য, দুটি লম্বকীয় প্রথম ক্রম হারমাইট-গাউস আলোক রশ্মি, তৈরি করা হয়েছে ফেজ-অনলি স্পেশিয়াল লাইট মডুলেটর ব্যবহার করে এবং দুর্বল মান পরিবর্ধন সেটআপে ব্যবহৃত হয়। পরীক্ষামূলক তথ্য উভয় মোডের জন্য অভ্যন্তরীণ পূর্ণপ্রতিফলন অঞ্চলে গুস-হ্যানচেন স্থানান্তরের কৌণিক নির্ভরতা উপস্থাপন করে। প্রথম ক্রম হারমাইট-গাউস মোডের জন্য স্থানান্তর মানের তুলনা সিম্পল গাউসিয়ান লাইট রশ্মির সাথে স্পষ্টভাবে গাউসিয়ান রশ্মির উপর উচ্চ ক্রম আলোক রশ্মি ব্যবহারের সুবিধা নির্দেশ করে।

এরপর, ট্রান্সভার্স ম্যাগনেটিক এবং ট্রান্সভার্স ইলেকট্রিক পোলারাইজড গাউসিয়ান লাইট রশ্মি ব্যবহার করে ট্রান্সভার্স এবং দ্রাঘিমাংশীয় দিকে ফোটোনিক স্পিন স্প্লিটিং এর অধ্যয়ন তদন্ত করা হয়। সিলিকন ডাই অক্সাইড - সিলিকন সাবস্ট্রেটে স্থাপন করা একস্তর টাংস্টেন ডাই-সেলেনাইড ইন্টারফেসে আংশিক প্রতিফলনের সময় তদন্তটি ব্রিউস্টার আপতন কোণের কাছে কেন্দ্রীভূত করা হয়। পরিশেষে, একটি ঘূর্ণি আলোক রশ্মি ব্যবহার করে, সাধারণীকৃত *ফোটোনিক স্পিন স্প্লিটিং* কীভাবে আজিমুথাল সূচক, নির্বাচন-পরবর্তী কোণ এবং বিভিন্ন আপতন কোণে পোলারাইজেশন অবস্থা দ্বারা পরিবর্তিত হয় তা বায়ু-কাচের ইন্টারফেসে তদন্ত করা হয়। যেহেতু প্রচলিত দুর্বল মান পরিবর্ধন ফর্মালিজম শক্তিশালী সংযোগ এবং অর্থোগোনাল প্রাক- এবং নির্বাচন-পরবর্তী অবস্থার খুব কাছাকাছি ব্যবস্থায় সীমাবদ্ধ, পরীক্ষামূলকভাবে প্রাপ্ত ফলাফলগুলিকে সমর্থন করার জন্য তরঙ্গ ভেক্টর ফর্মালিজম ব্যবহার করে একটি উন্নত দুর্বল পরিমাপ মডেল তৈরি করা হয়েছে। উন্নত সাধারণীকৃত তাত্ত্বিক মডেলটি উপরে উল্লিখিত সীমাবদ্ধতা নির্বিশেষে শোষণকারী উপাদান মিথস্ক্রিয়া পৃষ্ঠ থেকে বাহ্যিক এবং অভ্যন্তরীণ প্রতিফলনের জন্য বৈধ। সর্বাধিক বর্ধিত *ফোটোনিক স্পিন স্প্লিটিং* পেতে প্রাক- এবং নির্বাচন-পরবর্তী অবস্থার সর্বোত্তম ওভারল্যাপও বিশদভাবে ব্যাখ্যা করা হয়েছে। এই থিসিসের গুরুত্বপূর্ণ ফলাফলগুলি অপটিক্যাল রশ্মি পরিবর্তনের বোঝাপড়াকে সমৃদ্ধ করবে এবং তরঙ্গফ্রন্ট ম্যানিপুলেশন, অপটিক্যাল প্যারামিটার নির্ধারণ, অপটিক্যাল সেন্সিং এবং ন্যানো-ফোটোনিক্সে বিভিন্ন প্রয়োগের সম্ভাবনা উন্মুক্ত করবে।

List of figures

List of Abbreviations

2D	: Two-Dimensional
3D	: Three-Dimensional
PWE	: Paraxial wave equation
TMDC	: Transition Metal Di-chalcogenides
TM	: Transverse magnetic
TE	: Transverse electric
GH	: Goos-Hänchen
IF	: Imbert-Fedorov
PSHS	: Photonic Spin Hall Shift
PSHE	: Photonic Spin Hall Effect
PSS	: Photonic Spin Splitting
SOI	: Spin orbit interaction
PR	: Partial Reflection
TIR	: Total Internal Reflection
ML	: Monolayer
QWM	: Quantum Weak Measurement
WVA	: Weak Value Amplification
OAM	: Orbital Angular Momentum
HG	: Hermite-Gauss
LG	: Laguerre - Gauss
BSS	: Beam Splitter Scanning
QS	: Quantum system
PS	: Pointer state
IWVA	: Interferometric weak value amplification
SP	: Stokes Parameters
HWP	: Half-wave Plate
SLM	: Spatial light modulator
QWP	: Quarter-wave Plate
GLP	: Glan-Thompson Linear Polarizer
BP	: Beam Profiler
L1/L2	: Plano-convex lens

LIST OF SYMBOLS

$\Delta_{GH,IF}$	: Spatial GH, IF Shift
$\Theta_{GH,IF}$	: Angular GH, IF Shift
θ	: Angle of incidence / Incident angle
n	: Refractive index
λ	: Wavelength of incident light
ε	: Angle of deviation / rotation from orthogonal condition
γ	: Polarization angle
α	: Pre-selection angle
β	: Post-selection angle
δ	: Relative phase difference between p- & s-polarization
η	: Initial phase difference between p- and s-polarization
r	: Complex Fresnel reflection coefficient
R	: Amplitude of the reflection coefficient
ϕ	: Phase of the reflection coefficients
ϱ	: Real part of 1st order derivative of reflection coefficient
φ	: Imaginary part of 1st order derivative of reflection coefficient
w_0	: Beam waist
z, z_r	: Propagation distance
z_R	: Rayleigh range
x_{wvas}	: Amplified photonic spin splitting in longitudinal direction
y_{wvas}	: Amplified photonic spin splitting in transverse direction

List of publications

[*]**1. S. Mandal**, D. C. Dey, A. Sett, and M. Pradhan, "Photonic spin splitting with orbital angular momentum pointer states via modified weak measurement," ***Physical Review A*** 112, 033511 (**2025**).

[*]**2. S. Mandal**, A. Sett, D. C. Dey and M. Pradhan, "Observation of the Goos-Hänchen shift in monolayer WSe_2 for an arbitrary linearly polarized incident light beam using weak measurement," ***Journal of the Optical Society of America B*** 41 (12), 2714-2720 (**2024**).

[*]**3. S. Mandal**, A. Das, and M. Pradhan, "Simultaneous observation of transverse and longitudinal photonic spin splitting in monolayer WSe_2 via quantum weak measurement," ***Journal of Applied Physics*** 135 (20) (**2024**).

[*]**4. S. Mandal**, A. Das, and M. Pradhan, "Weak measurement of the Goos–Hänchen shift for a Hermite–Gaussian laser beam," ***Journal of Optics*** 26 (4), 045403 (**2024**).

[*]**5. S. Mandal**, A. Das, and M. Pradhan, "Polarization-controlled Goos–Hänchen shift by weak value amplification in total internal reflection," ***Journal of the Optical Society of America B*** 41 (3), 750-755 (**2024**).

6. S. Mandal, A. Rehman, D. C. Dey, A. Sett, M. W. Horn, M. Pradhan, and A. Lakhtakia, "Transmission-mode geometric phase and photonic-spin-Hall-effect characteristics of circular Bragg phenomenon through quantum weak measurements", ***(Under review)*** **(2025).**

7. A. Sett[$], **S. Mandal[$],** D. C. Dey, and M. Pradhan, "Investigation of orbital angular momentum sidebands in anisotropic few-layered ReS_2," ***Journal of Optics*** 27, 085401 **(2025)** ($ contributed equally).

8. D. C. Dey[$], **S. Mandal[$],** A. Sett, and M. Pradhan, "Observation of non-cyclic Pancharatnam-Berry phase in monolayer $ReSe_2$," ***Journal of the Optical Society of America B*** 42, 1746-1752 **(2025)** ($ contributed equally).

9. A. Pal, K. Mondal, S. Mandal, S. Chakraborty, I. Patra, and M. Pradhan, "LED-based broadband cavity-enhanced spectrometer for high-sensitive optical detection of diacetyl in gas phase," ***Journal of Chemical Sciences*** 136 (4), 87 **(2024).**

10. A. Das, S. Mandal, R. A. Fiallo, M. W. Horn, A. Lakhtakia, and M. Pradhan, "Geometric phase and photonic spin Hall effect in thin films with architected columnar morphology," ***Journal of the Optical Society of America B*** 40, 2418-2428 **(2023).**

11. A. Das, S. Mandal and M. Pradhan, "Signature of the photonic spin Hall effect in monolayer MoS_2 via weak measurement," ***Journal of the Optical Society of America B*** 39, 1822-1828 **(2022).**

12. A. Das, S. Mandal and M. Pradhan, "Observation of Imbert–Fedorov shift in monolayer MoS_2 via quantum weak measurement," ***Optics Letters*** 46, 5826-5829 **(2021).**

* Included in this thesis

INTRODUCTION

Optical beam shift, one of the most fascinating light matter interactions, have become a center of active research in last few decades because of its fundamental importance as well as huge application possibilities. This sub-wavelength scale phenomena have led to not only rigorous theoretical studies but also several advanced optoelectronic and sensors applications are being proposed. Consequently, it is becoming more and more obvious to investigate the details of this light-matter interaction and its modulating parameters. However, the measurement of this tiny effect is challenging and the weak value amplification technique is utilized. In this thesis, we not only will unveil interesting characteristics of beam shifts experimentally but also developed appropriate theoretical models that support the experimental findings. We have demonstrated that the displacement of beam centroid position in longitudinal (Goos-Hänchen shift) and transverse (Imbert-Fedorov shift/Photonic spin Hall effect) direction can be manipulated by properties of incident light beam (polarization state, beam shape, orbital angular momentum), interaction medium and the configuration parameters of the experimental setup (angle of incidence, post-selection angle) as will be elaborated in detail in this thesis.

Since the discovery of optical beams carrying intrinsic orbital angular momentum (OAM) by Allen et. al in 1992, it has been proven to have diverse applications in the field of wave front manipulations, optical trapping, high resolution imaging, data transmission and optical communications, and even in quantum information owing to its extra-ordinary properties such as helical phase structure, phase singularity at the core of intensity profile and multi-dimensional topological charges, respectively.

In recent years, the advancement of science and technology has generated immense curiosity in layered materials. A whole new branch of two-dimensional (2D) materials has emerged in the community. There are several members in 2D materials such as graphene, transition metal di-chalcogenides (TMDC) and more are being added day by day. Due to their inherent properties, TMDCs show a lot of interesting phenomena like charge density waves, magnetism, and superconductivity making them a focus of the research community. Molybdenum di-sulphide (MoS_2) is one of the most studied TMDCs which have great potential in nano-electronics and optoelectronics. Keeping in mind the importance of 2D materials in optics and optical applications, we have chosen them as the basic system to study optical beam shift both theoretically and experimentally.

Starting from the solutions of Maxwell's equations in various coordinate systems - including Cartesian (plane wave), spherical, and cylindrical - we have introduced the concept of beam-like solutions via the paraxial approximation in *Chapter* 1. We then discussed several optical beams, including Gaussian, Hermite–Gaussian, and Laguerre–Gaussian beams, highlighting their key properties and applications in nano-photonics. A brief overview of techniques for generating higher-order beams using different optical elements is provided, with particular emphasis on the role, advantages, and limitations of spatial light modulators (SLMs). The chapter concludes with an introduction to vector beams, setting the stage for their further exploration in subsequent chapters.

Chapter 2 starts with the basic introduction to the phenomena of optical beam shifts. Different types of non-specular effects, their origin and related initial controversy, final explanation, several modulating parameters, and the available application possibilities are discussed in detail.

Chapter 3 provides a brief overview of the available experimental techniques and difficulties in the measurement of the small shift values. Then the idea of quantum weak measurement along with the optical analog of it and its application in the study of detecting tiny optical effects are briefly discussed.

In *Chapter* 4, we investigate the polarization-controlled Goos-Hänchen (GH) shift near the critical angle of incidences in total internal reflection condition. A general theoretical model using Jones matrix formalism is proposed for the reflection of a Gaussian light beam. Along with the polarization dependence, the incident angle dependence is also presented for arbitrary linear polarization state. The application idea of tunable GH shift values in bio-sensor or polarization-controlled devices is also discussed in detail.

Chapter 5 mainly deals with the interaction surface dependent variation of GH shifts. Due to the interaction of incident light beam with monolayered (ML) tungsten di-selenide (WSe_2) placed on SiO_2-Si substrate the critical angle drastically shifted to other angle of incidence as compared to the glass-air interface. Then the variation of small GH shifts values with angle of incidence, post-selection angle and linear polarization state are elaborated experimentally. Using transfer matrix method (TMM) the reflection coefficients are calculated and used in the theoretical model of weak value amplified GH shifts. Also, a comparison with the previous work is discussed to establish the benefit of using ML WSe_2/SiO_2-Si structure and the weak value amplification technique over other ones.

Chapter 6 explores how the beam shape can affect the magnitude of optical beam shifts near the critical angle of incidences. To do so, two orthogonal first order Hermite-Gauss (HG) light beam, HG_{10} and HG_{01} are created using phase only spatial light modulator (SLM) and the experimental setup is upgraded as we will see. The experimental data presents angular dependence of GH shifts in TIR region for both the modes. A comparison of shift values for HG modes with the case simple Gaussian light beam (TEM_{00}) clearly dictate the advantage of using higher order light beams over Gaussian beam. Also, the manipulation of beam shape at orthogonal condition and a compatible theoretical model based on propagation of light through different optical elements are elaborated.

In *Chapter* 7, the study of photonic spin splitting (PSS) in transverse as well as longitudinal direction is investigated using p- and s-polarized Gaussian light beam. The investigation is focused near the Brewster angle of incidence during the partial reflection at ML WSe_2/SiO_2-Si interface. Interesting features of PSS depending upon the incident angle, polarization state, and post-selection angle are described. Theoretically an improved weak measurement model is developed using wave vector formalism to support the experimentally obtained amplified PSS in both transverse and longitudinal direction.

Chapter 8 describes a rigorous study of generalized PSS using arbitrary linearly polarized orbital angular momentum (OAM) incident light beam at air-glass interface. How the PSS values can be tuned using post-selection angle, polarization angle at different incident angle and topological charge of incident light beam are thoroughly investigated. The developed generalized theoretical model using angular spectrum representation is valid for external as well as internal reflection from absorptive material interaction surface also irrespective of coupling strength. Even the optimum overlap of pre- and post-selection states to get maximum amplified PSS is also elaborated. The experimental data proves the consistency of theoretical model is at strong (angle of incidence near Brewster angle) and weak coupling (far from Brewster incidence) region.

Finally, *chapter* 9 discloses the overall summary and future prospectives of the works extensively presented in this thesis.

Contents

1 Different Optical Beams

Beginning with Maxwell's equations, their solutions are examined in different coordinate systems, with particular emphasis on beam-like solutions such as Gaussian, Hermite–Gaussian, and Laguerre–Gaussian beams. In parallel, various techniques for generating these beam profiles are outlined, and the applications of higher-order light beams in nano-photonics are summarized here.

1.1 Introduction

The visible light constitutes only a small portion of the broad electromagnetic spectrum, which extends from γ-rays at one extreme to radio waves at the other. Between these two limits lie X-rays, ultraviolet radiation, visible light, infrared radiation, and microwaves, arranged in decreasing order of frequency. It is well known that light exhibits a dual character - showing both particle-like (photon) and wave-like behaviours - though these two aspects are mutually exclusive in a single measurement. In general, the propagation of light in free space or in a medium can be well described by classical electrodynamics, whereas the interaction of light with matter requires a quantum mechanical framework.

In this thesis, our primary focus is on the study of *optical beam shifts* using different *optical beam profiles*, which correspond to the wave nature of light. Beginning with the classical formulation based on Maxwell's equations, we derive the wave equation and explore its solutions in various forms, including plane, spherical, and cylindrical waves. We then obtain the exact Helmholtz equation and show how, under the paraxial approximation, it leads to beam-like solutions in different coordinate systems. This formalism allows us to establish that light beams possessing specific azimuthal phase structures carry orbital angular momentum (OAM). The essential characteristics and generation techniques of such optical beams are discussed briefly. The *chapter* concludes with an introduction to vector beams and a discussion on the potential applications of higher-order light beams as established in contemporary research.

1.2 Maxwell Equation

The set of Maxwell's equations describe the behavior of the electromagnetic field, encompassing both its electric and magnetic properties. The most general form of the macroscopic Maxwell's equations in SI units can be written as [1],

$$\nabla . \boldsymbol{D}(\boldsymbol{r}, t) = \rho(\boldsymbol{r}, t) \tag{1.1}$$

$$\nabla . \boldsymbol{B}(\boldsymbol{r}, t) = 0 \tag{1.2}$$

$$\nabla \times \boldsymbol{E}(\boldsymbol{r}, t) + \frac{\partial \boldsymbol{B}(\boldsymbol{r}, t)}{\partial t} = 0 \tag{1.3}$$

$$\nabla \times \boldsymbol{H}(\boldsymbol{r}, t) - \frac{\partial \boldsymbol{D}(\boldsymbol{r}, t)}{\partial t} = \boldsymbol{J}(\boldsymbol{r}, t) \tag{1.4}$$

Where, the sources, $\rho(\boldsymbol{r},t)$ and $\boldsymbol{J}(\boldsymbol{r},t)$ present in the right, are the free charge and current densities, respectively.

The fields appearing on the left-hand side of Maxwell's equations can be grouped into two categories: the vacuum fields, represented by the electric field $\mathbf{E}(\mathbf{r},t)$ and the magnetic flux density $\mathbf{B}(\mathbf{r},t)$, and the macroscopic fields, represented by the electric displacement $\mathbf{D}(\mathbf{r},t)$ and the magnetic field intensity $\mathbf{H}(\mathbf{r},t)$. Together, these equations describe the interdependence between the electric and magnetic fields and their physical sources.

The first equation (1.1), commonly known as Gauss's law, states that electric charges act as the sources or sinks of electric displacement field lines. Equation (1.2) indicates that magnetic field lines have neither sources nor sinks, implying that magnetic monopoles do not exist in nature. Equation (1.3), known as Faraday's law of electromagnetic induction, reveals that a time-varying magnetic field gives rise to a circulating electric field. Finally, equation (1.4), or the Ampère–Maxwell law, embodies two fundamental observations: first, that electric currents produce circulating magnetic fields (Ampère's law), and second, that a time-varying electric displacement field also generates a circulating magnetic field, as introduced by Maxwell.

1.3 Wave Equation

The solutions of Maxwell's equations cannot be determined without knowledge of the material properties of the medium with which the electromagnetic fields interact. Specifically, it is essential to establish the relationships between the electric field $\mathbf{E}(\mathbf{r},t)$ and the electric displacement field $\mathbf{D}(\mathbf{r},t)$, as well as between the magnetic field $\mathbf{H}(\mathbf{r},t)$ and the magnetic induction $\mathbf{B}(\mathbf{r},t)$. Considering the propagation of an electromagnetic (light) wave through a medium characterized by permittivity ε and permeability μ, the constitutive relations connecting these quantities are expressed as [1],

$$\boldsymbol{D}(\boldsymbol{r},t) = \epsilon \boldsymbol{E}(\boldsymbol{r},t) \tag{1.5}$$

$$\boldsymbol{B}(\boldsymbol{r},t) = \mu \boldsymbol{H}(\boldsymbol{r},t) \tag{1.6}$$

Where $\epsilon = \epsilon_0(1+\chi^e)$, $\mu = \mu_0(1+\chi^m)$ with ϵ_0 and μ_0 denoting the vacuum permittivity and permeability, respectively and χ^e, χ^m represent the electric and magnetic susceptibilities, respectively.

In general, the permittivity ε and permeability μ of a medium are tensor quantities and may also be complex-valued, depending on the material properties. Their tensorial nature accounts for anisotropy, while the complex components represent absorption or loss within the medium. These parameters determine whether the medium behaves linearly or nonlinearly under the influence of electromagnetic fields. A detailed discussion of these aspects lies beyond the scope of the present work, as they are not central to the objectives of this thesis. Comprehensive treatments can be found in standard textbooks on Electromagnetism [1-3].

The electric and magnetic fields appearing in Maxwell's equations are inherently coupled. However, in a source-free medium, where $\rho(\mathbf{r}, t) = 0$ and $\mathbf{J}(\mathbf{r}, t) = 0$, these equations can be decoupled, leading to the homogeneous form of Maxwell's equations in vacuum, expressed as follows:

$$\nabla . \boldsymbol{E}(\boldsymbol{r}, t) = 0 \tag{1.7}$$

$$\nabla . \boldsymbol{B}(\boldsymbol{r}, t) = 0 \tag{1.8}$$

$$\nabla \times \boldsymbol{E}(\boldsymbol{r}, t) + \frac{\partial \boldsymbol{B}(\boldsymbol{r}, t)}{\partial t} = 0 \tag{1.9}$$

$$\nabla \times \boldsymbol{B}(\boldsymbol{r}, t) - \mu\epsilon \frac{\partial \boldsymbol{E}(\boldsymbol{r}, t)}{\partial t} = 0 \tag{1.10}$$

By taking the curl of equation (1.9) and interchanging the order of the curl and time derivative in the second term, followed by substituting equation (1.10) into the resulting expression, we obtain:

$$\nabla \times [\nabla \times \boldsymbol{E}(\boldsymbol{r}, t)] = -\mu\epsilon \frac{\partial^2 \boldsymbol{E}(\boldsymbol{r}, t)}{\partial t^2} \tag{1.11}$$

Using the well-known vector identity, $\nabla \times (\nabla \times \boldsymbol{f}) = \nabla(\nabla . \boldsymbol{f}) - \nabla^2 \boldsymbol{f}$, equation (1.11) can be written as,

$$\nabla[\nabla . \boldsymbol{E}(\boldsymbol{r}, t)] - \nabla^2 \boldsymbol{E}(\boldsymbol{r}, t) = -\mu\epsilon \frac{\partial^2 \boldsymbol{E}(\boldsymbol{r}, t)}{\partial t^2} \tag{1.12}$$

Finally, using equation (1.7) in (1.12), we have,

$$\nabla^2 \boldsymbol{E}(\boldsymbol{r}, t) - \mu\epsilon \frac{\partial^2 \boldsymbol{E}(\boldsymbol{r}, t)}{\partial t^2} = 0 \tag{1.13}$$

This represents the wave equation for the vector field $\boldsymbol{E}(\boldsymbol{r},t)$, where the propagation speed is given by $v = \frac{1}{\sqrt{\mu\epsilon}}$. In a similar manner, by taking the curl of equation (1.10) and employing equations (1.8) and (1.9), an analogous wave equation for $\boldsymbol{B}(\boldsymbol{r},t)$ can be derived as,

$$\nabla^2\boldsymbol{B}(\boldsymbol{r},t) - \mu\epsilon\frac{\partial^2\boldsymbol{B}(\boldsymbol{r},t)}{\partial t^2} = 0 \tag{1.14}$$

Thus, both of the wave equation (1.13) and (1.14) are linear, homogeneous, second-order differential equation. Owing to its linearity, the principle of superposition holds true. This principle states that if $\boldsymbol{E}_i(i = 1,2,3,\dots,n)$ are individual solutions of the wave equation, then any linear combination $\sum_i \alpha_i\boldsymbol{E}_i$ also represents a valid solution, where α_i are arbitrary constants (real or complex).

The specific form of the solutions depends on the physical conditions of the system. All light fields in a homogeneous medium must satisfy the wave equation; however, realizing a particular solution experimentally requires precise control of external parameters. Some solutions are mathematically convenient yet difficult to achieve in practice. Conversely, deliberate manipulation of external conditions can yield a specific class of solutions - the generation of coherent light in a laser being a prominent example of this principle.

In the following sections, several monochromatic solutions of the wave equation in a homogeneous medium are discussed in detail.

1.3.1 Plane Wave Solution

The general solution of the wave equation (1.13) and (1.14) can be written in the form as,

$$\boldsymbol{E}(\boldsymbol{r},t) = \boldsymbol{E_0}(\boldsymbol{r},t)\exp[i\phi(\boldsymbol{r},t)] \tag{1.15}$$

$$\boldsymbol{B}(\boldsymbol{r},t) = \boldsymbol{B_0}(\boldsymbol{r},t)\exp[i\phi(\boldsymbol{r},t)] \tag{1.16}$$

Where $\boldsymbol{E_0}(\boldsymbol{r},t)$and $\boldsymbol{B_0}(\boldsymbol{r},t)$ are the amplitude of electric and magnetic field of EM waves and $\phi(\boldsymbol{r},t)$ is the phase of the wave. A plane wave is characterized by phase $\phi(\boldsymbol{r},t)$ at any given time; remain constant in a plane perpendicular to the direction of propagation of the wave. The phase,

$$\phi(\boldsymbol{r}, t) = \tilde{\boldsymbol{k}}.\boldsymbol{r} - \omega t \tag{1.17}$$

obeys this condition as the dot product $\tilde{\boldsymbol{k}}.\boldsymbol{r}$ remains constant ($\tilde{k}r_0$) as the tip of the position vector, $\boldsymbol{r}$ moves over a given plane perpendicular to the direction of propagation $\tilde{\boldsymbol{k}}$. Here, r_0 is the component of $\boldsymbol{r}$ in the direction of propagation. In general, the wave vector is complex given by,

$$\tilde{\boldsymbol{k}} = \boldsymbol{k} + i\boldsymbol{\varsigma} \tag{1.18}$$

Where $\boldsymbol{k}$ is the real part of the propagation vector and $\boldsymbol{\varsigma}$ is real attenuation vector denoting the attenuation (or the gain) of the amplitude of a wave during the propagation through a medium. It can be shown that, any well-behaved function of $(\pm\tilde{\boldsymbol{k}}.\boldsymbol{r} - \omega t)$ can represent a plane wave.

Now, by substituting equation (1.15) into Maxwell's equations (1.7) - (1.10), we obtain:

$$\tilde{\boldsymbol{k}}.\boldsymbol{E_0} = 0 \tag{1.19}$$

$$\tilde{\boldsymbol{k}}.\boldsymbol{B_0} = 0 \tag{1.20}$$

$$\boldsymbol{B_0} = \frac{\tilde{\boldsymbol{k}} \times \boldsymbol{E_0}}{\omega} \tag{1.21}$$

$$\boldsymbol{E_0} = -\frac{\tilde{\boldsymbol{k}} \times \boldsymbol{B_0}}{\mu\epsilon\omega} \tag{1.22}$$

The above equations represent the transversality condition for the complex field amplitudes $\boldsymbol{E}_0$ and $\boldsymbol{B}_0$. It should be noted that the electric and magnetic fields are transverse to the real wave vector $\boldsymbol{k}$ only when the medium is non-absorbing ($\boldsymbol{\varsigma} = 0$). Furthermore, by combining equations (1.21) and (1.22) and applying the vector triple product identity, we can obtain,

$$\tilde{\boldsymbol{k}}^{\boldsymbol{2}} = \tilde{\boldsymbol{k}}.\tilde{\boldsymbol{k}} = \mu\epsilon\omega^2 = \tilde{n}^2\frac{\omega^2}{c^2} \tag{1.23}$$

Where,

$$\tilde{n}^2 = \mu\epsilon c^2 \tag{1.24}$$

With $\tilde{n}$ being the complex refractive index of the medium which is given by,

$$\tilde{n} = n + i\tau \tag{1.25}$$

Where n and τ are known as the refractive and extinction indices of the medium, respectively. A few simple steps following equations (1.23) - (1.25), we can get,

$$k^2 - \varsigma^2 = (n^2 - \tau^2)\frac{\omega^2}{c^2} \qquad (1.26)$$
$$\boldsymbol{k}.\boldsymbol{\varsigma} = n\tau\frac{\omega^2}{c^2}$$

So, it can be concluded that in place of permittivity and permeability, the complex refractive can now describe the bulk properties of an optical material.

1.3.2 Cylindrical and Spherical Wave Solution

An infinite line source located at $r = 0$ in an isotropic medium produces coaxial cylindrical wavefronts that either propagate outward or converge inward toward the line at $r = 0$. The harmonic cylindrical wave solution of the wave equation can thus be expressed as,

$$E(r,t) = \frac{A}{\sqrt{r}}\exp[i(\pm kr - \omega t)] \qquad (1.27)$$

Similarly, a point source generates spherical wavefronts that either propagate radially outward from $r = 0$ or converge toward $r = 0$. The scalar electric field of a harmonic spherical wave can, in general, be expressed as,

$$E(r,t) = \frac{A}{r}\exp[i(\pm kr - \omega t)] \qquad (1.28)$$

In both cases, the radial dependence - $1/\sqrt{r}$ for cylindrical waves and $1/r$ for spherical waves - can be derived by integrating the wave equation expressed in cylindrical or spherical coordinates, respectively, while taking into account the principle of energy conservation.

1.3.3 Beam-like Solution: Helmholtz Equation and Paraxial Approximation

One of the most striking characteristics of laser light is its exceptional directionality, closely resembling that of a plane wave. However, unlike a plane wave, the field amplitude of laser light decreases rapidly in the transverse plane. Additionally, laser light exhibits divergence during propagation, although for short distances this divergence is much smaller than that of a spherical wave. While laser light is not perfectly monochromatic, it represents the closest practical approximation to monochromatic light. Therefore, to model a solution that closely approximates laser light, the field should be nearly monochromatic, highly directional, and exhibit minimal divergence.

We begin by assuming that both the refractive index of the medium and the propagation vector of the light wave are real, so that the electric field of a single-frequency wave can be expressed as,

$$\boldsymbol{E}(\boldsymbol{r},t) = Re\{\boldsymbol{\mathcal{E}}(\boldsymbol{r})\exp(-i\omega t)\} \tag{1.29}$$

Where ω is the angular frequency of oscillation and $\boldsymbol{\mathcal{E}}(\boldsymbol{r})$ is the complex spatially dependent part of the electric field. Similar type of equation also exists for the magnetic field.

Now, substituting equation (1.23) into equation (1.13), we obtain the vector Helmholtz equation for the complex electric field as follows:

$$\nabla^2\boldsymbol{\mathcal{E}}(\boldsymbol{r}) + k^2\boldsymbol{\mathcal{E}}(\boldsymbol{r}) = 0 \tag{1.30}$$

Where $k = \omega/c$ is the wave vector with 'c' being the speed of light in vacuum.

This is a vector equation that specifies the direction of oscillation of the electric field. However, as noted by Lax et al. [4], the paraxial approximation of the Helmholtz equation (1.30) applied to a single polarization is not fully consistent with Maxwell's equations (1.7)–(1.10) and therefore must be treated with caution. To avoid such inconsistencies, it is preferable to formulate the Helmholtz equation in terms of the vector potential $\boldsymbol{A}$ [4]. The concept of the vector potential $\boldsymbol{A}$ can be introduced starting from equation (1.8) as follows:

$$\boldsymbol{B} = \nabla \times \boldsymbol{A} \tag{1.31}$$

Again, using this in equation (1.9), we get,

$$\nabla \times \left(\boldsymbol{E} + \frac{\partial \boldsymbol{A}}{\partial t}\right) = 0 \tag{1.32}$$

which gives us the idea of existence of a scalar potential Φ defined as,

$$\nabla\Phi = -\left(\boldsymbol{E} + \frac{\partial \boldsymbol{A}}{\partial t}\right) \tag{1.33}$$

Now, the equation (1.31) and (1.33) identically satisfies the Maxwell's equation (1.8) and (1.9). To find out the dynamical behavior of scalar and vector potential we need to substitute equation (1.31) and (1.33) in (1.7) and (1.10), respectively.

Next, utilizing the Lorentz gauge, $\nabla.\boldsymbol{A} + \frac{1}{c^2}\frac{\partial\Phi}{\partial t} = 0$, we can get,

$$\nabla^2 \boldsymbol{A} - \frac{1}{c^2}\frac{\partial^2}{\partial t^2}\boldsymbol{A} = 0 \tag{1.34}$$

$$\nabla^2 \Phi - \frac{1}{c^2}\frac{\partial^2}{\partial t^2}\Phi = 0 \tag{1.35}$$

From these, the Helmholtz equation for the vector potential can be derived by considering the ansatz, $\boldsymbol{A} = Re[\boldsymbol{\mathcal{A}} \exp(-i\omega t)]$ for a monochromatic wave, yielding:

$$\nabla^2 \boldsymbol{\mathcal{A}} + k^2 \boldsymbol{\mathcal{A}} = 0 \tag{1.36}$$

By solving this as we get the equation of vector potential, the electric field can be calculated as,

$$\boldsymbol{\mathcal{E}} = i\omega \left[\boldsymbol{\mathcal{A}} + \frac{\boldsymbol{\nabla}(\boldsymbol{\nabla}.\boldsymbol{\mathcal{A}})}{k^2}\right] \tag{1.37}$$

The vector form of the Helmholtz equation can be reduced to a scalar form by assuming a constant polarization vector of unit magnitude. Let the optical axis be along the z-direction, and choose the vector fields to be polarized transverse to this axis. Introducing a general symbol $\boldsymbol{\Psi}$ to represent the electric field, magnetic induction, or the vector potential, and denoting the unit polarization vector by $\mathbf{s}$, we can write:

$$\boldsymbol{\Psi} = \boldsymbol{s}\xi(\boldsymbol{r}) \tag{1.38}$$

Following this ansatz, the vector Helmholtz equation (1.30) can be reduced to scalar form:

$$\nabla^2 \xi + k^2 \xi = 0 \tag{1.39}$$

So, this is the starting point of the analysis of *several optical beams* having different shape and properties.

In geometric optics, a ray that makes a very small angle with the optical axis is referred to as *paraxial*. Similarly, if the angular spectrum of a light beam is composed primarily of plane waves whose propagation directions lie close to the beam's main propagation axis (here, the z-axis), the beam is termed a *paraxial light beam*. Consequently, for a paraxial light beam, the dominant component of the wave vector $\boldsymbol{k}$ lies along the z-direction and can be expressed as:

$$k_z = \sqrt{k^2 - \kappa^2} \approx k - \frac{\kappa^2}{2k} \tag{1.40}$$

Where $\kappa = \sqrt{k_x^2 + k_y^2}$ is denoted as transverse wave number.

For a field propagating predominantly along the z-axis, a suitable solution to the scalar Helmholtz equation (1.39) can be expressed as:

$$\xi(\boldsymbol{r}) = v(\boldsymbol{r})\, exp(ikz) \tag{1.41}$$

Where $v(\boldsymbol{r})$ is the amplitude distribution that slowly varies with respect to z. This is because the primary factor $exp(ikz)$ has been written explicitly. Now, substituting Eq. (1.41) into (1.39), we obtain a partial differential equation for the amplitude distribution v,

$$\nabla_t^2 v + \frac{\partial^2}{\partial z^2} v + 2ik \frac{\partial}{\partial z} v = 0 \tag{1.42}$$

Considering the slow variation of the profile in z direction as compared to the variation in transverse plane, we can say,

$$\left|\frac{\partial^2 v}{\partial z^2}\right| \ll |\nabla_t^2 v| \tag{1.43}$$

The other consideration is that the second derivative with respect to z is much smaller than the first derivative multiplied by the overall wavenumber,

$$\left|\frac{\partial^2 v}{\partial z^2}\right| \ll k \left|\frac{\partial v}{\partial z}\right| \tag{1.44}$$

Applying both of the above conditions to equation (1.42) we get,

$$\nabla_t^2 v + 2ik \frac{\partial}{\partial z} v = 0 \tag{1.45}$$

This is known as *paraxial wave equation (PWE)* which describes a wave that propagates in a highly directional manner along the z-axis. So, we are looking for a restricted class of solution of PWE which are also well known in the context of laser optics [5].

The most well-known solution of the paraxial wave equation (PWE) is the Gaussian beam. Other important and widely used solutions include the Hermite–Gaussian (HG), Laguerre–Gaussian (LG), and Bessel–Gaussian (BG) beams, which naturally arise as solutions in rectangular and cylindrical coordinate systems. Among these, the Bessel beam is particularly significant due to the separability of its transverse and longitudinal components. Collectively, these beam types form a complete set of solutions to the PWE. While HG beams do not possess orbital angular momentum (OAM), both LG and BG beams can carry OAM, which makes them valuable for various advanced optical applications. To understand the key characteristics

of these fundamental beam types, we begin with the Gaussian beam, followed by brief discussions of the others.

(a) Gaussian beam

For Gaussian beam, the intensity in the plane $z = 0$, called the *waist plane* is assumed as of a Gaussian form,

$$I(x, y, 0) = v(x, y, 0)v^*(x, y, 0) = I_0 e^{-2(x^2+y^2)/w_0^2} \tag{1.46}$$

Where I_0 is the peak intensity and w_0 is the root mean square width in the waist plane.

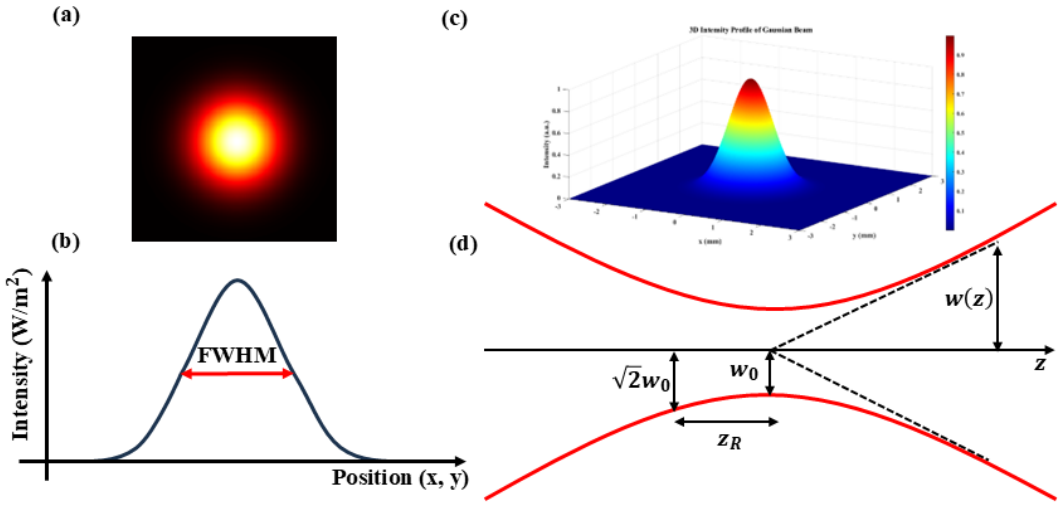

Figure 1.1 (a) Transverse intensity profile of a Gaussian beam propagating in z direction. (b) Variation of intensity with transverse coordinate (x, y) (c) 3d intensity distribution (d) Gaussian beam width, $w(z)$ as a function of distance z along the beam, which forms a hyperbola, w_0: waist size of the beam, z_R: Rayleigh range.

As evident from experiment that the transverse intensity profile remains Gaussian, the form of the possible solution is assumed as,

$$v_G(\boldsymbol{r}) = A_0 e^{ik(x^2+y^2)/2q(z)} e^{ip(z)} \tag{1.47}$$

Where $q(z)$ and $p(z)$ are complex functions which need to be determined.

Substituting (1.47) in equation (1.42), rigorous calculations afterwards lead us to the solution of the form,

$$v_G(\boldsymbol{r}) = A_0 e^{-i\Phi_G(z)} \left[\frac{1}{\sqrt{1+z^2/z_R^2}} e^{ik(x^2+y^2)/2R(z)} \right] e^{-(x^2+y^2)/w^2(z)} \tag{1.48}$$

Where, $R(z) = z + z_R^2/z$ is the radius of curvature, $w(z) = w_0\sqrt{1+z^2/z_R^2}$ is the effective beam width as function of z, $\Phi_G(z) = \tan^{-1}(z/z_R)$ is the Gouy phase shift, $z_R = \pi w_0^2/\lambda$ is the Rayleigh range, and $A_0 = \sqrt{I_0}$ is the amplitude of the Gaussian beam.

It is evident that the plane $z = 0$ corresponds to the location of minimum beam width and is referred to as the beam waist. The Rayleigh range is defined as the distance from the waist at which the beam width increases by a factor of $\sqrt{2}$ compared to the waist radius (w_0) [Figure 1.1]. It should be noted that a Gaussian beam is shape-invariant during propagation, meaning that although its width varies along the z-axis, it retains its Gaussian intensity profile throughout.

(b) Hermite-Gaussian (HG) beam

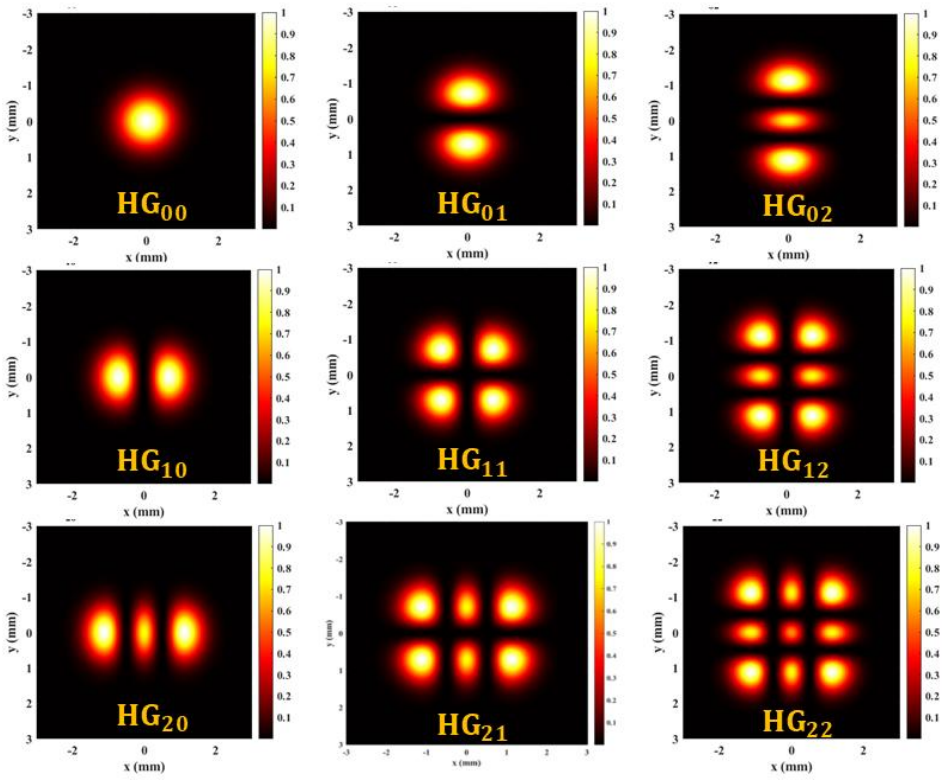

Figure 1.2 Transverse intensity distribution of higher order Hermite-Gauss light beam at z = 0 plane.

In Cartesian co-ordinates it is possible to separate the amplitude function $v(x,y,z)$ into two functions where one of which depends upon one transverse variable, x or y, and on the longitudinal variable z in the following way:

$$v_{mn}^{HG}(x,y,z) = v_m^{HG}(x,z)v_n^{HG}(y,z) \tag{1.49}$$

Where *m* and *n* denote the order of the Hermite polynomial in v_m and v_n, respectively.

Each of these functions follows the PWE in one transverse dimension and that can be obtained by solving the PWE in either one dimension as,

$$\left(\frac{\partial^2}{\partial x^2} + 2ik\frac{\partial}{\partial z}\right)v_m^{HG}(x,z) = 0 \tag{1.50}$$

The solution of this can be presented as a product of Gaussian with a Hermite polynomial in the following form [2],

$$v_m^{HG}(x,z) = \frac{A_m^{HG}}{\sqrt{w(z)}}\exp\left[ik\frac{x^2 z}{2(z^2+z_R^2)}\right]\exp\left(-\frac{x^2}{w^2(z)}\right)\exp\left[-i\left(m+\frac{1}{2}\right)\chi(z)\right]H_m\left(\frac{\sqrt{2}x}{w(z)}\right) \tag{1.51}$$

Here, $A_m^{HG} = \sqrt{1/2^m m!}\,(2/\pi)^{(1/4)}$ is the normalization constant and H_m is the Hermite polynomial of order m.

Following a similar approach, $v_n^{HG}(y,z)$ can be obtained in the same manner. By combining both components, the complete Hermite–Gaussian mode $v_{mn}^{HG}(x,y,z)$ is derived. Figure 1.2 illustrates the intensity profiles for several Hermite–Gaussian beams of different mode orders. Here, the indices m and n represent the number of nodal lines along the x- and y-directions, respectively. The parameters w_0, $w(z)$, $R(z)$, and z_R retain the same definitions as those for the fundamental Gaussian beam discussed earlier. It is evident that for $m = n = 0$, the solution reduces to the fundamental Gaussian beam. The variations in the transverse profiles along x and y at any given z arise solely from the Hermite polynomial factors corresponding to the mode indices m and n. However, the evolution of the Gouy phase in Hermite–Gaussian beams is modified as:

$$\Phi_{HG}(z) = (N+1)\Phi_G(z) = (N+1)\tan^{-1}(z/z_R) \tag{1.52}$$

Where the combined order of the mode, $N = m + n$.

So, in case of higher order modes the Gouy phase will be increased by the factor $(N+1)$ as compared to Gaussian mode.

(c) Laguerre – Gaussian (LG) beam

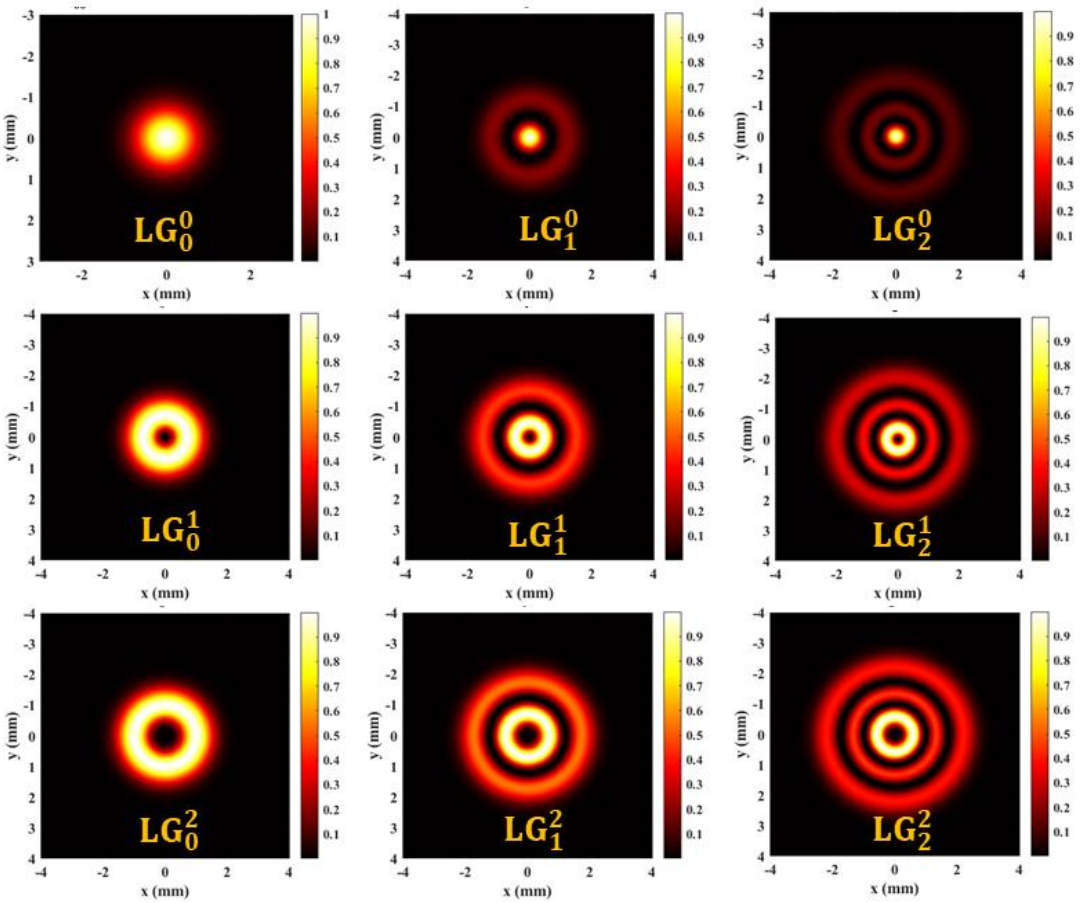

Figure 1.3 Transverse intensity distribution of several Laguerre-Gauss light beam at $z = 0$ plane.

Another complete set of beams are the Laguerre-Gaussian (LG) modes which are the solution of PWE in cylindrical co-ordinates:

$$\left(\frac{1}{\rho}\frac{\partial}{\partial\rho}+\frac{\partial^2}{\partial\rho^2}+\frac{1}{\rho^2}\frac{\partial^2}{\partial\varphi^2}+2ik\frac{\partial}{\partial z}\right)v_{lp}^{LG}=0 \tag{1.53}$$

Where ρ and φ are the radial co-ordinate and azimuthal angle, respectively. The normalized form of the LG beams is given as [2],

$$v_{lp}^{LG}(\rho,\varphi,z) = \frac{A_{lp}^{LG}}{\sqrt{w(z)}}\left(\frac{\rho\sqrt{2}}{w(z)}\right)^{|l|}\exp\left(-\frac{\rho^2}{w^2(z)}\right)L_p^{|l|}\left(\frac{2\rho^2}{w^2(z)}\right) \times \exp\left[-ik\frac{\rho^2 z}{2(z^2+z_R^2)}\right]\exp(il\varphi)\exp[-i\Phi_{LG}(z)] \tag{1.54}$$

Here, $L_p^{|l|}$ are the generalized Laguerre polynomials with appropriate normalization constant $A_{lp}^{LG} = \sqrt{2^{|l|+1}p!/\pi(p+|l|)!}$ and $\Phi_{LG}(z) = (2p+|l|+1)\Phi_G(z)$ is the Gouy phase shift. The LG beams also form an orthonormal set in the mode index p when integrated over the radial coordinate as,

$$\int_0^\infty v_{lp}^{LG}(\rho,\varphi,z)\left[v_{lq}^{LG}(\rho,\varphi,z)\right]^*\rho\, d\rho = \delta_{pq} \tag{1.55}$$

The orthogonality property of the Laguerre–Gaussian (LG) modes give rise to the generalized Laguerre polynomials [6]. The transverse intensity profiles of LG beams exhibit concentric rings, the number of which is determined by the radial index p, as illustrated in Figure 1.3. The second mode index appears in the azimuthal phase term $\exp(il\varphi)$, which produces $|l|$ intertwined helical wavefronts - surfaces of constant phase. The handedness of these helices is determined by the sign of l. The orbital angular momentum (OAM) associated with LG modes originates from this azimuthal phase structure.

Furthermore, the LG modes are orthogonal with respect to the azimuthal index $l$when integrated over the azimuthal variable φ, and in fact, they are orthonormal in both mode indices (p, l) under integration over the entire (ρ, φ) plane, as expressed by:

$$\int_0^{2\pi} d\phi \int_0^\infty \rho\, d\rho\; v_{lp}^{LG}(\rho,\varphi,z)\left[v_{l'q}^{LG}(\rho,\varphi,z)\right]^* = \delta_{ll'}\delta_{pq} \tag{1.56}$$

(d) Bessel - Gauss (BG) beam

The full Helmholtz equation also admits a class of solutions whose transverse profiles remain invariant during propagation. Consequently, these beams were termed *"diffraction-free beams"* by Durnin *et al.* [7]. These are exact solutions of the complete Helmholtz equation; however, they possess infinitely extended transverse profiles. Therefore, their practical realization is constrained by the finite aperture of any real optical system. Another notable feature of these beams is that their field distributions can be separated into radial, azimuthal, and axial components. The corresponding amplitude distribution can be expressed as [2]:

$$\xi_l^B(\rho, \varphi, z) = J_m(\kappa\rho)\exp(il\varphi)\exp(ik_z z) \tag{1.57}$$

Here, $J_m(\kappa\rho)$ denotes the Bessel function [8]. As observed, Bessel beams also possess similar azimuthal phase factor, $\exp(il\varphi)$, as the Laguerre–Gaussian (LG) modes and therefore it also carries orbital angular momentum (OAM). A closer examination reveals that, in transitioning from the full Helmholtz equation to the paraxial wave equation (PWE), the transverse part of the differential equation remains unchanged; however, the relationship among the wavenumbers k, κ, and k_z is get modified. Consequently, the ansatz for the solution of the PWE can be expressed as,

$$v_l^B(\varrho, \varphi, z) = J_m(\kappa\rho)\exp(il\varphi)\exp\left(i\widetilde{k_z}z\right) \tag{1.58}$$

Where $\widetilde{k_z} = k_z - k$, is the reduced longitudinal wavenumber.

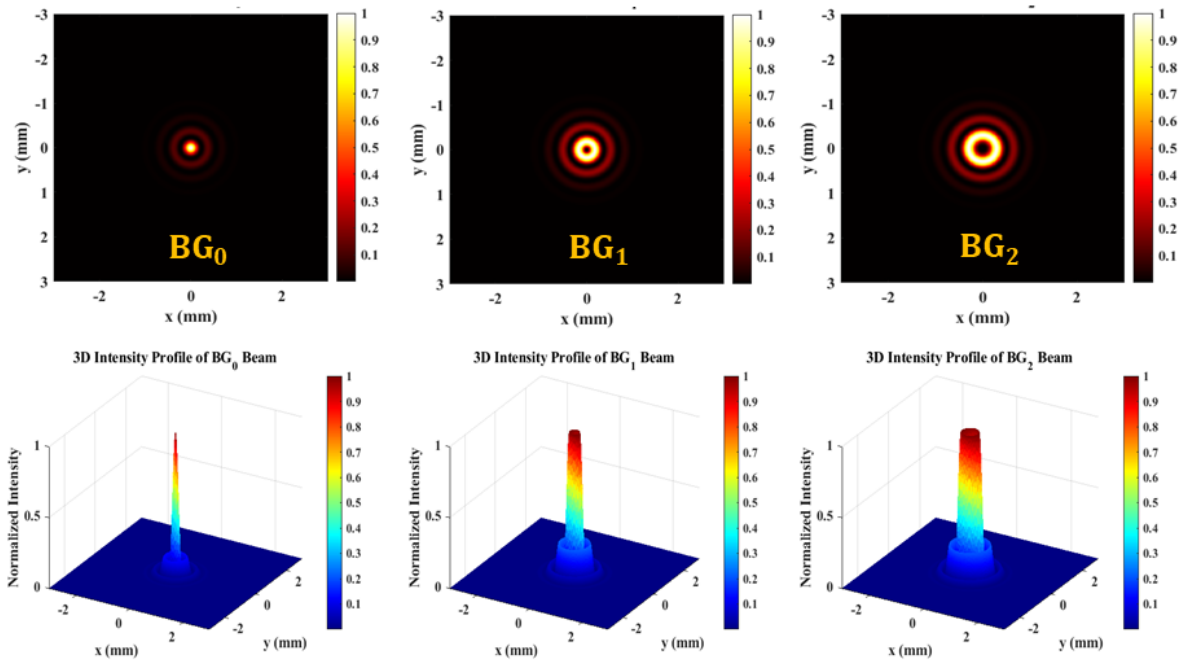

Figure 1.4 2D and 3D intensity distribution of Bessel-Gauss light beam.

The 2D (at $z = 0$ plane) and 3D intensity profiles of Bessel beams are illustrated in Figure 1.4. As evident from the figure, the fundamental (zero-order) Bessel beam exhibits an amplitude maximum at the origin, whereas higher-order Bessel beams (HOBBs) possess an axial phase singularity along the beam axis, where the amplitude vanishes. HOBBs may exist in both vortex (helicoidal) and non-vortex forms.

Unlike conventional optical (or acoustic) beams, Bessel beams maintain their transverse profiles during propagation - showing neither diffraction nor spreading - despite being tightly localized. Another remarkable property of Bessel beams is their self-healing ability: even when partially obstructed, the beam reconstructs itself after a certain propagation distance. Furthermore, it has been both theoretically predicted [8] and experimentally demonstrated [9] that Bessel beams can be engineered to accelerate along arbitrary trajectories in free space, and can even compensate for attenuation during propagation through absorbing media.

1.4 Generation of Different Optical Beams

In optics, a Gaussian beam is an idealized electromagnetic wave whose transverse amplitude envelope follows a Gaussian function, leading to a characteristic Gaussian intensity distribution. It is characterized by a symmetric, single-lobed intensity distribution, minimal divergence, and high spatial coherence. The most straightforward way to generate a Gaussian beam is by employing a single-transverse-mode laser, such as a He–Ne laser, diode laser with spatial filtering, fiber laser, Ti: sapphire laser, or Nd: YAG laser, which naturally emits a Gaussian beam in its fundamental mode. In cases where the laser does not produce a perfect Gaussian beam, several techniques can be employed to achieve a Gaussian profile, including spatial filtering, single-mode optical fiber coupling, or designing the laser cavity to favor fundamental-mode operation.

Although laser beams are often well described by Gaussian modes mathematically, many lasers naturally emit higher-order Gaussian beams. The most common examples of these are the Hermite–Gaussian (HG) beams. Unlike the fundamental Gaussian beam, which has a single-lobed intensity distribution, higher-order HG beams exhibit multiple intensity spots corresponding to their mode indices. There are several approaches to convert a fundamental Gaussian beam into a Hermite–Gaussian beam. One method involves designing the laser cavity to introduce astigmatism using cylindrical lenses or tilted mirrors, allowing the cavity to support higher-order HG modes [10]. While this approach can directly generate pure HG modes from the laser, it is relatively complex and requires precise alignment. An alternative, simpler method is to use two cylindrical lenses placed at specific distances to convert a Gaussian beam into HG_{mn} modes [11].

As discussed earlier, in most cases the transverse field distribution of a laser beam is actually a superposition of Hermite-Gaussian (HG) modes. For a laser cavity with rectangular symmetry, HG modes naturally occur. However, even in cavities with circular symmetry, the

output mode is rarely a pure Laguerre-Gaussian (LG) mode. In circular cavities, astigmatism breaks the frequency degeneracy among the constituent HG modes, resulting in the observation of a “doughnut” mode rather than a pure LG mode. By eliminating astigmatism - either through specially designed laser cavities [12] or by using cylindrical lenses [13] - pure LG modes can be generated.

Apart from transforming HG modes into LG modes, several optical elements such as *spiral phase plates* and *q-plates* can generate LG modes with non-zero orbital angular momentum (OAM) directly from a Gaussian input beam [14]. These elements have an optical thickness that increases continuously with the azimuthal angle, completing a full cycle around the beam. This structure imparts a helical phase front to the transmitted beam. Spiral phase plates require extremely tight mechanical tolerances to ensure that the step height corresponds exactly to an integer multiple of the optical wavelength. Alternatively, they can be deliberately designed with a step height that is *not* an integer multiple of the wavelength, which produces *fractional orbital angular momentum.*

Another interesting optical element in the field of optics is the *axicon lens* [15]. An axicon, also referred to as a rotationally symmetric prism, is a lens with one conical surface and one plano surface. It can convert a Gaussian beam into a non-diffractive Bessel-like beam or a conical, non-diverging beam. During this conversion, the plano side of the axicon should face the collimated input beam. Further details on axicons can be found in [16].

Another convenient method to generate LG mode structures is the use of *holograms*. Holograms are similar to diffraction gratings but are designed so that the first-order diffracted beam acquires a specific phase and amplitude profile. Experimentally, the required grating can be created by interfering the desired beam with a reference beam - for example, a pure Gaussian beam. The resulting interference pattern can be recorded on a holographic film, which, once developed, produces the desired beam when illuminated by the reference beam. Alternatively, the diffraction grating can be calculated numerically and implemented on a *spatial light modulator (SLM)* [17], a commercially available device capable of dynamically controlling the phase or intensity of an optical beam.

Among other useful techniques, the use of diffractive optical elements (DOE) or spatial light modulators (SLM) is particularly prominent. These devices impose a specific phase pattern on an incoming beam, thereby altering its wavefront [17]. This methodology is highly flexible, allowing the creation of arbitrary beam modes and enabling dynamic switching

between different modes. In the following, we briefly discuss the use of SLMs, as this instrument has been employed to generate higher-order light beams in the studies presented in the following chapters.

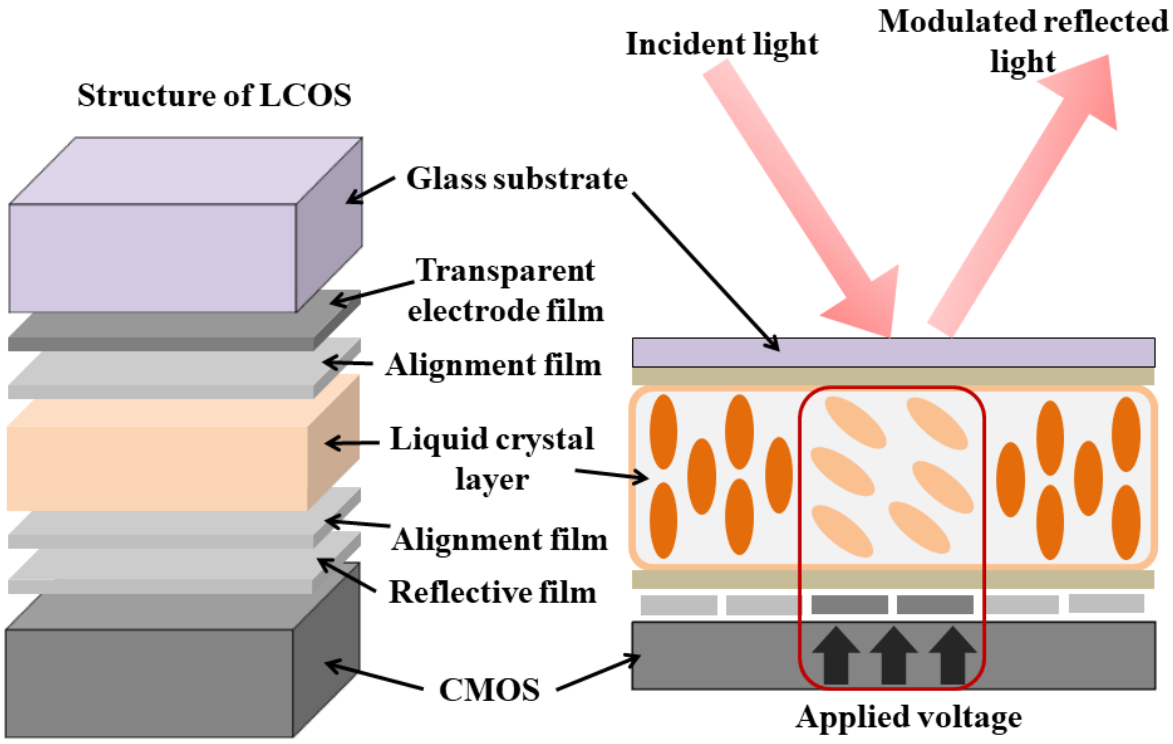

Figure 1.5 Schematic of the structure of spatial light modulator (SLM) and how it works.

Spatial light modulators (SLMs) are essential components in modern optical systems and are extensively used in advanced applications including holography, laser beam shaping, and optical communications. Various types of SLMs are commercially available, including liquid crystal (LC), digital micromirror devices (DMD), electro-optic (EO), waveguide, acousto-optic (AO), and magneto-optic (MO) based SLMs. Among these, the liquid crystal on silicon (LCOS) SLM is particularly popular.

In an LCOS device, the reflective liquid crystal display panel consists of three layers: a silicon backplane, a liquid crystal layer, and a glass substrate with a transparent electrode, as shown in Figure 1.5. When a voltage is applied to the millions of electrodes (pixels) on the silicon backplane, the liquid crystal molecules rotate in response to the electric field. This rotation changes the refractive index of the liquid crystal layer, thereby modulating the phase

of the reflected light. Since each pixel can be individually controlled with different voltages, LCOS SLMs offer precise two-dimensional phase modulation. This capability makes them highly suitable for applications requiring accurate optical control, such as holography and wavefront corrections.

1.5 Vector Beams

So far, we have provided a detailed discussion of scalar solutions to the paraxial wave equation (PWE), which are independent of the polarization of light. In these cases, the polarization state is uniform across the entire beam and does not influence the solution. In contrast, *vector beams* are defined as non-separable combinations of spatial and polarization degree of freedoms. This expanded modal space gives rise to a fascinating class of beams with unique properties and novel applications.

The concept of vector beams is not new; early studies on higher-order spatial modes already hinted at the possibility of combining spatial and polarization degrees of freedom. The first vector beam to gain widespread attention was the *radial vector beam*, a ring-shaped beam with linear polarization oriented radially. When focused, radial beams develop a longitudinal electric field component, which can be exploited in applications such as charged particle acceleration. Moreover, focusing a radial beam produces a tighter beam waist, which is useful for optical manipulation of microscopic objects using optical tweezers.

With the advent of spatial light modulators (SLMs), the production of more complex vector beams - coupling spatial modes with polarization - has become increasingly accessible. Vector beams also exhibit polarization singularities. By combining Hermite–Gaussian (HG) or Laguerre–Gaussian (LG) modes with polarization, a variety of first-order vector beams, including radial, azimuthal, anti-vortex, and mixed vector beams, can be generated. A more detailed tutorial review on vector beams is available in [18].

1.6 Applications

Optical beams with distinct spatial structures and propagation characteristics play vital roles in various fields of optics and photonics. Among them, the Gaussian, Hermite-Gaussian (HG), Laguerre-Gaussian (LG), and Bessel-Gauss (BG) beams are the most commonly studied families, each offering unique advantages suited to specific applications.

(a) Gaussian Beam

The fundamental Gaussian beam (TEM_{00} mode) represents the lowest-order solution of the PWE [equation(1.45)] and exhibits the smallest possible beam divergence for a given waist size. Owing to its high spatial coherence, minimal divergence, and well-defined propagation behaviour, it serves as the basis of most laser systems. Gaussian beams are extensively used in laser material processing, precision cutting, optical communication, microscopy, and fibre coupling, where tight focusing and high beam quality are essential [11, 19]. The simplicity of Gaussian beam optics also makes it an indispensable tool in designing and analysing optical resonators and imaging systems.

(b) Hermite-Gaussian Beam

Hermite-Gaussian (HG) beams, which form an orthogonal set of solutions in Cartesian coordinates, are characterized by rectangular symmetry and multiple intensity lobes defined by Hermite polynomials. They are particularly important in laser cavity mode analysis, where higher-order modes (HG_{mn}) describe deviations from the fundamental Gaussian mode. Controlled generation of HG beams enables structured light formation, beam diagnostics, and mode decomposition in complex laser systems [11]. Furthermore, HG beams have found applications in structured illumination microscopy and laser patterning, where their lobed intensity profiles are exploited to create tailored illumination structures.

(c) Laguerre-Gaussian Beam

Laguerre-Gaussian (LG) beams are the cylindrical-coordinate analogues of HG beams, characterized by azimuthal and radial indices (l, p). Beams with non-zero azimuthal index ($l \neq 0$) possess a helical phase structure and carry orbital angular momentum (OAM) of $l\hbar$ per photon [20]. This unique property allows LG beams to impart mechanical torque to microscopic particles, leading to their wide use in optical trapping, micromanipulation, and optical tweezers [21]. In addition, the ring-shaped intensity profile of LG beams is advantageous in laser drilling, material processing, and optical lithography. The OAM degree of freedom also enables mode-division multiplexing in classical and quantum communication systems, thereby enhancing channel capacity [22]. Their propagation resilience through turbulent or scattering media further extends their potential in free-space optical communication and remote sensing.

(d) Bessel-Gauss Beam

Bessel-Gauss (BG) beams are finite-energy approximations of ideal Bessel beams, featuring a central bright core surrounded by concentric rings [Figure 1.4]. Unlike Gaussian beams, Bessel–Gauss beams exhibit quasi-nondiffracting propagation and a remarkable self-healing property, reconstructing their structure after encountering obstacles [9]. These characteristics make them highly suitable for optical trapping over extended distances, deep tissue imaging, and light-sheet fluorescence microscopy [9]. In laser micromachining and material processing, their long depth of focus and uniform axial intensity distribution enable precision drilling and extended focal machining. Moreover, due to their robustness in scattering environments, BG beams are increasingly utilized in free-space optical links and bio-imaging applications [23].

As a whole, the Gaussian beam provides the foundation for high-quality focusing and coupling; HG modes enable structured illumination and mode analysis; LG beams introduce orbital angular momentum for optical manipulation and multiplexing; while BG beams offer propagation invariance and self-healing for imaging and trapping in complex environments. The diverse spatial and propagation properties of these beams thus support a broad spectrum of applications ranging from fundamental research in light-matter interaction to advanced technologies in optical communication, metrology, and biomedical imaging.

1.7 Concluding remarks

In this chapter, we began with the fundamentals of Maxwell's equations and explored their solutions in plane, spherical, and cylindrical coordinates. We then focused on beam-like solutions, deriving the Helmholtz equation and introducing the paraxial approximation. Solutions of the paraxial wave equation in different coordinate systems were presented, yielding Hermite-Gaussian, Laguerre-Gaussian, and Bessel-Gaussian modes under rectangular and cylindrical symmetries. Various techniques for generating these scalar light beams are discussed, followed by an introduction to vector beams and their unique properties. Additionally, the role of *spatial light modulators (SLMs)* in producing both scalar and vector beams, along with their potential applications, are highlighted.

This comprehensive discussion of higher-order light beams - including their theoretical foundations, generation methods, and applications - provides a solid framework for the analysis of *optical beam shifts using higher-order light beams* in the subsequent chapters.

References

1. J. D. Jackson, *Classical Electrodynamics*, 3rd ed. (John Wiley & Sons, New York, 1998).
2. K. K. Sharma, *Optics: Principles and Applications* (Academic Press, 2006).
3. M. Born and E. Wolf, *Principles of Optics: Electromagnetic Theory of Propagation, Interference and Diffraction of Light* (Elsevier Science, 2013).
4. M. Lax, W. H. Louisell, and B. McKnight, Phys. Rev. A **11**(4), 1365–1370 (1975).
5. A. E. Siegman, *Lasers* (University Science Books, 1986).
6. M. Abramowitz and I. S. Stegun, *Handbook of Mathematical Functions* (Dover Publications, Mineola, NY, 1974).
7. J. Durnin, J. J. Micelli, and J. H. Eberly, Phys. Rev. Lett. **58**(15), 1499–1501 (1987).
8. J. Durnin, J. Opt. Soc. Am. A **4**, 651–654 (1987).
9. F. O. Fahrbach and A. Rohrbach, Opt. Express **18**, 24229–24244 (2010).
10. W. Gao *et al.*, Opt. Express **20**(7), 7128–7134 (2012).
11. R. Paschotta, "Hermite–Gaussian modes," *RP Photonics Encyclopedia* (2022).
12. C. Tamm and C. O. Weiss, J. Opt. Soc. Am. B **7**(6), 1034–1038 (1990).
13. M. W. Beijersbergen, L. Allen, H. E. L. O. van der Veen, and J. P. Woerdman, Opt. Commun. **96**, 123–132 (1993).
14. M. W. Beijersbergen, R. P. C. Coerwinkel, M. Kristensen, and J. P. Woerdman, Opt. Commun. **112**, 321–327 (1994).
15. J. H. McLeod, J. Opt. Soc. Am. **44**(8), 592–597 (1954).
16. Edmund Optics Inc., "An In-Depth Look at Axicons," (accessed 2020).
17. A. D. Fisher, *A Review of Spatial Light Modulators*, Optical Computing, TuC1 (1985).
18. D. L. Andrews and M. Babiker (Eds.), *The Angular Momentum of Light* (Cambridge University Press, 2012).

19. IDEX Optics & Photonics, “Gaussian Beam Optics Tutorial,” (2020).

20. L. Allen *et al.*, Phys. Rev. A **45**, 8185–8189 (1992).

21. D. G. Grier, Nature **424**, 810–816 (2003).

22. N. Bozinovic *et al.*, Science **340**, 1545–1548 (2013).

23. K. Khonina *et al.*, Appl. Sci. **10**, 7597 (2020).

2 Optical Beam Shifts

This introductory chapter reviews the literature on optical beam shifts, focusing on the Goos-Hänchen and Imbert-Fedorov effects. Their origin, key dependencies, and practical applications are demonstrated in detail. While extensive studies exist, certain aspects remain insufficiently explored, thereby motivating the investigations undertaken in this thesis.

2.1 Introduction

In optics, the study of reflection and refraction at the interface between two dielectric media forms a fundamental aspect of light–matter interaction. When the incident light is modelled as a plane wave, this problem can be accurately described using Snell's law and Fresnel equations [1]. However, in practice, real laser beams consist of a superposition of infinitely many plane waves with slightly different wave vectors. In such cases, Snell's law and Fresnel equations no longer provide a complete description of reflection and refraction. While each constituent plane wave individually satisfies these laws, their collective superposition exhibits unconventional behaviour, giving rise to a range of intriguing phenomena, including the Goos–Hänchen (GH) shift, the Imbert–Fedorov (IF) shift, and the photonic spin Hall effect (PSHE) [2].

Building on the discussion from the previous chapter, we begin here with the reflection and refraction of plane waves. We then briefly introduce the non-specular phenomena mentioned above, outlining their underlying mechanisms and dependence on various optical parameters. A unified framework for describing optical beam shifts of arbitrarily shaped incident beams will also be presented. Finally, we highlight the applications of optical beam shifts in optical sensing and metrology, concluding with the primary objectives of this thesis.

2.1.1 Laws of reflection

The well-known laws of reflection were first formulated by the ancient Greek mathematician Euclid around 300 BCE. Those can be summarized as follows:

(a) The incident ray, the reflected ray, and the normal at the point of incidence all lie in the same plane.

(b) The angle of incidence (θ_i) is equal to the angle of reflection (θ_r), i.e., $\theta_i = \theta_r$.

Depending on the nature of the reflecting surface, reflection is generally classified into two categories: regular reflection and irregular (or diffuse) reflection. Regular reflection occurs when light strikes a smooth, polished surface such as a mirror or metal plate, where it is reflected at the same angle as the incident beam [Figure 2.1]. In contrast, irregular reflection takes place when light falls on a rough surface, causing the reflected rays to scatter in different directions. In practice, most real-world surfaces are rough at the scale of the wavelength of light, and our visual perception of objects arises largely due to this diffuse reflection.

The fundamental origin of light reflection can be understood from Maxwell's equations, since light is an electromagnetic wave. When a light wave is incident on a material surface, it drives the electrons of the medium into oscillation, leading to the polarization of the atoms. These oscillating charges then emit secondary wavelets in all directions. According to the *Huygens–Fresnel* principle, the superposition of these secondary waves gives rise to the observed phenomena of reflection and refraction.

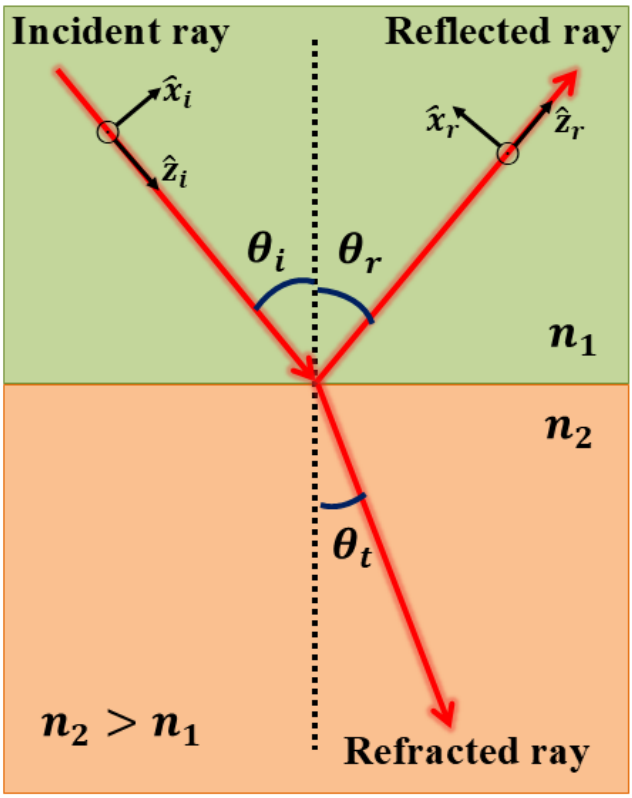

Figure 2.1 Pictorial depiction of reflection and refraction at the boundary of two dielectric mediums having refractive indices n_1 and n_2.

2.1.2 Laws of refraction

One of the earliest quantitative studies of refraction was carried out by the Egyptian astronomer Ptolemy, who proposed that the angle of refraction is proportional to the angle of incidence. However, the complete law of refraction was first discovered by the Iraqi mathematician Ibn Sahl. A major advancement came in 1621, when the Dutch astronomer Willebrord Snellius established the precise mathematical relation between the angles of incidence and refraction at the boundary between two media, now universally known as Snell's law. Later, in 1657, the

French mathematician Pierre de Fermat offered an elegant derivation of Snell's law using his principle of least time, which states that light always follows the path that minimizes the travel time between two points.

When light traveling in one transparent medium encounters a boundary with another (for example, air and glass), part of the light is reflected back into the first medium while the rest is transmitted into the second medium. The transmitted portion undergoes a change in direction as it enters the new medium; this bending of the light path is known as refraction [Figure 2.1].

The relationship governing this phenomenon is expressed by the law of refraction, or Snell's law, which relates the angle of incidence (θ_i) and the angle of refraction (θ_t), both measured with respect to the normal (a line perpendicular to the surface). Mathematically, it is written as:

$$n_1 \sin\theta_i = n_2 \sin\theta_t \tag{2.1}$$

where n_1 and n_2 are the refractive indices of the first and second medium, respectively.

The index of refraction of a medium is a dimensionless constant defined as the ratio of the speed of light in vacuum to its speed in that medium. Refraction occurs because light travels at different speeds in different media. This change in speed causes the bending of light as it crosses the boundary between two media. When light enters a denser medium, it slows down and the refracted ray bends toward the normal. Conversely, when light emerges obliquely from a denser to a rarer medium, it speeds up and the ray bends away from the normal.

2.2 Concept of beam shifts

The classical laws of reflection and refraction provide an accurate geometrical optics description of light propagation. However, for a real optical beam with finite width - that is, a beam comprising a spectrum of plane waves - the behaviour becomes more complex. In such cases, the reflected and transmitted beams deviate from the predictions of geometrical optics at the wavelength scale. Neglecting shape deformations of the secondary beams, these deviations can be primarily classified into four types: in-plane and out-of-plane spatial shifts, and the corresponding angular deflections [2]. A schematic representation of these shifts is presented in Figure 2.2. Spatial and angular shifts can also be interpreted as changes in the beam's coordinate and momentum, respectively, altering the positions and propagation

directions of the secondary beams. In conventional terminology, these phenomena are referred to as spatial and angular Goos–Hänchen (GH) and Imbert–Fedorov (IF) shifts. In addition, another fundamental non-specular effect, the transverse photonic spin Hall effect (PSHE), arises during partial reflection and shares a common physical origin with the IF shift. Notably, these basic beam shifts can occur in virtually any beam reflection or refraction scenario across optical systems. In recent years, GH, IF, and PSHE have attracted significant research interest, particularly in the context of nano-photonics, where light-matter interactions at subwavelength scales are of central importance.

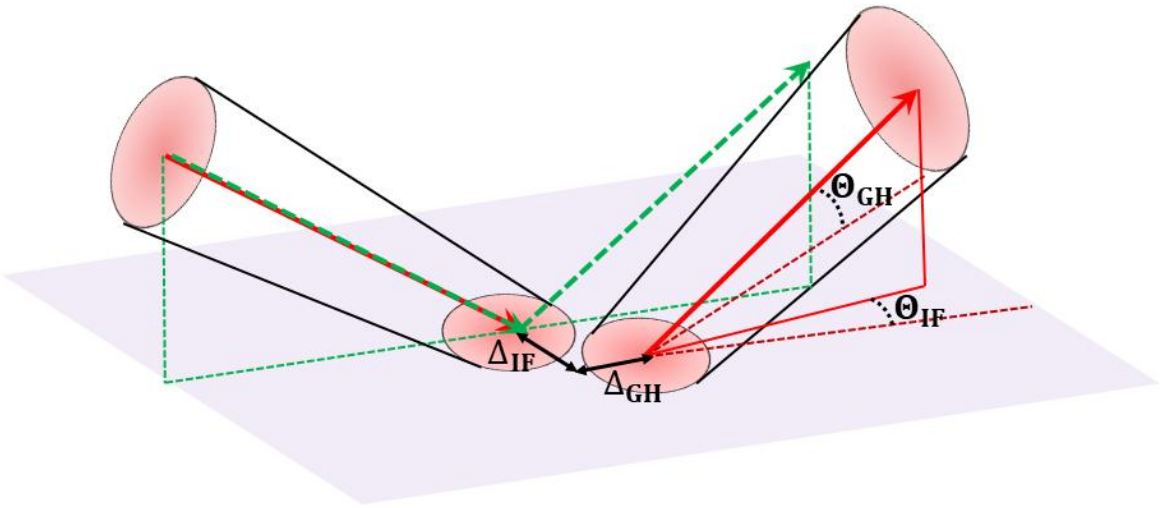

Figure 2.2 Schematic representation of Goos-Hänchen (GH) and Imbert-Fedorov (IF) shifts, both spatial (Δ) and angular shifts (Θ) are shown explicitly.

In the following sections, we provide a concise discussion of the origin, influencing factors, and potential applications of GH, IF, and PSHE phenomena.

2.2.1 Longitudinal shift (Goos-Hänchen shift)

The first prediction of a displacement of the beam centroid during total internal reflection (TIR) was made by Sir Isaac Newton in his seminal work *Opticks* (1704), where he attributed this effect to the penetration of light into the rarer medium [3]. The first experimental observation, however, was reported by H. Goos and H. Hänchen in 1947, who employed multiple reflections to demonstrate that this longitudinal shift is intrinsically linked to the wave nature of light [4].

Theoretical modelling of this phenomenon was subsequently developed by Artmann (1948) [5], using the stationary phase approximation, and independently by Von Fragstein (1949) [6], based on energy flux conservation.

Artmann's approach treated the incident beam as a superposition of multiple plane waves, where the rapidly varying phases largely cancel out, and the stationary phase condition determines the dominant contribution to the optical path. During TIR, the imaginary component of the Fresnel reflection coefficients generates an additional Goos–Hänchen phase, which leads to a longitudinal displacement of the optical path. Although initially verified only for transverse electric (TE) polarization, Artmann's formulation was later extended to transverse magnetic (TM) polarization. While generally successful, his model diverges near the critical angle, where experimental measurements indicate a finite shift. This divergence issue was addressed by Wolter [7] and subsequently, more effectively, by Artmann himself [8]. Further investigations in the 1970s by Brekhovskikh [9] and Lotsch [10] demonstrated that discrepancies between theory and experiment arose from limitations in the analytical derivation, which breaks down in the vicinity of the critical angle.

Mathematically, the theoretical expressions of GH shift for the incident TE (s) and TM (p) polarized beam was derived by Lotsch [10] as,

$$D_s = \frac{\lambda}{\pi}\frac{\sin\theta}{\sqrt{sin^2\theta\ -\ n^2}}\left[\frac{1\ -\ sin^2\theta}{1\ -\ n^2}\right] \tag{2.2}$$

$$D_p = \frac{\lambda}{\pi}\frac{\sin\theta}{\sqrt{sin^2\theta\ -\ n^2}}\left[\frac{n^2(\sin\theta\ -\ n^2 sin\,\theta\ -\ sin^2\theta + n^2)}{\sin\theta\,(n^4 cos^2\theta + sin^2\theta\ -\ n^2)}\right] \tag{2.3}$$

where, λ is the wavelength of incident light, n is the refractive index of the medium and θ being the angle of incidence.

Meanwhile, Renard proposed an alternative theoretical approach based on energy flux conservation, in which the time-averaged Poynting vector of the evanescent wave above a totally reflecting surface acquires a finite, non-zero value [11]. A schematic representation of this energy flux is shown in Figure 2.3, where the center of the incident beam is denoted by O and the reflected beam is shifted by a distance 'd' relative to the incident beam. Energy flux crosses the MN plane, and since the incident and reflected beams have identical intensities

under TIR, the principle of energy conservation dictates that this flux transfer can occur only if the reflected beam is shifted from the position predicted by geometrical optics. As a result, a downward flux component of the incident beam is introduced, which is not compensated by the upward flux component of the reflected beam through the COD plane. This flux difference is localized in a strip of width $'d'$ near the beam center, and by conservation of energy, it must correspond to the energy flux carried by the evanescent wave across the MN plane.

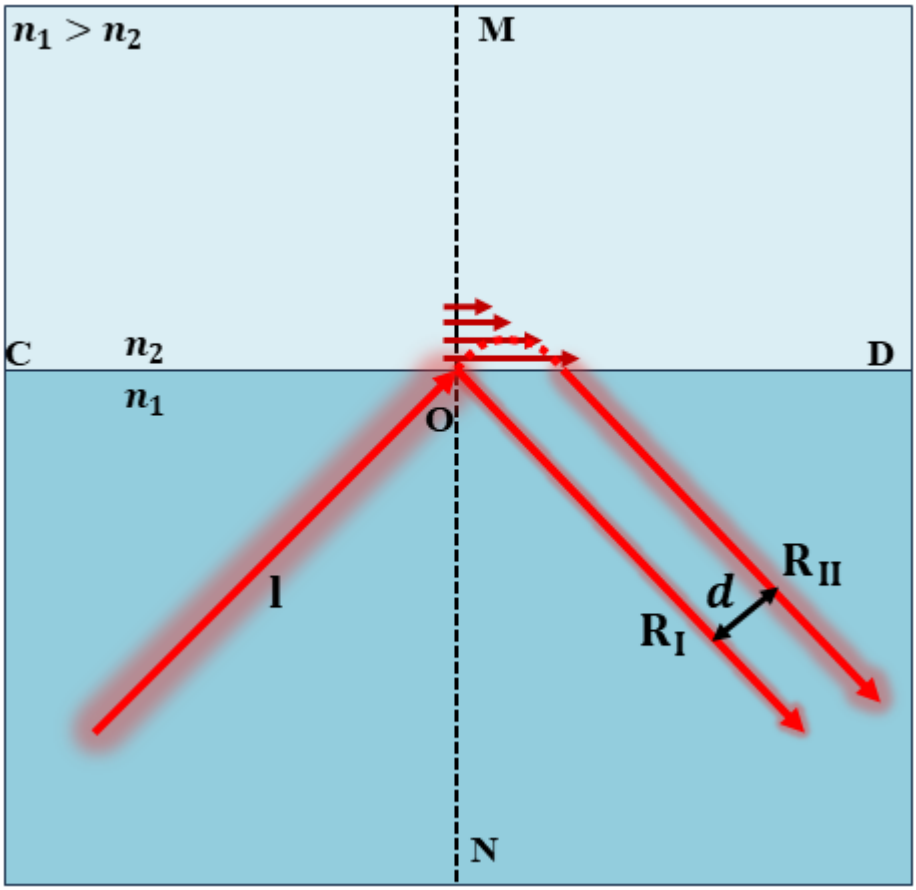

Figure 2.3 Schematic of total reflection where I: incident beam, R_I: partially reflected beam, R_{II}: displaced reflected beam owing to the energy conservation principle that leads to GH shift (d).

According to energy flux conservation approach [11], the GH shift for s- and p-polarized incident plane wave are given by,

$$D_s = \frac{\lambda}{\pi} \frac{\sin\theta}{\sqrt{n^2 sin^2\theta - 1}} \tag{2.4}$$

$$D_p = \frac{\lambda}{\pi} \frac{n^2 \sin\theta}{\sqrt{n^2 sin^2\theta \ - \ 1}} \tag{2.5}$$

This formalism demonstrated that the GH shift is a direct consequence of energy flux conservation under total internal reflection. While conceptually distinct from Artmann's stationary phase approach - particularly away from the critical angle - the two models converge as the incidence angle approaches the critical region. The inaccuracies in this derivation were later addressed by Lai et al. in 1986 [12]. In the intervening period, several researchers, including Horowitz and Tamir [13] as well as Cowan and Aničin [14], developed alternative theoretical models by performing direct integration of the reflected electric field, further refining the understanding of beam shift phenomena.

In parallel with studies of the spatial GH shift, angular deflections from the estimates of ray optics were also recognized and analyzed, particularly for partially reflected or transmitted beams. In 1973, Ra et al. investigated this type of shift by analyzing the integrated reflected beam for internal reflection, establishing the critical angle as a boundary separating spatial and angular GH shifts [15]. Subsequent studies by Antar and Boerner [16], White et al. [17], and Chan and Tamir [18] provided more detailed theoretical analyses of the angular GH shift near the Brewster angle and offered insights into its physical interpretation. In 2009, Aiello and Woerdman revisited angular deviations in the Brewster region [19, 20], deriving explicit expressions for both s- and p-polarized incident beams as,

$$\langle \Delta\theta_x \rangle = \frac{\iint \theta_x R(\theta_x, \ \theta_y)\, I(\theta_x, \theta_y)\, d\theta_x\, d\theta_y}{\iint R(\theta_x, \ \theta_y)\, I(\theta_x, \theta_y)\, d\theta_x\, d\theta_y} \tag{2.6}$$

where, $R(\theta_x, \theta_y)$ is the intensity reflection coefficient of the plane wave (θ_x, θ_y) and $R(\theta_x, \theta_y) I(\theta_x, \theta_y)$ represent the reflected beam.

Finally, it has been theoretically established that GH shifts originate from the dispersion of the Fresnel reflection or transmission coefficients, as expressed in [21],

$$X_s = \ -i \frac{\partial}{\partial\theta} ln\, r_s \tag{2.7}$$

$$X_p = \ -i \frac{\partial}{\partial\theta} ln\, r_p$$

Here, $r_{p,s}$ denotes the Fresnel reflection coefficients, and the real and imaginary parts of $X_{p,s}$ correspond to the spatial and angular GH shifts, respectively.

It is evident from equation (2.7) that, under total internal reflection or upon interaction with complex dispersive interfaces, the reflection coefficient generally becomes complex, resulting in both spatial and angular GH shifts. Specifically, for TIR at a non-dispersive interface, the spatial GH shift is determined by the angular gradient of the phase of the Fresnel reflection coefficient. In contrast, the angular GH effect arises from the angular gradients of the amplitude of the Fresnel coefficients in cases of partial reflection or refraction with real coefficients. Therefore, both spatial and angular GH shifts are intimately linked to the spatial dispersion of the scattering coefficients. Although the eigenmodes of GH shifts correspond to s- and p-linearly polarized waves, polarization is not essential for the existence of these phenomena, as scalar wave models can also reproduce GH effects - a point explored in detail in recent studies [2].

In the past decade, numerical methods have been employed to investigate the validity ranges of existing analytical formulas and to identify the incidence angles that yield maximum shifts [22]. Recent analytical and numerical studies by De Leo et al. [23] and Araújo et al. have further explored phenomena such as frequency crossover [24], symmetry breaking, and composite GH shifts [25, 26].

2.2.2 Transverse shift (Imbert-Fedorov shift)

After the discovery of the longitudinal Goos–Hänchen (GH) shift, Soviet physicist Fedor Fedorov (1955) was the first to point out that, during total internal reflection, the time-averaged Poynting vector associated with the evanescent field possesses a component perpendicular to the plane of incidence within the lower refractive index medium [27]. Consequently, a transverse (out-of-plane) displacement of the reflected beam is also expected. Building upon Artmann's stationary phase approach, Schilling (1965) [28] was the first to derive an analytical expression for this transverse shift in the case of circularly polarized light, which can be written as,

$$Y_T = \pm\left(\frac{\lambda}{\pi}\right)\left(\frac{sin^3\theta\, cos\,\theta}{sin^2\theta - n^2 cos^2\theta}\right) \tag{2.8}$$

Where (+) and (-) signs represent for the right and left circularly polarized beam and λ denotes the wavelength of incident beam.

The peculiarity of Schilling's approach lies in the fact that the field quantities within the evanescent region do not explicitly appear in his calculations. Instead, his derivation relies solely on the boundary conditions of the electric and magnetic fields, along with the linearity of the governing wave equations.

Later, in 1970, French physicist Christian Imbert experimentally confirmed the existence of such transverse beam shifts. Subsequently, he also provided a theoretical formulation of the effect [29], deriving an expression for the transverse displacement using the concept of transverse energy flux within Fresnel's evanescent field. His analysis was based on an energy conservation argument analogous to those previously employed by Kristoffel [30] and Renard [11] in their derivations of the longitudinal Goos–Hänchen (GH) shift. Imbert's formulation was both compact and consistent with the experimental observations. It was further noted that the magnitude of the Imbert–Fedorov (IF) shift is significantly smaller than that of the GH shift; even under optimal conditions - namely, circular polarization and incidence angles approaching the critical angle - it remains finite and on the order of approximately half a wavelength.

According to Imbert's calculation the transverse shift for circularly polarized incident light beam is given by [29],

$$Y_T = \pm\left(\frac{\lambda}{\pi}\right)\left(\frac{1}{1-n^2}\right)\left(\frac{sin^3\theta\, cos\,\theta}{sin^2\theta - n^2 cos^2\theta}\right) \tag{2.9}$$

However, certain limitations were inherent in this approach as well. In the conventional treatment based on energy flux conservation, within the region where the incident and reflected beams overlap (as illustrated in Figure 2.3), the total Poynting vector is generally considered as the simple superposition of the individual Poynting vectors of the incident and reflected beams. Nevertheless, according to Maxwell's electromagnetic theory, such a direct superposition principle does not strictly apply to Poynting vectors, since they are quadratic in the field quantities.

As a consequence, both of these early approaches failed to accurately describe the behavior of the transverse shift for incidence angles below the critical angle. Thus, the study of the Imbert–Fedorov (IF) shift has long been a subject of debate and controversy within the optics community. In 1987, Fedoseyev and Player [31, 32] demonstrated that the IF shift is fundamentally linked to the balance and conservation of the total angular momentum (AM) of light, incorporating the intrinsic spin AM associated with circular polarization. Later, in 1992,

Liberman and Zel'dovich [33] rederived the IF effect and Schilling's formula by introducing the concept of spin–orbit interaction of light. Subsequently, in 2004, Onoda *et al.* [34] interpreted the transverse shift as a manifestation of the spin Hall effect of light, related to the geometric Berry phase, and once again obtained Schilling's expression through angular momentum conservation arguments. More recently, Bliokh and Bliokh [35, 36] provided a comprehensive theoretical framework for the IF shift, derived an exact and generalized expression improving upon Schilling's result, and further predicted the existence of the angular Imbert–Fedorov shift.

The complete theoretical formula for transverse shifts is given by [37],

$$Y_s = -i\frac{a_p}{a_s}\left(1+\frac{r_p}{r_s}\right)cot\,\theta \tag{2.10}$$

$$Y_p = i\frac{a_s}{a_p}\left(1+\frac{r_s}{r_p}\right)cot\,\theta \tag{2.11}$$

Where, a_p, a_s are the complex amplitudes which determines the polarization of the incident light beam.

This formulation clearly indicates that the Imbert–Fedorov (IF) shifts fundamentally originate from the intrinsic polarization properties of light. In the case of partial reflection or transmission, the eigenmodes corresponding to the spatial IF shift are circularly polarized waves, whereas linearly polarized waves are responsible for the angular IF shift [38].

It is noteworthy that, while a clear theoretical explanation of the Goos–Hänchen (GH) effect was established long ago following its discovery, an accurate and comprehensive formulation of the IF shift - along with its experimental verification - has been achieved only in recent years [35–39]. The primary reason for this lies in the fact that GH shifts can be fully described within the two-dimensional geometry of the plane of incidence, whereas the IF effect inherently involves more intricate three-dimensional physics and requires a precise characterization of the polarization states of both the incident and reflected fields [36].

2.3 Unified approach to beam shape dependent shift

It can be observed from equations (2.7), (2.10), and (2.11) presented in the previous sections that the expressions for the Goos-Hänchen (GH) and Imbert-Fedorov (IF) shifts are completely independent of the beam's spatial profile. However, these formulations cease to be valid under

conditions where the beam shape becomes distorted due to interaction with the interface. Such deformation typically occurs when the beam is incident at the Brewster angle, for which $r_p \rightarrow 0$ and Y_p becomes ill-defined. In this case, a special theoretical treatment is required (details are provided in *Chapter* 8).

Considering a well-collimated monochromatic light beam with wavenumber k, propagating along the z_i-direction (as illustrated in Figure 2.1), the real electric field of the beam can be expressed as,

$$E'(x', y', z', t) = Re[A'(x', y', z')\, exp\, (-ikct)] \tag{2.12}$$

Where 'c' denotes the speed of light in vacuum and

$$A'(x', y', z') = \left(a_p \hat{x}_i + a_s \hat{y}_i\right) f(x', y', z') \tag{2.13}$$

is the complex analytic signal associated to the real signal $E'(x', y', z', t)$. Here, the two complex amplitudes a_p and a_s define the polarization of the beam and $f(x', y', z')$, the complex scalar function represent the spatial shape of the beam.

For example, $f(x', y', z')$ can be Gaussian, Hermite-Gaussian or Laguerre-Gaussian function which are widely used in optics [40].

After reflection, the analytic signal $A'(x', y', z')$ get modified to $A(x, y, z)$ as [41],

$$\begin{aligned} A(x, y, z) = {} & a_p r_p(\theta) f\left(-x + X_p, y - Y_p, z\right)\hat{x}_r \\ & + a_s r_s(\theta) f(-x + X_s, y - Y_s, z)\hat{y}_r \end{aligned} \tag{2.14}$$

where $r_p(\theta)$, $r_s(\theta)$ are the Fresnel reflection coefficients evaluated at the incident angle $\theta_i = \theta$. The negative sign in the x-dependence of the shifted distribution arises from the parity inversion introduced by reflection, as observed in the reference frame of the reflected beam.

The four dimensionless complex shift parameters have been defined in the previous section [see equations (2.7), (2.10), and (2.11)]. Expressing in terms of their real and imaginary components, these complex shifts $X$and Ycan be written as,

$$X = X_r + iX_i \tag{2.15}$$

$$Y = Y_r + iY_i$$

The center of the reflected beam can now be determined as the centroid of the overall intensity distribution in the x-y plane. Denoting $x_1 = x$ and $x_2 = y$ in the Cartesian coordinate system, the beam centroid is defined as

$$\langle x_a \rangle(z) = \frac{\int x_a \left(I_p + I_s\right) dx\ dy}{\int \left(I_p + I_s\right)\ dx\, dy}\ , (a\ =\ 1{,}2) \tag{2.16}$$

where,

$$I_{p,s} = \left|a_{p,s} r_{p,s}\right|^2 \left|f\left(-x + X_{p,s}, y - Y_{p,s}, z\right)\right|^2 \tag{2.17}$$

represent the total reflected intensity distribution functions in the transverse plane for p- and s-polarizations, respectively.

Then the position of this centroid with respect to origin $(x\ =\ 0, y\ =\ 0)$ on the $z\ =\ const.$ plane, defines both the spatial and angular GH and IF shifts as,

$$\Delta_{GH} = \langle x \rangle(0), \qquad \Theta_{GH} = \frac{\partial \langle x \rangle(z)}{\partial z} \tag{2.18}$$

$$\Delta_{IF} = \langle y \rangle(0), \qquad \Theta_{IF} = \frac{\partial \langle y \rangle(z)}{\partial z} \tag{2.19}$$

Here, the integration always denotes the definite integrals over the whole x-y plane keeping $z\ =\ const.$ In terms of physical interpretation, equation (2.16) implies that the first moments of the intensity distributions $I_{p,s}$ correspond to the relative shifts $\langle x_a \rangle(z)$ of the reflected beam.

Now, by substituting the expressions from the previous sections into equation (2.17) and performing a rigorous calculation assuming a square-integrable function $f(x, y, z)$, A. Aiello derived the general formulas for the Goos–Hänchen (GH) and Imbert–Fedorov (IF) shifts for an arbitrary beam shape [37],

$$\begin{bmatrix} \langle x \rangle \\ \langle y \rangle \end{bmatrix} = \begin{bmatrix} X_r \\ Y_r \end{bmatrix} + \begin{bmatrix} u_{11} & u_{12} \\ u_{21} & u_{22} \end{bmatrix} \begin{bmatrix} X_i \\ Y_i \end{bmatrix} \tag{2.20}$$

Where,

$$u_{mn} = 2 \frac{\int f^* \left(x_m \frac{\partial}{\partial x_n}\right) f\ dx\ dy}{\int |f|^2 dx\ dy} \tag{2.21}$$

.

The first term on the right-hand side of equation (2.20) indicates that if the beam centroid is initially centered at the origin of the x-y plane, it will experience real displacements X_r and Y_r along the x and y directions, respectively.

The second term is particularly interesting. The diagonal elements of the 2×2 matrix connect the imaginary parts of the complex shifts X and Y with the real displacements of the intensity distribution. As equation (2.21) shows, all elements of the matrix are functions of z only; hence, the imaginary parts X_i and Y_i describe the propagation-dependent behaviour of the shifts. Specifically, the diagonal elements u_{11} and u_{22} are responsible for the angular Goos–Hänchen (GH) and Imbert–Fedorov (IF) shifts, respectively.

Moreover, the off-diagonal elements u_{12} and u_{21} mix the real part of $X(Y)$ in the $x(y)$ direction with the imaginary part of the shift $Y(X)$ in the $y(x)$ direction. The presence of these non-zero off-diagonal elements is a distinctive feature of the shifted distribution and can be exploited to enhance beam shifts using specially shaped light beams.

For example, considering Laguerre – Gauss paraxial beam described in *chapter* 1 [equation (1.54)], it can be shown following the above discussed formalism that,

$$\langle x \rangle^l \cong X_r + \frac{z}{z_R}(1 + |l|)X_i - lY_i \tag{2.22}$$

$$\langle y \rangle^l \cong Y_r + \frac{z}{z_R}(1 + |l|)Y_i + lX_i \tag{2.23}$$

If $l = 0$, the LG beam reduces to the fundamental Gaussian beam and the above equations become:

$$\langle x \rangle^0 \cong X_r + \frac{z}{z_R}X_i \tag{2.24}$$

$$\langle y \rangle^0 \cong Y_r + \frac{z}{z_R}Y_i \tag{2.25}$$

Denoting $X_{r,i}$ and $Y_{r,i}$ in terms of spatial and angular GH and IF shifts as,

$$X_r = \Delta^0_{GH}, \qquad X_i = z_R\Theta^0_{GH} \tag{2.26}$$

$$Y_r = \Delta^0_{IF}, \qquad Y_i = z_R\Theta^0_{IF} \tag{2.27}$$

We can obtain,

$$\langle x \rangle^l \cong \Delta_{GH}^0 + z(1+|l|)\Theta_{GH}^0 - lz_R\Theta_{IF}^0 \tag{2.28}$$

$$\langle y \rangle^l \cong \Delta_{IF}^0 + z(1+|l|)\Theta_{IF}^0 + lz_R\Theta_{GH}^0 \tag{2.29}$$

It is evident that the orbital angular momentum (OAM) of light exerts a two-fold effect on the Goos-Hänchen (GH) and Imbert–Fedorov (IF) shifts. First, it enhances the angular longitudinal or transverse shifts by an amount proportional to $|\ l\ |$. Second, it induces an algebraic mixing of the spatial GH (IF) and angular IF (GH) shifts, proportional to l. These effects are universal for Laguerre-Gaussian (LG) beams, implying that they are independent of both the polarization of the incident beam and the material composition of the interacting medium.

This type of mixing was predicted previously [42]; however, we have elaborated on it in greater detail through rigorous calculations and experimental verification using vortex beams in *Chapter* 8. Additionally, using Hermite-Gaussian and fundamental Gaussian beams, both GH and IF shifts are examined in *Chapters* 6 and 7, respectively.

2.4 Dependence of optical beam shifts

As discussed earlier, several intrinsic and extrinsic parameters associated with the incident optical beam - such as its spatial width, state of polarization, transverse field distribution (beam shape), wavelength, and the electromagnetic properties of the reflecting or refracting interface - collectively govern the interaction dynamics at the boundary. Variations in these parameters can modify the phase and amplitude response of the reflected or transmitted field components, thereby leading to corresponding modulations in the spatial and angular beam shifts. In the subsequent discussion, these parameters are enumerated and their individual contributions to the beam shift phenomena are briefly examined.

(a) Wavelength

Early theoretical and experimental studies have firmly established that the magnitude of optical beam shifts is generally of the order of the incident light's wavelength, indicating an inherent proportionality between them. Consequently, an increase in the operating wavelength generally leads to an enhancement in the observed beam shift [2].

(b) Beam width

The beam width of the incident optical beam plays a crucial role in governing the magnitude and behaviour of beam shifts, as it directly influences the modal composition of the beam [43].

For Gaussian beams, the number of supported modes varies with the beam width, resulting in distinct reflected intensity profiles. When the incident Gaussian beam has a relatively small waist, the reflected field exhibits significant distortion due to the presence of multiple higher-order modes. Conversely, for beams with larger widths, the number of contributing modes decreases, leading to reduced distortion and a more ideal Gaussian profile upon reflection. Hence, a beam with a sufficiently large width more closely approximates a perfect Gaussian mode, minimizing modal loss during reflection.

Previous studies [43] have also shown that for a narrow Gaussian beam, the field penetrates deeper into the medium, and since the penetration depth is proportional to the magnitude of the beam shift, a relatively larger displacement is observed. As the beam width increases, the magnitude of the shift decreases rapidly and eventually saturates to a nearly constant value for sufficiently large widths. This behaviour arises from the fact that a wide Gaussian beam tends to approximate a uniform plane wave, for which beam shift effects become negligible.

(c) Polarization of incident light

Since the first observations of optical beam shifts, it has been well established that both Goos–Hänchen (GH) and Imbert–Fedorov (IF) shifts are highly dependent on the polarization state of the incident beam. Specifically, the eigenmodes associated with GH shifts correspond to linearly polarized transverse magnetic (TM, or *p*) and transverse electric (TE, or *s*) modes, whereas circularly polarized light gives rise to IF shifts. In the following *chapters*, we will demonstrate how the GH shift can be precisely controlled by varying the polarization angle of the incident beam. Furthermore, even for purely p-polarized light, the transverse beam shifts can be significantly enhanced in the vicinity of the Brewster angle.

(d) Beam shape

The spatial profile of the incident beam is another critical factor influencing both GH and IF shifts, as discussed in the previous section. The most commonly studied beam shapes in optical beam shift investigations are Gaussian, Hermite–Gaussian (HG), and Laguerre–Gaussian (LG) modes. Recently, several studies have extended these investigations to more complex beam structures, including paraxial Bessel beams [44], non-paraxial Bessel beams [45], LG beams with higher radial orders [46], HG beams [47], multi-Gaussian Schell-model beams [48], and dipole radiation [49]. General considerations of beam shape effects on beam shifts have also

been reviewed in Ref. [37]. However, the dependence of beam shifts on beam shape has been subject to considerable debate over time [50, 51]. In the forthcoming *chapters*, we aim to clarify some of these issues, which fall within the scope of this thesis.

(e) Surface of interaction

The characteristics of the reflecting and refracting interface play a crucial role in determining the magnitude and direction of GH and IF shifts. Numerous studies have explored these effects by varying the intrinsic and extrinsic properties of different materials, including the use of thin films versus bulk media, modulation of sample thickness, application of external magnetic fields, and the engineering of artificial metamaterials [52]. In the subsequent chapters, we will examine in detail how the properties of the reflecting surface influence optical beam shifts, with specific consideration of air–glass interfaces and monolayer transition metal dichalcogenide (TMDC) sample.

(f) Special angles

Certain angles of incidence, such as the critical angle, the pseudo-Brewster angle during internal reflection, and the Brewster angle during external reflection, are associated with rapid variations in the Fresnel reflection coefficients. Consequently, both spatial and angular beam shifts exhibit anomalous behavior near these specific angles. Previous studies have reported that GH shifts are enhanced near the critical angle, whereas the photonic spin Hall effect (PSHE) is amplified close to the Brewster angle. However, it is important to note that these enhancements are not universal; the behavior of GH and IF shifts at these special angles can vary significantly depending on the optical properties of the reflecting interface. This thesis addresses this issue in detail, providing a comprehensive analysis of beam shift behavior near exceptional incidence angles.

(g) Experimental parameters

As will be discussed in the following *chapter*, several experimental techniques are available to investigate optical beam shifts. It has been observed that parameters specific to each experimental method can significantly influence the measured magnitude of these subtle effects. In the context of the weak value amplification method [39], propagation distance and post-selection angle are particularly important. The angular deflection of the beam can be enhanced by increasing the propagation distance after the beam interacts with the sample.

Furthermore, the influence of the post-selection angle on GH shifts and the PSHE for specific angles of incidence is analyzed in detail in the subsequent *chapters*.

2.5 Applications of optical beam shift

As discussed in the previous sections, research on optical beam shifts has been ongoing for several decades, leading to a wide range of intriguing applications. As previously noted, GH and IF shifts are sensitive to the intrinsic properties of the interacting medium, including thickness, refractive index, conductivity, susceptibility, and other exotic characteristics [52]. This sensitivity enables the precise determination of these material parameters through experimental measurement of beam shifts; a technique commonly referred to as precision metrology of optical parameters.

The process generally involves three key steps: first, establishing a quantitative relationship between the beam shift and the relevant physical parameters; second, experimentally measuring the specific beam shifts using an appropriate technique; and third, using the measured shifts as a pointer to accurately characterize the material parameters.

To date, both GH shifts and the photonic spin Hall shifts (PSHS) have demonstrated significant utility in precision metrology for a variety of materials, including nanometallic films, semiconductors, and two-dimensional atomic crystals, as well as in biomolecular sensing. Further applications of optical beam shift phenomena include optical beam shift spectroscopy, detection of chemical concentrations and reaction rates, optical differential operations, image edge detection, and optical computing [52]. Consequently, the study of GH and IF shifts has become a critical component in the advancement of modern optical research.

2.6 Concluding remarks

In summary, this chapter has provided an overview of the reflection and refraction of both plane waves and optical beams, highlighting the emergence of the fundamental non-specular phenomena, namely Goos-Hänchen (GH) and Imbert-Fedorov (IF) shifts. The origin of these beam shifts has been examined in detail, along with a historical perspective on the development of the relevant theoretical models. The influence of higher-order light beams on GH and IF shifts has also been discussed. Finally, the key factors affecting beam shifts were identified, and the chapter concluded with a discussion of their applications in precision metrology, particularly within the domain of nano-optics.

References

1. M. Born and E. Wolf, Principles of Optics: Electromagnetic Theory of Propagation, Interference and Diffraction of Light (Elsevier Science, 2013).
2. K. Y. Bliokh and A. Aiello, J. Opt. **15**, 014001 (2013).
3. I. Newton, Opticks: or, a Treatise of the Reflexions, Refractions, Inflexions and Colours of Light (Dover Publications, 1998).
4. F. Goos and H. Hänchen, Ann. Phys. **436**, 333 (1947).
5. K. Artmann, Ann. Phys. **437**, 87 (1948).
6. C. V. Fragstein, Ann. Phys. **439**, 271 (1949).
7. H. Wolter, Z. Naturforsch. A **5**, 143 (1950).
8. K. Artmann, Ann. Phys. **8**, 270 (1950).
9. L. M. Brekhovskikh, Waves in Layered Media (Academic Press, New York, 1960).
10. H. K. V. Lotsch, J. Opt. Soc. Am. **58**, 551 (1968).
11. R. H. Renard, J. Opt. Soc. Am. **54**, 1190 (1964).
12. H. M. Lai, F. C. Cheng, and W. K. Tang, J. Opt. Soc. Am. A **3**, 550 (1986).
13. B. R. Horowitz and T. Tamir, J. Opt. Soc. Am. **61**, 586 (1970).
14. J. J. Cowan and B. Aničin, J. Opt. Soc. Am. **67**, 1307 (1977).
15. J. W. Ra, H. L. Bertoni, and L. B. Felsen, SIAM J. Appl. Math. **24**, 396 (1973).
16. Y. M. Antar and W. M. Boerner, Can. J. Phys. **52**, 962 (1974).
17. I. A. White, A. W. Snyder, and C. Pask, J. Opt. Soc. Am. **67**, 703 (1977).
18. C. C. Chan and T. Tamir, Opt. Lett. **10**, 378 (1985).
19. A. Aiello and J. P. Woerdman, arXiv:0903.3730 [physics.optics] (2009).
20. M. Merano, A. Aiello, M. P. van Exter, and J. P. Woerdman, Nat. Photonics **3**, 337 (2009).
21. M. Ornigotti and A. Aiello, J. Opt. **15**, 014004 (2013).
22. M. P. Aráujo, S. De Leo, and G. G. Maia, Phys. Rev. A **93**, 023801 (2016).
23. S. De Leo and G. G. Maia, J. Mod. Opt. **66**, 2142 (2019).
24. M. P. Aráujo, S. A. Carvalho, and S. De Leo, J. Mod. Opt. **60**, 1772 (2013).
25. M. P. Araújo, S. A. Carvalho, and S. De Leo, Phys. Rev. A **90**, 033844 (2014).
26. M. P. Aráujo, S. De Leo, and G. G. Maia, Phys. Rev. A **95**, 053836 (2017).
27. F. I. Fedorov, Dokl. Akad. Nauk SSSR **105**, 465 (1955).
28. H. Schilling, Ann. Phys. **471**, 122 (1965).
29. C. Imbert, Phys. Rev. D **5**, 787 (1972).

30. N. Kristoffel, Scient. Acta, Tartu State Univ. (1956).
31. V. G. Fedoseyev, J. Phys. A: Math. Gen. **21**, 2045 (1988).
32. M. A. Player, J. Phys. A: Math. Gen. **20**, 3667 (1987).
33. V. S. Liberman and B. Y. Zel'dovich, Phys. Rev. A **46**, 5199 (1992).
34. M. Onoda, S. Murakami, and N. Nagaosa, Phys. Rev. Lett. **93**, 083901 (2004).
35. K. Y. Bliokh and Y. P. Bliokh, Phys. Rev. Lett. **96**, 073903 (2006).
36. K. Y. Bliokh and Y. P. Bliokh, Phys. Rev. E **75**, 066609 (2007).
37. A. Aiello, New J. Phys. **14**, 013058 (2012).
38. Y. Qin, Y. Li, X. Feng, Y.-F. Xiao, H. Yang, and Q. Gong, Opt. Express **19**, 9636 (2011).
39. O. Hosten and P. Kwiat, Science **319**, 787 (2008).
40. A. E. Siegman, Lasers (University Science Books, Mill Valley, 1986).
41. M. Merano, N. Hermosa, J. P. Woerdman, and A. Aiello, Phys. Rev. A **82**, 023817 (2010).
42. K. Y. Bliokh, I. V. Shadrivov, and Y. S. Kivshar, Opt. Lett. **34**, 389 (2009).
43. Y. Wang, Y. Liu, J. Xu, H. Zhang, L. Bai, Y. Xiao, J. Yan, and X. Zhang, J. Opt. A: Pure Appl. Opt. **11**, 105701 (2009).
44. A. Aiello and J. P. Woerdman, Opt. Lett. **36**, 543 (2011).
45. E. Nordblad, Phys. Rev. A **85**, 013847 (2012).
46. N. Hermosa, A. Aiello, and J. P. Woerdman, Opt. Lett. **37**, 1044 (2012).
47. D. Golla and S. Dutta Gupta, Pramana J. Phys. **76**, 603 (2011).
48. M. Tang, H. Zhang, Y. Yang, S. Dong, Y. Zhou, and X. Li, J. Opt. Soc. Am. A **42**, 1417 (2025).
49. M. V. Berry, Proc. R. Soc. A **467**, 2500 (2011).
50. W. Löffler, A. Aiello, and J. P. Woerdman, Phys. Rev. Lett. **109**, 213901 (2012).
51. M. Merano, G. Umbriaco, and G. Mistura, Phys. Rev. A **86**, 033842 (2012).
52. S. Liu, S. Chen, S. Wen, and H. Luo, Opto-Electron. Sci. **1**, 220007 (2022).

3 Experimental Methodologies

Here, we examine different experimental approaches for the measurement of Goos-Hänchen and Imbert-Fedorov shifts. Through a discussion of their strengths and limitations, the effectiveness of the 'weak value amplification' technique is also demonstrated.

3.1 Introduction

In the previous chapter, we noted that the magnitude of optical beam shifts is extremely small. Specifically, the spatial shift is usually on a sub-wavelength scale, whereas the angular shift is typically on the order of milliradians. Consequently, detecting such subtle effects is experimentally very challenging. This may explain why, although the concept of beam shifts was first proposed by Newton [1], their experimental observation was not achieved until 1947 by H. Goos and H. Hänchen [2]. Among these effects, the Goos-Hänchen (GH) shift is generally the most prominent, as the Imbert-Fedorov (IF) and spin Hall shifts are typically an order of magnitude smaller [3,4]. Owing to this scanty nature, numerous attempts were made from the 1970s onward to measure these effects more accurately [5–11]. However, early experiments were limited in scope: they primarily examined beam shifts near the critical angle of incidence, where the shifts are comparatively larger, but did not systematically explore variations with parameters such as angle of incidence, wavelength, or the properties of the interaction medium.

The first major breakthrough in the experimental study of beam shifts and their applications came with the landmark experiment by Onur Hosten and Paul Kwiat in 2008, where weak value amplification (WVA) was employed for the first time to detect the minute photonic spin Hall effect [12]. Since then, numerous modifications have been introduced to improve amplification efficiency and achieve closer alignment with theoretical predictions [13–15]. In parallel, several alternative experimental techniques have also been developed, each offering distinct advantages depending on the specific requirements of a given study.

In this *chapter*, first, we have provided a concise outline of the evolution of experimental techniques used to study optical beam shifts. Subsequently, five different methods are discussed in the following sections, along with their respective advantages or disadvantages.

3.2 Different experimental techniques

In their pioneering experiment, H. Goos and H. Hänchen showed that, under total internal reflection, the point where the reflected ray emerges is shifted from the geometrical intersection of the incident ray with the dielectric interface. The central idea of their work was to exploit multiple reflections of the incident beam in order to amplify the longitudinal displacement of the reflected beam centroid relative to a reference ray. To achieve this, they used a thin plane-parallel glass plate with silver strips placed at the reflection points, thereby generating the

reference beam. The detailed configuration of the setup is illustrated in Figure 3.1. By employing multiple reflections, the displacement D_{GH} became sufficiently enhanced to be observable even with the naked eye.

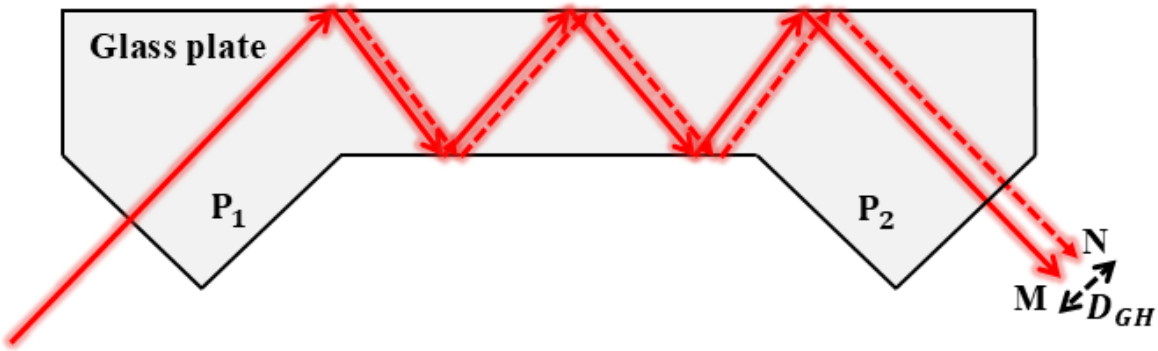

Figure 3.1 Principle of multiple reflections. P1 and P2 are two right-angled prisms attached to the ends of the glass plate using immersion oil. The solid path PM corresponds to reflections from the silver strips (without shift), while the dotted path PN represents reflections from the glass plate (with Goos–Hänchen shift).

Within a few years of the original work, the Goos–Hänchen (GH) effect was revisited multiple times. In 1973, Green *et al.* repeated the measurements using a setup similar to that of Goos and Hänchen (1947, 1949), achieving improved accuracy [5]. Building on the fact that the GH shift is proportional to the incident wavelength, Cowan and Anićin (1977) carried out the first measurement using single reflections of longer-wavelength microwaves [6], thereby significantly enhancing the observable shift. Their method relied on generating a reference beam from a metallic coating, which suppressed the formation of evanescent waves and ensured reflection without displacement. The relative shift was then measured with respect to the displaced centroid of the beam reflected from the prism base. They investigated the longitudinal shift for parallel, perpendicular, and intermediate linear polarizations, and their observations were consistent with the predictions of stationary phase theory. However, the beam quality in this case was relatively poor, with a transverse size on the order of the wavelength. This resulted in a broad distribution of incident wave vectors and, consequently, an averaging of the GH shift's dependence on the angle of incidence. Later, in 1992, Bretenaker *et al.* reported the first experimental measurement of the GH shift arising from a single reflection using a He–Ne laser source [7].

In parallel with investigations of the spatial GH effect, angular deflections from the predictions of ray optics were also identified and studied all over the twentieth century. This phenomenon, now referred to as the angular Goos-Hänchen shift, attracted considerable theoretical attention. Several studies - by Ra. *et al.* [8], Antar and Boerner [9], White *et al.* [10], and Chan and Tamir [11] - mathematically analyzed in-plane angular deflections under partial reflection during the 1970s. However, it was not until 2006 that the first experimental observation of the angular GH shift was reported using microwaves [16]. Shortly thereafter, in 2009, Aiello *et al.* achieved its detection for a single reflection of a laser beam [17], firmly establishing the angular GH effect as an experimentally accessible phenomenon.

On the other hand, only a few years after the discovery of the GH effect, Christian Imbert experimentally confirmed the existence of a transverse displacement of circularly polarized light during total internal reflection in 1970 [4]. Unlike Goos and Hänchen, he did not employ the multiple-reflection method, since in this case the transverse displacements would cancel out due to their opposite signs at successive reflections. Instead, Imbert significantly modified the experimental approach to reveal this far more delicate effect. Later, in 1977, J. J. Cowan and B. Anićin revisited the transverse shift using bounded microwave beams with circular polarization and succeeded in detecting an Imbert–Fedorov (IF) shift of about 6 mm [6].

However, these earlier methods were not sufficiently versatile to allow the experimental detection of beam shifts in a wide range of applications. A major breakthrough came with the development of weak value amplification in the 1990s [18–20], which not only enabled the detection of the photonic spin Hall effect in 2008 [12], but also facilitated precise studies of spatial and angular GH and IF shifts in subsequent years [21–25]. Over time, several other techniques have been proposed and gained popularity within the research community due to their relative ease of implementation [26–30].

To provide a comprehensive overview, the following sections present five commonly used experimental methods for measuring optical beam shifts. Each method is described briefly along with its working principle, advantages, and typical applications. This structured discussion will allow us to understand not only the historical development but also the practical considerations that guide the choice of technique in modern research.

3.2.1 Weak value amplification

In quantum mechanics, the idea of 'measurement' is counter intuitive in contrast to the classical mechanics as it is impossible to perform a 'quantum measurement' without disturbing the system measured which is so called collapsing of a quantum state [31]. For this reason, John Von Neumann introduced experimentally implementable idea of quantum measurement where 'the system', i.e. the quantum state to be measured and 'a pointer', that gives an experimental readout to the resulting change in the system after measurement are coupled by an impulse function [32]. Here, the relative uncertainty in the meter state should be somewhat smaller than the measurement perturbation to get meaningful results after the measurement, which is known as 'strong quantum measurement'. However, in this case it is impossible to extract information of both the canonical variables of a quantum system restricted by uncertainty relations of conjugate variables [33]. In the opposite limit, in a 'weak measurement' situation, the initial uncertainty of the 'pointer' is larger than the measurement strength, which again restricts to get information on this variable [34].

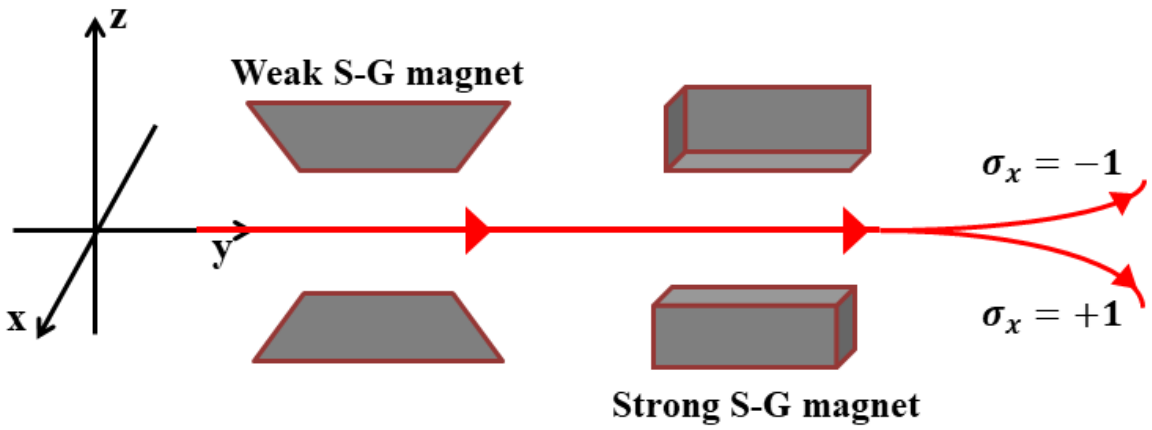

Figure 3.2 The Stern–Gerlach experimental setup as proposed by Aharonov et al. to measure the weak value of the electron's spin. In this configuration, a beam of particles with spin oriented along an arbitrary direction first passes through a weak magnetic field aligned along the *z*-axis. It then encounters a strong, inhomogeneous magnetic field along the *x*-axis, which separates the beam. The resulting deflection of the spot on the detection screen in the *z*-direction is proportional to the weak value of the spin.

Following the Von Neumann measurement idea aided with pre- and post-selection, Aharonov, Albert and Vaidmann (AAV) introduced a unique idea to extract information from quantum weak measurement in terms of "weak value" in 1988 [34]. Their study claims that 'the result

of a measurement of a component of the spin of a spin ½ particle can turn out to be 100' implying that when the post-selected state is nearly orthogonal to the pre-selected state, the corresponding weak value becomes extremely large and may even lie outside the eigenvalue spectrum of the measured observable which is referred to as weak value amplification (WVA) [Figure 3.2].

Consequently, Duck et al [19] and Ritchie et al [20] established all these features of WVA using standard classical wave interference approach which leads to widespread applications in optics domain. Over the next decade, WVA technique was utilized to improve precision in detecting small optical effect, such as beam displacement [26], phase shifts [35], angular rotations [36], time delays [37] and many more. Even it was utilized extensively in the field of quantum information science, through several tasks like state tomography [38], detecting wave function [39], measurement problems [40], Hardy's paradox [41] etc. Finally, the groundbreaking work by Hostein and Kwiat in 2008 explored the measurement of tiny photonic spin Hall effect (PSHE) during the transmission of linearly polarized light beam, proving again the colossal importance of WVA in observing fundamental weak effects. Following their work, the experimental detection of amplified Goos–Hänchen shift [21], Imbert-Fedorov shift [23] and the photonic spin Hall effect [24] was accomplished. Even in the transmission case, those measurements were also executed at different mediums like uniaxial crystal, 2D materials [42]. These studies lead to huge application of WVA combined with optical beam shifts in precision optical measurements like concentration, chemical reaction rate detection, non-destructive optical parameter such as optical conductivity, absorption, refractive index, thickness, layer numbers of 2D materials detection [43].

Here, we will briefly discuss the idea of weak measurements and its optical analog. The detailed experimental technique with proper theoretical background of measuring the GH shift, Photonic spin splitting will be discussed in the subsequent *chapters* where it is needed.

The typical procedure of WVA is depicted in Figure 3.3. A two-level quantum system (QS) is first pre-selected in state $|\psi_i\rangle = cos\,(\theta_i/2)|0\rangle + sin\,(\theta_i/2)e^{i\phi_i}|1\rangle$. The initial pointer state (PS) is prepared as a Gaussian superposition state given by,

$$|\varphi\rangle = \int dq\, \frac{1}{(2\pi\sigma^2)^{1/4}} exp\left[-\frac{q^2}{4\sigma^2}\right]|q\rangle = \int dp \left(\frac{2\sigma^2}{\pi}\right)^{1/4} exp\,[-\sigma^2 p^2]|p\rangle \tag{3.1}$$

where 'q' and 'p' are conjugate variables for example position and momentum, respectively. Correspondingly, $|q\rangle$ and $|p\rangle$ denote the position and momentum eigenstate of meter observable $\hat{Q}$ and $\hat{P}$, respectively. The QS interacts with the PS through the coupling Hamiltonian, $\hat{H} = g\delta(t - t_0)\hat{A} \otimes \hat{P}$, where $\hat{A}$ represent an observable of the QS and 'g' is the coupling strength. The interaction leads to the entangled joint state,

$$\Psi_{js} = exp\left(-i\int \hat{H}dt\right)|\psi_i\rangle \otimes |\varphi\rangle \tag{3.2}$$

Next, the joint state is post-selected in the state, $|\psi_f\rangle = cos(\theta_f/2)|0\rangle + sin(\theta_f/2)e^{i\theta_f}|1\rangle$ of the QS. After post-selection the PS is given by $|\Phi_f\rangle = \langle\psi_f|\Psi_{js}\rangle/\sqrt{p_f}$ with the success probability $p_f = |\langle\psi_f|\Psi_{js}\rangle|^2$. In the weak measurement scenario (g $\ll \sigma$), the final PS can be approximated to

$$\begin{aligned}|\Phi_f\rangle &= \frac{1}{\sqrt{p_f}}\langle\psi_f|exp\left(-ig\hat{A}\hat{P}\right)|\psi_i\rangle|\varphi\rangle \approx \frac{1}{\sqrt{p_f}}\langle\psi_f|\left(1 - ig\hat{A}\hat{P}\right)|\psi_i\rangle|\varphi\rangle \\ &= \frac{\langle\psi_f|\psi_i\rangle}{\sqrt{p_f}}\left(1 - ig\langle\hat{A}\rangle_w\hat{P}\right)|\varphi\rangle\end{aligned} \tag{3.3}$$

Where the weak value is defined as,

$$\langle\hat{A}\rangle_w = \frac{\langle\psi_f|\hat{A}|\psi_i\rangle}{\langle\psi_f|\psi_i\rangle} \tag{3.4}$$

Taking into account the additional condition of AAV approximation,

$$max_n g\frac{\left|\langle\psi_f|\hat{A}^n|\psi_i\rangle\right|^{1/n}}{|\langle\psi_f|\psi_i\rangle|} \ll \sigma \text{ for n } = 1, 2, \ldots, \tag{3.5}$$

the final PS can be written as,

$$|\Phi_f\rangle \approx exp\left(-ig\langle\hat{A}\rangle_w\hat{P}\right)|\varphi\rangle. \tag{3.6}$$

From equation (3.4), it is evident that when the pre- and post-selected states of QS are very close to orthogonal to each other i.e. $\langle\psi_f|\psi_i\rangle \to 0$, then the modulus of the weak value $|\langle\hat{A}\rangle_w|$ becomes significantly larger than the maximum eigenvalue of the observable $\hat{A}$. This weak value can also be complex in general [44]. In both cases, the weak value referred as anomalous. Both the real and imaginary parts of the large weak value can be obtained by the average value of the corresponding observables ($\hat{Q}$ or $\hat{P}$) of the PS as,

$$\langle \hat{Q} \rangle_f = g\, Re\langle \hat{A} \rangle_w \tag{3.7}$$

$$\langle \hat{P} \rangle_f = \frac{g}{2\sigma^2}\, Im\langle \hat{A} \rangle_w \tag{3.8}$$

With $\langle \cdot \rangle_f$ being the mean value of the observable in $|\Phi_f\rangle$. This amplification form represents the initial and widely form of WVA which is named as standard WVA. Since the observables $\hat{Q}$ and $\hat{P}$ are incompatible, the measurement of either observable may not extract the complete information of a complex weak value. For a given problem, researchers generally choose the weak value to be either purely real or purely imaginary in a WVA scheme, depending on the specific requirements of the study. For example, considering pre- and post-selected states as $\theta_i = \pi/2 - \epsilon$, $\theta_f = -\pi/2$ and $\varphi_i = \varphi_f = 0$, with a small ϵ (φ), a large real weak value $2/\epsilon$ can be obtained. However, this amplification comes at the cost of a corresponding decrease in the success probability of post-selection, approximately given by $p_f \approx \epsilon^2$.

Now, in different context depending upon the precise measurement of the parameter, the pointer state and the quantum system get changed [45]. Here, as we are focusing on the problem of optical beam shift measurement, we will briefly discuss the optical analog of WVA, where the polarization and the transverse spatial mode of photons serve as the quantum system (QS) and the pointer system (PS), respectively.

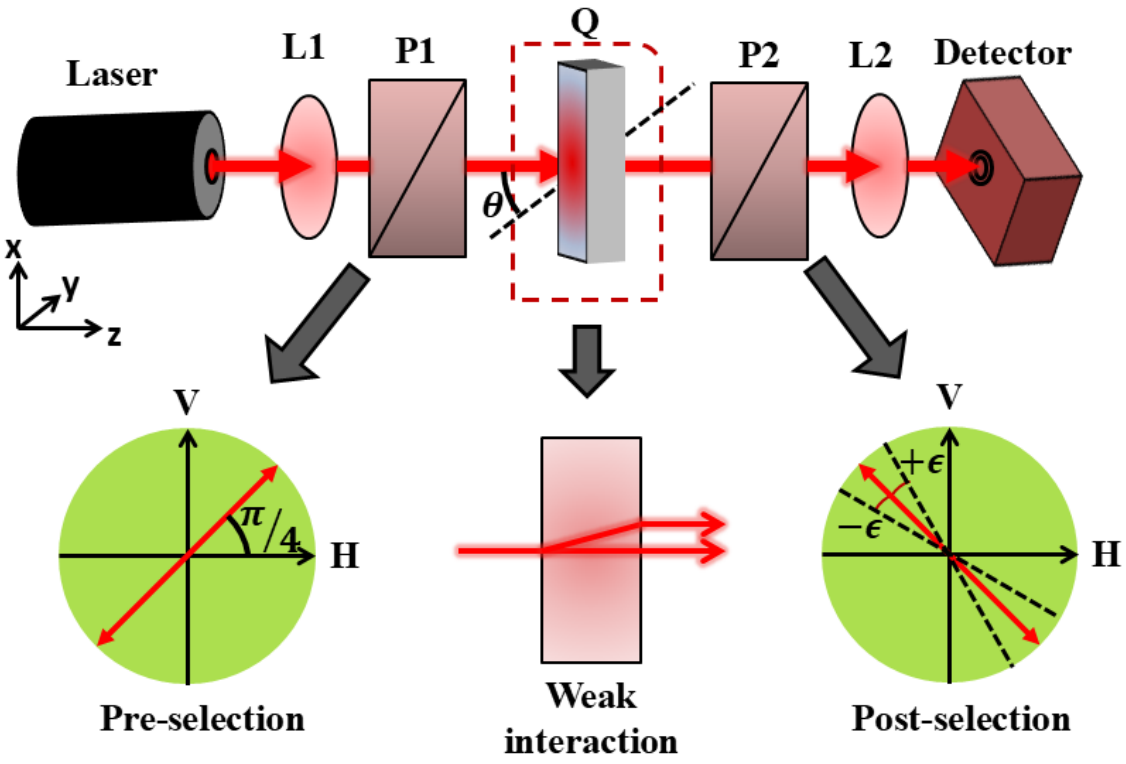

Figure 3.3 Schematic representation of optical analogue of weak value amplification along with the pictorial presentation of pre-selection, weak interaction and the post-selection.

The arrangements of different optical components are presented in Figure 3.3. Here, a He-Ne laser producing good quality fundamental Gaussian light beam is used as source and the pre- and post-selection procedures are executed using two polarizers. Meanwhile, the weak interaction is performed by a birefringent crystalline quartz plate that separated the two orthogonal polarization states of the laser beam by a distance which is much less than the waist of the laser beam.

The electric field of the incident light is given by,

$$E_i = E_0 \, exp\left[-\frac{(x^2+y^2)}{w_0^2}\right][\hat{x}\, cos\, \alpha + \hat{y}\, sin\, \alpha] \tag{3.9}$$

where, the incident linearly polarized beam oscillating at an angle α with respect to the x axis is propagating along the z-direction and w_0 is the beam waist.

The optic axis of the uniaxial crystal is along the x axis and the plane is rotated from the y-axis by an angle θ as shown in Figure 3.3. The uniaxial birefringent crystal spatially separates the two orthogonal linear polarization components (the ordinary and extra-ordinary rays) of the

incident light field, by a distance 'δl' which is small as compared to the beam waist. In addition, a phase difference ϕ between the two rays is also introduced by the birefringence plate due to the slight optical path difference. Neglecting the displacement caused by refraction present in both polarizations, the electric field of the emergent beam is given by,

$$E_o = E_0 \, exp\left[-\frac{x^2}{w_0^2}\right]\left\{\hat{x}\, e^{i\phi}\, cos\, \alpha \, exp\left[-\frac{(y+\delta l)^2}{w_0^2}\right] + \hat{y}\, sin\, \alpha \, exp\left[-\frac{y^2}{w_0^2}\right]\right\} \tag{3.10}$$

Next, the polarizer is applied to post-select the output electric filed at an angle 'β' w.r.t x-axis. As a result, the post-selected electric field becomes,

$$E_f = E_0 \, exp\left[-\frac{x^2}{w_0^2}\right]\left\{ e^{i\phi}\, cos\, \alpha \, cos\, \beta \, exp\left[-\frac{(y+\delta l)^2}{w_0^2}\right] + sin\, \alpha \, sin\, \beta \, exp\left[-\frac{y^2}{w_0^2}\right]\right\}\{\hat{x}\, cos\, \beta + \hat{y}\, sin\, \beta\} \tag{3.11}$$

Now, the intensity distribution of the transmitted light beam in the transverse plane can be expressed as $\left|E_f(x=0)\right|^2$ which is given by,

$$I(y) = I_0\left[cos^2\alpha\, cos^2\beta\, exp\left[-\frac{2(y+\delta l)^2}{w_0^2}\right] + sin^2\alpha\, sin^2\beta\, exp\left[-\frac{2y^2}{w_0^2}\right] + 2cos\, \phi\, cos\, \alpha\, cos\, \beta\, sin\, \alpha\, sin\, \beta\, exp\left[-\frac{(y+\delta l)^2+y^2}{w_0^2}\right]\right] \tag{3.12}$$

with 'I_0' being the maximum intensity of the light beam.

The displacement between the e-ray and o-ray, $\delta l \ll w_0$. To get maximum displacement, $\alpha = \pi/4$ is considered.

Considering $\beta = \alpha$, the resultant intensity $I(y)$ will be generated by the constructive superposition of two Gaussian distribution. This, $I(y)$ is nearly single, un-shifted Gaussian. When the second polarizer in the output is rotated by, $\beta = (\alpha + \pi/2)$, then destructive interference happens and the beam centroid splits into two parts by a distance $\sqrt{2}w_0$. Next, as we rotate the P2 by post-selection angle, ϵ from orthogonal condition the beam centroid positions will get displaced in a specific direction. In this case, if $\delta l/2w_0 \ll \epsilon \ll 1$ satisfied, the interference would yield a single Gaussian with the centroid shifted by the weak value given by,

$$A_w \approx \frac{1}{2}\,\delta l \times cot\,\epsilon \tag{3.13}$$

As the 'ϵ' is very small considered, the weak value, A_w becomes enormously large as compared to δl. On the other hand, the intensity at this condition is given by, $I = \frac{1}{2e}\left(\frac{\delta l}{w_0}\right)^2 I_0$, which is reduced significantly. Therefore, Ritchie et al [20] showed that the birefringence induced separation, δl is amplified up to 20 times larger than the actual displacement, demonstrating the potential of weak value to amplify small optical effects. This is the basic principle of optical analogue of WVA which used in the experimental studies of optical beam shifts later [21-24].

3.2.2 Interferometric weak value amplification

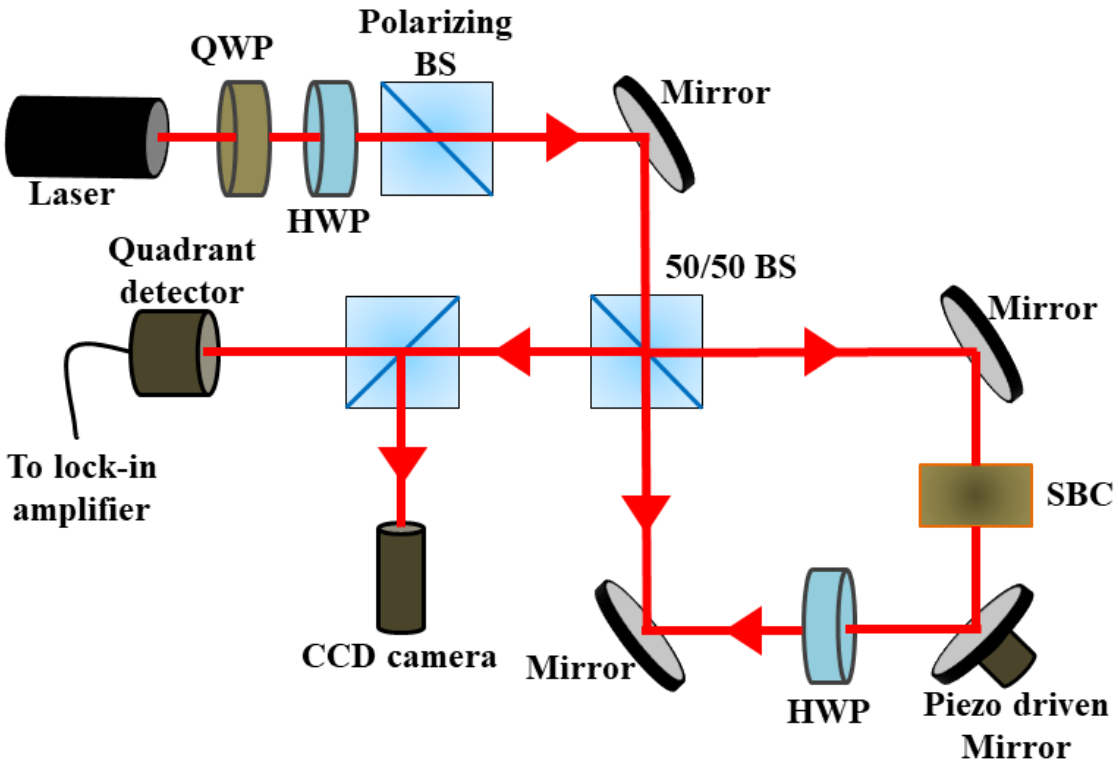

Figure 3.4 Pictorial representation of interferometric weak value amplification used to enhance the small deflection induced by a piezo-driven mirror.

It has been shown that by considering the spin of photons - represented by left- or right-circular polarization - as the quantum system (QS) and the transverse spatial mode as the pointer system (PS), the tiny spin Hall effect of light can be amplified by four orders of magnitude [12]. In 2009, Dixon et al. introduced an interferometric weak value amplification (IWVA) technique to detect ultra-small mirror tilts, achieving a sensitivity of 400 frad [26]. In their setup, the

which-path information - clockwise or counterclockwise - inside a Sagnac interferometer serves as the quantum system (QS), while the transverse spatial distribution of photons functions as the pointer system (PS). A small mirror tilt, induced by a piezo actuator, establishes the coupling between the QS and PS. Post-selection is achieved by monitoring the dark port of the interferometer, where the imaginary weak value translates the minute mirror tilt into a detectable shift in the transverse beam position. This study broadened the scope of WVA from exploring fundamental physical phenomena to enabling practical applications in precision parameter sensing.

To implement this measurement technique, consider the pictorial representation of the IWVA concept shown in Figure 3.4. The light beam enters a Sagnac interferometer composed of a 50/50 beam splitter and mirrors that direct the beam along one of two possible paths. In an ideal Sagnac interferometer, all the light exits through the input port (the bright port), while the other port remains dark. Constructive interference occurs at the entrance due to two 2π phase shifts.

This symmetry is intentionally broken by introducing a half-wave plate and a Soleil–Babinet compensator, which create a relative phase ϕ between the two paths, allowing the dark port to be tuned toward brightness. Essentially, this setup is a modified form of classical optical interferometry. As the beam traverses the interferometer, the spatial shift of light emerging from the dark port is monitored. The transverse position of the beam, labelled 'x', serves as the detection meter. A slight tilt is applied to a mirror at a symmetric point in the interferometer, imparting a transverse momentum shift to the beam. This tilt breaks the symmetry of the interferometer, causing one propagation direction to bend left of the optical axis and the other to bend right.

The final shift can be expressed as the position expectation as,

$$\langle x \rangle = 2k|A_w| \frac{\sigma^2 r_{lm} + w\sigma r_{md}}{r_{lm} + r_{md}} \tag{3.14}$$

where, $\sigma = a(r_{lm} + r_{md})/s_i$ is the beam size at the detector, r_{lm} is the distance from the lens image to the moving mirror, r_{md} is the distance from the moving mirror to the detector, and 'w' is the radius of initial collimated beams.

This technique offers several advantages. First, it can be applied to a wide range of beam deflection sources and is not restricted to polarization-dependent deflections. Second, the post-

selection is straightforward, relying simply on detecting a photon emerging from a specified interferometer port. Third, the post-selection attenuation is independent of the deflection source, as it arises solely from the destructive interference between the two paths. Additionally, the weak measurement, which involves monitoring the transverse position of the photon, can provide partial information about the system while minimally disturbing it.

3.2.3 Interferometric technique

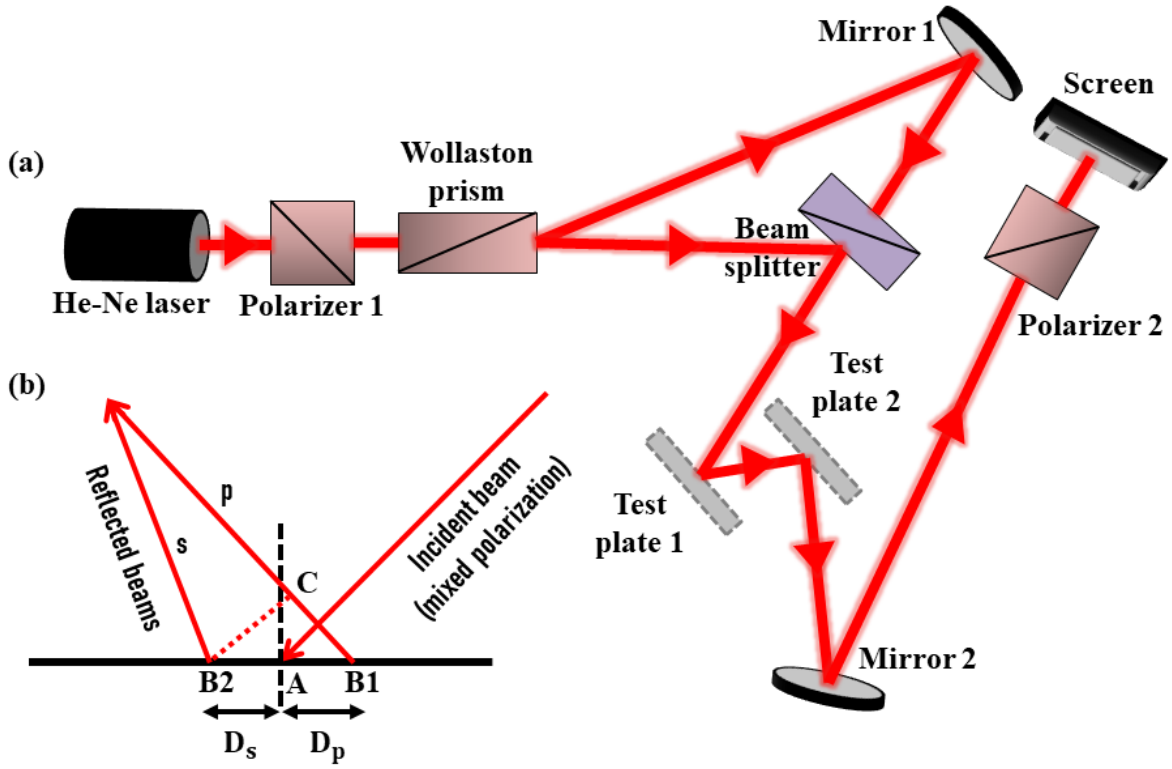

Figure 3.5 (a) Experimental setup to detect GH effect using interferometric technique (b) Schematic of GH effect appearing due to reflection of p- and s-polarized light beams.

The interferometric technique for studying the Goos–Hänchen (GH) effect was first introduced by Prajapati et al. in 2013 [27]. Qualitatively, the GH shift can be understood as follows: if A is the point of incidence for p- and s-polarized beams, the two beams shift upon reflection due to the GH effect. Let one polarized beam reflect from point B1 and the other from point B2; they then interfere on a screen. If the GH phase shift introduced between p- and s-polarized beams is $\phi_p - \phi_s$, the corresponding path change is given by $(\lambda/2\pi)(\phi_p - \phi_s)$, where $\phi_p - \phi_s$ represent the experimentally determined difference in phase after reflection. From this, the relative GH shift between the p- and s-polarized beams can be readily calculated as,

$$D_p - D_s = \frac{\lambda}{2\pi}\frac{(\phi_p - \phi_s)}{sin\,\theta} \tag{3.15}$$

where θ is the angle of incidence. The schematic of this phenomenon and the experimental setup to detect this phase shift using interferometry is shown in Figure 3.5.

In this setup, an unpolarized He-Ne laser operating at 633 nm is first directed through a polarizer, followed by a Wollaston prism. The polarizer controls the relative intensity of the *p*- and *s*-polarized beam components to achieve maximal fringe visibility, while the Wollaston prism separates the orthogonally polarized p- and s-components. One polarized beam is reflected by Mirror 1 and then passes through a beam splitter, while the other beam is directly reflected by the beam splitter. Mirror 1 is positioned such that both beams travel together and undergo partial reflection from the test plates, where the GH shift occurs.

Two parallel test plates arranged in a periscopic configuration are used to eliminate beam rotation when the angle of incidence is varied, converting it into a transverse displacement of the beam. This arrangement also enhances the GH shift through multiple reflections. After reflection from the test plates, the two beams co-propagate toward the screen, where they interfere after passing through a polarizer oriented at 45° or 135° relative to the p- and s-polarized beams. An additional polarizer, P2, is employed to simultaneously observe the interference fringes at both 45° and 135° orientations. The resulting fringe patterns are recorded at different angles of incidence, from which the GH shift is calculated.

This method offers several advantages. It is relatively easy to set up and allows measurement of the GH shift across the entire cross-section of the beam, rather than being limited to the beam centroid as in earlier techniques. The method is self-calibrating, as a scale is established on the image plane using the interference fringes corresponding to the laser wavelength, enabling direct measurement of the shift in terms of the wavelength. Additionally, it is tolerant of mild wavefront curvature or surface imperfections, since the fringes represent contours of equal phase and the shift is determined by comparing the fringe positions between closely adjacent points in the image.

3.2.4 Beam splitter scanning

Another useful technique for investigating the GH effect, known as the ‘beam splitter scanning (BSS) method’, was introduced by Li et al. in 2014 [28]. Using a focused light source, they observed a significant lateral shift of the beam centroid at graphene interfaces of varying

thickness when the polarization of the incident light changed from transverse magnetic (p) to transverse electric (s) mode, indicating that the GH shift in graphene is polarization-dependent. Furthermore, their study revealed that the GH shift increases with the thickness of the graphene layer.

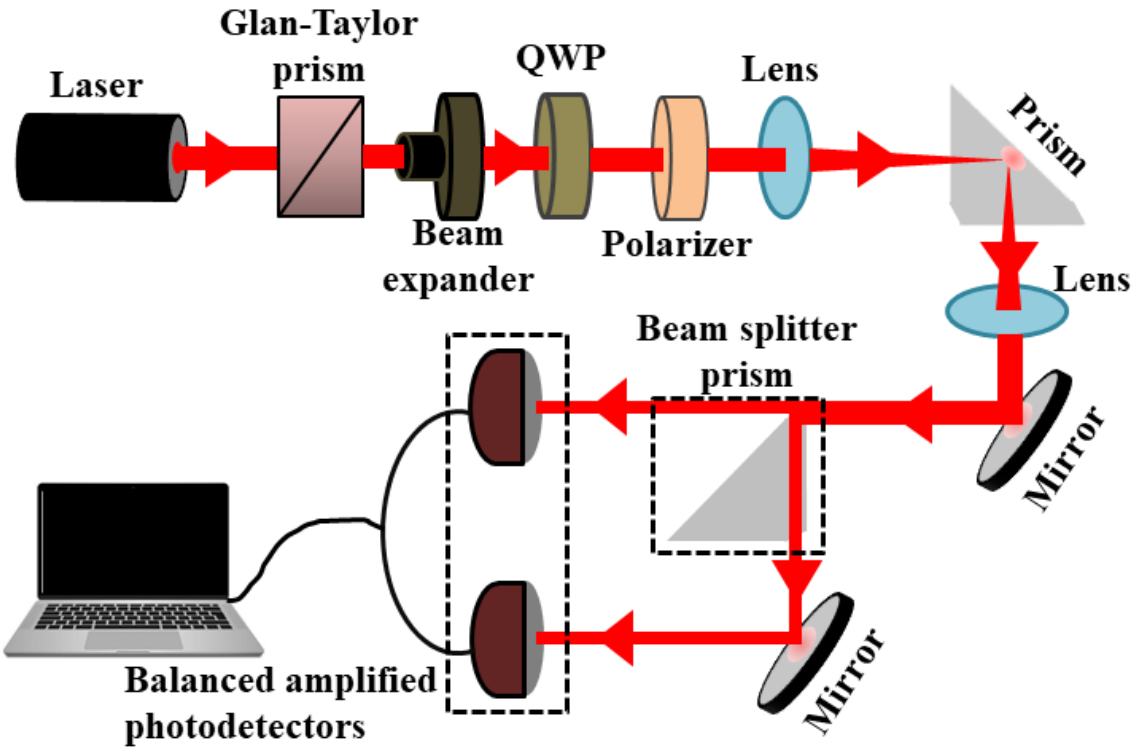

Figure 3.6 Schematic arrangement of optical components for detecting the GH shift using the beam splitter scanning method.

The schematic diagram of the experimental setup is presented in Figure 3.6. The optical path comprises of three main components: (i) generation of polarized light, (ii) the total internal reflection (TIR) structure, and (iii) the beam splitter detector. A He–Ne laser at 632.8 nm is used to produce a Gaussian light beam. The combination of a quarter-wave plate (QWP) and a polarizer is employed to control the polarization and beam profile of the incident light, allowing easy adjustment between p- and s-polarization.

After undergoing total internal reflection, the light beam is collimated using a lens and then split into two parts by a beam splitter prism, with the prism edge positioned at the centre of the beam to divide it into two halves. These halves are collected by a large-area balanced amplified photodetector, which uses two well-matched photodiodes to detect differences in

signal between the two beams. The resulting output voltage is proportional to the difference in photocurrent from the photodiodes. Prior to the experiment, the voltage response of the balanced detector was monitored to ensure it changed significantly when the incident light polarization was switched from transverse magnetic (TM) to transverse electric (TE).

The key advantage of this technique is that it allowed the identification of the polarization dependence of the GH effect, with significant variations in the lateral shift clearly distinguishing graphene samples of different thicknesses.

3.2.5 Stokes polarimetric method

In 1852, Sir George Gabriel Stokes demonstrated that the polarization behaviour of light could be described using observable quantities and introduced four measurable parameters, now known as the Stokes parameters (SP) [46]. The first parameter corresponds to the total intensity of the optical field, while the remaining three describe its polarization state. Stokes demonstrated that these parameters are valid for unpolarized light, as well as for partially and fully polarized light. The influence of an optical system on light polarization can be analyzed by constructing the Stokes vector of the incident light and applying Mueller calculus [47] to obtain the corresponding output Stokes vector.

Although Stokes's original work was largely overlooked for nearly a century, it was revived in 1947 when Subrahmanyan Chandrasekhar employed the SPs to formulate radiative transfer equations describing the scattering of partially polarized light, formally naming them the 'Stokes parameters [48]'. Since then, they have become a cornerstone of optical science, with wide-ranging applications in imaging, biomedical optics, optical engineering, remote sensing, electro-optic phenomena, and astronomical studies [49–51].

Considering a plane monochromatic wave propagating along the z-direction that is a superposition of two electric field components, the Stokes parameters are defined as [52],

$$\begin{aligned} S_0 &= a_x^2 + a_y^2 \\ S_1 &= a_x^2 - a_y^2 \\ S_2 &= 2a_x a_y \cos\delta \\ S_3 &= 2a_x a_y \sin\delta \end{aligned} \tag{3.16}$$

where a_x and a_y represent the instantaneous electric field amplitudes of the polarized laser beam along x and y directions, respectively, and δ is the instantaneous phase difference between the x- and y- components of the electric field.

The amplitude is measured in volts per meter (V/m), while the phase difference is expressed in degrees. The Stokes parameters S_0, S_1, S_2, S_3 are actual, empirically measurable quantities that can be determined using standard photodetectors, typically in units of microwatts (μW). Here, S_0, the first Stokes parameter, represents the total intensity of the light. S_1 quantifies the degree of linear horizontal or vertical polarization, S_2 describes the degree of linear +45° or –45° polarization, and S_3 indicates the amount of right- or left-circular polarization present in the beam.

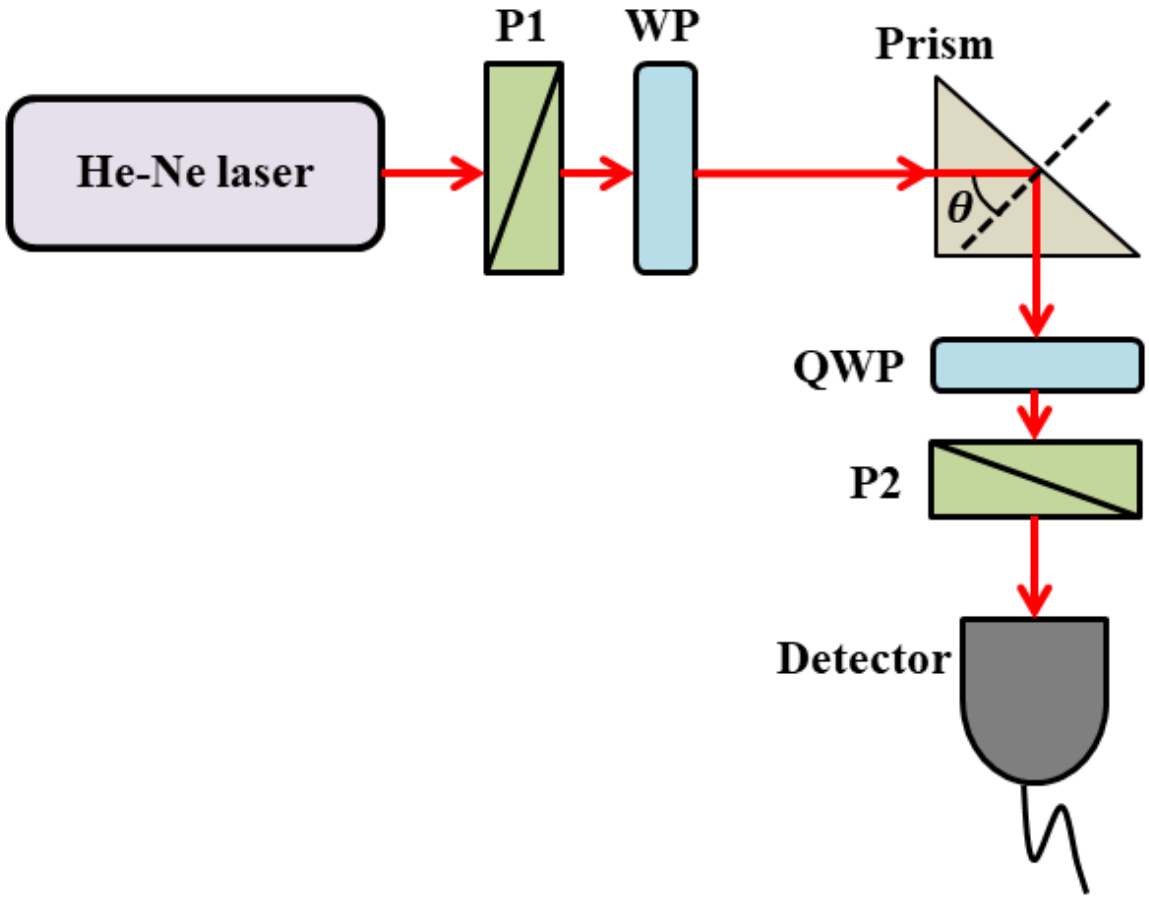

Figure 3.7 Schematic arrangement of optical components for measuring Stokes parameters resulting from internal reflection within a prism. By appropriately rotating the quarter-wave plate (QWP) and polarizer P2, different Stokes parameters can be measured directly.

The concept of measuring optical beam shifts using the Stokes polarimetric method was first proposed by Prajapati et al. [29] in 2014. Following the formulation of beam shifts by

Aiello and Woerdman [53], the Goos–Hänchen (GH) and Imbert–Fedorov (IF) shifts can be expressed as,

$$GH = \frac{\lambda}{2\pi}\frac{|r_s|^2 a_s^2\, Im\left(\frac{\partial ln\, r_s}{\partial \theta_i}\right) + |r_p|^2 a_p^2\, Im\left(\frac{\partial ln\, r_p}{\partial \theta_i}\right)}{|r_s|^2 a_s^2 + |r_p|^2 a_p^2} + \frac{z_r}{kz_R{}^2}\frac{|r_s|^2 a_s^2\, Re\left(\frac{\partial ln\, r_s}{\partial \theta_i}\right) + |r_p|^2 a_p^2\, Re\left(\frac{\partial ln\, r_p}{\partial \theta_i}\right)}{|r_s|^2 a_s^2 + |r_p|^2 a_p^2} \tag{3.17}$$

and

$$IF = -\frac{\lambda}{2\pi}\frac{a_p a_s\, cot\,\theta_i}{|r_s|^2 a_s^2 + |r_p|^2 a_p^2}\Big\{\left(|r_s|^2 + |r_p|^2\right) sin\,\eta + 2|r_s||r_p| sin\left(\eta + \phi_s - \phi_p\right)\Big\} - \frac{z_r}{kz_R{}^2}\frac{a_p a_s\left(|r_s|^2 - |r_p|^2\right) cot\,\theta_i}{|r_s|^2 a_s^2 + |r_p|^2 a_p^2} cos\,\eta \tag{3.18}$$

where $a_s = E_{0x}$ and $a_p = E_{0y}$ represent the amplitudes of the s- and p-polarized components of the incident beam; θ_i is the angle of incidence, z_r is the propagation distance, and z_R is the Rayleigh range. The wave vector is given by $k = 2\pi n/\lambda_0$, where λ_0 as the wavelength of light in vacuum and 'n' is the refractive index of the dielectric medium. In equation (3.17) and (3.18), the first term corresponds to the spatial shift, while the second term represents the angular shift.

As evident from the above equations, the GH and IF shifts depend on both the amplitude and the phase difference between the p- and s-polarized components. During partial or total internal reflection at a dielectric interface, the amplitude of a specific polarization may change, and a relative phase is introduced with respect to the incident beam. Experimentally, the Stokes parameters are measured using a combination of a quarter-wave plate (QWP) and a polarizer [29], or with a commercially available polarimeter [30], as illustrated in the experimental setup (Figure 3.7). From these measurements, the phase difference between the p- and s-polarized components can then be determined as,

$$\phi_s - \phi_p = arctan(S_3/S_2) - \eta \tag{3.19}$$

where η denotes the phase difference between the p- and s-components of the incident beam, which varies with the polarization state of the incident light. Specifically, $\eta = 0$ for pure p- or s-polarization; $\eta = 0$ or π for $\pm 45^{\circ}$linear polarization; and $\eta = \pm \pi/2$ for left- or right-circularly polarized (LCP/RCP) beams.

Besides, the amplitude of reflection is given by,

$$|r_s| = \sqrt{\frac{S_0 + S_1}{2E_{0x}^2}} \qquad (3.20)$$
$$|r_p| = \sqrt{\frac{S_0 - S_1}{2E_{0x}^2}}$$

Using equations (3.17) – (3.20), the spatial and angular GH and IF shifts for a specific incident polarization can be calculated straightforwardly. Although this approach is an indirect method, it is significantly faster than direct measurement techniques. The primary advantage of this method is its simplicity and versatility, as it is independent of beam shape and intensity. Consequently, it offers valuable new insights into the spatial and angular behavior of optical beam shifts.

3.3 Concluding remarks

To summarize, we began by reviewing the fundamental methodologies and then examined various experimental techniques currently available for measuring optical beam shifts, including the Goos–Hänchen, Imbert–Fedorov, and photonic spin Hall effects. We provided a brief overview of the underlying mechanisms of five experimental setups, highlighting their respective advantages and limitations. Among these, we identified the weak value amplification method as the most suitable approach for developing our laboratory setup. Accordingly, we implemented this technique and investigated optical beam shifts under different scenarios, the details of which will be presented in the following chapters. It is important to note, however, that depending on the specific research objectives, other techniques may also be employed as needed.

References

1. I. Newton, *Opticks* (Octavo, Palo Alto, 1998).
2. F. Goos and H. Hänchen, Ann. Phys. **436**, 333 (1947).

3. F. I. Fedorov, Dokl. Akad. Nauk SSSR **105**, 465 (1955).
4. C. Imbert, Phys. Rev. D **5**, 787 (1972).
5. M. Green, P. Kirkby and R. S. Timsit, Phys. Lett. A **45**, 259 (1973).
6. J. J. Cowan and B. Aničin, J. Opt. Soc. Am. **67**, 1307 (1977).
7. F. Bretenaker, A. Le Floch and L. Dutriaux, Phys. Rev. Lett. **68**, 931 (1992).
8. J. W. Ra, H. L. Bertoni and L. B. Felsen, SIAM J. Appl. Math. **24**, 396 (1973).
9. Y. M. Antar and W. M. Boerner, Can. J. Phys. **52**, 962 (1974).
10. I. A. White, A. W. Snyder and C. Pask, J. Opt. Soc. Am. **67**, 703 (1977).
11. C. C. Chan and T. Tamir, Opt. Lett. **10**, 378 (1985).
12. O. Hosten and P. Kwiat, Science **319**, 787 (2008).
13. S. Chen, X. Zhou, C. Mi, H. Luo and S. Wen, Phys. Rev. A **91**, 062105 (2015).
14. W. Long *et al.*, Photonics Res. **7**, 1273 (2019).
15. Z. Qin, Q. Liu, C. Yue and X. Zhou, J. Phys. D: Appl. Phys. **52**, 495106 (2019).
16. D. Müller, D. Tharanga, A. A. Stahlhofen and G. Nimtz, Europhys. Lett. **73**, 526 (2006).
17. M. Merano, A. Aiello, M. P. van Exter and J. P. Woerdman, Nat. Photonics **3**, 337 (2009).
18. Y. Aharonov, D. Z. Albert and L. Vaidman, Phys. Rev. Lett. **60**, 1351 (1988).
19. I. M. Duck, P. M. Stevenson and E. C. G. Sudarshan, Phys. Rev. D **40**, 2112 (1989).
20. N. W. M. Ritchie, J. G. Story and R. G. Hulet, Phys. Rev. Lett. **66**, 1107 (1991).
21. G. Jayaswal, G. Mistura and M. Merano, Opt. Lett. **38**, 1232 (2013).
22. G. Jayaswal, G. Mistura and M. Merano, Opt. Lett. **39**, 6257 (2014).
23. G. Jayaswal, G. Mistura and M. Merano, Opt. Lett. **39**, 2266 (2014).
24. Y. Qin, Y. Li, H. He and Q. Gong, Opt. Lett. **34**, 2551 (2009).
25. S. Goswami, M. Pal, A. Nandi, P. K. Panigrahi and N. Ghosh, Opt. Lett. **39**, 6229 (2014).
26. P. B. Dixon, D. J. Starling, A. N. Jordan and J. C. Howell, Phys. Rev. Lett. **102**, 173601 (2009).
27. C. Prajapati, D. Ranganathan and J. Joseph, J. Opt. Soc. Am. A **30**, 741 (2013).
28. X. Li, P. Wang, F. Xing, X. D. Chen, Z. B. Liu and J. G. Tian, Opt. Lett. **39**, 5574 (2014).
29. C. Prajapati, S. Pidishety and N. K. Viswanathan, Opt. Lett. **39**, 4388 (2014).
30. A. Das and M. Pradhan, J. Opt. **22**, 105004 (2020).

31. V. B. Braginsky and F. Y. Khalili, *Quantum Measurement* (Cambridge University Press, Cambridge, 1995).
32. J. von Neumann, *Mathematical Foundations of Quantum Mechanics* (Princeton University Press, Princeton, 2018).
33. A. Steinberg, A. Feizpour, L. Rozema, D. Mahler and A. Hayat, Phys. World **26**, 35 (2013).
34. Y. Aharonov, D. Z. Albert and L. Vaidman, Phys. Rev. Lett. **60**, 1351 (1988).
35. N. Brunner and C. Simon, Phys. Rev. Lett. **105**, 010405 (2010).
36. O. S. Magaña-Loaiza, M. Mirhosseini, B. Rodenburg and R. W. Boyd, Phys. Rev. Lett. **112**, 200401 (2014).
37. M. Asano *et al.*, Nat. Commun. **7**, 13488 (2016).
38. Y. Kim *et al.*, Nat. Commun. **9**, 192 (2018).
39. J. S. Lundeen *et al.*, Nature **474**, 188 (2011).
40. M. E. Goggin *et al.*, Proc. Natl. Acad. Sci. USA **108**, 1256 (2011).
41. J. S. Lundeen and A. M. Steinberg, Phys. Rev. Lett. **102**, 020404 (2009).
42. K. Y. Bliokh *et al.*, Optica **3**, 1039 (2016).
43. S. Liu, S. Chen, S. Wen and H. Luo, Opto-Electron. Sci. **1**, 220007 (2022).
44. R. Jozsa, Phys. Rev. A **76**, 044103 (2007).
45. L. Xu and L. Zhang, Prog. Quantum Electron. **96**, 100518 (2024).
46. G. G. Stokes, Trans. Cambridge Philos. Soc. **9**, 399 (1851).
47. S. N. Savenkov, Light Scattering Rev. **4**, 71 (2009).
48. S. Chandrasekhar, *Radiative Transfer* (Dover, New York, 1960).
49. M. Izdebski, R. Ledzion and W. Kucharczyk, J. Opt. Soc. Am. B **34**, 2281 (2017).
50. D. Clarke, *Stellar Polarimetry* (Wiley, New York, 2009).
51. N. Ghosh and A. Vitkin, J. Biomed. Opt. **16**, 110801 (2011).
52. D. H. Goldstein, *Polarized Light* (CRC Press, Boca Raton, 2017).
53. A. Aiello and J. P. Woerdman, Opt. Lett. **33** 1437–9 (2008).

4 Polarization Controlled Goos-Hänchen Shift

The content of this chapter is adapted from the following published article:

S. Mandal, A. Das, and M. Pradhan, "Polarization-controlled Goos–Hänchen shift by weak value amplification in total internal reflection," ***Journal of the Optical Society of America B*** 41 (3), 750-755 (**2024**).

4.1 Introduction

Optical beam shift, one of the most exciting light-matter interactions, happens when a light beam with finite width is reflected or refracted at an optical interface. Depending on the nature of the interaction surface and the characteristics of the incoming light, the reflected or refracted beam centroid position may be shifted at an alternate location, deviated in-plane and/or out-of-plane following diffractive corrections to the geometrical optics representation [1-3]. These in-plane (longitudinal) and out-of-plane (transverse) shifts are often known as Goos-Hänchen (GH) and Imbert-Fedorov (IF) shifts, respectively [Figure 4.1] [4-9]. The angular counterparts of both GH and IF shifts exist, and they show as shifts in wave vector space [10-11]. Although both of these phenomena have been extensively investigated in the context of total internal reflection (TIR), they can also be seen in partial reflection and refraction [12-14].

Extensive analytical and experimental research has been conducted in this domain in recent years due to its numerous applications in the fields of optical sensors [15-16], precision measurement of optical constants [17], image edge detection [18], chemical reaction analysis [19-20], and optical switches [21] etc. In recent years, the GH and IF shifts have also been explored in several material mediums, including as graphene [22-23], TMDCs [24-25], photonic crystals [26], topological semimetals [27], metamaterials [28], and plasmonic materials [16].

Due to polarization fluctuation and the beam reshaping effect [29], it is challenging to detect small beam shifts using position-sensitive detectors alone. As a result, there is a fundamental propensity to enhance and accurately identify such minute changes by adjusting the light-matter interactions, either by means of peculiar material characteristics or distinctive features of incident light beam. Furthermore, a number of developmental techniques have been used in earlier research to identify such minute shifts, including “Stokes polarimetry [30]”, “Quantum weak measurement (QWM) [31]”, and “Beam splitter scanning method [32]” (Discussed in *Chapter* 3). We took advantage of the QWM technique among them because of its ultra-high precision measurement of small shifts and straightforward experimental setups. Aharonov, Albert, and Vaidman (AAV) [33] established the QWM formalism, and Ritchie et al. [34] applied it to the optical system for the first time. The three fundamental phases of weak measurement are pre-selection, weak coupling, and post-selection. In order to significantly enhance the optical beam shifts, we first preselect the system in a specific polarization state, after which a weak coupling occurs between the system and the pointer state during the

interaction process. Finally, we appropriately monitor the mutual orientations of the polarizers so that the output state is almost orthogonal to the input state of the light.

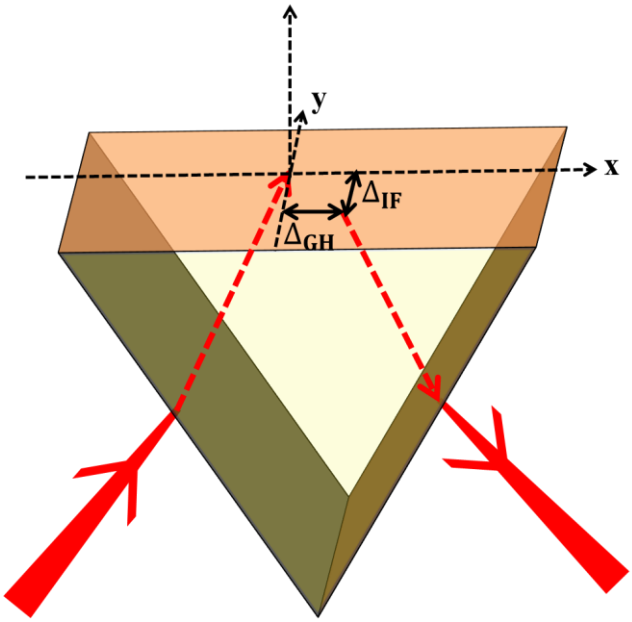

Figure 4.1 Schematic illustration of the GH & IF shifts for total internal reflection of light from a prism-air interface.

As previously mentioned, the GH shift is dependent on a number of regulating factors, including the incoming light's wavelength, polarization [35], beam shape [36], orbital angular momentum (OAM) [37], and the characteristics of the associated medium. Since the TM (p) and TE (s) linearly polarized modes are frequently referred to as the eigenmodes of the GH shift, most of the earlier experimental studies [38] on the GH shift were carried out using specific polarizations of light. However, in weak value amplification scenario, the polarization degree of freedom is a crucial aspect that has not yet been conveniently investigated.

The purpose of this article is to clarify the significance of incident light beam polarization in the investigation of GH shifts, particularly in the neighborhood of the critical angle, by continuously adjusting the light's polarization. To verify the experimental findings, a novel theoretical approach has also been created concurrently.

4.2 Theory

In order to formulate a mathematical framework, we first take an incident light beam's arbitrary polarization state into consideration as,

$$|\Psi_{in}\rangle = \begin{pmatrix} \alpha_1 \\ \alpha_2 e^{i\eta} \end{pmatrix} \tag{4.1}$$

For linear polarization states of light, $\eta = 0$. Equation (4.1) can be presented in this following form, for simplicity:

$$|\Psi_{in}\rangle = \begin{pmatrix} \alpha_1 \\ \alpha_2 \end{pmatrix} = \begin{pmatrix} cos\ \phi \\ sin\ \phi \end{pmatrix} \tag{4.2}$$

Where, ϕ = 0°, 90°, 45° signify *p*-polarized, *s*-polarized, and 45° linearly polarized light, respectively. In our experiment, we continually alter this parameter. The weak measurement situation generates tremendous amplification of the GH shift, as stated by [39],

$$\Omega = \frac{\langle \Psi_{out} | \hat{X}_{GH} | \Psi_{in} \rangle}{\langle \Psi_{out} | \Psi_{in} \rangle} \tag{4.3}$$

Where $\hat{X}_{GH} = \begin{pmatrix} -i\frac{\partial\ ln\ r_p}{\partial\theta} & 0 \\ 0 & -i\frac{\partial\ ln\ r_s}{\partial\theta} \end{pmatrix}$ is the GH shift operator, $|\Psi_{out}\rangle$ is the reflected beam, post-selected by another polarizer (GLP2) to a state almost orthogonal to the pre-selected state, i.e. $\langle \Psi_{out} | \Psi_{in} \rangle \approx 0$, in the weak value amplification. After post-selection at an angle β, the final amplified GH shift can be represented as,

$$\Omega = \pm\frac{i}{\varepsilon}\left[\frac{\partial\ ln\ r_s}{\partial\theta} - \frac{\partial\ ln\ r_p}{\partial\theta}\right]\alpha_1\alpha_2 - i\left[\alpha_1^2\frac{\partial\ ln\ r_p}{\partial\theta} + \alpha_2^2\frac{\partial\ ln\ r_s}{\partial\theta}\right] \tag{4.4}$$

The real and imaginary part of the above equation provide the amplified spatial (Δ_{GH}) and angular (Θ_{GH}) GH shifts respectively as,

$$\Delta_{GH} = \frac{1}{k} Re[\Omega] \tag{4.5}$$

$$\Theta_{GH} = \frac{1}{kz_R} Im[\Omega] \tag{4.6}$$

Where, $z_R = kw_0{}^2/2$ is the Rayleigh range and 'w_0' is the width of the incident light beam.

4.3 Experimental Methodology

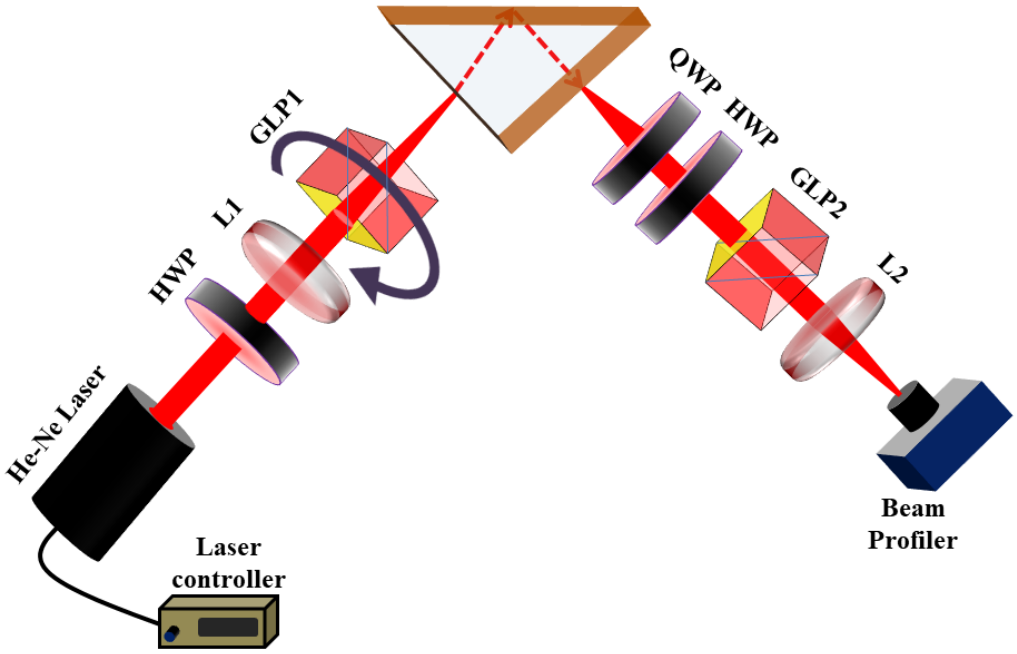

Figure 4.2 The experimental setup for an optimized quantum weak measurement to detect polarization-dependent GH shift near the critical region. L1, L2: plano-convex lenses, HWP (QWP): half (quarter) wave plate, GLP1, GLP2: Glan-Thompson polarizers.

Figure 4.2 depicts the experimental setup for QWM technique. To conduct the experiment, a plano-convex lens L1 (LA1433, Thorlabs) with a focal length of 150 mm was used to collimate and focus the incident light beam generated by a 633 nm He-Ne laser (30991, Research Electro Optics, Inc.) source to a width of approximately 180 µm. The beam profiler (LBP 4 USB, 6610d, Newport) was then used to examine this width. The intensity of the incident laser beam is controlled by the introduction of a half-wave plate (HWP) (WPMH10M-633, Thorlabs). After that, the optic axis of Glan-Thompson polarizer (GLP1) (GTH10M-A, Thorlabs) is rotated to preselect the incident light beam's polarization at a specific polarization angle (ϕ), which is managed by a high precision rotation mount (PRM1/M, Thorlabs). A right-angled prism (refractive index, n = 1.5151, N-BK7 RA, Thorlabs) is set up on a stable stage (PRM1Z8, Thorlabs). The angle of incident of the light beam is controlled by a high precision rotation system (KPRM1E, Thorlabs) connected to the stage. The beam then undergoes a GH shift (

Δ_{GH}) during total internal reflection at the prism surface where the weak interaction of the light with the glass-air interface takes place.

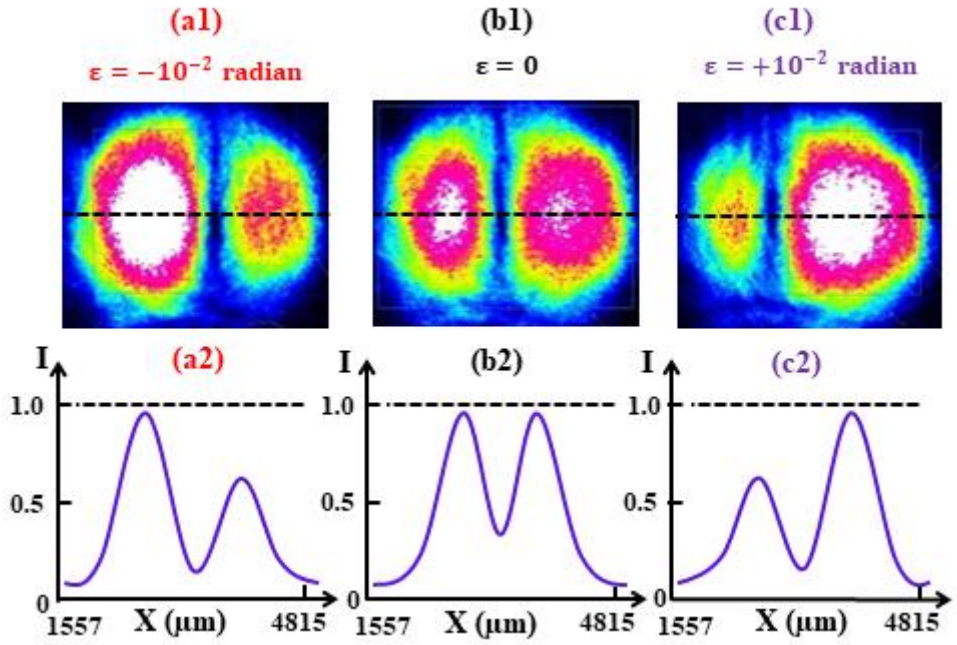

Figure 4.3 Variation of the beam profile as the post-selection state is modulated by the rotation of the polarizer (GLP2) by angle, $\beta = (\phi + \pi/2) \pm \varepsilon$ **(a)** $\varepsilon = -10^{-2}$ radian **(b)** $\varepsilon = 0$, and **(c)** $\varepsilon = +10^{-2}$ radian. **Upper panel**: Nature of beam profile, **Lower panel**: Intensity (**I**) variation along the horizontal (**X**) cross-section of the beam.

The reflected light beam then passes through the post-selection unit consisting of quarter wave plate (QWP) (WPMQ10M-633, Thorlabs), HWP and another Glan-Thompson polarizer (GLP2) (GTH10M-A, Thorlabs). A Stokes polarimeter (PAX1000VIS/M, Thorlabs) is used to monitor the appropriately rotating HWP and QWP combinations, which eliminates the additional phase (δ) that resulted from TIR. Then the GLP2 is rotated to a position so that we get minimal intensity at the output. This is referred to as the least intensity setting, and it is nearly orthogonal ($\phi + \pi/2$) to the incident light beam's polarization state. The incident beam profile breaks into two distinct Gaussian profiles at this location, separated by $\sqrt{2}w_0$. In order to eliminate any polarization rotation that might have arisen as a result of geometric phase during light focusing and collimation, we used a second plano-convex lens (L2) after GLP2. This weak value amplification is explained in Figure 4.3. Now, the post-selection is conducted by positioning GLP2 at an angle (β) close to the orthogonal location with regard to GLP1 (ϕ): $\beta = (\phi + \pi/2) \pm \varepsilon,\ \varepsilon \to 0$. Beam profiler data is used to determine the beam centroid

position for each post-selection angle ($\pm\varepsilon$), which is then used to compute amplified GH shift [Δ_{GH} cot(ε)] [31].

As we described before, in our experiment, we have set $\varepsilon = 10^{-2}$ radian as it gives an amplification of 100. The upper row of Figure 4.3 represents the reflected beam centroid as recorded by the beam profiler (LBP 6610d, Newport), and the lower row gives the horizontal cross-section of the same reflected beam. The middle column [Figure 4.3 (b1, b2)] signifies the case of exact orthogonality (ε = 0) when GLP2 is placed perpendicular to GLP1. This is a singularity condition at which the beam splits up in two separate Gaussian lobes. Figure 4.3 (a1, a2) and (c1, c2) denote the cases of $\varepsilon = -10^{-2}$ rad and $\varepsilon = +10^{-2}$ rad, respectively. Here, the angle of incidence is too close to the critical angle, resulting in the formation of two peaks, one more intense than the other [41]. We can then quickly determine the ultimate spatial GH shift from there.

4.4 Results & Discussions

Utilizing the QWM approach, we begin by examining the polarization dependency of the spatial GH shift. In order to conduct the experiment, we fixed the angle of incidence (θ) at a predetermined angle and continuously tailored the incident beam's angle of polarization (ϕ) while maintaining the polarization state as "linearly polarized". Basically, we have changed the angle of polarization (ϕ) continuously to transform the linearly polarized light from p-polarization ($\phi = 0^{\circ}$) to s-polarization ($\phi = 90^{\circ}$). Therefore, following total internal reflection of incident light with a particular angle of polarization from the prism (NBK7), we track the amplified GH shift (Δ_{GH}).

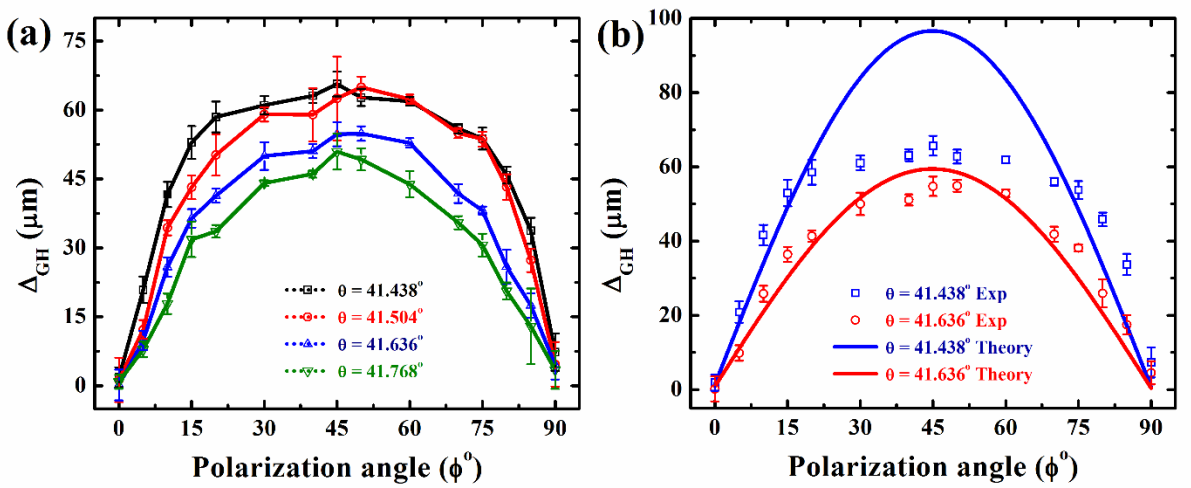

Figure 4.4 Variation of GH shifts (Δ_{GH}) with the angle of polarization (ϕ) for fixed angles of incidence (θ = 41.438º, 41.504º, 41.636º, and 41.768º): (a) experimental data, (b) comparison of experimental data with the theoretical model.

Figure 4.4(a) displays the outcomes of the experiment. Four distinct angles of incidence, θ = 41.4º, 41.5º, 41.6º, and 41.7º, were selected, and ϕ was continually altered for each angle of incidence from 0° to 90°. We have selected these specific angles of incidence as we like to operate close to the critical angle of incidence (θ_c), which shows the greatest GH shifts. This fact has also been confirmed by our subsequent results (Figure 4.6). The vanishing of Δ_{GH} below θ_c caused us to select angles of incidence greater than the critical angle ($\theta > \theta_c$) (Figure 4.6 (a)). Since beam distortion occurs, the Fresnel theory fails, and the theoretical model breaks down, we have avoided the exact critical angle (θ_c).

The amplified GH shift begins at zero at $\phi = 0^{\circ}$, raises monotonically to a maximum, and then decreases monotonically to zero at $\phi = 90^{\circ}$, as shown in Figure 4.4(a). After critically examining this graph, we can arrive at a set of conclusions. First, for p-polarized ($\phi = 0^{\circ}$) and s-polarized ($\phi = 90^{\circ}$) light, the amplification is zero. Second, for linearly polarized light with $\phi = 45^{\circ}$, the GH shift is at its highest. Therefore, this is the ideal state of incident light polarization to achieve maximum amplification of the GH shift. Third, based on the four distinct angles of incidence, it can be concluded that the spatial GH shift is greater for angles near the critical angle and diminishes as we move farther away from it ($\theta_c = 41.4^{\circ}$).

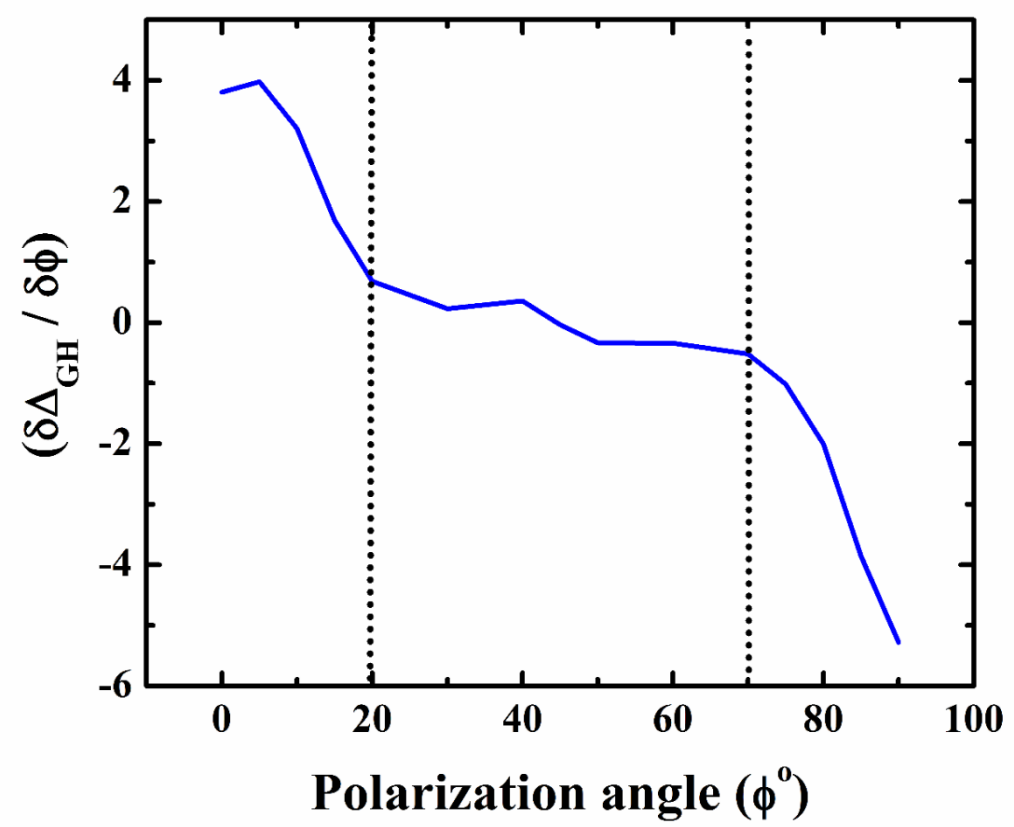

Figure 4.5 Nature of the slope of spatial GH shift with respect to the polarization angle.

Fourth, we have determined the slope of the GH shift with respect to the polarization angle and plotted it against the polarization angle (as shown in Figure 4.5) in order to further establish the dependency of the spatial GH shift on polarization. The graph's nature makes it clear that the slope is nearly constant in the $\phi = 20^{\circ}$ to 70° polarization angle range. Therefore, it is appropriate to select this specific region of polarization angle if one wishes to eliminate the impact of polarization on the spatial GH shift.

Lastly, we established a theoretical model equation (4.5) to validate the experimental findings. We next computed the amplified GH shifts and contrasted the theoretical curve with the experimental data in Figure 4.4(b). The experimental data and the theoretical curve agree fairly well. Around the polarization angle $\phi = 45^{\circ}$, there is a small disagreement about the angle of incidence $\theta = 41.438^{o}$. This is due to the fact that the theoretical model diverges at the critical angle of incidence, which we are quite near to. The agreement is nearly flawless as we move away from this critical angle.

Parallel to this, we also wanted to show how the spatial GH shift (Δ_{GH}) depends on the angle of incidence (θ). Even though this is a well-known result, we have demonstrated

something novel here. Figure 4.6(a) displays the angular dependency of the spatial GH shift for various polarization angle (ϕ) values. As can be seen in Figure 4.6(a), we have selected several polarization angles, $\phi = 0^{\circ}$, 30°, 50°, 70°, and 90°. We are aware that the highest at the critical angle is Δ_{GH} [40]. The non-trivial behavior of the Fresnel reflection coefficients causes Δ_{GH} to go up at the critical angle (θ_c) [40]. Δ_{GH} disappears below the critical angle (Figure 4.6(b)). When the enhanced spatial shift Δ_{GH} exceeds the critical angle, it rapidly diminishes.

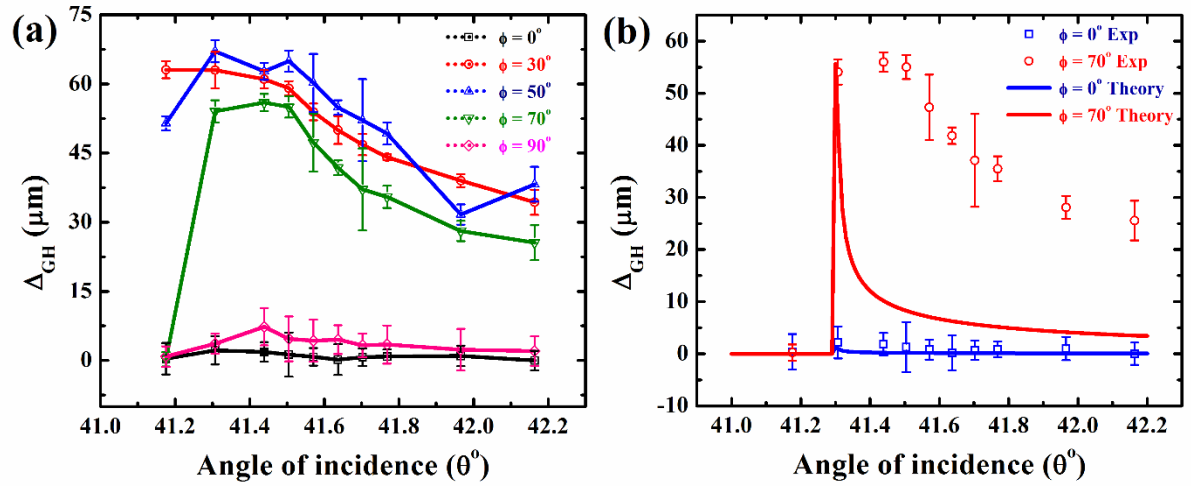

Figure 4.6 Variation of GH shifts (Δ_{GH}) with the angle of incidence (θ) for specific angles of polarization (ϕ = 0º, 30º, 50º, 70º, and 90º): (a) experimental data, (b) comparison of experimental data with the theoretical model.

Additionally, we used our theoretical findings to support the experimental findings. Figure 4.6 (b) illustrates the relative comparison between the experimental data and the theoretical outcomes. Because of the additional contributions from optical loss components in real-time experiments, the theoretically estimated spatial shift dies down faster than the experimental curve.

4.5 Concluding remarks

In summary, we found that arbitrary linearly polarized light incident on a prism next to its critical angle exhibits polarization-controlled spatial Goos-Hänchen (Δ_{GH}) shift. By using weak measurement, the study determines the ideal working zone of polarization angle that provides the greatest amplification of the spatial GH shift. Polarization-controlled photonic devices, such as optical sensors, switches, etc., can benefit greatly from this kind of tailoring of the spatial GH shift by the incident light's polarization angle. The experimental findings and the

suggested theoretical model show a very strong agreement. A similar methodology, with slightly altered weak measuring conditions, can be used to investigate the IF shift with modifying additional parameters like as wavelength, surface of interaction, etc. Furthermore, one can examine the region adjacent to Brewster's angle to determine whether it contains any non-trivial responses. Our findings may contribute to our understanding of the generic GH shift and pave the way for future device and sensor applications.

References:

1. K. Y. Bliokh and A. Aiello, J. Opt. 15, 014001 (2013).
2. F. Töppel, M. Ornigotti and A. Aiello, New J. Phys. 15, 113059 (2013).
3. A. Aiello, New J. Phys. 14, 013058 (2012).
4. F. Goos, H. Hänchen, Annalen der Physik, 436, 333-346 (1947).
5. F. Bretenaker, A. Le Floch, and L. Dutriaux, Phys. Rev. Lett. 68, 931 (1992).
6. C. Imbert, Phys. Rev. D 5, 787 (1972).
7. M. Ornigotti and A. Aiello, J. Opt. 15, 014004 (2013).
8. M. R. Dennis and J. B. Götte, New J. Phys. 14, 073013 (2012).
9. J. B. Götte, W. Löffler, and M. R. Dennis, Phys. Rev. Lett. 112, 233901 (2014).
10. A. Aiello and J. P. Woerdman, Opt. Lett. 33, 1437-1439 (2008).
11. S. D. Leo, L. Maggio, and M. d'Ambrosio, Photonics, 9, 643 (2022).
12. S. Grosche, M. Ornigotti and A. Szameit, Opt. Express 23, 30195-203 (2015).
13. A. Das and M. Pradhan, "Goos-Hänchen shift for Gaussian beams impinging on monolayer-MoS_2-coated surfaces," JOSA B 35, 1956-1962 (2018).
14. S. Goswami, S. Dhara, M. Pal, A. Nandi, P. K. Panigrahi, and N. Ghosh. Opt. Express 24, 6041-6051 (2016).
15. W. Xianping, C. Yin, J. Sun, H. Li, Y. Wang, M. Ran, and Z. Cao, Opt. Express 21, 13380-13385 (2013).
16. X. Yin and L. Hesselink, Appl. Phys. Lett. 89, 261108 (2006).
17. S. Chen, X. Ling, W. Shu, H. Luo and S. Wen, Phys. Rev. Appl. 13, 014057 (2020).
18. D. Xu, S. He, J. Zhou, S. Chen, S. Wen, & H. Luo, Appl. Phys. Lett. 116 (2020).
19. J. Liu, K. Zeng, W. Xu, S. Chen, H. Luo and S. Wen, Appl. Phys. Lett. 115, 251102 (2019).
20. R. Wang, J. Zhou, K. Zeng, S. Chen, X. Ling, W. Shu, H. Luo and S. Wen, Apl. Photonics 5, 016105 (2020).

21. X. Wang, C. Yin, J. Sun, J. Gao, M. Huang and Z. Cao, J. Opt. 15, 014007 (2013).
22. S. Chen, C. Mi, L. Cai, M. Liu, H. Luo and S. Wen, Appl. Phys. Lett. 110, 031105 (2017).
23. M. Shah, A. Akbar, N. A. Khan, Q. Zaman, S. Iqbal, W. Ali, M. Javed, and M. Shah, JOSA B 39, 1082-1090 (2022).
24. A. Das and M. Pradhan, Opt. Comm. 437 312-320 (2019).
25. M. Shah, M. Sajid, and M. S. Anwar, Phys. E: Low-Dimens. Syst. Nanostructures 134, 114819 (2021).
26. S. Du, W. Zhang, W. Liu, Y. Zhang, M. Zhao, and L. Shi, Nanophotonics 11, 4531-4536 (2022).
27. Q. Yue, X. Zhou, D. Deng, New J. Phys. 25, 018001 (2023).
28. Y. Kang, Y. Xiang, and C. Luo, Appl. Phys. B 124 (2018).
29. P. Xiao, JOSA B 28,1895-1898 (2011).
30. C. Prajapati, S. Pidishety, and N. K. Viswanathan, Opt. Lett. 39, 4388-4391 (2014).
31. G. Jayaswal, G. Mistura, and M. Merano, Opt. Lett. 38, 1232-1234 (2013).
32. X. Li, P. Wang, F. Xing, X. Chen, Z. Liu, and J. Tian, Opt. Lett. 39, 5574-5577 (2014).
33. Y. Aharonov, D. Albert, and L. Vaidman, Phys. Rev. Lett. 60, 1351 (1988).
34. N. W. M. Ritchie, J. G. Story, and R. G. Hulet, Phys. Rev. Lett. 66, 1107 (1991).
35. Z. Qin, L. Zhang, R. Zhang, P. Zhang, R. Qi, Q. Zhang, L. Ren, and L. Jiang, Opt. Express 31, 853-863 (2023).
36. K. N. Pichugin, D. N. Maksimov, and A. F. Sadreev, JOSA A 35, 1324-1329 (2018).
37. M. Merano, N. Hermosa, J. P. Woerdman, and A. Aiello. Phys. Rev. A 82, 023817 (2010).
38. A. Haibel, G. Nimtz, and A. A. Stahlhofen, Phys. Rev. E 63, 047601 (2001).
39. S. Goswami, M. Pal, A. Nandi, P. K. Panigrahi, and N. Ghosh, Opt. Lett. 39, 6229-6232 (2014).
40. A. Aiello and J. P. Woerdman, arxiv 0903 (2009).
41. O. J. Santana, S. A. Carvalho, S. De Leo, & L. E. de Araujo, Opt. Lett. 41, 3884-3887 (2016).

5 Goos-Hänchen Shift in Monolayer WSe_2

The content of this chapter is adapted from the following published article:

S. Mandal, A. Sett, D. C. Dey and M. Pradhan, "Observation of the Goos-Hänchen shift in monolayer WSe_2 for an arbitrary linearly polarized incident light beam using weak measurement," ***Journal of the Optical Society of America B*** 41 (12), 2714-2720 (**2024**).

5.1 Introduction

As a consequence of the wave nature of light, when a bounded beam of light interacts with a planar boundary, the reflected or refracted light beam does not strictly adhere to the laws of geometrical optics. After the interaction, it can be displaced or deflected in the plane (longitudinal) and out of the plane (transverse) of the incident light beam at the wavelength scale, which are famously known as the Goos-Hänchen (GH) and Imbert-Fedorov (IF) shifts [1-2], respectively in total internal reflection conditions. A similar type of longitudinal or transverse shift (also known as the photonic spin Hall effect) can occur during external reflection [3-5]. Depending on the interaction circumstances, spatial or angular beam changes may occur [6]. It is well established that the GH shifts are caused by the dispersion of reflection or transmission coefficients, whereas the IF shift results from the conservation of total angular momentum, including the intrinsic spin angular momentum associated with circular polarization, during the interaction process [7, 8]. Ref [9, 10] provides a thorough review of optical beam shift.

Even though the optical beam shift was discovered about 70 years ago, research on it is still going strong due to its fundamental nature and vast potential in many different areas of optics which manipulate light at the sub-wavelength scale [11]. Numerous precision measurement applications have made substantial use of it, including polarization beam splitters [12], temperature sensors [13], optical switches [14], optical differential operation and edge detection [15], and many more [16,17]. However, there is a drawback to the experiment: the magnitude of the shift value is very small, about the wavelength of the incident light. Hence, it must be enhanced to improve the actual sensitivity and precision of the experimental measurement. Thus, since the very beginning, individuals have been searching for further ways to improve the shift value. The critical angle for internal reflection and the Brewster angle for external reflection are two examples of angles of incidence where the optical beam shifts are significantly impacted [18,19].

The conductivity, chemical potential, and refractive indices of the interacting surface are among the other characteristics that influence it [20-22]. Because of this, previous research on the beam shift phenomenon has employed a range of material mediums, such as graphene [23], TMDCs and other 2D materials [24], metamaterials [25], hyperbolic metamaterials [26], photonic crystals [27], and surface plasmon resonators [28], to significantly increase the beam shift value. The values of the beam shifts can also be varied by using various characteristics of

the incident light beam, such as polarization, wavelength, beam shape, or angular momentum [29, 30]. Additionally, from an experimental standpoint, weak value amplification is a potentially helpful tool for the simple measurement of the beam shift [5, 31, 32].

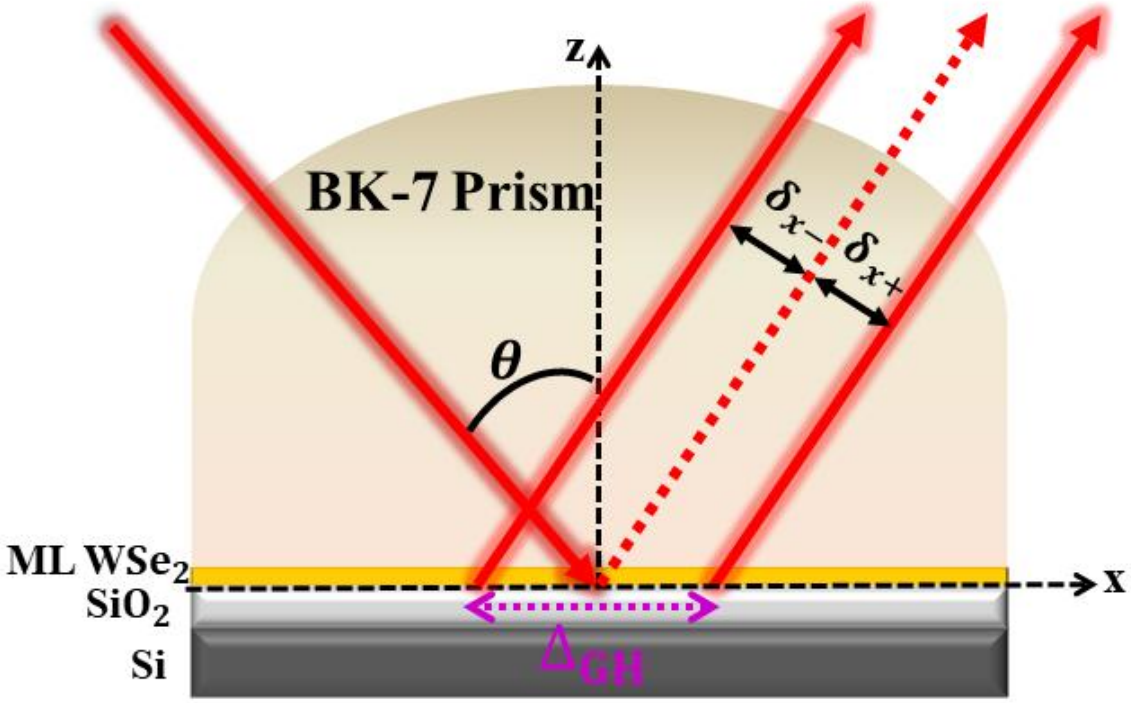

Figure 5.1 Schematic illustration of the spatial Goos-Hänchen shift (Δ_{GH}) caused by TIR of an arbitrarily polarized incident light beam from the ML WSe_2 – SiO_2/Si interface at the angle of incidence θ. The transverse displacement isn't shown here.

Among all the two-dimensional materials, monolayer transition metal di-chalcogenides have received a lot of attention due to the appearance of distinctive electrical and optical properties at reduced dimensions [33]. Because of the indirect to direct band gap transition, larger direct band gap, strong spin-orbit interaction, and lack of inversion symmetry in the monolayer limit, ML TMDCs have displayed enhanced photoluminescence quantum efficiency, strong light-matter interactions, accessible valley degrees of freedom, and other opto-electronic applications, respectively [34, 35].

In this *chapter,* we have attempted to investigate how the properties of the interaction medium can be used to modify the spatial Goos-Hänchen shift (Δ_{GH}) characteristics. Because

of its optical response in the visible frequency range, tungsten di-selenide (WSe_2) ML on a SiO_2/Si [Figure 5.1] substrate is chosen over all other 2D materials [36]. Additionally, it exhibits a strong spin-orbit coupling (SOC), a high quantum yield in photoluminescence (PL), and a high absorption coefficient in the visible to infrared region [37]. WSe_2 offers an excellent system for spin and valley-controlled materials because its SOC is significantly larger than that of MoS_2 in both the conduction ($2\lambda_c$ = 30 meV) and valence band ($2\lambda_v$ = 450 meV) bands [38]. Additionally, the band gap of ML WSe_2 (1.65 eV) is smaller than that of ML MoS_2 (1.8 eV), but their band gaps in bulk form are comparable at roughly 1.2 eV, and it is still debatable whether this band gap is of the direct or indirect type [39, 40].

Therefore, we have tried to investigate how the angle of incidence, polarization angle, and post-selection angle in the aforementioned structure affect the longitudinal optical beam shift in the TIR condition using the weak value amplification technique. To enable a simple determination of the polarization dependency on spatial longitudinal beam shift, the TIR area is considered to be the region where the intensity of the reflected light beam is consistently maintained in comparison to external reflections.

5.2 Theoretical model

Before measuring spatial GH shifts experimentally, we theoretically analyze the reflection coefficient to determine the exact angular region in the glass-ML WSe_2-SiO_2/Si combination where total internal reflection can occur. It is clear that this is a multi-layered structure of thin films. Thus, we have utilized the transfer matrix approach and the slab model to get the reflection coefficients, $r_{p,s}$, for p- and s-polarized light beams, which are given by [41],

$$r_{p,s} = \frac{r_{p,s}^{12} + r_{p,s}^{23} e^{2i\delta_2}}{1 + r_{p,s}^{12} r_{p,s}^{23} e^{2i\delta_2}} \tag{5.1}$$

here, $\delta_2 = \frac{2\pi}{\lambda} n_2 h_2 \cos\theta$ is the phase factor, where n_2 is the complex refractive index of the 2D material, h_2 is the thickness of that material, θ is the angle of incidence and $r_{p,s}^{ij}$ denotes the Fresnel reflection coefficients between the interface of i^{th} and j^{th} layer.

In our theoretical model, the parameters we selected are commonly used in the literature. For example, the wavelength of incident light beam is 632.8 nm, the wave dense/wave sparse medium interface is the ML WSe_2/SiO_2 interface. Considering the refractive indices of glass, ML WSe_2 and SiO_2 layers as n_1 = 1.515, n_2 = 3.7+0.012i [35], n_3 = 1.4636 + 0.001i [35],

respectively, the critical angle for this configuration is obtained near 23° as shown in Fig. 4.2. The thickness (h_2) is taken as 0.7 nm [35].

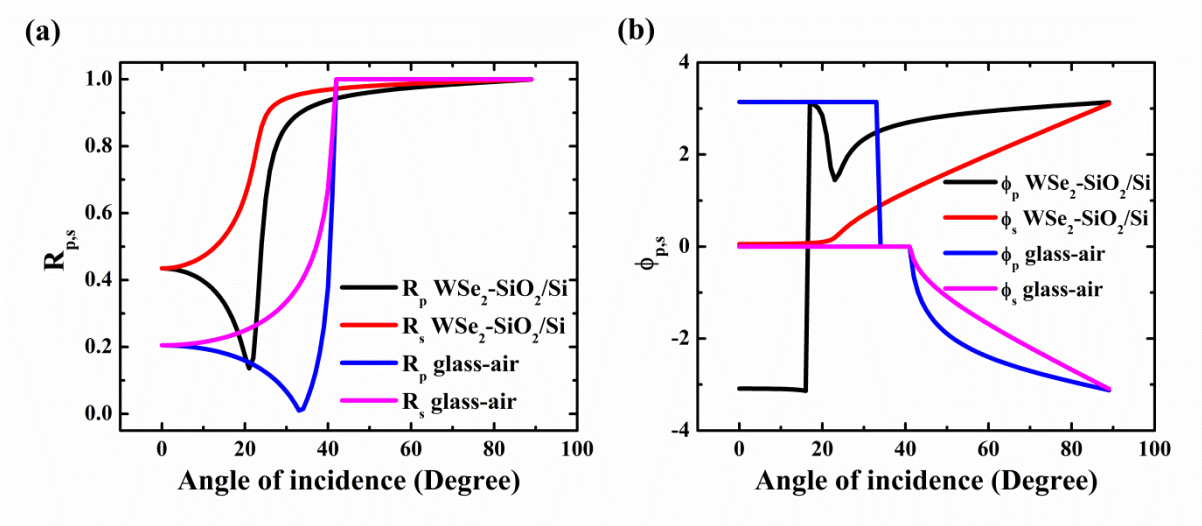

Figure 5.2 Angular dependence of (a) modulus ($R_{p,s}$) and (b) phase ($\phi_{p,s}$) of the reflection coefficient in case of ML WSe_2/SiO_2-Si and glass-air configuration in TIR condition.

From the plot of absolute value ($R_{p,s}$) and phase ($\phi_{p,s}$) of $r_{p,s} = R_{p,s}\exp(i\phi_{p,s})$ in Figure 5.2(a) & (b), it is clearly evident that both the critical angle and pseudo-Brewster angle for this structure are significantly shifted to 23.31° and 23.15° as compared to the simple glass-air configuration which was at 41.3° and around 33°, respectively. In this case, the critical angle and the pseudo-Brewster angle are extremely near to one another. Figure 5.2(a) also shows the signature of the material's absorbing nature because, unlike in the glass-air interface scenario, the $R_{p,s}$ simply does not display a unit value at the TIR region. Further, the TIR properties are similarly displayed by the phase curve in Figure 5.2 (b).

Thus, a theoretical model for the weak value amplification of spatial GH shift for total internally reflected arbitrary linearly polarized incident light beam from an absorbing material interface is developed using the polarization operator-based formulation due to its inherent mathematical simplicity. In this formalism, a Glan-Thompson polarizer (GLP1) is used to preselect the incident Gaussian light beam in the arbitrary polarization state as,

$$|\psi_{pre}\rangle = \begin{pmatrix} \cos\gamma \\ e^{i\beta}\sin\gamma \end{pmatrix} \tag{5.2}$$

where, β and γ represent the polarization phase and the polarization angle of the polarization state of the incident light beam, respectively.

In our case, $\beta = 0$, as only linearly polarized light beam is considered that interact with the ML WSe_2-SiO_2/Si configuration. Following the total internal reflection from the prism coupled ML WSe_2/SiO_2-Si system [Figure 5.3], the reflection matrix, $M_R = \begin{pmatrix} r_p & 0 \\ 0 & r_s \end{pmatrix}$, will transform the polarization state of the system into [42],

$$|\psi_{ref}\rangle = M_R|\psi_{pre}\rangle = \begin{pmatrix} e^{-i\frac{\delta}{2}}\ cos(\gamma) \\ e^{+i\frac{\delta}{2}}\ sin(\gamma) \end{pmatrix} \tag{5.3}$$

Where, $\delta = \phi_p - \phi_s$ is the relative phase difference between *p*- and *s*- polarization in the reflected light beam, r_p and r_s are the Fresnel reflection coefficients of *p*- and *s*-polarization states, which can be written as $r_{p,s} = |r_{p,s}| \exp(i\phi_{p,s})$. Under TIR condition, $|r_{p,s}| = 1$, and $r_{p,s} = \exp(i\phi_{p,s})$. So, $|\psi_{ref}\rangle$ will be in an elliptical polarization state generally, which is different for different incident polarization angles (γ) of the light beam. Tiny GH shifts appear at the interface between the SiO_2/Si substrate surface and ML WSe_2 during the interaction of the specific polarized light beam. The weak coupling between the spatial and polarization degrees of freedom occurred here. Now, following quantum mechanical formalism, this GH shift can be represented in operator form as [43],

$$\widehat{GH} = \begin{pmatrix} X_p & 0 \\ 0 & X_s \end{pmatrix} \tag{5.4}$$

Where,

$$X_{p,s} = \frac{1}{nk_0}\frac{\partial\phi_{p,s}}{\partial\theta_i} - i\frac{1}{nk_0|r_{p,s}|}\frac{\partial|r_{p,s}|}{\partial\theta_i} \tag{5.5}$$

Next, the post-selection of the reflected light beam is executed by using the combination of a quarter wave plate (QWP), a half wave plate (HWP) and another polarizer (GLP2). The action of QWP, HWP combination is represented as $\begin{pmatrix} e^{i\frac{\delta}{2}} & 0 \\ 0 & e^{-i\frac{\delta}{2}} \end{pmatrix}$, so that the extra relative phase δ is compensated. Then the optic axis of GLP2 is rotated to $(\varrho \pm \varepsilon)$, where $\varrho = \left(\frac{\pi}{2} + \gamma\right)$ and ε is the post-selection angle; so that the final projected state is given by [42],

$$\langle \psi_{post}| = (\cos(\varrho \pm \varepsilon) \quad \sin(\varrho \pm \varepsilon)) \tag{5.6}$$

Now, the weak value of the GH shifts can be easily calculated using the following formula [44] as,

$$\frac{\langle \psi_{post}|\widehat{GH}|\psi_{pre}\rangle}{\langle \psi_{post}|\psi_{pre}\rangle} = \frac{\sigma}{2}\left(X_p - X_s\right) sin(2\gamma)\, cot(\varepsilon) + (cos^2\gamma\, X_p + \, sin^2\gamma\, X_s) \tag{5.7}$$

where $\sigma = \pm 1$, represents the reflected light beam splits into two spin components right-circularly polarized (+1) and left-circularly polarized (-1), respectively. In equation (5.7), the first and second terms represent the spin-dependent spatial (Δ_{GH}) and spin-independent angular (Θ_{GH}) GH shifts.

In the experiment, we measured the difference between the beam centroid positions on the beam profiler for the post-selected states with post-selection angle (±ε). Considering the beam propagation effect, the final expression for amplified spatial GH shift can be obtained as [23,45],

$$\Delta_{GH} = \frac{\sigma}{2}\left\{Re\left[\left(X_p - X_s\right)\right] + \frac{z}{z_r} Im[\left(X_p - X_s\right)]\right\} cot(\varepsilon)\, sin(2\gamma) \tag{5.8}$$

where z and z_r represent the propagation distance and the Rayleigh range, respectively.

It is important to note that in the case of TIR from a simple glass-air contact, only the real component of $X_{p,s}$ survives; as a result, only the first term in equation (5.8) will be significant. However, the refractive index will be complex due to the absorptive nature of our selected sample (ML WSe_2/SiO_2-Si), and as a result, the amplified GH shift values will contain a contribution from the second part of equation (5.8) also.

5.3 Experimental procedure

The experimental setup used to investigate the polarization-dependent spatial GH shift in the TIR condition using weak value amplification is shown in Figure 5.3. As a pointer in our experiment, we employed a He-Ne laser (30991, Research Electro Optics, Inc.) beam with Gaussian intensity profile of wavelength of 633 nm. Because of the specific polarization of the light beam that emerges from the laser, the half-wave plate (HWP) (WPMH10M-633, Thorlabs) is employed to control the incident light beam's intensity. It is then focused using a plano-convex lens L1 (LA1433, Thorlabs) with a focal length of 150 mm to a spot size of 180 μm at the interaction surface. Next, using a high-precision rotation mount (PRM1/M, Thorlabs)

to control the optic axis of the Glan-Thompson polarizer (GLP1) (GTH10M-A, Thorlabs), the incident light beam is pre-selected to a particular linear polarization state (polarization angle, γ). A right-angle prism (N-BK7 RA, Thorlabs, refractive index, n = 1.515) was set up on a reliable stage (PRM1Z8, Thorlabs) with the sample ML WSe_2 on SiO_2/Si substrate affixed to its base. A high-precision rotation system (KPRM1E, Thorlabs) attached to the stage precisely controls the angle of incidence of the incident light beam.

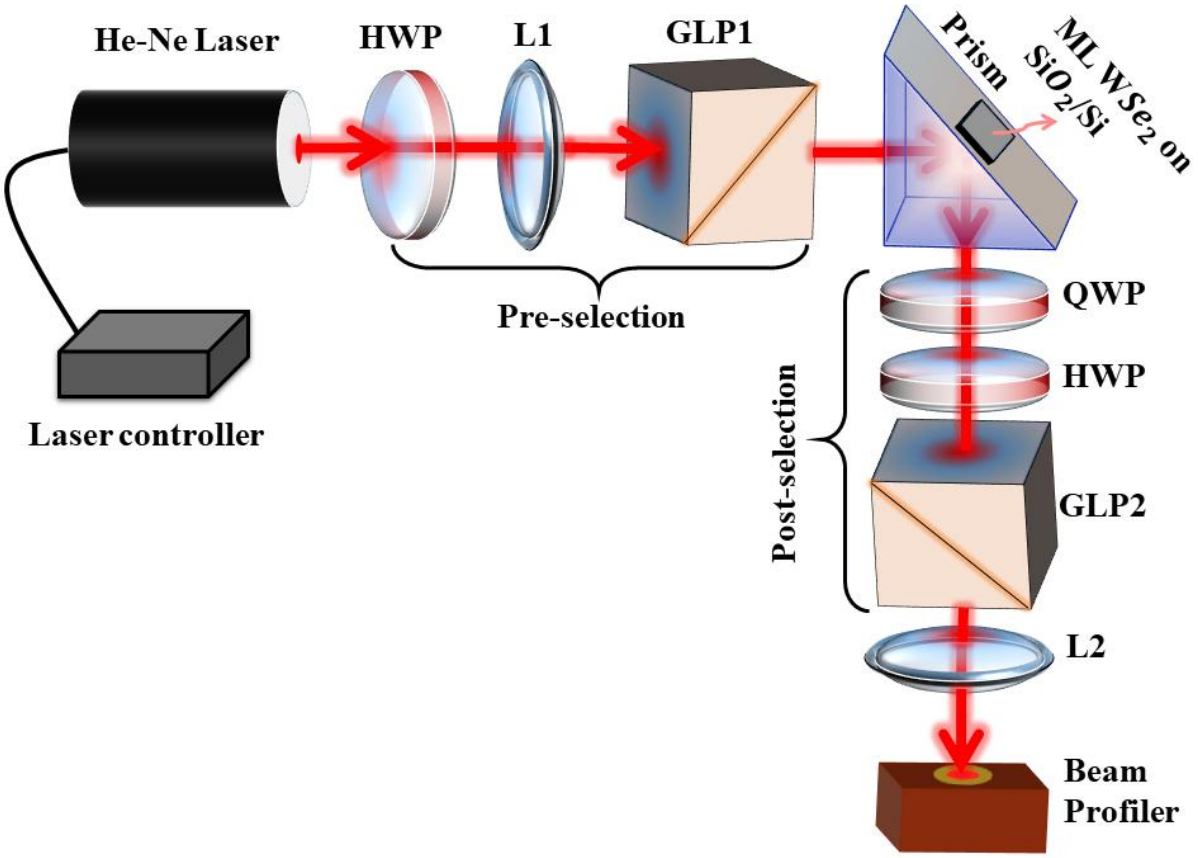

Figure 5.3 Schematic of the experimental setup: a Gaussian light beam generated by a He-Ne laser (632.8 nm). GLP1 and GLP2, Glan-Thompson polarizer; QWP/HWP, quarter/half-wave plate; L1 and L2, plano-convex lens with focal length 150 mm. Output data is collected using a beam profiler.

During total internal reflection, a sub-wavelength scale GH shift appears at the ML WSe_2-SiO_2/Si interface. TIR now causes the polarization state of the reflected light beam to change from linear to elliptical, as determined by the reflection coefficients. To eliminate the extra phase (δ) caused by TIR, a combination of QWP (WPMQ10M-633, Thorlabs) and HWP is used. The QWP and HWP are rotated in a specific manner so that the emerging beam has

the same polarization state as the incident light beam, which has been tracked using a Stokes polarimeter (PAX1000VIS/M, Thorlabs). To achieve the lowest intensity at the output, the GLP2 is then rotated to a position that is almost orthogonal ($\gamma+\pi/2$) to the polarization state of the incoming light beam. Under these circumstances, as illustrated in Figure 5.4 ($\varepsilon = 0^{\circ}$) [31], the beam profile separates into two distinct Gaussian profiles in the horizontal direction, separated by $\sqrt{2}w$. In order to eliminate any polarization rotation that may have arisen as a result of geometric phase during light focusing and collimation, a second plano-convex lens (L2) with a focal length of 150 mm is positioned in front of the beam profiler to create a 4f system. Lastly, the high-precision beam profiler (LBP 4 USB, 6610d, Newport) is used to track the intensity profile and the positions of the beam centroid.

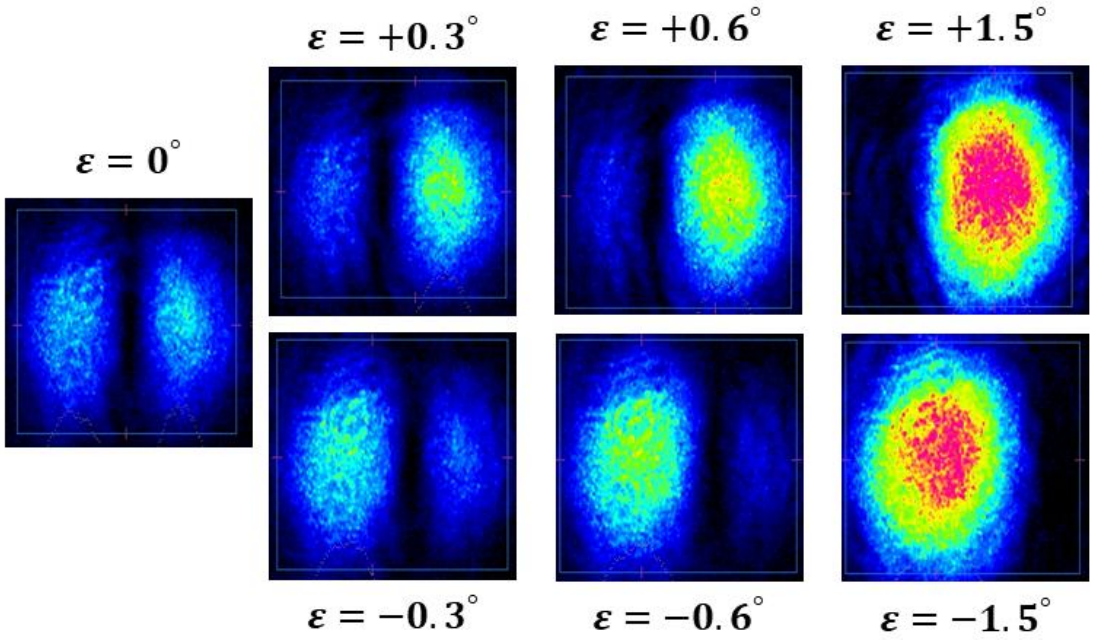

Figure 5.4 $\varepsilon = 0^{\circ}$ represent the intensity profile at the orthogonal condition obtained by adjusting the combination of QWP, HWP, and GLP2. The Variation of the intensity profiles of the reflected light beam after post-selection are shown for the post-selection angles $\varepsilon = \pm 0.3^{\circ}, \pm 0.6^{\circ}, \pm 1.5^{\circ}$.

Once the orthogonal condition is achieved, a high-precision motorized rotation system (KPRM1E, Thorlabs) rotates the optic axis of GLP2 in clockwise (+ε) and anti-clockwise (-ε) directions to a small post-selection angle. The intensity profiles of the reflected light beam after post-selection are shown in Figure 5.4 for the different post-selection angles $\varepsilon = \pm 0.3^{\circ}, \pm 0.6^{\circ}, \pm 1.5^{\circ}$. Lastly, the beam profiler data is used to calculate the relative position of the beam centroid.

5.4 Results and Discussions

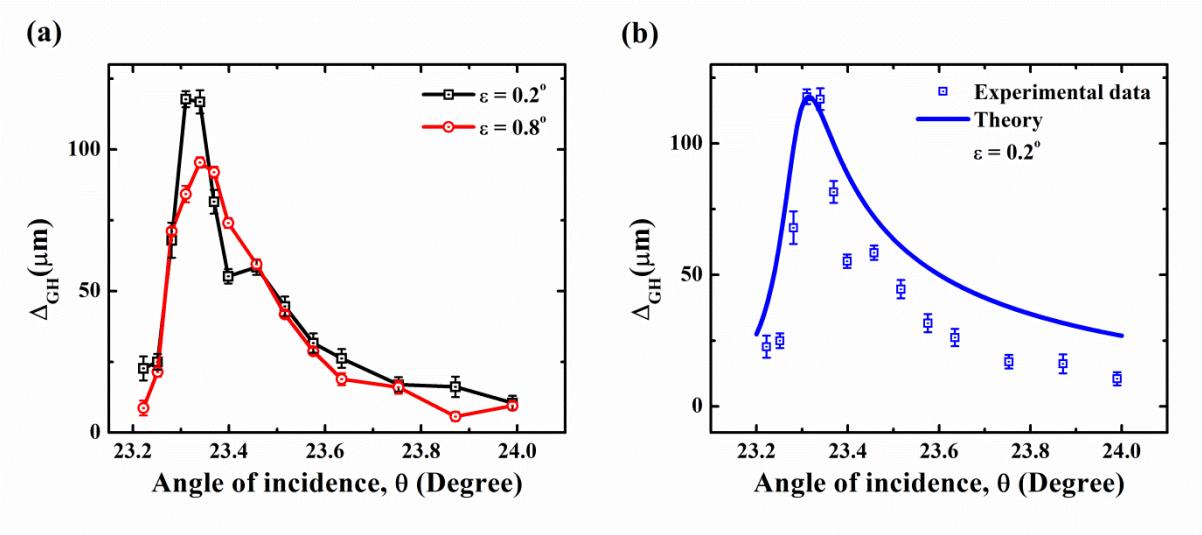

Figure 5.5 Representation of the (a) Experimental data and (b) theoretical comparison showing the variation of spatial Goos-Hänchen shift with the angle of incidence in the vicinity of the critical region.

The angular dependence of the spatial GH shift for our chosen configuration has been initially examined in Figure 5.5 for two different post-selection angles, 0.2° and 0.8°, respectively. Our experimental findings show that the critical angle for the ML WSe_2-SiO_2/Si arrangement is significantly changed to 23.31° angle of incidence compared to the glass-air or glass-graphene-air interface [23], which is normally at 41.3°. We also obtained the similar properties of the spatial GH shift at the critical region for this arrangement, albeit at a displaced angle of incidence. For a certain post-selection angle of 0.2°, the spatial GH shift starts at a tiny positive value and reaches approximately 116 μm at the critical angle of 23.31°. It then steadily dropped to miniscule shift values afterwards.

The enhanced spatial GH shift value we found in this work near the critical angle of incidence is somewhat similar to the amplified shift reported in the case of graphene [23] or monolayer MoS_2 [24], albeit being smaller in magnitude than the glass-air interface. Furthermore, we can see that the maximum shift value at the critical angle decreases with increasing post-selection angles. The degree to which the established theoretical model agrees with the experimental data is also shown in Figure 5.5(b). Moreover, by applying the weak value amplification methodology, we obtain nearly 7 to 8 times higher enhanced shift values

in the neighborhood of the critical angle of ML WSe_2-SiO_2/Si structure compared to the longitudinal shift values recorded using the beam splitter scanning method [46].

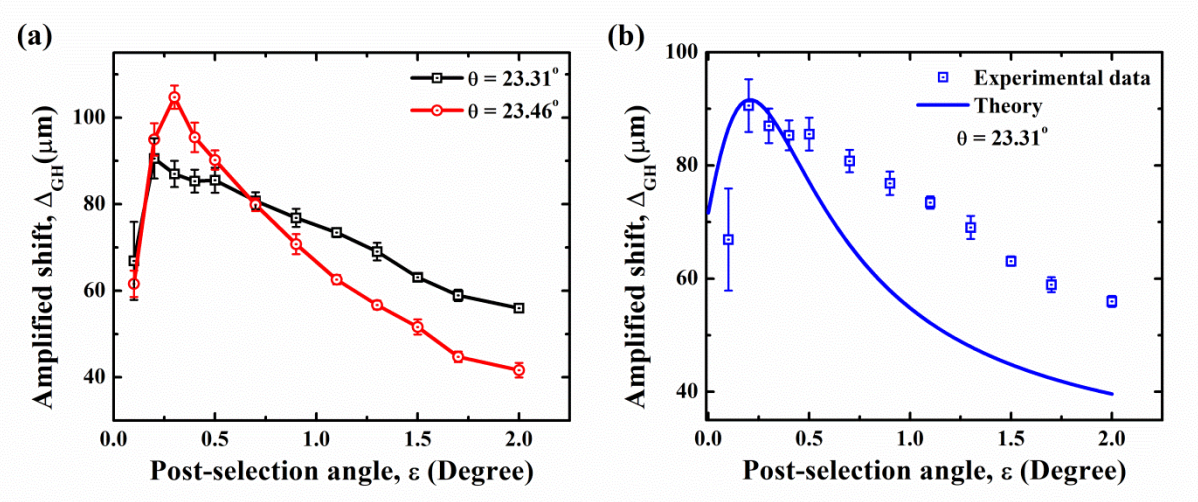

Figure 5.6 Representation of the (a) Experimental data and (b) theoretical comparison showing the variation of amplified spatial Goos-Hänchen shift with post-selection angle for 45° linearly polarized light at the angle of incidences in the critical region.

To further investigate the dependence of the spatial GH shift value on the post-selection angle, we then looked at 45° linearly polarized incident light beam for two different angles of incidence in the total internal reflection region, 23.31° and 23.46°, respectively, as illustrated in Figure 5.6. After attaining a maximum value for a particular post-selection angle, we observe that the amplified shift values progressively decrease as the post-selection angle increases. The highest shift of approximately 90 μm and 100 μm is found at 0.2° and 0.3° post-selection angles for the angle incidences of 23.31° and 23.46°, respectively. Thus, the maximum shift value is determined by the incidence angle and the post-selection angle selection. It is also observed that at incidence angles larger than the critical angle, which is 23.46°, the shift values decrease more rapidly. Furthermore, it varies more slowly at higher post-selection angles than it does at lower ones, causing the slope of the curves decrease.

A comparison between the experimental results and the theoretical model is shown in Figure 5.6(b). There is a small discrepancy for higher post-selection angles, but overall, the trend of the theoretical curve and the experimental results are similar. This deviation may be caused by improperly chosen exact orthogonal conditions or undesired diffraction of the

reflected light beam as it passes through multiple optical elements; these factors are not taken into account in the theoretical formalism. Compared to earlier research in glass-graphene-air or glass-air interface [23], which was roughly around 0.8°, we achieved the greatest shift value with a reduced post-selection angle of about 0.2°.

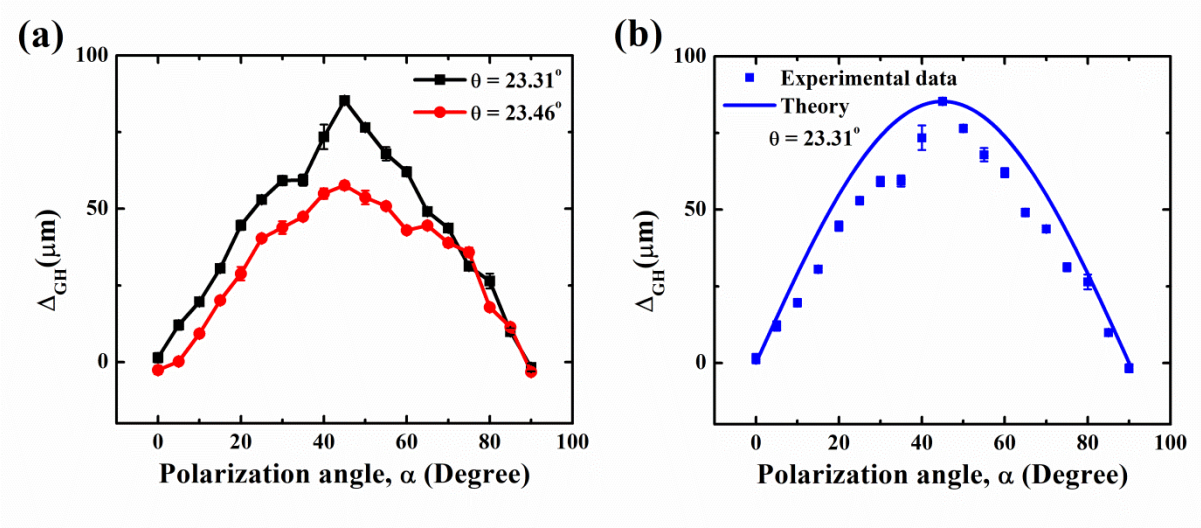

Figure 5.7 Representation of the (a) Experimental data and (b) theoretical comparison showing the variation of amplified spatial Goos-Hänchen shift with the polarization angle considering the angle of incidence in the critical region.

Polarization-dependent analysis of the spatial GH shift at 2D material interfaces was absent from the earlier studies [23–27]. As a result, we tried to investigate its behavior with reference to the ML WSe_2 deposited on SiO_2/Si substrate, one of the significant members of the TMDC family. For a number of angles of incidence near the critical angle, Figure 5.7 illustrates how the spatial GH shift values change with the linear polarization state of incoming light beam. The post-selection angle is fixed at 1.5° in this instance because, as shown in Figure 5.5, the shift value essentially remains constant at higher post-selection angles. It is apparent that the shift values increase gradually with increasing polarization angle, peak for a 45° linear polarization state, and then start to fall with increasing polarization angle. The spatial GH shift is negligible for p- (polarization angle - 0°) and s- (polarization angle - 90°) polarization states, as demonstrated by the well-established theoretical model [equation (5.8)], which also shows that the amplification factor is polarization dependent. For a 45° linearly polarization condition, we obtain the largest spatial GH shift at the critical angle of around 85 μm, which is also close to the maximum limit of the GH shift here. For incidence angles greater than the critical angle

(e.g. 23.46°), the overall shift values fall, but the trend of the spatial GH shift variations with polarization angle stays the same. Figure 5.7(b) compares the experimental results with the theoretical model and shows a high degree of consistency. This study suggests that the spatial GH shift value can be easily controlled from lower to greater values by precisely altering the polarization state of the incident light beam.

The ML WSe_2-SiO_2/Si arrangement's adjustable shift values could be useful for photonic manipulations such as optical sensors and optical differential operation. Furthermore, it is possible to precisely extract information regarding optical constants like permittivity, surface susceptibility, and conductivity of ML WSe_2 without destroying the sample itself by creating an adequate connection between these kinds of non-specular phenomena and those optical parameters.

5.5 Concluding remarks

The present work concludes by examining the precise manipulation of the longitudinal beam shift in total internal reflection condition, also referred to as the GH shift, in absorbing material interface- ML WSe_2-SiO_2/Si configuration. Compared to the typical glass-air contact, the critical angle is substantially different. Three parameters—the angle of incidence, the polarization state of the input light beam, and the post-selection angles for our chosen configuration—that were not examined in previous studies are experimentally demonstrated to be crucial for precisely controlling the shift values. The experimental inquiry is supported by a broader theoretical model that has been constructed. The underlying information offered by these results will be useful for the technological development of photonic devices based on ML WSe_2 and other transition metal dichalcogenides. More precisely, the use of ML WSe_2-SiO_2/Si arrangement for sub-wavelength optical beam manipulation will create new opportunities for future advancements in a number of domains, such as image edge detection and biosensors, where precise shift values are required to accomplish particular objectives.

References

1. F. Goos and H. Hänchen, Ann. Phys. **436**(7-8), 333–346 (1947).
2. C. Imbert, Phys. Rev. D **5**, 787 (1972).
3. M. Onoda, S. Murakami, and N. Nagaosa, Phys. Rev. Lett. **93**, 083901 (2004).
4. Y. Qin, Y. Li, X. B. Feng, Y.-F. Xiao, H. Yang, and Q. Gong, Opt. Express **19**, 9636–9645 (2011).

5. O. Hosten and P. Kwiat, Science **319**(5864), 787–790 (2008).
6. M. Merano, A. Aiello, M. P. Van Exter, and J. P. Woerdman, Nat. Photonics **3**, 337-340 (2009).
7. K. Artmann, Ann. Phys. **437**, 87-102 (1948).
8. K. Y. Bliokh, and Y. P. Bliokh, Phys. Rev. E **75**, 066609 (2007).
9. K. Y. Bliokh, and A. Aiello, J. Opt. **15**, 014001 (2013).
10. S. De Leo, and G. G. Maia, J. Mod. Opt. **66**, 2142-2194 (2019).
11. S. Liu, S. Chen, S. Wen, and H. Luo, Opto-Electron. Sci. **1**, 220007 (2022).
12. Q. Zhang, and K. S. Chan, Appl. Phys. Lett. **105**, (2014).
13. X. Wang, C. Yin, J. Sun, H. Li, Y. Wang, M. Ran, and Z. Cao, Opt. Express **21**, 13380 – 85 (2013).
14. T. Sakata, T. Hiroyoshi, and F. Shimokawa, Appl. Phys. Lett. **76**, 2841–2843 (2000).
15. D. Xu, S. He, J. Zhou, S. Chen, S. Wen, and H. Luo, Appl. Phys. Lett. **116** (2020).
16. S. Chen, X. Ling, W. Shu, H. Luo, and S. Wen, Phys. Rev. Appl. **13**, 014057 (2020).
17. J. Liu, K. Zeng, W. Xu, S. Chen, and S. Wen, Appl. Phys. Lett. **115**, 251102 (2019).
18. H. Luo, X. Zhou, W. Shu, S. Wen, and D. Fan, Phys. Rev. A **84**, 043806 (2011).
19. A. Das, and M. Pradhan, Opt. Communications **437** 312-320 (2019).
20. Z. Ullah, S. Ahmad, T. Khan, M. N. Jan, and M. S. A. Jabar, J. Phys. B **53**, 155401 (2020).
21. M. Shah, A. Akbar, N. A. Khan, Q. Zaman, S. Iqbal, W. Ali, M. Javed, and M. Shah, J. Opt. Soc. Am. B **39**, 1082-1090 (2022).
22. Q. Jiang, J. Chen, B. Liang, Y. Wang, J. Hu, and S. Zhuang, Opt. Lett. **42**, 1213-1216 (2017).
23. S. Chen, C. Mi, L. Cai, M. Liu, H. Luo, and S. Wen, Appl. Phys. Lett. **110** (2017).
24. A. Das, and M. Pradhan, J. Opt. Soc. Am. B **38**, 387-391 (2021).
25. I. V. Shadrivov, A. A. Zharov, and Y. S. Kivshar, Appl. Phys. Lett. **83**, 2713-2715 (2003).
26. Y. Q. Kang, Y. Xiang, and C. Luo, Appl. Phys. B **124** 1-6 (2018).
27. Y. P. Wong, Y. Miao, J. Skarda, and O. Solgaard, Opt. Lett. **43**, 2803-2806 (2018).
28. N. I. Petrov, V. A. Danilov, V. V. Popov, and B. A. Usievich, Opt. Express **28**, 7552-7564 (2020).
29. S. Mandal, A. Das, and M. Pradhan, J. Opt. **26**, 045403 (2024).
30. K. N. Pichugin, D. N. Maksimov, and A. F. Sadreev, J. Opt. Soc. Am. A **35**, 1324-1329 (2018).

31. N. W. M. Ritchie, J. G. Story, and R. G. Hulet, Phys. Rev. Lett. **66**, 1107 (1991).
32. S. Mandal, A. Das, and M. Pradhan, J. Opt. Soc. Am. B **41**, 750-755 (2024).
33. Q. Ma, G. Ren, K. Xu, and J. Z. Ou, Adv. Opt. Mater. **9**, 2001313 (2021).
34. J. D. Elliott, Z. Xu, P. Umari, G. Jayaswal, M. Chen, X. Zhang, A. Martucci, M. Marsili, and M. Merano, Phys. Rev. B **101**, 045414 (2020).
35. C. Hsu, R. Frisenda, R. Schmidt, A. Arora, S. M. De Vasconcellos, R. Bratschitsch, H. SJ van der Zant, and A. C. Gomez, Adv. Opt. Mater. **7**, 1900239 (2019).
36. M. Tahir, Physica E **97**, 184-190 (2018).
37. X. L. Li, W. P. Han, J. B. Wu, X. F. Qiao, J. Zhang, and P. H. Tan, Adv. Funct. Mater. **27**, 1604468 (2017).
38. H. Guan, N. Tang, H. Huang, X. Zhang, M. Su, X. Liu, L. Liao, W. Ge, and B. Shen, ACS Nano **13**, 9325-9331 (2019).
39. P. Maurizia, M. Bernardi, and J. C. Grossman, Nano Lett. **15**, 2794-2800 (2015).
40. A. Ramasubramaniam, Phys. Rev. B **86**, 115409 (2012).
41. D. K. Li, S. Y. Wang, X. Q. Yan, B. W. Su, Z. Hu, Z. B. Liu, and J. G. Tian, Appl. Phys. Lett. **120** (2022).
42. G. Jayaswal, G. Mistura, and M. Merano, Opt. Lett. **38**, 1232-1234 (2013).
43. F. Töppel, M. Ornigotti, and A. Aiello, New J. Phys. **15**, 113059 (2013).
44. S. Goswami, S. Dhara, M. Pal, A. Nandi, P. K. Panigrahi, and N. Ghosh, Opt. Express **24**, 6041-6051 (2016).
45. A. Aiello, and J. P. Woerdman, Opt. Lett. **33**, 1437-1439 (2008).
46. X. Li, P. Wang, F. Xing, X. Chen, Z. Liu, and J. Tian, Opt. Lett. **39**, 5574-5577 (2014).

6 Goos-Hänchen Shift Using Hermite-Gaussian Laser Beam

The content of this chapter is adapted from the following published article:

S. Mandal, A. Das, and M. Pradhan, "Weak measurement of the Goos–Hänchen shift for a Hermite–Gaussian laser beam," ***Journal of Optics*** 26 (4), 045403 (**2024**)

6.1 Introduction

The solution of the paraxial wave equation (Helmholtz equation) in rectangular coordinates is the Hermite-Gaussian (HG) optical beam, one of the important higher-order optical beams that have been the focus of intensive study on sophisticated beam manipulation for several decades. The order of the beam is defined as (*m, n*), where m and n are integer values greater than or equal to zero and represent the x and y directions in the plane perpendicular to the direction of propagation z. It has complete, unique orthonormal spatial modes with rectangular symmetry [1]. The sum (*n*+*m*) is the denoted as spatial order of the mode. Even though HG beams do not carry orbital angular momentum (OAM), beams with circular or elliptical polarization can nonetheless carry spin angular momentum.

In contrast to the simple Gaussian (TEM_{00}) mode, higher-order HG modes feature intriguing characteristics like multiple intensity lobes [2], self-acceleration [3], self-healing [4], etc.as discussed in detail in *chapter* 1. Consequently, these modes find use in a wide range of domains, such as electron acceleration [3], optical communication [5], optical manipulation [6], quantum entanglement [7], and many more. Small particles can be confined by using the beam's super oscillation characteristics and linear momentum [8]. A two-qubit quantum phase gate can also be constructed using the Gouy phase obtained by HG beams [9]. The advantages of selecting higher-order HG beams in gravitational wave detectors to lower the thermal noise have also been investigated recently [1,10].

Given that each of these events is linked to transmission or reflection of beam at a particular interface, thorough studies [11] have developed a formalism based on wave vector analysis involving generalized HG modes. However, an actual optical beam composed of an infinite number of plane waves with different wave vectors cannot be sufficiently described by the Fresnel formulation in terms of either transmission or reflection. A variety of non-specular phenomena arise due to the unusual behavior of the combination of plane waves, such as the Goos-Hänchen (GH) shift, the Imbert-Fedorov (IF) shift, and the photonic spin Hall effect (PSHE) [12, 13]. Whereas PSHE and IF shifts are defined as the transverse shift orthogonal to the plane of incidence of the beam centroid position when incident light beams undergo reflection or refraction at a particular optical interface, the Goos-Hänchen shift is typically used to describe the displacement in the plane of incidence. The reflected or transmitted beam can appear to be simultaneously deflected (angularly) and displaced (spatially) [14], depending upon the light-matter interaction. Lately, unified theories [15, 16] have been established to

describe all kinds of beam shifts. It is quite challenging to detect subtle beam shift since their numerical magnitude is of the order of the incident light's wavelength. As a result, several initiatives were undertaken to improve those small shift values by means of experimental techniques [17–18], higher-order optical beams [19–21], or innovative material compositions [22–25].

Generally speaking, first-order beam deformation effects are represented as shifts in the beam centroid position. Depending on the incident light beam's angular distribution shape, complex beam patterns experience finer higher-order deformation effects [26]. One easy way to add complexity to the incoming beam pattern is to include the orbital angular momentum. Vortex light beams can be used to control the symmetries of the longitudinal or transverse optical beam shift and photonic spin splitting [27]. However, vortex or Laguerre-Gauss beams with finite orbital angular momentum (OAM) were the main focus of the majority of beam shape-dependent experimental [28–29] or theoretical [30] investigations of optical beam shift. The phenomenon of beam shifts employing the higher-order Hermite-Gaussian beams has been the subject of very few theoretical investigations [31–32].

Now, spatial, angular, as well as the composite GH shift near critical angle of incidence, IF shift, PSHE are already well investigated for fundamental mode (TEM_{00}) incident light beam using the weak measurement [33-35]. The idea of the weak value amplification (WVA) formalism [36] was introduced by Aharonov, Albert, and Vaidman in 1988. Here, two parties called "system" and "pointer" interact weakly through a coupling coefficient that is related to the unknown parameter that needs to be measured. By performing suitable pre- and post-selection on the system, it is possible to extract information about the parameters from the significant changes in the pointer state. To enhance the performance of precision measurements, higher-order optical beams have recently been employed as pointer states in weak measurements [37-38]. Additionally, compared to standard Gaussian pointer states, it was found that for nth order HG modes, the precision of measurements can be increased by a factor of $\sqrt{(2n+1)}$ [39, 40].

This *chapter* presents an experimental demonstration of a generalized optical arrangement that uses a phase-only spatial light modulator (SLM) to create a higher-order HG optical beam. The optical GH shifts at the prism-air interface near the critical angle of incidence for two orthogonal HG modes (HG_{10} and HG_{01}) are then investigated using this arrangement

in a WVA scheme. This in-depth study explores on how the incident light beam's shape, polarization, angle of incidence, and post-selection angle affect GH shifts.

6.2 Theoretical model

To conduct the quantum weak measurement (QWM) as WVA scheme with Hermite-Gaussian probe state, we considered the weak interaction between the pre-selected state system $|\psi_i\rangle$ and the HG probe state $|\varphi_i\rangle$. The total initial state is then represented as $|\Psi_i\rangle = |\psi_i\rangle|\varphi_i\rangle$. The evolution of the whole system is governed by the Von Neumann interaction Hamiltonian which is represented as [29],

$$\hat{H} = g\,(A^{GH} \otimes \hat{P}_x) \tag{6.1}$$

where, g is the sufficiently small coupling constant, $\hat{P}_x$ is the momentum observable of the probe conjugate to the commuting position variable $\hat{X}$, and A^{GH} represents the quantum mechanical operator of Goos-Hänchen shift [14], which is given by,

$$A^{GH} = \begin{bmatrix} \chi_p(\theta) & 0 \\ 0 & \chi_s(\theta) \end{bmatrix} \tag{6.2}$$

where $\chi_p(\theta) = -i\partial\, ln(r_p)/\partial\theta$ and $\chi_s(\theta) = -i\partial\, ln(r_s)/\partial\theta$; with θ being the angle of incidence and r_p, r_s are the Fresnel reflection coefficients for *p*- and *s*- polarized light beam, respectively.

After the weak interaction, if we post-select the system onto the state $|\psi_f\rangle$, then the pointer state evolves to the following state given by,

$$|\varphi_f\rangle = \langle\psi_f|\, exp\left[-ig\,(A^{GH} \otimes \hat{P}_x)\right]|\psi_i\rangle|\varphi_i\rangle \tag{6.3}$$

Finally, the spatial displacements of the HG pointer state can be calculated as [39],

$$X_w = \langle\varphi_f|\hat{X}|\varphi_f\rangle = g\; Re\,(A_w^{GH}) \tag{6.4}$$

Where A_w^{GH} is the weak value of GH shifts given by,

$$A_w^{GH} = \frac{\langle\psi_{post}|A^{GH}|\psi_{pre}\rangle}{\langle\psi_{post}|\psi_{pre}\rangle} \tag{6.5}$$

To implement the whole thing experimentally, we preselect the incident light beam to a particular polarization state as,

$$|\psi_{pre}\rangle = cos\,\alpha\ |H\rangle + sin\,\alpha\,|V\rangle \tag{6.6}$$

with α being the polarization angle. The HG mode is employed as the pointer state of the measuring device. It is initially prepared in state, $|\varphi_i\rangle = \int dx\,dy\,\varphi_i(x,y)|x,y\rangle$. The complex amplitude of incident HG beam is given by [11],

$$\varphi_i(x,y) = H_m(\sqrt{2}x/w)H_n(\sqrt{2}y/w)\left[\frac{1-\frac{iz}{Z_{R,i}}}{\sqrt{1+\left(\frac{z}{Z_{R,i}}\right)^2}}\right]^{m+n} \times \frac{1}{1+\frac{iz}{Z_{R,i}}}exp\left[-\frac{\frac{x^2+y^2}{{w_0}^2}}{1+\frac{iz}{Z_{R,i}}}\right] \tag{6.7}$$

where, 'w_0' is the waist of the Gaussian function. After passing through a Glan-Thompson polarizer (GLP), which is making angle 'α' with the x-axis, the form of incident light beam in the plane z = 0, will be,

$$\binom{cos\,\alpha}{sin\,\alpha} H_m\left(\frac{\sqrt{2}x}{w_0}\right)H_n\left(\frac{\sqrt{2}y}{w_0}\right)exp[-(x^2+y^2)/{w_0}^2] \tag{6.8}$$

After the total internal reflection of the light beam,

$$\begin{pmatrix} cos(\alpha)\,e^{-\frac{i\delta}{2}}\,exp\left[-\frac{(x-D_p)^2}{{w_0}^2}\right] \\ sin(\alpha)\,e^{+\frac{i\delta}{2}}\,exp\left[-\frac{(x-D_s)^2}{{w_0}^2}\right] \end{pmatrix} e^{-\frac{y^2}{w^2}}\,H_m(x)H_n(y) \tag{6.9}$$

where $\delta = \delta_p - \delta_s$ is the phase difference between *p*- and *s*-polarized light beam and D_p, D_s are the spatial GH shifts due to TIR which can be calculated using the formulas developed in [29].

We introduced the quarter ($\lambda/4$) and half-wave ($\lambda/2$) plates consecutively to compensate the extra phase appearing due to TIR. The Jones matrix representing their combined effect is given by $\begin{pmatrix} e^{i\delta/2} & 0 \\ 0 & e^{-i\delta/2} \end{pmatrix}$. Therefore, the beam emerging from the retarders has the form,

$$\begin{pmatrix} cos(\alpha)\, exp\left[-\frac{\left(x-D_p\right)^2}{{w_0}^2}\right] \\ sin(\alpha)\, exp\left[-\frac{(x-D_s)^2}{{w_0}^2}\right] \end{pmatrix} e^{-\frac{y^2}{{w_0}^2}} H_m(x)H_n(y) \tag{6.10}$$

Finally, another Glan-Thompson polarizer (GLP) in the output is rotated to an angle β, which project out the final state as,

$$\begin{pmatrix} cos(\alpha)\, cos(\beta)\ exp\left[-\frac{\left(x-D_p\right)^2}{w^2}\right] \\ sin(\alpha)\, sin(\beta)\, exp\left[-\frac{(x-D_s)^2}{w^2}\right] \end{pmatrix} \left(\frac{2\sqrt{2}}{w}\right) x\, e^{-\frac{y^2}{{w_0}^2}} \tag{6.11}$$

and

$$\begin{pmatrix} cos(\alpha)\, cos(\beta)\, exp\left[-\frac{\left(x-D_p\right)^2}{w^2}\right] \\ sin(\alpha)\, sin(\beta)\, exp\left[-\frac{(x-D_s)^2}{w^2}\right] \end{pmatrix} \left(\frac{2\sqrt{2}}{w}\right) y\, e^{-\frac{y^2}{{w_0}^2}} \tag{6.12}$$

for HG_{10} and HG_{01} mode, respectively. Following Duck et. al's [41] formalism, these states can be finally represented as,

$$\sim xe^{-y^2/w^2} \left[(1+\epsilon)\, exp\left(-\frac{\left(x-\frac{1}{2}\Delta_{GH}\right)^2}{{w_0}^2}\right) - (1-\epsilon)\, exp\left(-\frac{\left(x+\frac{1}{2}\Delta_{GH}\right)^2}{{w_0}^2}\right)\right] \tag{6.13}$$

for the HG_{10} mode and

$$\sim ye^{-y^2/w^2} \left[(1+\epsilon)\, exp\left(-\frac{\left(x-\frac{1}{2}\Delta_{GH}\right)^2}{{w_0}^2}\right) - (1-\epsilon)\, exp\left(-\frac{\left(x+\frac{1}{2}\Delta_{GH}\right)^2}{{w_0}^2}\right)\right] \tag{6.14}$$

for HG_{01} mode, respectively. Graphical representations of equation (6.13) and (6.14) are shown in Figure 6.1 (b) and (c), while (a) represents the same for the fundamental mode.

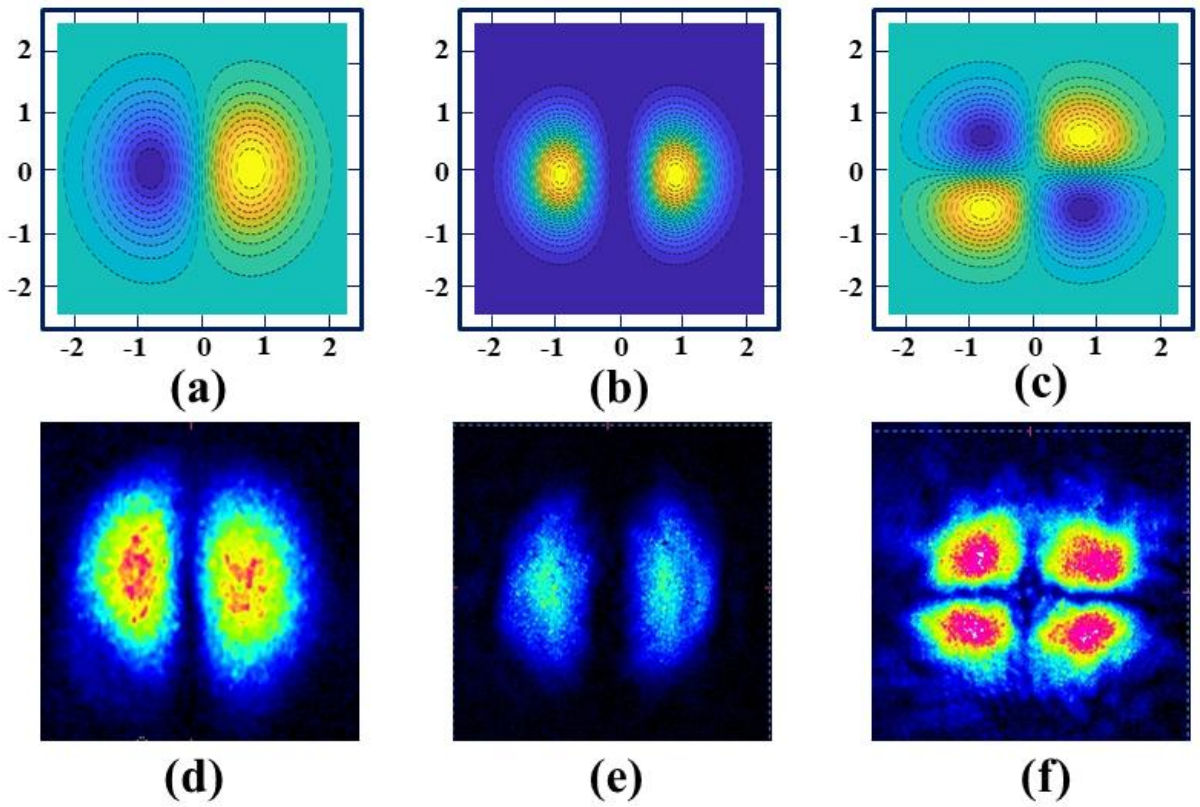

Figure 6.1 The intensity distribution of total internally reflected light beam at orthogonal condition for HG_{00} {(a), (d)}, HG_{10} {(b), (e)}, HG_{01} {(c), (f)} modes of light beam. 1st and 2nd row represent the theoretically simulated and experimentally obtained beam profiles, respectively.

6.3 Modified experimental setup for weak value amplification using a higher-order light beam

To experimentally investigate the GH shift for higher order Hermite-Gauss beams, we used a 633 nm He-Ne laser generating output power around 5 mW (30991, Research Electro Optics Inc) and a reflective phase-only SLM (HOLOEYE PLUTO-2.1VIS) to generate two orthogonal HG modes. The schematic diagram of our implemented setup is illustrated in Figure 6.3. The Gaussian light beam was passed through a half wave plate aligned along the orientation of liquid crystal inside the SLM and reflects from it. A set of holograms were multiplexed on the SLM to generate two different HG beams, each with a unique beam shape. Those holograms were created using the combination of phase masks as shown in Figure 6.2. The combination of Figure 6.2 (a) & (b) produce the phase mask Figure 6.2 (c) which is then fed onto the SLM and as the light beam reflects off the SLM, the first order diffraction pattern manifest as HG_{10} mode Figure 6.2 (d). By similar procedure, we obtain the HG_{01} mode as depicted in Figure 6.2 (e, f, g and h).

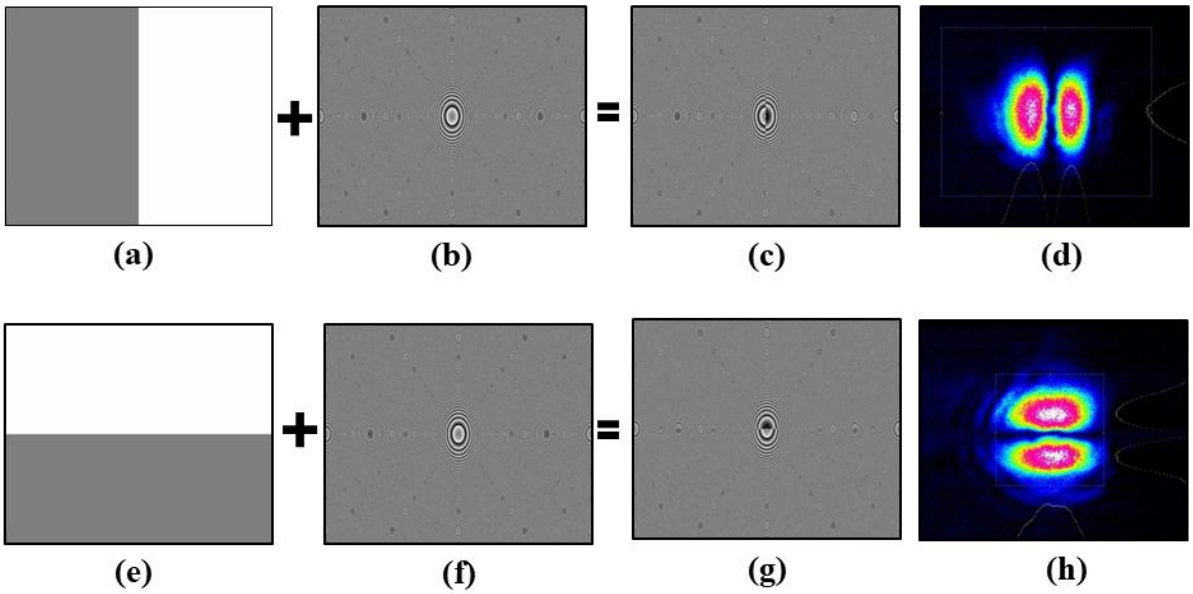

Figure 6.2 The combination of several holograms {(a), (b)} and {(e), (f)} to form specific phase masks (c) and (g) which are fed into the spatial light modulator (SLM) to generate HG_{10} (d) and HG_{01} (h) modes, respectively.

Other unwanted diffraction orders of the reflected beam except the first order diffraction pattern is removed by properly adjusting iris combination (I1 & I2) and steering the phase pattern in SLM as shown in Figure 6.3.

The position and quality of the reflected beam is analyzed by a beam profiler (LBP 4 USB, 6610d, Newport). Then, the specific beam profiles (HG_{00}, HG_{01}, HG_{10}) are passed through the pre-selection unit consisting of half wave plate (HWP), plano-convex lens (L1) and Glan Thompson polarizer (GLP1). The HWP is utilized to control the intensity of incident light beam. A plano-convex lens (L1) of focal length 150 mm is used to collimate and focus the incident light beam to a particular width around ~ 200 μm. We fixed the polarization state as 45° linearly polarized (LP) by properly rotating the optic axis of GLP1 which is monitored using a Stokes polarimeter (PAX1000VIS/M, Thorlabs).

Then the total internal reflection takes place from a prism (N-BK7 RA, Thorlabs) of refractive index 1.5151 which is placed on a motorized rotation stage (M-481-A, Newport). The angle of incident of light beam is regulated by a high-precision rotation mount (PRM1/M, Thorlabs) connected to the stage. Next, the combination of quarter-wave plate (QWP) and half-

wave plate (HWP) is introduced to compensate the extra-phase (δ) appearing due to total internal reflection (TIR) of light beam. To post-select the light beam, another Glan Thompson polarizer (GLP2) is used which acts as an analyzer. We employed another plano-convex lens (L2) after GLP2 to remove any type of polarization rotation arising due to geometric phase during light focusing and collimating.

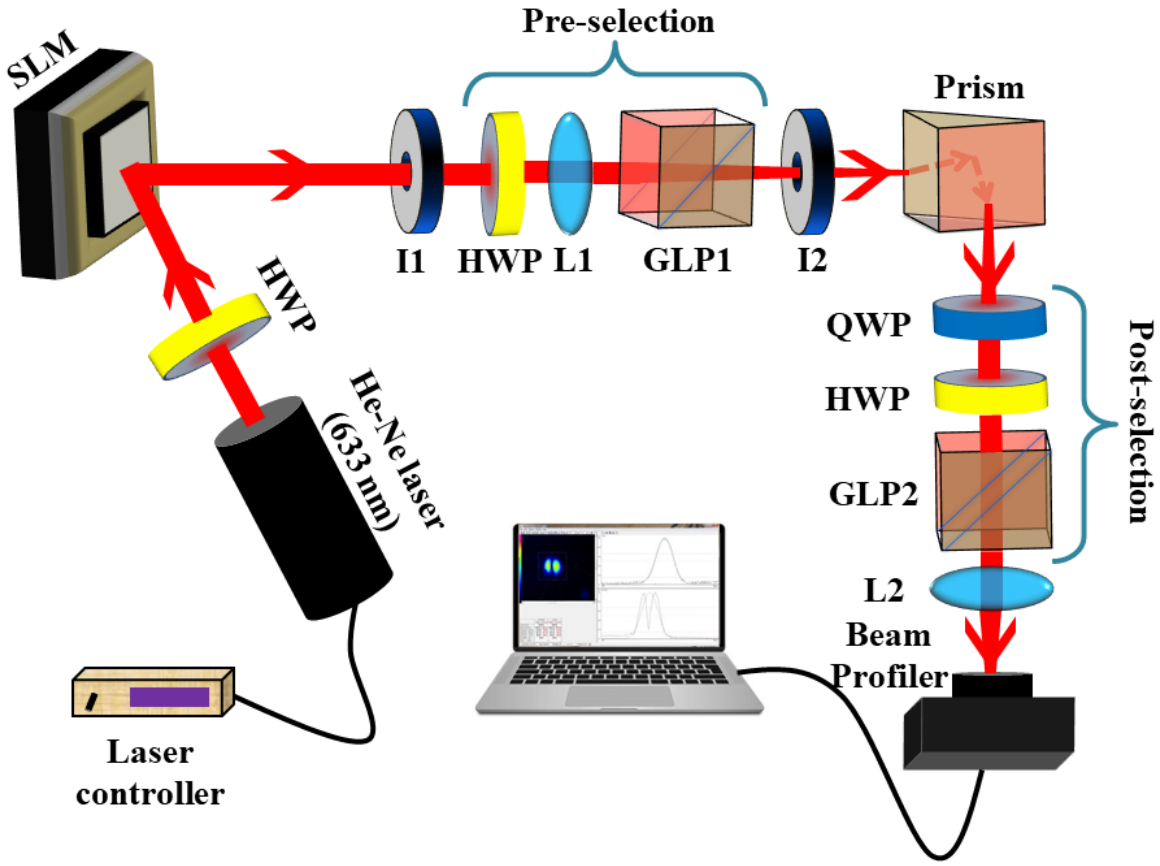

Figure 6.3 Schematic representation of the implemented weak value amplification (WVA) setup for measurement of tiny optical beam shift using higher-order optical beam. HWP/QWP: half/quarter-wave plate; I1/2: iris 1/2; L1/2: plano-convex lens 1/2; GLP1/2: Glan Thompson polarizer 1/2; SLM: phase only spatial light modulator.

Finally, the resultant nature of output beam is observed using a high-precision beam profiler. After compensating the extra-phase (δ), the GLP2 is then rotated precisely by a computer-controlled rotation mount (PRM1/M, Thorlabs) to a position orthogonal with respect to GLP1 to verify the breakdown criteria of beam profile. At this position, the separation between the lobes of HG_{10} increased more [Figure 6.1(e)] and the HG_{01} mode breaks in horizontal direction as a result it appears as four lobes [Figure 6.1 (f)] which looks like HG_{11}

mode depicted in Figure 6.1. Now, for particular angle of incidence, the optic axis of GLP2 is rotated clockwise and anticlockwise by post-selection angle +ε and –ε, respectively and the beam centroid position is noted from the beam profiler data which will be used to calculate the amplified GH shift i.e. $\Delta_{GH}\cot(\varepsilon)$.

6.4 Results and Discussions

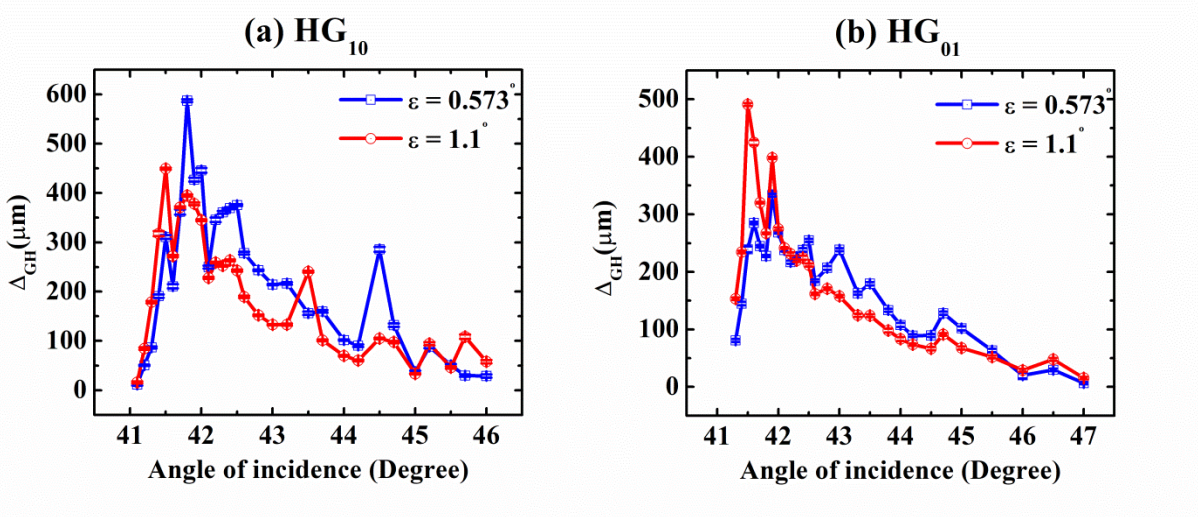

Figure 6.4 Variation of the amplified spatial GH shift with angle of incident for two different post-selection angles (ε) using (a) HG_{10} and (b) HG_{01} modes, respectively.

In Figure 6.4, we illustrate how the GH shift varies with the incident angle in the neighborhood of the critical angle for the two mutually orthogonal HG modes (HG_{10} and HG_{01}) for two distinct values of post-selection angle (0.573° and 1.1°). There is a sharp maximum observed at critical angle (41.5°) of incidence for both incident modes which is due to discontinuity of phase at critical angle. Then the shift value decreases continuously and vanishes as we move further away from the critical region. Few sharp peaks are observed at some higher angles of incidence.

Though the shift values are large for small post-selection angles in HG_{10} mode, a contrary behavior is observed for its orthogonal counterpart HG_{01} mode due to different mode structures. The post selection angle also plays an important role in governing beam shifts. It is evident from Figure 6.5 that the amplified horizontal GH beam shifts for the HG modes are highly dependent upon the post-selection angle (ε).

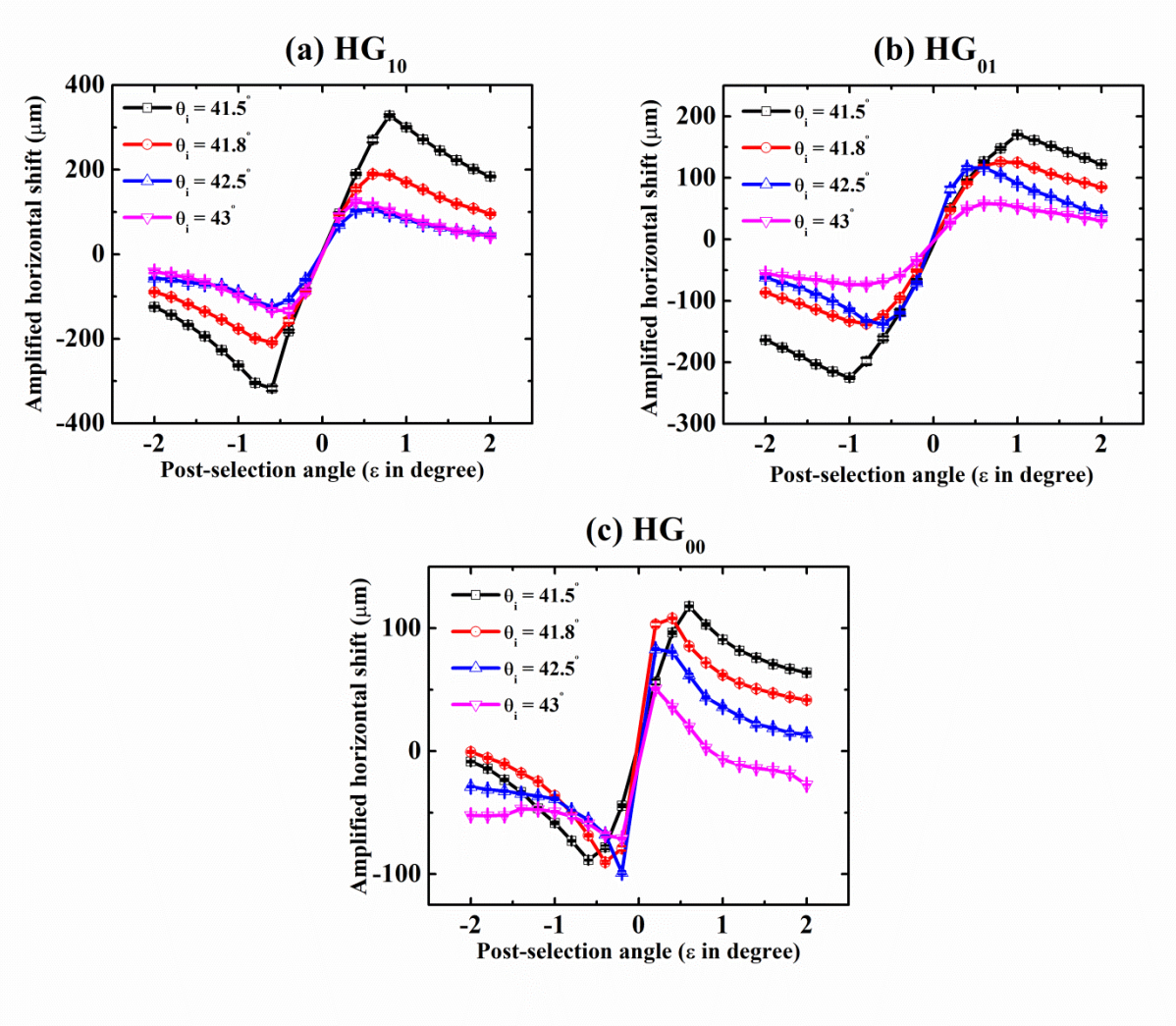

Figure 6.5 Variation of the amplified horizontal beam shift with post-selection angles for different angle of incidences using (a) HG_{10} and (b) HG_{01} (c) HG_{00} modes, respectively.

Although the nature of the GH beam shift is similar for all the modes, however we can get several interesting features from those plots. First, as we move from the orthogonal condition, the shift value increases in positive or negative direction for clockwise or anti-clockwise rotation of GLP2, respectively at and above the critical angle for both the modes. After reaching a peak value in positive and negative direction, the amplified GH shifts decrease gradually to small values for larger post-selection angles. Second, at critical angle, we get the maximum positive and negative amplified shifts for both the modes. Third, as we increase the angle of incidence, the post-selection angle at which we get maximum shift values is getting closer to orthogonal position. We can then draw the conclusion that selecting a definite angle of incidence (θ) and post-selection angle (ε) i.e. θ-ε combination one can fine-tune the GH shift to a desired value for maximum shift. Finally, comparing all the three plots, we can observe

that at critical angle of incidence, amplified horizontal shift can reach up to ~ 350 μm for HG_{10} mode and the curve for fundamental Gaussian beam is only about ~ 100 μm.

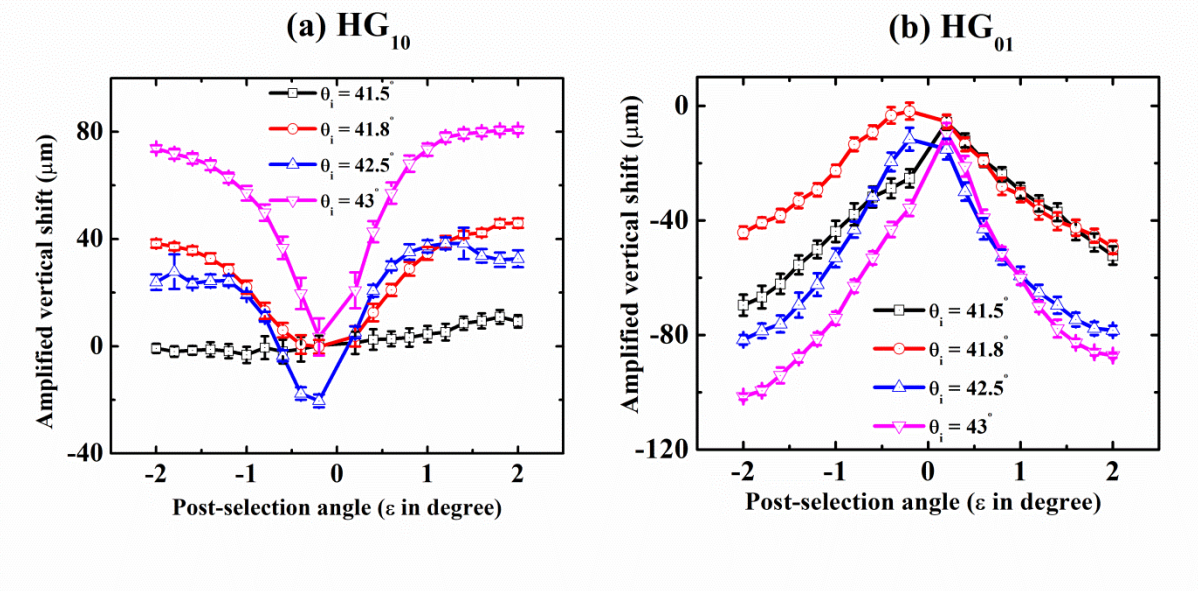

Figure 6.6 Variation of the amplified vertical beam shift with post-selection angles for different angle of incidences using (a) HG_{10} and (b) HG_{01} modes, respectively.

In Figure 6.6, the amplified vertical shift values of the beam centroid with the post-selection angles varying from -2° to +2° for different angle of incidence near critical angle are presented. The values of vertical shifts are lower than those of horizontal shifts. The vertical shifts between HG_{10} and HG_{01} modes are significantly distinct. The peak value of amplified shift and its related post-selection angle differ depending on the incidence angles corresponding to different horizontal or vertical shifts. It is noteworthy to mention that for the HG_{10} mode, positive shifts symmetric around the orthogonal position are achieved for greater angle incidences, and these shifts steadily rise as the post-selection angle is increased in both the clockwise and anti-clockwise directions, remaining nearly constant until it reaches its maximum. Moreover, when HG_{01} mode is used instead of HG_{10} mode, the behavior of the amplified vertical shift of the beam centroid position is completely different. Here, negative shift values are symmetric about the orthogonal position, and it increases as we move towards higher post-selection angles. As the angle of incidences increases, the vertical shift values increase.

Finally, we have compared the variation of GH shift values with angle of incidences near critical angle for the fundamental and first order HG modes, HG_{00}, HG_{10} & HG_{01} as shown in Figure 6.7. For all three of the distinct beam profiles, the nature of shift values with angle of incidences remains the same, although there is a large variation of the quantitative estimates in shift values. We observed more shift values for the HG modes as compared to the Gaussian mode. We found specifically three times more shift values for the HG_{10} mode at critical angle of incidence as compared to the Gaussian mode. The shift values gradually decline for all three of the modes as the angle of incidence rises, with the exception of a few high peaks shown for the HG modes, where it decreases smoothly for the Gaussian mode of the light beam.

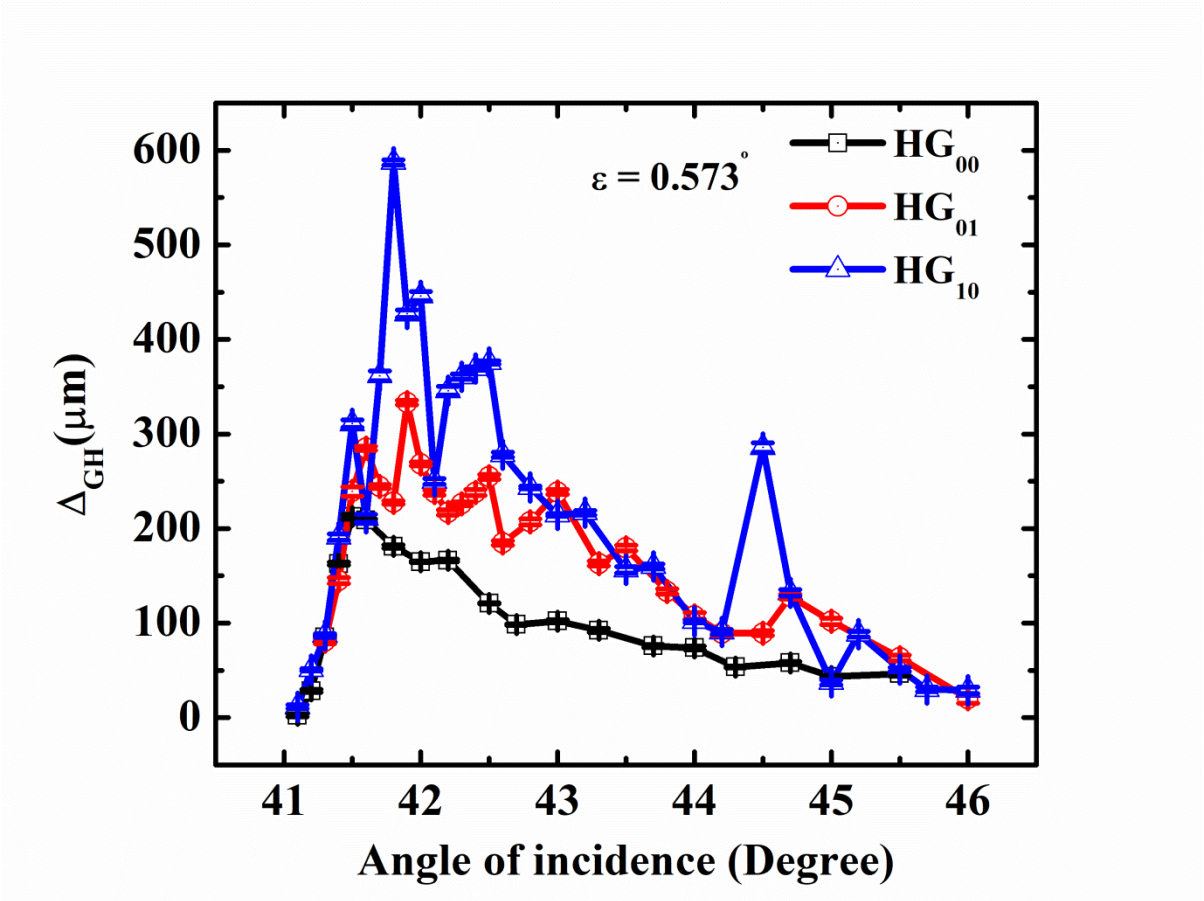

Figure 6.7 Comparison of the amplified spatial GH shift with angle of incident considering a specific post-selection angle ($\varepsilon = 0.573^{\circ}$) for different beam profiles HG_{00}, HG_{10} and HG_{01}.

6.5 Concluding remarks

In summary, using a spatial light modulator, we have demonstrated experimentally the higher-order Hermite-Gaussian (HG) modes in a generalized manner and subsequently investigated their Goos-Hänchen (GH) shifts close to the critical angle of incidence by means of weak value amplification (WVA) technique. We have offered a theoretical framework that uses HG probe states to explain how beam profiles evolve during WVA technique. In comparison to the fundamental mode beam (HG_{00}), we observed two to three times greater GH shift for the first order HG_{10} and HG_{01} modes. Our findings demonstrate how the combination of the angle of incidence and the post-selection angle can help tuning the GH shifts for complex light modes. Finally, our work paves a new way to the fields of optical beam manipulation and weak measurement of optical beam shifts phenomena.

References:

1. T. Liu, A. Green and P. Fulda, *Phys. Rev. D* **102** 122002 (2020).
2. X. Liu, D. Jiang, Y. Zhang, L. Kong, Q. Zeng and K. Qin, *Photonics* **9** 9070478 (2022).
3. H. S. Ghotra and N. Kant, *Laser and Particle Beams* **34** 385-393 (2016).
4. Z. Xu, X. Liu, Y. Chen, F. Wang, L. Liu, Y. E. Monfared, S. A. Ponomarenko, Y. Cai and C. Liang, *Opt. Express* **28** 2828–2837 (2020).
5. K. Kiasaleh, *Opt. Eng.* **56** 076106 (2017).
6. S. Al-Awfi, S. Bougouffa and M. Babiker *Opt. Commun.* **283** 1022–1025 (2010).
7. Y. Zhang, S. Prabhakar, C. Rosales-Guzmán, F. S. Roux, E. Karimi and A. Forbes, *Phys. Rev. A* **94** 033855 (2016).
8. B. K. Singh, H. Nagar, Y. Roichman and A. Arie, *Light Sci Appl* **6** e17050 (2017).
9. W. F. Balthazar, D. P. Caetano, C. E. R. Souza and J. A. O. Huguenin, *Braz J Phys* **44** 658–664 (2014).
10. A. Stefan, S. Di Pace, J. Millo, M. Pichot, M. Turconi, N. Christensen and W. Chaibi, *Phys. Rev. D* **103** 042008 (2021).
11. M. Wanqi, Z. Cui, S. Ren, Y. Shi and Z. Liu, *Appl. Opt.* **62** 5516-5525 (2023).
12. K. Y. Bliokh and A. Aiello, *J. Opt.* **15** 014001 (2013).
13. F. Töppel, M. Ornigotti and A. Aiello, *New J. Phys.* **15** 113059 (2013).
14. S. Goswami, M. Pal, A. Nandi, P. K. Panigrahi and N. Ghosh *Opt. Lett.* **39** 6229-6232 (2014).
15. C. F. Li, *Phys. Rev. A* **76** 013811 (2007).

16. A. Aiello and J. P. Woerdman, *Opt. Lett.* **33** 1437–1439 (2008).
17. G. Jayaswal, G. Mistura and M. Merano, *Opt. Lett.* **38** 1232-1234 (2013).
18. M. Merano, A. Aiello, M. P. Van Exter, E. R. Eliel and J. P. Woerdman, *Opt. Express* **15** 15928-15934 (2007).
19. K. Y. Bliokh, I. V. Shadrivov and Y. S. Kivshar, *Opt. Lett.* **34** 389-391 (2009).
20. P. Chandravati and N. K. Viswanathan *OSA Continuum* **1** 872-881 (2018).
21. W. Zhen and D. Deng, *Opt. Express* **28** 24104-24114 (2020).
22. M. Shah, A. Akbar, N. A. Khan, Q. Zaman, S. Iqbal, W. Ali, M. Javed and M. Shah, JOSA B **39** 1082-1090 (2022).
23. A. Das and M. Pradhan, *Opt. Comm.* **437** 312-320 (2019).
24. Y. Qi, Z. Li, L. Jiang, J. Guo, X. Dai and Y. Xiang, *J. Phys. D: Appl. Phys.* **53** 015107 (2019).
25. C. Xu, J. Xu, G. Song, C. Zhu, Y. Yang and G. S. Agarwal, *Opt. Express* **24** 21767-21776 (2016).
26. M. P. Araújo, S. De Leo, and G. G. Maia, *Phys. Rev. A* **93** 023801 (2016).
27. W. Zhen, X. L. Wang, J. Ding, and H. T. Wang, *Phys. Rev. A* **108** 023514 (2023).
28. M. Merano, N. Hermosa, J. P. Woerdman and A. Aiello, *Phys. Rev. A* **82** 023817 (2010).
29. W. Long, J. Pan, X. Guo, X. Liu, H. Lin, H. Zheng, J. Yu, H. Guan, H. Lu, Y. Zhong and S. Fu, *Photon. Res.* **7** 1273-1278 (2019).
30. A. Aiello, *New J. Phys.* **14** 013058 (2012).
31. C. Prajapati and D. Ranganathan, *JOSA A* **29** 1377-1382 (2012).
32. D. Golla and S. D. Gupta, *Pramana J. Phys.* **76** 603–612 (2011).
33. M. P. Araújo, S. De Leo, and G. G. Maia, *Annalen der Physik* **529** 1600357 (2017).
34. A. Das, and M. Pradhan, *Laser Phys. Lett.* **17** 066001 (2020).
35. O. J. Santana, S. A. Carvalho, S. De Leo, and L. E. de Araujo, *Opt. Lett.* **41** 3884-3887 (2016).
36. Y. Aharonov, D. Z. Albert and L. Vaidman, *Phys. Rev. Lett.* **60** 1351 (1988)
37. G. Puentes, N. Hermosa and J. P. Torres, *Phys. Rev. Lett.* **109** 040401 (2012).
38. D. K. Sharma, V. Kumar, A. B. Vasista, S. K. Chaubey and G. P. Kumar, *Opt. Lett.* **43** 2474-2477 (2018).
39. Y. Turek, H. Kobayashi, T. Akutsu, C. P. Sun and Y. Shikano, *New J. Phys.* **17** 083029 (2015).

40. B. Xia, J. Huang, C. Fang, H. Li and G. Zeng, *Phys. Rev. Appl.* **13** 034023 (2020).

41. I. M. Duck, P. M. Stevenson and E. C. G. Sudarshan, *Phys. Rev. D* **40** 2112–17 (1989).

7 Simultaneous Detection of Longitudinal and Transverse Photonic Spin Splitting

The content of this chapter is adapted from the following published article:

S. Mandal, A. Das, and M. Pradhan, "Simultaneous observation of transverse and longitudinal photonic spin splitting in monolayer WSe_2 via quantum weak measurement," ***Journal of Applied Physics*** 135 (20) (**2024**).

7.1 Introduction

The photonic spin Hall effect (PSHE) of light is the separation of a linearly polarized incident light beam to right and left circularly polarized (RCP and LCP) light in the transverse direction during reflection or transmission process [1]. This phenomenon is equivalent to the electronic spin Hall effect, in which photons and refractive index gradient, respectively, substitute for the electronic charges and electric fields. The origin of this shift is intimately linked to the spin-orbit interaction (SOI) of the light beam, which is made up of two components: conservation of total angular momentum including the spin angular momentum and finite geometric phase [2-4].

Depending upon the nature of the interacting surface, geometric phase appears as the light beam interacts with a specific optical interface, and the phase gradient manifests as the separation between the two opposite spins (RCP and LCP) of the reflected light beam while preserving the total angular momentum of the incident light beam throughout [5, 6]. Photonic spin splitting (PSS) can occur in both the transverse and longitudinal directions of the incident light beam [Figure 7.1], depending on a variety of factors such as the angle of incidence, interaction medium, or several properties of the incident light beam such as polarization, spin, orbital angular momentum, and so on [7-11].

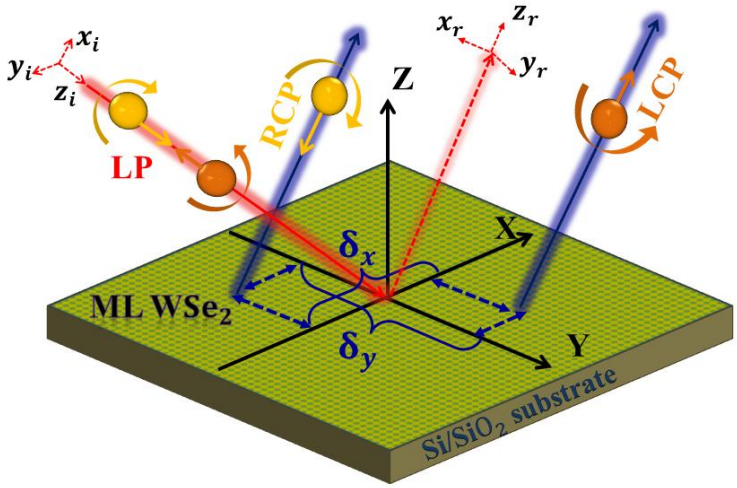

Figure 7.1 Geometry of "in-plane" and "out-of-plane" photonic spin splitting (PSS) of incident linearly polarized light beam as right and left circular polarized light in reflection from monolayer (ML) WSe_2 interface (δ_x: in-plane; δ_y: out-of-plane).

In order to study the spin, valley, electrical, and optical properties of the well-known 2D material graphene as well as its applications, a number of new experimental and theoretical research fields were opened up after its discovery, including spintronics, valleytronics, and opto-electronics [12]. Subsequently, materials with unique properties were found and introduced into the field of study, including Dirac semimetals, photonic crystals, topological insulators, and transition metal dichalcogenides (TMDCs) [13,14]. The ultrathin TMDCs (MX_2, M = Mo, W, Re; X = S, Se, Te) have attracted a lot of interest among those special category members of the new era because of their exceptional chemical and mechanical stability, tunable electrical and optical properties, and strong light-matter interactions brought about by exciton effects [15]. Furthermore, strain effects, electric/magnetic fields, thickness, and chemical compositions can all be used to regulate the band gap of TMDCs [16].

It has already been demonstrated that the optical conductivity of the surface of interaction affects the photonic spin Hall shift (PSHS) [17]. If multi-layered material structures such as graphene, TMDCs, black phosphorus, metamaterials, topological insulators, and Weyl semimetals are used, PSHS can therefore be modified over a few times in comparison to the shifts for the air-glass interface [18-21]. The PSHS has garnered a lot of interest lately in a variety of application domains, including plasmonics, image processing and edge detections, precision metrology, and sensing technologies, because of these fascinating characteristics [9].

Nevertheless, the PSHS is minuscule, with a size comparable to a fraction of the incident light beam's wavelength. As a result, we need a precise method to measure these small changes accurately. The groundbreaking work of Hosten and Kwiat [22] developed the experimental implementation of weak value amplification to detect the transverse shift of the opposite polarization components using a transmitted light beam. The system must first be pre-selected to a specific polarization state in order to perform the optical analog of weak measurement. As the light beam interacts with the particular optical contact, the polarization and spatial degrees of freedom are then related via weak coupling. Finally, the reflected light beam's polarization state is post-selected to a state that is almost orthogonal to the preselected state [23-26].

A polarization-dependent analysis of the in-plane and out-of-plane PSS of reflected light beams from the glass-air interface has been previously reported using the QWM technique [27, 28]. Due to the strong coupling in this angle of incidence region, Luo et al.'s later report of the switchable PSHS near the Brewster angle raised questions over the suitability of weak measurement formalism [29]. When the pre- and post-selected states are very nearly orthogonal

to one other, the weak value can likewise become arbitrarily large. In order to address these problems, taking into account the horizontally (p-) and vertically (s-) polarized pre-selection states, modified weak measurement models were developed which may be applied to both absorbent and non-absorbent media [30, 31]. It is important to keep in mind that these models are limited to transverse shifts. An optimal weak measurement of generalized PSS has been determined for incident light beams with arbitrary linear polarizations interacting with a glass-air contact [32]. For arbitrary linear polarization, a recent work has also demonstrated an optimized weak measurement model with broader applicability for both in-plane and out-of-plane PSS by treating the reflection coefficients as complex values rather than real numbers in general [33]. The simultaneous detection of in-plane and out-of-plane shifts for an arbitrary linearly polarized incident light beam has not, however, been directly verified experimentally in that study. In fact, when the arbitrary linearly polarized light beam was reflected from the surfaces of the absorbent material, the intensity of the reflected light beam either decreased considerably or the beam was distorted due to enhanced scattering and absorption. The reflection coefficients of the material surfaces might cause an unexpected variation in the polarization of the reflected light beam. Consequently, for incident light beams that were arbitrarily polarized, very little shift value was observed using QWM.

In order to thoroughly examine the transverse (δ_y) and longitudinal (δ_x) PSS employing horizontally (p-) and vertically (s-) polarized light waves, as covered in this *chapter*, we have taken into consideration a monolayer (ML) of tungsten di-selenide (WSe_2) deposited on a SiO_2/Si substrate as the interaction surface. In comparison to the extensively researched prototype TMDC material, MoS_2, it has distinct and complementing features [8]. The band gap of ML WSe_2 is 1.65 eV, lower than that of MoS_2 (1.8 eV) [34]. Whether this band gap is direct [35] or indirect [36] is still up for dispute. Additionally, WSe_2 exhibits a strong spin-orbit coupling, a high quantum yield in photoluminescence (PL), and a high absorption coefficient in the visible-to-infrared region [37-39]. Finally, as far as we are aware, this is the first thorough experimental study of PSS employing the quantum weak measurement technique close to the Brewster angle of incidence at the interface of ML WSe_2 deposited on a SiO_2/Si substrate.

7.2 Theoretical model

As shown in Figure 7.1, we have studied the external reflection of the Gaussian light beam (TEM_{00}) from the air-monolayer WSe_2 interface. The theoretical model of the PSS is developed

using the classical optics theory (including both the longitudinal shift (δ_x) and transverse shift (δ_y) during external reflection). The electric field of the incident arbitrary linearly polarized Gaussian light beam can be defined using the angular spectrum representation as [8],

$$E_i = \begin{pmatrix} E_i^p \\ E_i^s \end{pmatrix} \propto \begin{pmatrix} cos\,\gamma \\ sin\,\gamma \end{pmatrix} exp\left[-\frac{z_R(k_{ix}^2 + k_{iy}^2)}{2k_i}\right] \tag{7.1}$$

where γ denotes the polarization angle, E_i^p and E_i^s are the electric field components corresponding to the *p*- ($\gamma = 0^\circ$) and *s*- ($\gamma = 90^\circ$) polarized incident light beam. Here, $z_R = k_i w_0^2/2$ is the Rayleigh length, $k_i = 2\pi/\lambda$ is the wave vector corresponding to the wavelength (λ) of the incident light beam and k_{ix} , k_{iy} denote the wave vector components in the $\hat{x}_i$ and $\hat{y}_i$ directions respectively. Applying the appropriate boundary conditions after reflection from the surface, the reflected electric field can be obtained as,

$$E_r = \begin{pmatrix} r_p\,cos\,\gamma + \dfrac{(r_p + r_s)k_{iy}\,cot\,\theta}{k_i} sin\,\gamma \\ -\dfrac{(r_p + r_s)k_{iy}\,cot\,\theta}{k_i} cos\,\gamma + r_s\,sin\,\gamma \end{pmatrix} exp\left[-\frac{z_R(k_{ix}^2 + k_{iy}^2)}{2k_i}\right] \tag{7.2}$$

where $r_p = R_p\,exp\,i\phi_p$, $r_s = R_s\,exp\,i\phi_s$ denote the complex-valued Fresnel reflection coefficients for the *p*- and *s*- polarized incident light beams from the isotropic mono-layered WSe_2 interface, respectively.

The two preferred approaches to figure out the reflection coefficient are the (i) surface current model [18,40] and (ii) slab model [8,41]. However, for multilayered configurations with different thicknesses and refractive indices, the slab model offers a more convenient way of studying the reflection coefficient as compared to the surface current model [42-44]. Therefore, we used the slab model to determine r_p and r_s, treating WSe_2 monolayer as a homogenous medium with thickness '*d*', which is considered as 0.7 nm in the theoretical calculation. The reflection coefficients in the slab model are calculated as [8],

$$r_p(\theta, d) = R_p\,exp\,i\phi_p = \frac{r_p^{12} + r_p^{23}\,exp(2ik_{2z}d)}{1 + r_p^{12}r_p^{23}\,exp(2ik_{2z}d)} \tag{7.3}$$

$$r_s(\theta, d) = R_s\,exp\,i\phi_s = \frac{r_s^{12} + r_s^{23}\,exp(2ik_{2z}d)}{1 + r_s^{12}r_s^{23}\,exp(2ik_{2z}d)} \tag{7.4}$$

where $r_p^{ij} = \frac{\varepsilon_j k_{iz} - \varepsilon_i k_{jz}}{\varepsilon_j k_{iz} + \varepsilon_i k_{jz}}$, $r_s^{ij} = \frac{k_{iz} - k_{jz}}{k_{iz} + k_{jz}}$, $k_{iz} = \frac{2\pi}{\lambda}\sqrt{\varepsilon_i - \varepsilon_1 sin^2\theta}$ and i, j denote the layers correspond to the different material compositions of the multilayered structure under consideration. ε_i and k_i represent the permittivity and wave vector related to i^{th} medium respectively.

The ML WSe_2, supported by SiO_2/Si substrate (285 nm thick SiO_2 film on top of Si wafer), behaves as an absorptive medium. It is evident that the thickness of the substrate is greater than that of ML WSe_2. However, it does not carry much significance in our theoretical model as the ML WSe_2 is highly absorbing in the visible domain [13,39]. The intensity of the p-polarized reflected light beam reaches a minimum at the Brewster angle, which is close to 76°, as can be seen from the modulus ($R_{p,s}$) and phase ($\phi_{p,s}$) of the reflection coefficient presented in Figure 7.2. For p-polarized incident light beam, R_P has shown two distinct dips near the angle of incidence 36° and 76°. The Brewster angle is near 76° as $R_P \rightarrow 0$ as shown in Figure 7.2 (a). Additionally, we have plotted the angular dependence of phase for both the polarizations. We can observe that the phase has shown sharp changes near 39° (ϕ_P) and 71° (ϕ_S) for *p*- and *s*-polarized incident light beam, respectively.

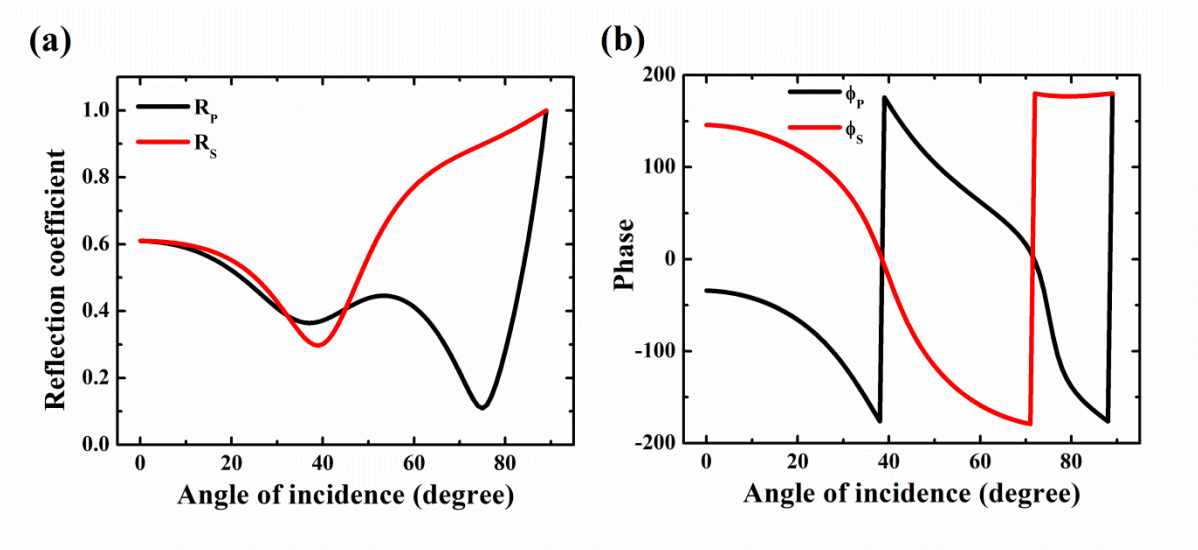

Figure 7.2 Angle of incidence dependence of (a) modulus and (b) phase of reflection coefficient (r_p and r_s) as determined using the slab model for the monolayer WSe_2 deposited on the SiO_2/Si substrate.

The incident light wave has a finite transverse extent, which results in varying angles of incidence for different plane wave components. Hence, we have used a Taylor series expansion of the Fresnel reflection coefficients (r_p and r_s) around $k_{ix} = 0$.

$$r_{p,s} = r_{p\theta,s\theta} + \frac{k_{ix}}{k_i}\frac{\partial r_{p\theta,s\theta}}{\partial \theta} \tag{7.5}$$

where $r_{p\theta}$ and $r_{s\theta}$ represent the Fresnel reflection coefficients of *p*- and *s*- polarized central incident light wave with the angle of incidence θ.

After plenty of rigorous calculations using the appropriate boundary conditions and inverse Fourier transform, we obtain the reflected electric field in position space as [45],

$$E_r = \begin{pmatrix} E_r^p \\ E_r^s \end{pmatrix} \propto \begin{pmatrix} \left(r_{p\theta} - \frac{\partial r_{p\theta}}{\partial \theta}\frac{x_r}{z_r - iz_R}\right) cos\,\gamma + \frac{(r_{p\theta} + r_{s\theta})y_r\, sin\,\gamma\, cot\,\theta}{z_r - iz_R} \\ \left(r_{p\theta} - \frac{\partial r_{p\theta}}{\partial \theta}\frac{x_r}{z_r - iz_R}\right) sin\,\gamma - \frac{(r_{p\theta} + r_{s\theta})y_r\, cos\,\gamma\, cot\,\theta}{z_r - iz_R} \end{pmatrix} \times exp\left[-\frac{k_i(x_r^2 + y_r^2)}{2(iz_r + z_R)}\right] \tag{7.6}$$

where E_r^p and E_r^s denote the electric field of the reflected light beam along the $\hat{x}_r$ and $\hat{y}_r$ axis, respectively.

In the weak value amplification (WVA) scenario, we need to post-select the reflected light beam to a specific polarization state, which is accomplished by another polarizer. If the transmission axis of this polarizer makes an angle β with the $\hat{x}_r$ axis, its Jones matrix is written as $M_{post} = \begin{pmatrix} cos^2\beta & \frac{1}{2}sin\,2\beta \\ \frac{1}{2}sin\,2\beta & sin^2\beta \end{pmatrix}$. After passing through the polarizer, the reflected electric field can be calculated as $E_{post} = M_{post}\,.E_r$. The post selection angle is chosen as the polarization angle, which is close to orthogonal with respect to the pre-selection angle (γ). So, for *p*- ($\gamma = 0^\circ$) and *s*- ($\gamma = 90^\circ$) polarized incident light beam, the polarization angle of the polarizer at the post-selection is fixed at $\beta = 90^\circ \pm \Delta$ and $\beta = \pm\Delta$ with respect to pre-selection, respectively, where Δ is the post-selection angle. The amplified PSS of the reflected beam after post-selection in the longitudinal and transverse directions can be obtained from the barycenter shift calculations given by,

$$x_{wvas}^{p,s} = \frac{\iint x_r |E_{post}^{p,s}(x_r,\ y_r, z_r)|^2 dx_r dy_r}{\iint |E_{post}^{p,s}(x_r,\ y_r, z_r)|^2 dx_r dy_r} \tag{7.7}$$

$$y_{wvas}^{p,s} = \frac{\iint y_r |E_{post}^{p,s}(x_r,\ y_r, z_r)|^2 dx_r dy_r}{\iint |E_{post}^{p,s}(x_r,\ y_r, z_r)|^2 dx_r dy_r} \tag{7.8}$$

Following long and tedious calculations, the detailed expressions of the longitudinal and transverse spin splitting in weak value amplification of shift (wvas) model are written as,

$$x_{wvas}^{p} = \frac{-2R_p(z_R\rho_p \sin\phi_p - z_R\varphi_p \cos\phi_p + z_r\rho_p \cos\phi_p + z_r\varphi_p \sin\phi_p)}{cot^2\theta\ cot^2\Delta\left[2R_pR_s\cos(\phi_p - \phi_s) + R_s^2 + R_p^2\right] + 2R_p^2 z_R k_r + (\rho_p^2 + \varphi_p^2)} \tag{7.9}$$

$$x_{wvas}^{s} = \frac{-2R_s(z_R\rho_s \sin\phi_s - z_R\varphi_s \cos\phi_s + z_r\rho_s \cos\phi_s + z_r\varphi_s \sin\phi_s)}{cot^2\theta\ cot^2\Delta\left[2R_pR_s\cos(\phi_p - \phi_s) + R_s^2 + R_p^2\right] + 2R_s^2 z_R k_r + (\rho_s^2 + \varphi_s^2)} \tag{7.10}$$

and

$$y_{wvas}^{p} = \frac{2R_p\ cot\,\theta\ cot\,\Delta\,[R_p z_r + R_s\cos(\phi_p - \phi_s)z_r + R_s\sin(\phi_p - \phi_s)z_R]}{cot^2\theta\ cot^2\Delta\left[2R_pR_s\cos(\phi_p - \phi_s) + R_s^2 + R_p^2\right] + 2R_p^2 z_R k_r + (\rho_p^2 + \varphi_p^2)} \tag{7.11}$$

$$y_{wvas}^{s} = \frac{2R_s\ cot\,\theta\ cot\,\Delta\,[R_s z_r + R_p\cos(\phi_p - \phi_s)z_r - R_p\sin(\phi_p - \phi_s)z_R]}{cot^2\theta\ cot^2\Delta\left[2R_pR_s\cos(\phi_p - \phi_s) + R_s^2 + R_p^2\right] + 2R_s^2 z_R k_r + (\rho_s^2 + \varphi_s^2)} \tag{7.12}$$

for p- and s- polarized incident light beams, respectively where $\rho_{p,s} = Re\left(\frac{\partial r_{p,s}}{\partial\theta}\right)$ and $\varphi_{p,s} = Im\left(\frac{\partial r_{p,s}}{\partial\theta}\right)$.

7.3 Experimental methodology

The experimental setup for weak measurement to investigate generalized spin splitting is shown in Figure 7.3. For the experiment, a 633-nm He–Ne laser (30991, Research Electro Optics, Inc.) generating a high-quality linearly polarized Gaussian beam with a power of 5.0 mW was mounted on a stable post kinematic V-clamp (C1513). The beam first passes through the pre-selection unit, which consists of a half-wave plate (HWP) (WPMH10M-633, Thorlabs), a plano-convex lens (L1) (LA1433, Thorlabs) with a focal length of 150 mm, and a Glan–Thompson polarizer (GLP1) (GTH10M-A, Thorlabs).

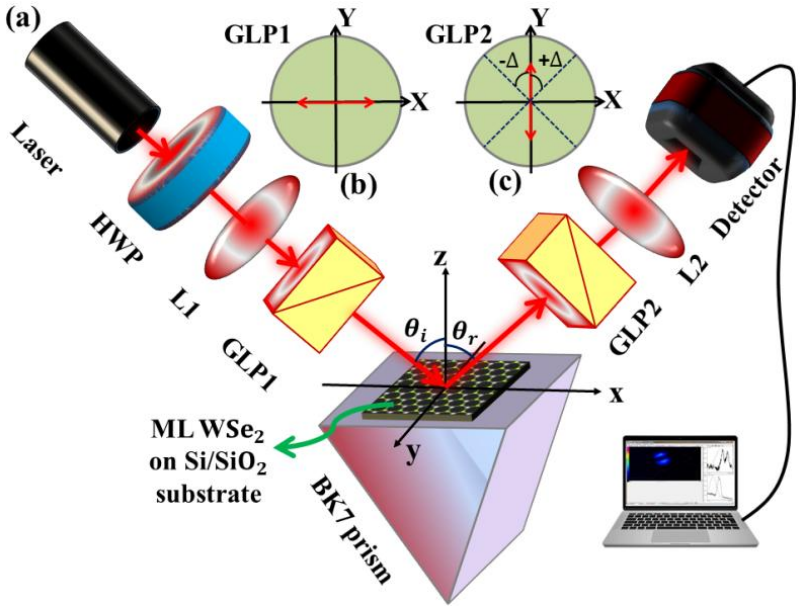

Figure 7.3 (a) Schematic of the experimental setup for measurement of transverse and longitudinal PSS in ML WSe_2 on SiO_2/Si substrate. The pre-selection and post-selection of the incident and reflected light beam have been shown in (b) and (c), respectively.

The HWP and GLP1 are mounted on a high-precision rotation mount (PRM1/M, Thorlabs), allowing precise control over both the intensity and polarization state of the incident light beam. By adjusting L1, the spot size of the incident beam (w_0) is set to approximately 180 µm. The polarization state is then pre-selected by rotating the optic axis of GLP1 to achieve either p-polarization ($\gamma = 0°$) or s-polarization ($\gamma = 90°$).

The light beam is externally reflected from the interface of a monolayer WSe_2 on a Si/SiO_2 substrate (2D Semiconductors, USA), which is mounted on the base of a right-angled prism (N-BK7 RA, Thorlabs, refractive index $n = 1.5151$) using refractive index matching liquid. The prism is positioned on a motorized precision rotation stage (PRM1Z8, Thorlabs), enabling precise control of the angle of incidence. The weak interaction for a specifically polarized light beam occurs at the sample surface.

The reflected light beam then passes through the post-selection unit, which comprises another Glan-Thompson polarizer (GLP2) (GTH10M-A, Thorlabs) mounted on a computer-controlled precision rotation stage (PRM1Z8, Thorlabs) and a plano-convex lens (L2) (f = 150 mm, LA1433, Thorlabs), with L1 and L2 forming a 4f system. After reflection, the beam propagates a fixed distance of 30 cm to achieve an appropriate enhancement of the shift through the propagation factor z_r/z_R [45]. To post-select the reflected beam at a specific angle (Δ), the

optic axis of GLP2 is rotated until the minimum light intensity is detected by the beam profiler (LBP-4 6610d, Newport). This corresponds to the orthogonal condition in the optical analog of weak value amplification, where the Gaussian beam splits into two separate Gaussians due to destructive interference [30].

Taking this position of GLP2 as the reference for beam shift measurements, it is rotated clockwise and counterclockwise by the post-selection angle (Δ), and the corresponding beam centroid positions are recorded using the high-precision beam profiler (LBP-4 6610d, Newport). From these measurements, the longitudinal and transverse shifts between the two opposing circular polarizations can be directly determined.

7.4 Results and Discussions

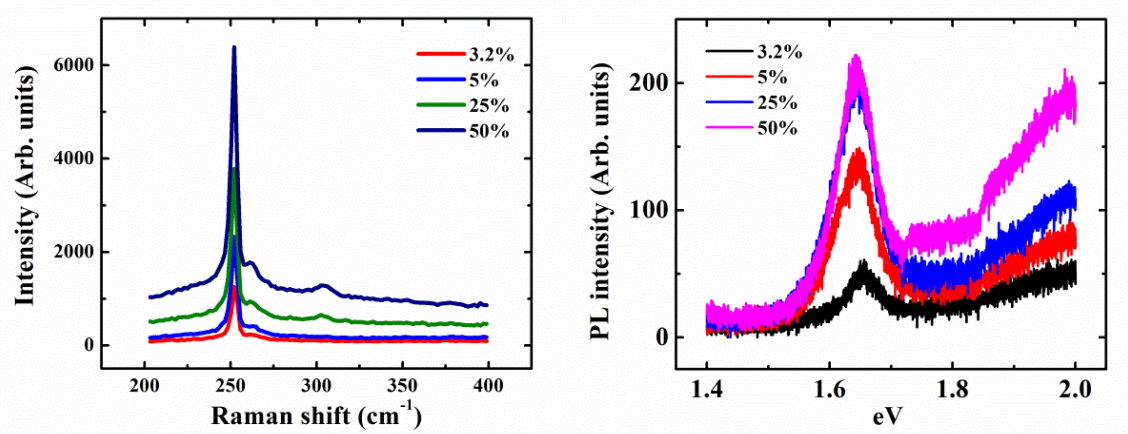

Figure 7.4 Characterization of monolayer WSe_2 (a) Raman (b) Photoluminescence (PL) spectroscopy.

Before measuring the in-plane and out-of-plane displacements of the specifically polarized incident light beam reflected from the 2D monolayer WSe_2 on the Si/SiO_2 substrate, the layer number and optical quality of the sample were verified using fast, non-destructive techniques such as Raman and photoluminescence (PL) spectroscopy performed at room temperature. The presence of prominent Raman peak E_{2g}^1 around 251 cm^{-1} and weak A_{1g} at a separation of 5-6 cm^{-1}; and the absence of B_{2g}^1 peak near 304 cm^{-1} clearly signify the monolayer structure of the WSe_2 sample [Figure 7.4(a)] [46]. Subsequently, [Figure 7.4(b)] presents the photoluminescence (PL) spectra for the specified sample. The experimentally observed symmetric, strong A-exciton emission peak around 1.66 eV confirms the direct bandgap nature of the high-quality CVD-grown monolayer WSe_2 sample.

We have now studied the region 65° to 80° to investigate how the transverse (δ_y) and longitudinal (δ_x) shifts depend upon the angle of incidence appearing due to the interaction of the visible light beam (633 nm) with the interface of monolayer WSe_2 placed on the SiO_2/Si substrate. This region covers Brewster's angle of incidence (~76°) for the present configuration (air-ML WSe_2 - Si/SiO_2) providing it more significance. Four distinct post-selection angles have been chosen as $\Delta = 0.2^\circ, 0.5^\circ, 1.0^\circ$ and 1.6°.

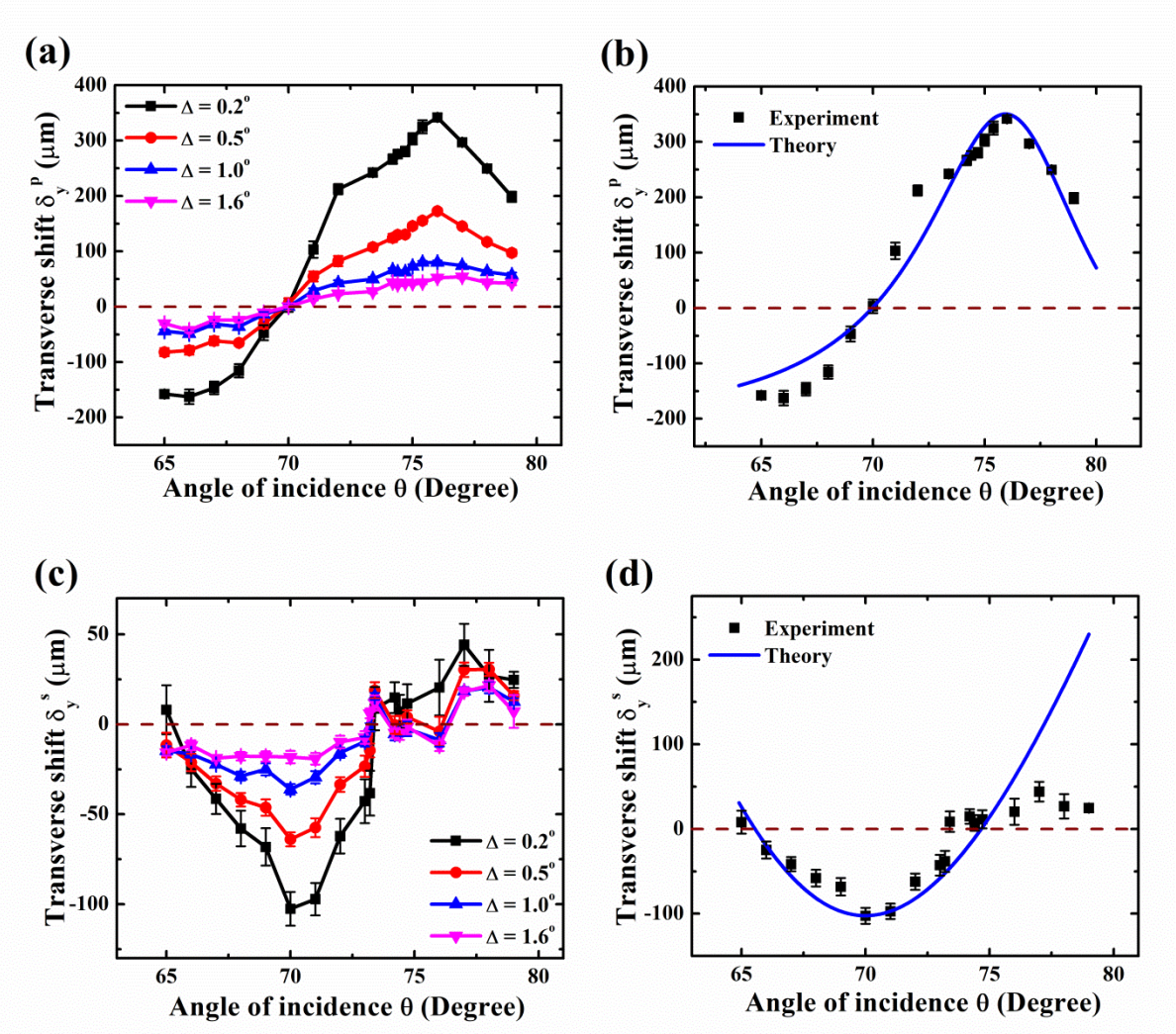

Figure 7.5 Experimental [(a), (c)] and theoretical [(b), (d)] representation of the variation of transverse shift (δ_y) for p- and s-polarized incident light beam with angle of incidence, respectively.

The transverse shift values (δ_y) for a p-polarized incident light beam are initially negative and eventually approach zero at an angle of incidence of 70°, referred to as the "zero-crossing angle" [8]. After that, for a post-selection angle of 0.2°, δ_y increases monotonically,

reaching a maximum value of roughly 350 μm at the Brewster angle of incidence. As we proceed away from the Brewster angle, after that, it gradually drops [Figure 7.5(a)]. The behavior of transverse shift values (δ_y) for an s-polarized incident light beam is significantly different, as illustrated in Figure 7.5(b). In this instance, it begins to grow in the opposite direction, achieves its maximum value of approximately 110 μm close to the angle of incidence of 70°, then drops to zero at roughly the angle of 75°, and exhibits a little positive value at higher incidence angles.

Moreover, lower shift values for both polarizations were found at larger post-selection angles. Our experimental findings have also been compared with the established theoretical framework [equation (7.11) and (7.12)]. For p-polarized light beams, we find that the theoretical model and experimental data match perfectly; but, for s-polarized light beams, we find a little mismatch, which we attribute to the increased scattering of reflected light beams at higher angles of incidence.

Subsequently, we have presented in Figure 7.6 the angle-dependent measurement of the longitudinal shift of two opposite circular polarizations. It is evident that for a p-polarized incident light beam, the longitudinal shift begins at a tiny positive value, passes zero at approximately 68° angle of incidence, and grows in the opposite direction, reaching a maximum of up to 70 μm [Figure 7.6(a)]. Then, close to the Brewster angle, it drops abruptly again to zero. We might infer that the transverse shift value is more prevalent close to the Brewster's angle of incidence.

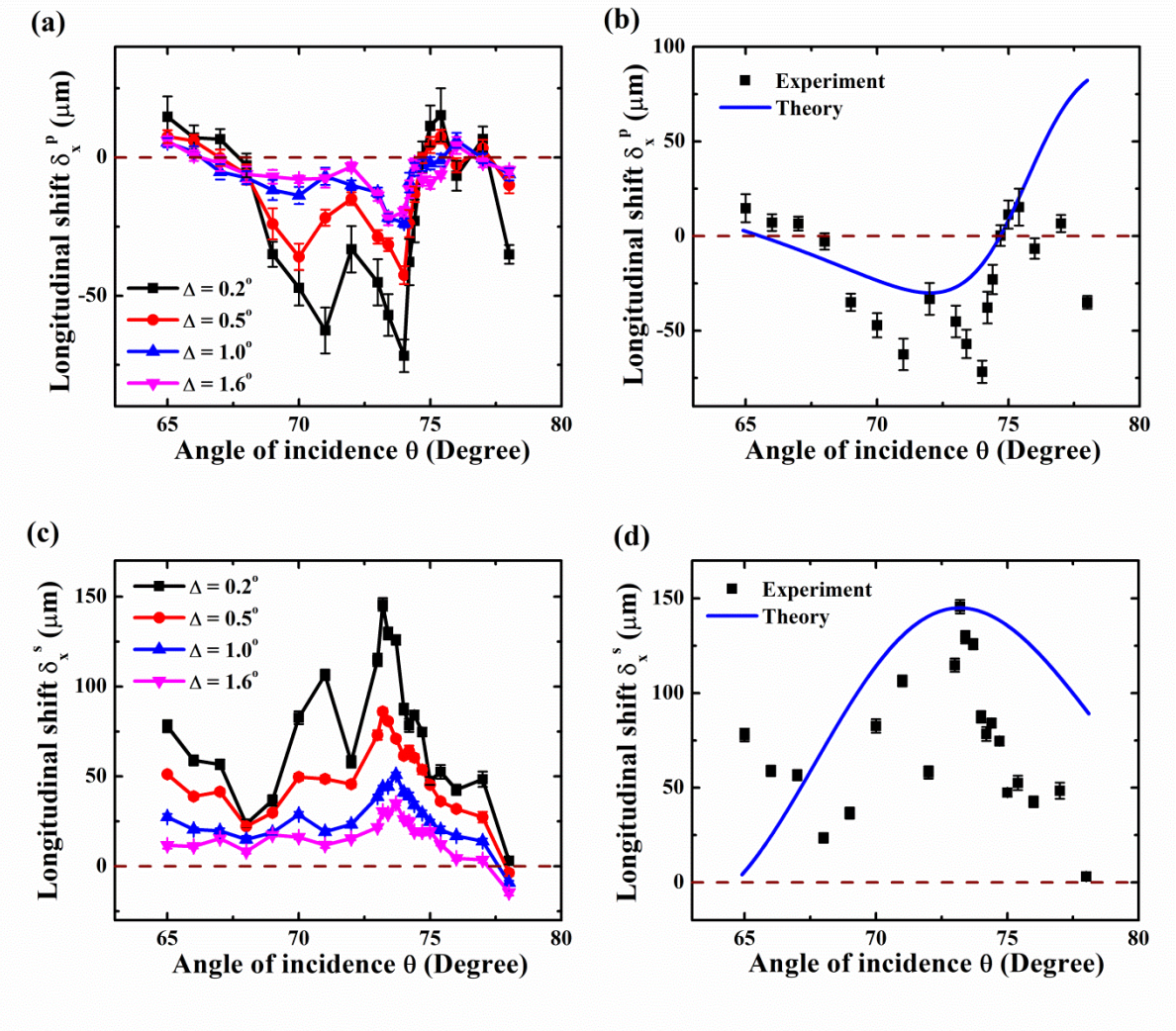

Figure 7.6 Experimental [(a), (c)] and theoretical [(b), (d)] representation of the variation of longitudinal shift (δ_x) for p- and s-polarized incident light beam with angle of incidence, respectively.

Meanwhile, the longitudinal shift for s-polarized light first showed a positive shift value before gradually decreasing to 23 μm at a 68° angle of incidence. Afterward, it increases monotonically to a maximum value of around 145 μm at a 73° angle of incidence, and at higher angles of incidence, it quickly drops to a small value, as seen in Figure 7.6(c). In order to compare the experimental data of longitudinal shift for both incidence polarizations, we have plotted the equations (7.9) and (7.10) as shown in Figure 7.6(b) and Figure 7.6(d). Here, it is observed that the theoretical model of the variation of δ_x with angle of incidence and the experimentally obtained results have similar trends. Although the data points are slightly apart with respect to the theoretical prediction, which is because the parameters appearing due to

oblique incidence and large scattering at higher angles of incidence are not considered in the theoretical model.

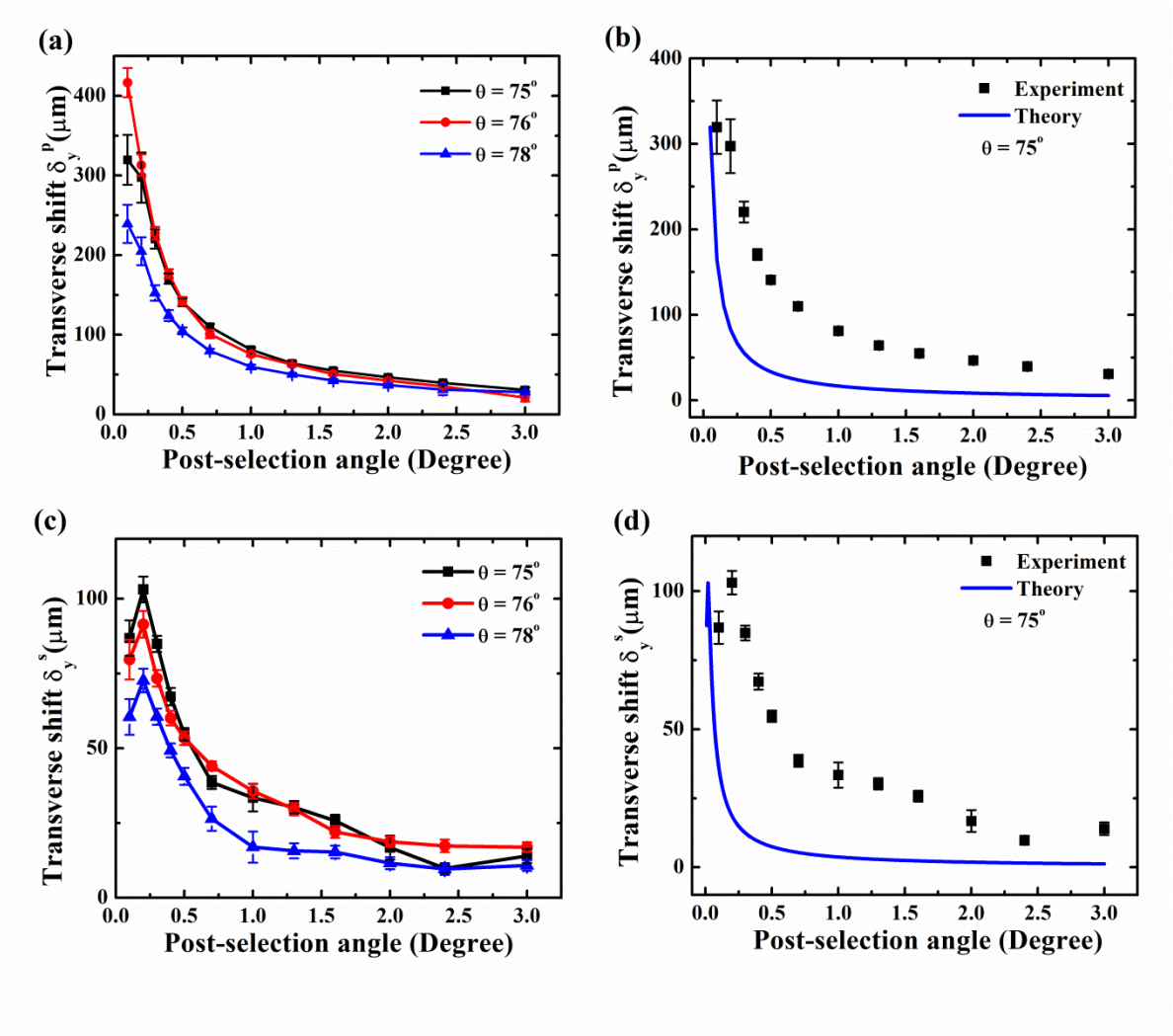

Figure 7.7 Experimental [(a), (c)] and theoretical [(b), (d)] representation of the variation of transverse shift (δ_y) for p- and s-polarized incident light beam with post-selection angle, respectively.

It is clear that the shift values also depend on the post-selection angles from the angle-dependent analysis of the longitudinal and transverse shifts for various post-selection angles. Therefore, we have plotted those with post-selection angles, taking into account both the p- and s- polarized incoming light beam for three distinct choices of incident angles ($\theta = 75^\circ, 76^\circ$, and 78°) in order to more thoroughly study the behavior of both shifts with post-selection angles. From the experimental data shown in Figure 7.7, multiple inferences can be made. First, the transverse shift is larger for a smaller value of the post-selection angle, and it decreases

slowly as we step up the post-selection angle. Secondly, we obtain the maximum transverse shift curve at the Brewster angle of incidence ($\theta = 76^{\circ}$) for p-polarized light waves Figure 7.7 (a). Third, with an s-polarized incident light beam, the maximum δ_y is found at the post-selection angle of 0.2° Figure 7.7 (c). Fourth, the larger transverse shift value curve (δ_y^S) for s-polarized light is obtained at a smaller angle of incidence. Furthermore, it is found that, at a given angle of incidence, p-polarization can yield approximately four times (400 μm) higher maximum δ_y values than s-polarized incident light beams (100 μm).

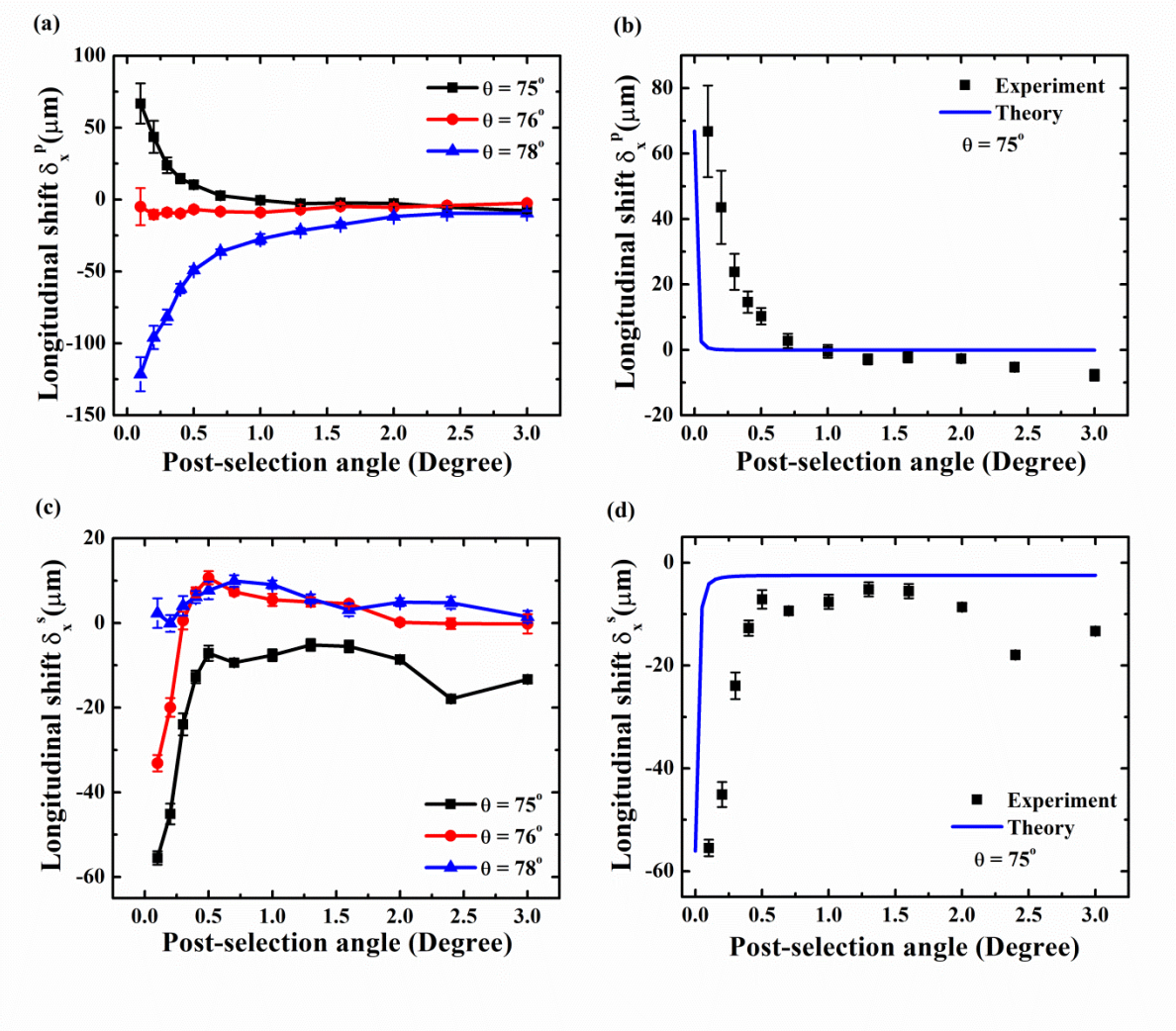

Figure 7.8 Experimental [(a), (c)] and theoretical [(b), (d)] representation of the variation of longitudinal shift (δ_x) for p- and s-polarized incident light beam with post-selection angle, respectively.

In addition, we have also demonstrated how the longitudinal displacement is dependent on the post-selection angle for both incident polarization states, as illustrated in Figure 7.8. The

p-polarized incident light beam, starting from positive and negative values, δ_x decreases slowly for the angles of incidence 75° and 78°, respectively, as we increase the post-selection angle Figure 7.8 (a). It is significant to observe that, for the Brewster incidence (76°), the longitudinal displacement is quite little, and mostly constant. Furthermore, δ_x starts from large negative values and reduces for a higher post-selection angle Figure 7.8 (c) for s-polarized incident light beam. The maximum negative shift is obtained at a lower angle of incidence.

Finally, the experimental data is supported by the theoretical model as well, as depicted in Figure 7.7 (b, d) and Figure 7.8 (b, d) for transverse and longitudinal spin splitting. It can be clearly observed that, although the data points do not match exactly with the theoretical model, but it follows a similar trend. As a result of strong excitonic absorption, the imaginary part of the permittivity (ε_{img}) shows exceptional large values in the visible optical region [25]. The stronger exciton absorption is also responsible for the energy loss of reflected photons. The absorption of incident s- and p-polarized light beams strongly depend upon the angle of incidence. Therefore, the complex reflection coefficient considered in our theoretical model plays a crucial role in manipulating the PSS in longitudinal and transverse directions. The amplification factor of the weak measurement is therefore no longer a constant that is independent of the incident angle and the preselected state, but rather, in contrast to traditional weak measurement, it is a dynamic quantity related to both the incident angle and the preselected state.

7.5 Concluding remarks

In conclusion, this article demonstrates the investigation of the simultaneous detection of the transverse (δ_y) and longitudinal (δ_x) spin separation of two opposite circular polarizations in the vicinity of the Brewster angle of incidence (partial reflection) for p- and s-linearly polarized pre-selected light beams reflected from ML WSe_2 deposited on Si/SiO_2 substrate using the weak value amplification technique. This work establishes the dependence of PSS for an absorbent material interface on the angle of incidence and post-selection angle. The generalized theoretical model that takes into account the imaginary reflection coefficient while maintaining generality provides strong support for our experimental findings. The modified expressions for δ_x and δ_y have been provided, which can be used irrespective of coupling strength (weak or strong) in weak measurement. Finally, we think that this study will lead to further investigations in the area of photonic spin manipulations and precision metrology.

References

1. M. Onoda, S. Murakami, and N. Nagaosa, Phys. Rev. Lett. **93**, 083901 (2004).
2. K.Y. Bliokh, Y.P. Bliokh, Phys. Rev. E **70**, 026605 (2004).
3. A. Das, S. Mandal, R. A. Fiallo, M. W. Horn, A. Lakhtakia, and M. Pradhan, J. Opt. Soc. Am. B **40**, 2418-2428 (2023).
4. K.Y. Bliokh, Y.P. Bliokh, Phys. Rev. Lett. **96**, 073903 (2006).
5. K.Y. Bliokh, Y.P. Bliokh, Phys. Rev. E **75**, 066609 (2007).
6. K.Y. Bliokh, F.J. Rodríguez-Fortuño, F. Nori, A. V. Zayats, Nat. Photonics **9**, 796 – 808 (2015).
7. X. H. Ling, X. X. Zhou, K. Huang, Y. C. Liu, C. W. Qiu, Rep. Prog. Phys. **80**, 066401 (2017).
8. A. Das, S. Mandal, and M. Pradhan, J. Opt. Soc. Am. B **39**, 1822-1828 (2022).
9. S. Liu, S. Chen, S. Wen, and H. Luo, Opto-Electronic Science **1**, 220007-1 (2022).
10. P. Chandravati and N. K. Viswanathan, OSA Continuum **1,** 872-881 (2018).
11. M. Merano, N. Hermosa, J. P. Woerdman and A. Aiello, Phys. Rev. A **82,** 023817 (2010).
12. A. Konstantin, Science **324**, 1530-1534 (2009).
13. Q. Ma, G. Ren, K. Xu, and J. Z. Ou, Advanced Optical Materials **9**, 2001313 (2021).
14. L. Xiaofeng, Q. Guo, and J. Qiu, Advanced Materials **29**, 1605886 (2017).
15. C. Peigang, T. W. Lo, Y. Fan, S. Wang, H. Huang, and D. Lei, Advanced Optical Materials **8**, 1901233 (2020).
16. A. Chaves, J. G. Azadani, H. Alsalman, D. R. Da Costa, R. Frisenda, A. J. Chaves, S. H. Song et al., npj 2D Materials and Applications **4**, 29 (2020).
17. C. Shizhen, X. Ling, W. Shu, H. Luo, and S. Wen, Phys. Rev. Appl. **13**, 014057 (2020).
18. S. Chen, X. Zhou, X. Ling, W. Shu, H. Luo, and S. Wen, Appl. Phys. Lett. **118**, 111104 (2021).
19. C. Liang, M. Liu, S. Chen, Y. Liu, W. Shu, H. Luo, and S. Wen, Phys. Rev. A **95**, 013809 (2017).
20. X. Wenhao, Q. Yang, G. Ye, W. Wu, W. Zhang, H. Luo, and S. Wen, Phys. Rev. A **101**, 023826 (2020).
21. J. G. Yi, Z. X. Huang, Q. Y. Ma, and G. Li, Nanophotonics **9**, 715-723 (2020).
22. O. Hosten O, P. Kwiat, Science **319**, 787–790 (2008).
23. Y. Aharonov, D. Z. Albert, L. Vaidman, Phys. Rev. Lett. **60**, 1351–1354 (1988).

24. N. W. M. Ritchie, J. G. Story, R. G. Hulet, Phys. Rev. Lett. **66**, 1107–1110 (1991).
25. I. M. Duck, M. P. Stevenson, and E. C. G. Sudarshan, Phys. Rev. D **40**, 2112 (1989).
26. A. Das, S. Mandal, and M. Pradhan, Opt. Lett. **46**, 5826-5829 (2021).
27. Y. Qin, Y. Li, H. Y. He, Q. H. Gong, Opt. Lett. **34**, 2551–2553 (2009).
28. Y. Qin, Y. Li, X. B. Feng, Y. F. Xiao, H. Yang, Opt. Express **19**, 9636–9645 (2011).
29. H. Luo, X. Zhou, W. Shu, S. Wen, and D. Fan, Phys. Rev. A **84**, 043806 (2011).
30. S. Chen, X. Zhou, C. Mi, H. Luo, and S. Wen, Phys. Rev. A **91**, 062105 (2015).
31. Z. Qin, Q. Liu, C. Yue, Y. Lang, and X. Zhou, J. Phys. D: Appl. Phys. **52**, 495106 (2019).
32. S. Lin, J. Hong, Z. Chen, Y. Chen, and X. Zhou, Opt. Express **30**, 4096-4105 (2022).
33. Z. Qin, R. Zhang, L. Zhang, L. Ren, P. Zhang, R. Qi, Q. Zhang, C. Wang, and L. Jiang, Opt. Communications **557**, 130283 (2024).
34. J.D. Elliott, Z. Xu, P. Umari, G. Jayaswal, M. Chen, X. Zhang, A. Martucci, M. Marsili, and M. Merano, Phys. Rev. B **101,** 045414 (2020).
35. A. Molina-Sánchez, D. Sangalli, L. Wirtz, and A. Marini, Nano Lett. **17**, 4549-4555 (2017).
36. W.T. Hsu, L.S. Lu, D. Wang, J.K. Huang, M.Y. Li, T.R. Chang, Y.C. Chou, Z.Y. Juang, H.T. Jeng, L.J. Li, and W.H. Chang, Nat. comm. **8**, 929 (2017).
37. G. Honggang, B. Song, M. Fang, Y. Hong, X. Chen, H. Jiang, W. Ren, and S. Liu, Nanoscale **11**, 22762-22771 (2019).
38. G. Hongming, N. Tang, H. Huang, X. Zhang, M. Su, X. Liu, L. Liao, W. Ge, and B. Shen, ACS nano **13**, 9325-9331 (2019).
39. N. Ansari and F. Ghorbani, J. Opt. Soc. Am. B **35**, 1179-1185 (2018).
40. G. Jayaswal, Z. Dai, X. Zhang, M. Bagnarol, A. Martucci, and M. Merano, Opt. Lett. **43**, 703–706 (2018).
41. S. Chen, C. Mi, L. Cai, M. Liu, H. Luo, and S. Wen, Appl. Phys. Lett. **110**, 031105 (2017).
42. D.K. Li, S.Y. Wang, X.Q. Yan, B.W. Su, Z. Hu, Z.B. Liu, and J.G. Tian, Appl. Phys. Lett. **120**, 053105 (2022).
43. G.H. Jung, S. Yoo, and Q. H. Park, Nanophotonics **8**, 263-270 (2019).
44. X. Li, P. Wang, F. Xing, X.D. Chen, Z.B. Liu, and J.G. Tian, Opt. Lett. **39**, 5574-5577 (2014).
45. A. Aiello A and J. P. Woerdman, Opt. Lett. **33,** 1437–1439 (2008).

46. W. Shi, M. L. Lin, Q. H. Tan, X. F. Qiao, J. Zhang, and P. H. Tan, 2D Materials **3**, 025016 (2016).

8 Photonic Spin Splitting Using Vortex Light

The content of this chapter is adapted from the following published article:

S. Mandal, D. C. Dey, A. Sett, and M. Pradhan, "Photonic spin splitting with orbital angular momentum pointer states via modified weak measurement," ***Physical Review A*** 112, 033511 (**2025**).

8.1 Introduction

Photonic spin splitting (PSS) refers to the phenomenon in which a linearly polarized light beam with finite spectral width separates into right- and left-circular polarization components by a subwavelength distance along both the longitudinal and transverse directions relative to the plane of incidence during reflection or transmission [1]. These longitudinal and transverse displacements are commonly known as the Goos–Hänchen (GH) and Imbert–Fedorov (IF) shifts, respectively [2]. Depending on the reflection conditions and the nature of the interaction medium, the beam shifts can exhibit both angular and spatial characteristics [3].

The origin of PSS is closely associated with the photonic spin-orbit interaction, which arises from the coupling between the light's orbital angular momentum (OAM) and its geometric phase [4,5]. As these non-specular light-matter interactions occur at interfaces, various degrees of freedom of light-including polarization [6,7], beam shape [8,9], wavelength [10], and several parameters of the interacting medium [11-14] - can influence the resulting shift magnitudes.

Since its discovery, the OAM of light has served as a powerful degree of freedom for tailoring beam structure [15], finding applications in diverse areas such as optical tweezers [16], imaging [17], wavefront manipulation [18], and quantum information science [19]. Previous studies have shown that, for external reflection of an OAM-carrying beam, the spatial GH (IF) and angular IF (GH) shifts become coupled by a factor of ($\mp 2l$), while the angular GH and IF shifts are enhanced by a factor of ($1 + |2l|$), where l denotes the OAM index of the incident beam [20-22].

Furthermore, the characteristics of beam shifts near the Brewster [23,24] and critical angles [25,26] have been extensively examined for OAM light beams. Recent research has also explored super-amplification effects through the combination of OAM and quantum weak measurement (QWM) techniques [27-29], as well as novel beam-shift behaviours arising from the interplay of OAM and material properties [30,31].

The concept of quantum weak measurement (QWM) was first introduced by Aharonov *et al.* [32]. It involves three essential steps: (i) pre-selection of the initial system state, (ii) a weak interaction between the system and the measuring pointer such that the pointer state remains nearly unaffected, and (iii) post-selection of the final system state. It was shown that when the pre- and post-selected states are nearly orthogonal, the resulting weak value becomes

anomalously large - sometimes even extending beyond the eigenvalue spectrum of the corresponding observable. This phenomenon is referred to as weak value amplification (WVA) [32,33].

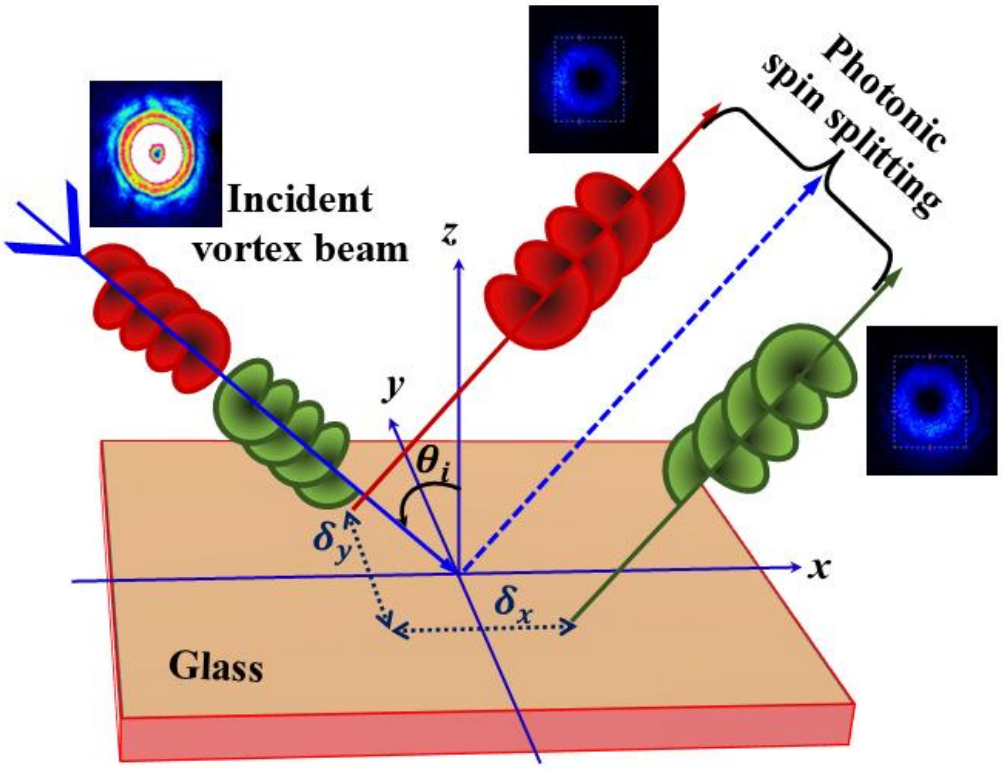

Figure 8.1 Schematic representation of longitudinal (δ_x) and transverse (δ_y) shift of beam centroid position due to partial reflection of linearly polarized vortex light beam at air-glass interface.

The optical analogue of WVA was later demonstrated to detect the amplified separation between ordinary and extraordinary rays in transmission [33,34], thereby opening a novel and rapidly expanding area of research focused on optical weak measurements [35]. Although the practical advantages of WVA have been debated [36], the framework has successfully been applied to address several foundational issues in quantum mechanics, including Hardy's paradox [37], the Heisenberg uncertainty principle [38], wave function reconstruction [39], and the quantum Cheshire Cat phenomenon [40].

Moreover, WVA has proven to be a highly effective tool in quantum metrology, enabling the detection and characterization of extremely subtle photonic effects such as photonic spin

splitting (PSS) [41], magneto-optical phenomena [42], frequency shifts [43], phase estimation [44], and time delays [45]. A comprehensive account of the recent advancements and applications of QWM can be found in the review by [46].

The conventional quantum weak measurement (QWM) framework employed to investigate photonic spin splitting (PSS) becomes inadequate under two critical conditions: (i) when the coupling strength is not sufficiently weak - particularly near the Brewster angle and the critical angle of incidence, where the beam shape undergoes distortion during partial or total internal reflection - and (ii) when the pre- and post-selected states are nearly orthogonal [$\langle\psi_{\text{post}} \mid \psi_{\text{pre}}\rangle \approx 0$], causing the weak value A_w to diverge and become discontinuous in the vicinity of orthogonality.

To overcome these challenges, Chen *et al.* [47] introduced a modified weak measurement model capable of describing such scenarios more accurately. However, their model was limited to transverse shifts and considered only *p*- and *s*-polarized incident beams interacting with non-absorbing materials. Subsequently, more generalized formulations were developed to address both longitudinal and transverse PSS, accounting for specific and arbitrary linear polarizations and reflections from absorbing material interfaces. These models were further validated through experimental observations [48–51].

Despite these advancements, all existing models have been formulated using the fundamental Gaussian mode ($l = 0$) as the pointer state. This inherent limitation restricts their applicability to higher-order structured light beams, such as Laguerre–Gaussian or Hermite–Gaussian modes, which possess intrinsic orbital angular momentum (OAM). As a result, the extension of weak measurement theory to accommodate higher-order beam modes and its implications for generalized PSS dynamics remain an open and unexplored area of research, forming the central motivation for the present study.

In light of the above discussions, the present work aims to develop a generalized theoretical and experimental framework for investigating photonic spin splitting (PSS) using arbitrarily linearly polarized higher-order orbital angular momentum (OAM) light beams [Figure 8.1]. A rigorous modified weak measurement model, formulated within the conventional wave-vector formalism, is proposed and validated experimentally. This model is versatile in that it can be applied to both internal and external reflections of light from absorbing

as well as non-absorbing media, and it remains reliable under the two critical conditions where the conventional weak measurement formalism fails.

The structure of this *Chapter* is organized as follows: Section 8.2 presents the mathematical formulation for the longitudinal and transverse displacements of the reflected light beam. Section 8.3 describes the experimental methodology employed to measure the amplified sub-wavelength shifts using a higher-order light beam generated through a spatial light modulator (SLM). The experimental observations and their comparison with theoretical predictions are discussed in Section 8.4, followed by a summary of the key findings and future perspectives in the Conclusion.

8.2 Theoretical formulation

For the sake of generality, we consider the external reflection of an arbitrarily linearly polarized higher-order OAM light beam from a planar interface. The geometrical configuration of the light–matter interaction follows the schematic described in Figure 8.1. The unit vectors $\hat{x}_a$, $\hat{y}_a$, and $\hat{z}_a$, with subscripts $a = i$ and r, define the Cartesian coordinate frames attached to the incident and reflected beams, respectively.

Using the angular spectrum representation, the electric field of the incident arbitrarily linearly polarized Laguerre-Gaussian (LG) beam with radial mode index $p = 0$ can be expressed as:

$$\tilde{E}_i = \begin{pmatrix} cos\,\alpha_i \\ sin\,\alpha_i \end{pmatrix} \tilde{u}_i^l(k_{ix}, k_{iy})\ exp[-\frac{z_R(k_{ix}^2 + k_{iy}^2)}{2k_i}] \tag{8.1}$$

where $\tilde{u}_i^l(k_{ix}, k_{iy}) = (k_{ix} + isgn(l)k_{iy})^{|l|}$; α_i represents the polarization angle of the incident beam, $k_i = \frac{2\pi}{\lambda_i}$ is the wave number corresponding to the wavelength λ_i of the incident light, and k_{ix} and k_{iy} are the wave vector components along the $\hat{x}_i$ and $\hat{y}_i$ directions, respectively. The Rayleigh length is given by $z_R = \frac{k_i w_0^2}{2}$, where w_0 denotes the beam waist of the incident beam.

Since each plane-wave component of the wave packet experiences a slightly different angle of incidence due to the finite transverse extent of the wave vector, the reflected electric field can be obtained by expanding the Fresnel reflection coefficients r_p and r_s in a first-order Taylor series around $k_{ix} = 0$, yielding:

$$\tilde{E}_r = \begin{pmatrix} (r_{p\theta} - \frac{k_{rx}}{k_i}\frac{\partial r_{p\theta}}{\partial \theta})\cos\alpha_i + \frac{(r_{p\theta} + r_{s\theta})k_{ry}\cot\theta}{k_i}\sin\alpha_i \\ -\frac{(r_{p\theta} + r_{s\theta})k_{ry}\cot\theta}{k_i}\cos\alpha_i + (r_{s\theta} - \frac{k_{rx}}{k_i}\frac{\partial r_{s\theta}}{\partial \theta})\sin\alpha_i \end{pmatrix} \times \tilde{u}_r^l(k_{rx}, k_{ry})\ exp[-\frac{z_R(k_{rx}^2 + k_{ry}^2)}{2k_i}] \quad (8.2)$$

where $r_{p\theta}$ and $r_{s\theta}$ denote the Fresnel reflection coefficients of *p*- and *s*-polarized central incident light wave with the angle of incidence θ, $k_{rx} = -k_{ix}$, $k_{ry} = k_{iy}$ and $\tilde{u}_r^l(k_{rx}, k_{ry}) = (-k_{rx} + isgn(l)k_{ry})^{|l|}$.

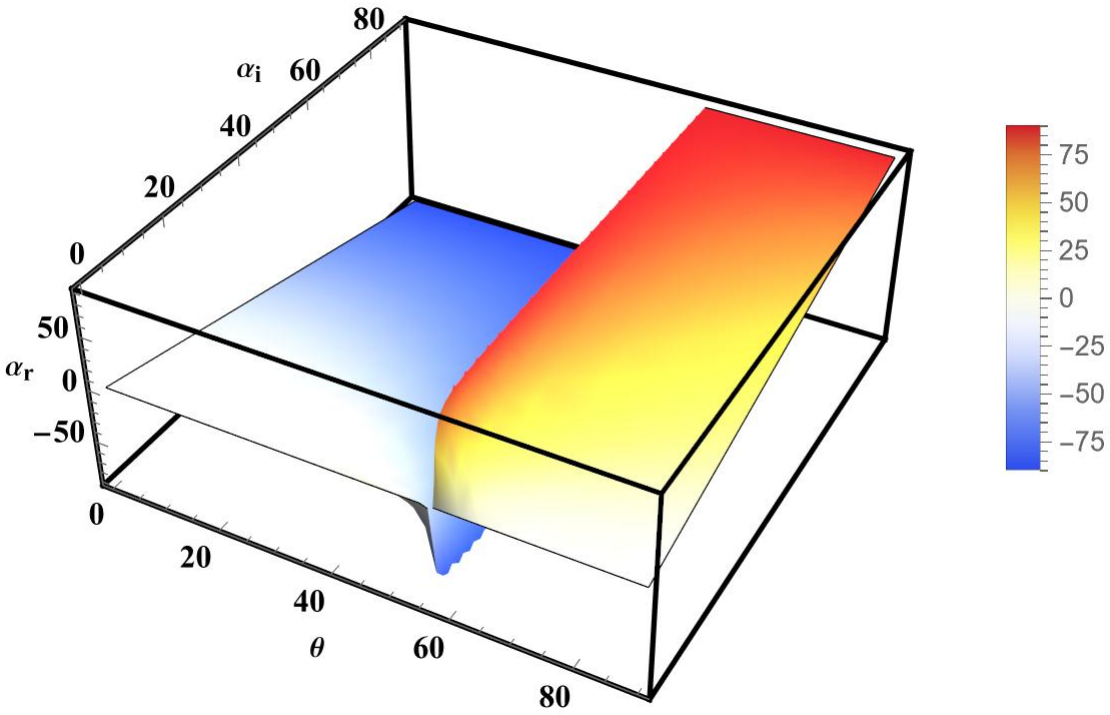

Figure 8.2 Polarization angle of reflected light beam (α_r) as a function of angle of incidence (θ) and linear polarization angle (α_i) of incident light beam.

Applying appropriate boundary conditions and inverse Fourier transform to equation (8.2), the reflected electric field in position space can be evaluated as [52],

$$E_r = \begin{pmatrix} E_r^p \\ E_r^s \end{pmatrix} = \tag{8.3}$$

$$\begin{bmatrix} \left(r_{p\theta} - \frac{x_r r_p'}{z_r - iz_R} + \frac{i|l|r_p'}{k(x_r - iy_r sgn[l])}\right) cos\,\alpha_i - \left(r_{p\theta} + r_{s\theta}\right) sin\,\alpha_i\, cot\,\theta \left(\frac{|l| sgn[l]}{k(x_r - iy_r sgn[l])} - \frac{y_r}{z_r - iz_R}\right) \\ \left(r_{s\theta} - \frac{x_r r_s'}{z_r - iz_R} + \frac{i|l|r_s'}{k(x_r - iy_r sgn[l])}\right) sin\,\alpha_i + \left(r_{p\theta} + r_{s\theta}\right) cos\,\alpha_i\, cot\,\theta \left(\frac{|l| sgn[l]}{k(x_r - iy_r sgn[l])} - \frac{y_r}{z_r - iz_R}\right) \end{bmatrix}$$
$$\times u_r(x_r, y_r$$

where $u_r(x_r, y_r) \sim [-x_r + isgn(l)y_r]^{|l|}\, exp\left[-\frac{k_r(x_r^2+y_r^2)}{2(iz_r+z_R)}\right]$, E_r^p and E_r^s represent the reflected electric field component for p-($\alpha_i = 0$) and s-($\alpha_i = 90$) polarized incident light beam along the x_r and y_r axis, respectively and $r_{p,s}' = \frac{\partial r_{p,s}}{\partial \theta}$.

In the weak value amplification (WVA) scheme, the reflected light beam is post-selected into a polarization state that is nearly orthogonal to the polarization state of the reflected light α_r. The polarization angle of the reflected beam is given by $\alpha_r = tan^{-1}(\frac{r_s}{r_p} tan\ \alpha_i)$, where r_p and r_s are the Fresnel reflection coefficients for p- and s-polarized light, respectively [48]. Figure 8.2 illustrates the dependence of α_r on the incident polarization angle α_i and the angle of incidence θ for reflection at a non-absorbing air–glass interface.

In the case of reflection from an absorbing material interface, the polarization angle α_r can become complex, depending on the arbitrary phase difference between r_p and r_s. As a result, the reflected light is generally elliptically polarized. The transmission axis of the analyzer (post-selection polarizer) is then set at $\alpha_p = (90 + \alpha_r) \pm \Delta$ with respect to the $\hat{x}_r$ axis, where Δ denotes the post-selection angle.

The Jones matrix of this operation is written as $M_{post} = \begin{pmatrix} cos^2\alpha_p & \frac{1}{2} sin\,2\alpha_p \\ \frac{1}{2} sin\,2\alpha_p & sin^2\alpha_p \end{pmatrix}$. After passing through the post-selection polarizer, the reflected electric field is given by $\mathrm{E}_f = M_{\mathrm{post}} \cdot \mathrm{E}_r$, where E_r is the reflected field. The generalized amplified photonic spin splitting (PSS) can then be evaluated by computing the barycentre shifts of the output beam profile as,

$$x_{wva}^l = \frac{\iint x_r |E_f(x_r,\ y_r, z_r)|^2 dx_r dy_r}{\iint |E_f(x_r,\ y_r, z_r)|^2 dx_r dy_r} \tag{8.4}$$

$$y_{wva}^{l} = \frac{\iint y_r |E_f(x_r,\ y_r, z_r)|^2 dx_r dy_r}{\iint |E_f(x_r,\ y_r, z_r)|^2 dx_r dy_r} \tag{8.5}$$

Following rigorous calculations, the detailed expressions of the amplified longitudinal and transverse PSS can be obtained as equations (8.6) and (8.7), respectively, as

$$x_{wva}^{l} = \frac{(\xi_{xp}^{l} + \xi_{xs}^{l} + \xi_{xps}^{l})}{\chi_{p}^{l} + \chi_{s}^{l} + \chi_{ps}^{l}} \tag{8.6}$$

$$y_{wva}^{l} = \frac{(\psi_{yp}^{l} + \psi_{ys}^{l} + \psi_{yps}^{l})}{\chi_{p}^{l} + \chi_{s}^{l} + \chi_{ps}^{l}} \tag{8.7}$$

where,

$$\xi_{xp}^{l} = 2r_p cos^2\alpha_i \left[r_p' z_r cot^2\alpha_p - \frac{|l|}{(|l|+1)} (r_p + r_s) z_R \cot\alpha_p \cot\theta \right] \tag{8.8}$$

$$\xi_{xs}^{l} = 2r_s sin^2\alpha_i \left[r_s' z_r + \frac{|l|}{(|l|+1)} (r_p + r_s) z_R \cot\alpha_p \cot\theta \right] \tag{8.9}$$

$$\begin{aligned} \xi_{xps}^{l} = sin\,2\alpha_i \Bigg[& (r_s' r_p + r_p' r_s) z_r \cot\alpha_p \\ & - \frac{|l| z_R}{(|l|+1)} \{ (1 - cot^2\alpha_p) r_p r_s + r_s^2 - r_p^2 cot^2\alpha_p \} \cot\theta \Bigg] \end{aligned} \tag{8.10}$$

$$\psi_{yp}^{l} = 2r_p cos^2\alpha_i \left[(r_p + r_s)\, z_r cot\,\theta\, cot\,\alpha_p + \frac{|l|}{(|l|+1)} z_R r_p' cot^2\alpha_p \right] \tag{8.11}$$

$$\psi_{ys}^{l} = 2r_s sin^2\alpha_i \left[-(r_p + r_s) z_r \cot\theta \cot\alpha_p + \frac{|l|}{(|l|+1)} z_R\, r_s' \right] \tag{8.12}$$

$$\begin{aligned} \psi_{yps}^{l} = sin\,2\alpha_i \Bigg[& \{ z_r (r_s^2 - r_p^2 cot^2\alpha_p) + r_p r_s z_r (1 - cot^2\alpha_p) \} \cot\theta \\ & + \frac{|l|}{(|l|+1)} z_R (r_s' r_p + r_p' r_s) \cot\alpha_p \Bigg] \end{aligned} \tag{8.13}$$

$$\begin{aligned} \chi_{p}^{l} = -cos^2\alpha_i \Bigg[& \left\{ \frac{2r_p^2 k z_R}{(|l|+1)} + r_p'^2 \left(1 + \frac{2|l| z_R^2 (1-k)}{(|l|+1)(z_r^2 + z_R^2)} \right) \right\} cot^2\alpha_p \\ & + (r_p + r_s)^2 cot^2\theta \Bigg] \end{aligned} \tag{8.14}$$

$$\begin{aligned} \chi_{s}^{l} = -sin^2\alpha_i \Bigg[& \left\{ \frac{2r_s^2 k z_R}{(|l|+1)} + r_s'^2 \left(1 + \frac{2|l| z_R^2 (1-k)}{(|l|+1)(z_r^2 + z_R^2)} \right) \right\} \\ & + (r_p + r_s)^2 cot^2\alpha_p cot^2\theta \Bigg] \end{aligned} \tag{8.15}$$

$$\chi_{ps}^{l} = \sin 2\alpha_i \cot \alpha_p \left[\left(r_p + r_s\right)^2 \cot^2\theta - \frac{2kZ_R}{(|l|+1)} r_p r_s - r_p' r_s' \left\{ 1 + \frac{2|l| z_R^2}{(z_r^2 + z_R^2)} \left(\frac{(|l|-1)! - |l|!}{(|l|+1)!} \right) \right\} \right] \tag{8.16}$$

with z_r being the propagation distance.

The above formulation [equation (8.8)–(8.16)] describes the interaction of a higher-order vortex beam with azimuthal index l at a non-absorbing (air–glass) interface, where the refractive index has a zero imaginary component. By accounting for a finite imaginary part of the refractive index, this formulation can be extended to interactions with absorbing materials, as detailed in the Appendix. Furthermore, the previously established models [49–51] for Gaussian beams interacting with arbitrary materials can be recovered by setting the azimuthal index $l = 0$, thereby validating our approach. The vortex-induced photonic spin splitting (PSS) in the transverse direction can also be interpreted as arising from the mutual interplay of spin, intrinsic, and extrinsic angular momentum of light [31].

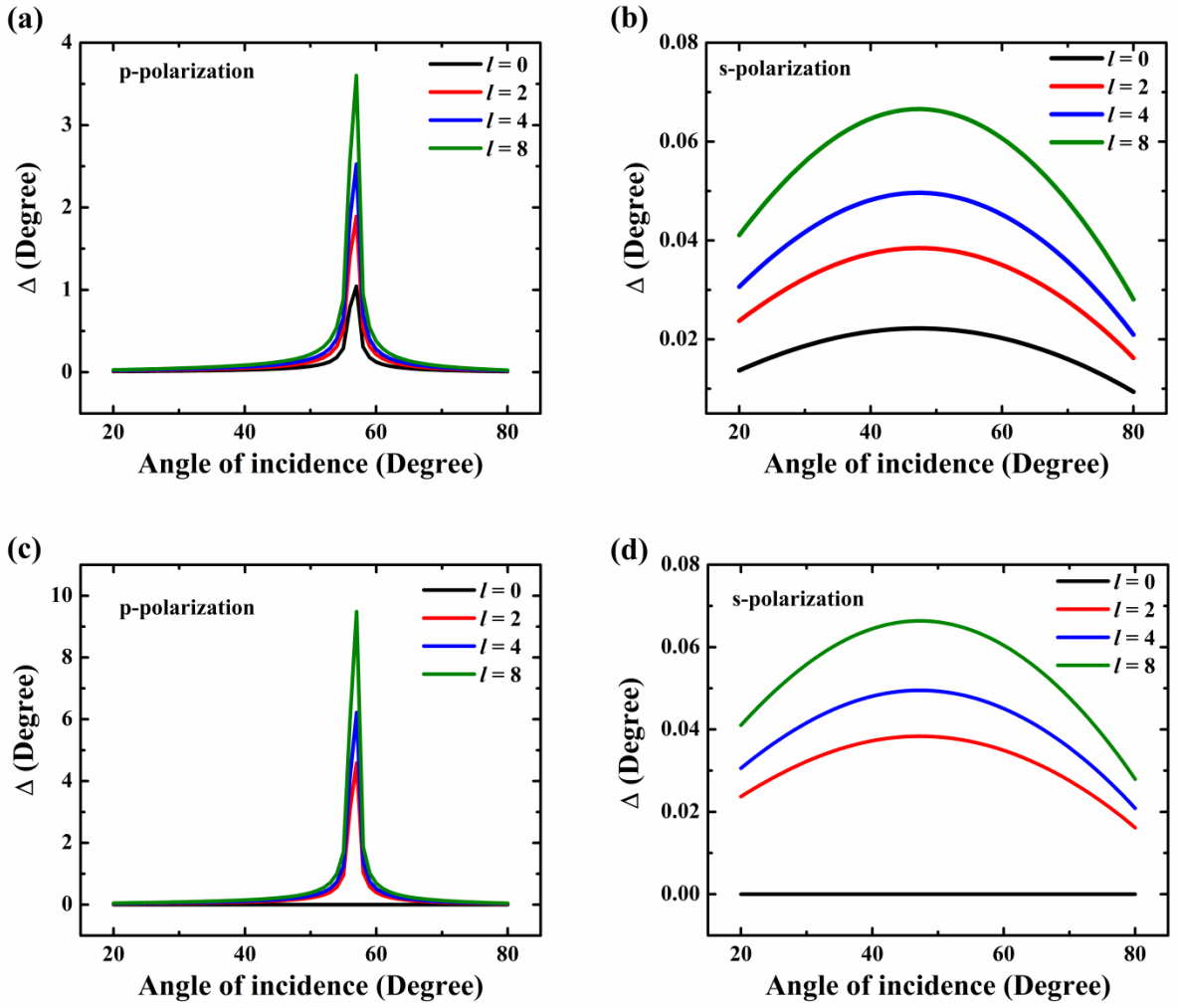

Figure 8.3 Incident angle dependent variation of post-selection angle to get maximum PSS in transverse [(a), (b)] and longitudinal [(c), (d)] direction for different topological charges of OAM light beam.

Additionally, by setting $\frac{\partial x_{wva}^{l}}{\partial \Delta} = 0$ and $\frac{\partial y_{wva}^{l}}{\partial \Delta} = 0$, one can determine how the post-selection angle depends on the angle of incidence and the topological charge of the vortex beam for a given linear polarization state, in order to achieve the maximum δ_x and δ_y values, as illustrated in Figure 8.3. For p-polarized incident light, the post-selection angle at which the transverse PSS reaches its maximum increases sharply near the Brewster angle due to the strong coupling between the pre- and post-selected states. In contrast, no such abrupt changes are observed for s-polarized incident light, as the weak coupling condition is maintained across all incident angles. For both polarization states, the optimal overlap increases with increasing values of l.

The PSS in the longitudinal direction exhibits additional interesting behaviour, as shown in Figure 8.3 (c) and (d). Null amplification of longitudinal shifts is observed when only p- or s-polarized Gaussian beams ($l = 0$) are considered, consistent with previous results showing that longitudinal shift amplification occurs only for mixed linear polarization [53]. For cases with $l \neq 0$, longitudinal shifts become coupled with transverse shifts [21], resulting in amplified longitudinal shifts even for non-mixed linearly polarized light (p- or s-polarized).

8.3 Experimental setup

Figure 8.4 illustrates the experimental setup used to detect the generalized photonic spin splitting (PSS) employing an arbitrarily linearly polarized higher-order vortex light beam, as supported by the modified weak measurement model. A Gaussian light beam generated from a He-Ne laser (wavelength 633 nm, power 5 mW; Model 30991, Research Electro-Optics Inc.) was used to illuminate a reflective phase-only spatial light modulator (SLM) (HOLOEYE PLUTO-2.1 VIS) for the generation of OAM beams.

Before reaching the SLM, the Gaussian beam passes through a half-wave plate (HWP) (WPMH10M-633, Thorlabs) and a beam expander (ZBE4A, Thorlabs). The HWP aligns the polarization axis of the incident beam along the orientation of the SLM's liquid crystal molecules, while the beam expander increases the beam diameter to ensure optimal modulation

efficiency. To generate vortex beams with azimuthal indices $l = 1$and $l = 2$, the SLM was encoded with fork-shaped phase holograms corresponding to the respective topological charges, combined with a horizontal diffraction grating, as shown in the insets of Figure 8.4. Upon reflection from the SLM, the first-order diffraction yields the desired vortex beam, while the higher-order diffraction components are suppressed using apertures A1 and A2, which are carefully positioned to block unwanted diffraction orders.

Meanwhile, the intensity, beam size (approximately 180 μm), and polarization state of the incident vortex beam are precisely controlled by the pre-selection unit, which consists of a half-wave plate (HWP), a plano-convex lens L1 (f = 300 mm), and a Glan–Laser polarizer (GLP1). The polarization state of the incident light is continuously monitored using a polarimeter (PAX1000VIS/M, Thorlabs) before it interacts with the air–glass interface. The light–matter interaction occurs at the base of a right-angled N-BK7 prism (refractive index n = 1.515 at 633 nm), which is mounted on a motorized rotation stage (PRM1/M, Thorlabs) to accurately control the angle of incidence. After reflection, the vortex beam passes through the post-selection unit, composed of a second Glan–Laser polarizer (GLP2)—mounted on a similar motorized rotation stage—and a plano-convex lens L2 (f = 150 mm).

Additionally, a quarter-wave plate (QWP) should be incorporated into the post-selection path before GLP2 and finely adjusted to compensate for any circular polarization component introduced by reflections from absorbing material interfaces. This configuration ensures accurate control over the post-selected polarization state and minimizes unwanted polarization distortions.

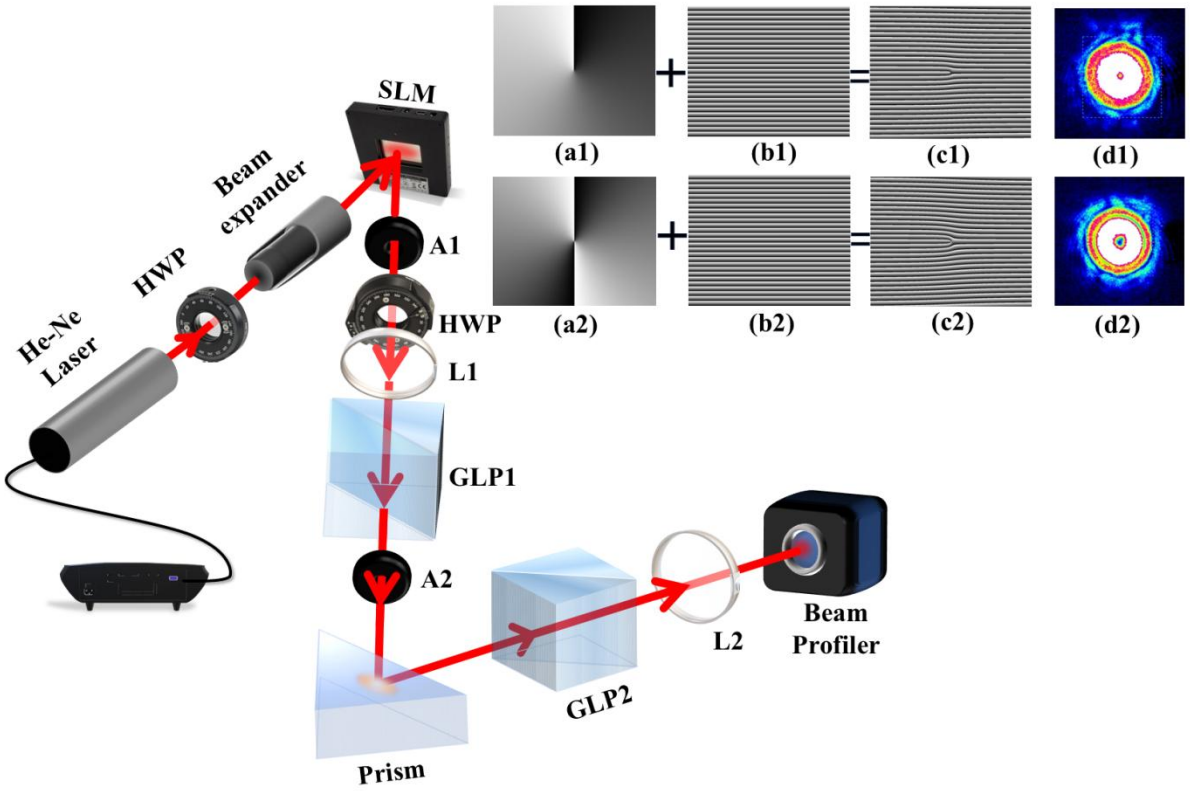

Figure 8.4 Schematic representation of the experimental setup to measure the PSS employing weak value amplification technique using higher order vortex light beam. Insets show the combination of vortex phase and horizontal diffraction grating to generate fork patterns for specific vortex light with l = 1(a1, b1, c1, d1) and l = 2 (a2, b2, c2, d2) along with their spatial intensity distribution, respectively.

The beam centroid positions and intensity profiles of the output vortex beams are analyzed using a high-precision beam profiler (LBP 4 USB, 6610d, Newport). For a given angle of incidence and polarization state, the post-selection polarizer (GLP2) is rotated to a position orthogonal to the polarization angle of the reflected beam (α_r), thereby minimizing the transmitted intensity. This configuration is referred to as the orthogonal condition [34]. Representative intensity profiles at the orthogonal condition for $l = 2$ are shown in Figure 8.8.

Using the beam centroid position at the orthogonal condition as a reference, GLP2 is then rotated clockwise and counterclockwise by a small post-selection angle (Δ). The corresponding two-dimensional centroid coordinates are recorded and employed to calculate the longitudinal and transverse components of the PSS simultaneously. All experimental measurements of the beam centroid displacements are reported in their actual magnitudes and

compared with the theoretical predictions derived from the modified weak measurement model.

8.4 Results and Discussions

We have considered three different angles of incidence, $\theta = 30°, 45°$, and $60°$, arranged in decreasing order relative to the Brewster angle (strong coupling region). Previous studies have shown that, for a given angle of incidence, δ_y dominates for p- and s-polarized beams, whereas δ_x dominates when the incident polarization is near diagonal ($\pm 45°$ LP) [48]. Considering p- and s-polarized beams with $l = 0, 1$, and 2, the variation of transverse shift values with post-selection angles is shown in Figure 8.5 .

The variation of δ_y is asymmetric about the orthogonal condition ($\Delta = 0$): it increases from zero at the orthogonal position, reaches a maximum at a specific Δ, and then decreases as Δ grows. The overall behaviour of δ_y reverses relative to the Brewster angle and increases with higher values of l. For instance, $\delta_y = 300\ \mu m$ is observed at $\theta = 60°$. The post-selection angle corresponding to the largest shift shifts toward higher values as the angle of incidence approaches the Brewster angle (θ_B), due to the strong coupling near θ_B.

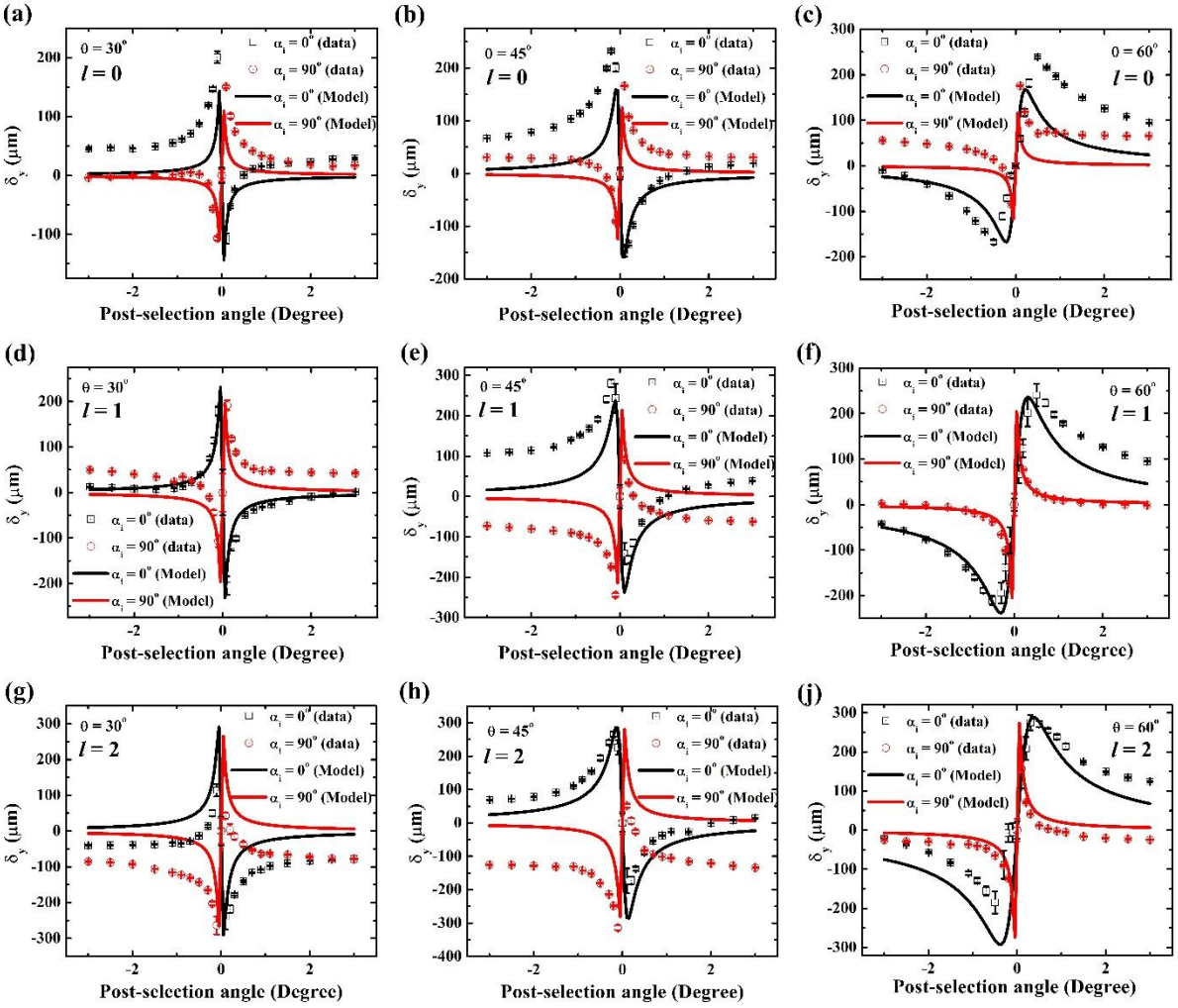

Figure 8.5 The amplified transverse (δ_y) shift values are shown as function of post-selection angle Δ for p-($\alpha_i = 0^\circ$)-(black) and s-($\alpha_i = 90^\circ$)-(red) polarized incident light beam with azimuthal index $l = 0$ [(a), (b), (c)], $l = 1$ [(d), (e), (f)] and $l = 2$ [(g), (h), (i)] for three different angle incidences $\theta = 30^\circ, 45^\circ, 60^\circ$. The dot centered square, circle denote the experimental data while solid lines represent the theoretical model.

Next, considering incident linear polarization angles $\alpha_i = 30°, 45°$, and $60°$, the post-selection angle dependence of δ_x is shown in Figure 8.6. Similar to δ_y, δ_x exhibits an asymmetric behavior about the orthogonal position: it initially increases, reaches a maximum at a specific Δ, and then gradually decreases to zero as Δ becomes larger. Unlike δ_y, the shape of the δ_x curves remain consistent across all polarization states, regardless of whether the angle of incidence is smaller or larger than θ_B. The magnitude of δ_x is smaller than that of δ_y. The maximum $\delta_x = 120\ \mu m$ is obtained for $\theta = 45°$, $\alpha_i = 30°$, and $l = 2$.

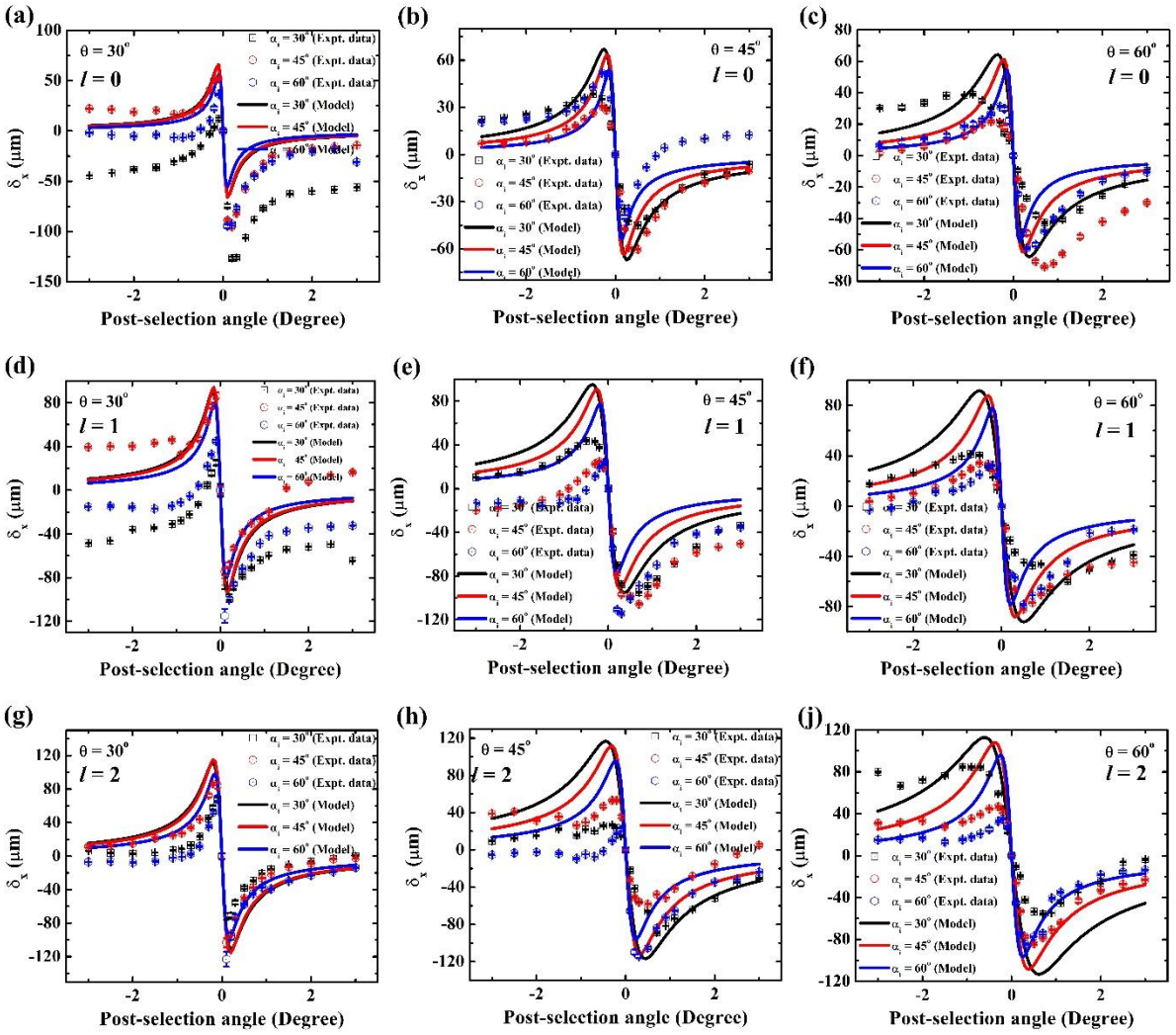

Figure 8.6 The amplified longitudinal (δ_x) shift values are shown as function of post-selection angle Δ for polarization angle of α_i=30˚(black), 45˚(red), and 60˚(blue) linearly polarized incident light beam with azimuthal index l = 0 [(a), (b), (c)], l = 1 [(d), (e), (f)] and l = 2 [(g), (h), (i)] for three different angle incidences $\theta = 30^{\circ}, 45^{\circ}, 60^{\circ}$. The dot centered square, circle, hexagon denote the experimental data while solid lines represent the theoretical model.

Next, we consider three fixed angles of incidence, $\theta = 30°, 45°$, and $60°$, and gradually rotate GLP1 to study the dependence of the absolute longitudinal ($|\ \delta_x\ |$) and transverse ($|\ \delta_y\ |$) shifts on the linear polarization angle (α_i) for three beam profiles, $l = 0,1$, and 2[Figure 8.7]. The post-selection angle is fixed at the optimum value, $\Delta = 0.3°$, in all cases [48]. For all considered incident angles, the sign of δ_x remains unchanged.

From Figure 8.7 (a) and (c), several interesting features of $|\ \delta_x\ |$ can be noted:

1. Starting from very small values, $|\delta_x|$ increases to around 150 μm and then decreases to zero as $\alpha_i$varies continuously from 0° to 90°.

2. The polarization angle α_i corresponding to the maximum $|\delta_x|$ shifts toward higher values (from 40° to 60°) as the angle of incidence increases from 30° to 60°.

3. For a given l, the maximum $|\delta_x|$ decreases with increasing incidence angle; for example, for $l = 2$, it is approximately 165, 139, and 124 μm for $\theta = 30°, 45°$, and 60°, respectively.

4. The separation between the curves for different $l$becomes significant in the region $\alpha_i = 30°–70°$.

5. $|\delta_x|$increases with increasing l.

Besides, starting from a significantly large value, $|\delta_y|$ decreases to nearly zero at $\alpha_i = 39°, 30°$, and 13° for $\theta = 30°, 45°$,and 60°, respectively, and then increases again as α_i varies continuously from 0° to 90°. This indicates that δ_y changes sign at different α_i due to the polarization- and incidence angle-dependent Fresnel reflection coefficients. Furthermore, the polarization angle at which $|\delta_y|$ vanishes shifts toward lower values as the angle of incidence approaches the Brewster angle ($r_p \to 0$).

The magnitude of $|\delta_y|$increases with increasing l; for instance, the maximum values for $\theta = 30°$ are approximately 175, 200, and 250 μm for $l = 0, 1,$ and 2, respectively. In contrast to $|\delta_x|$, the separation between $|\delta_y|$ curves for different l is more pronounced in the regions $\alpha_i = 0°–20°$ and 70°–90° for a given incidence angle.

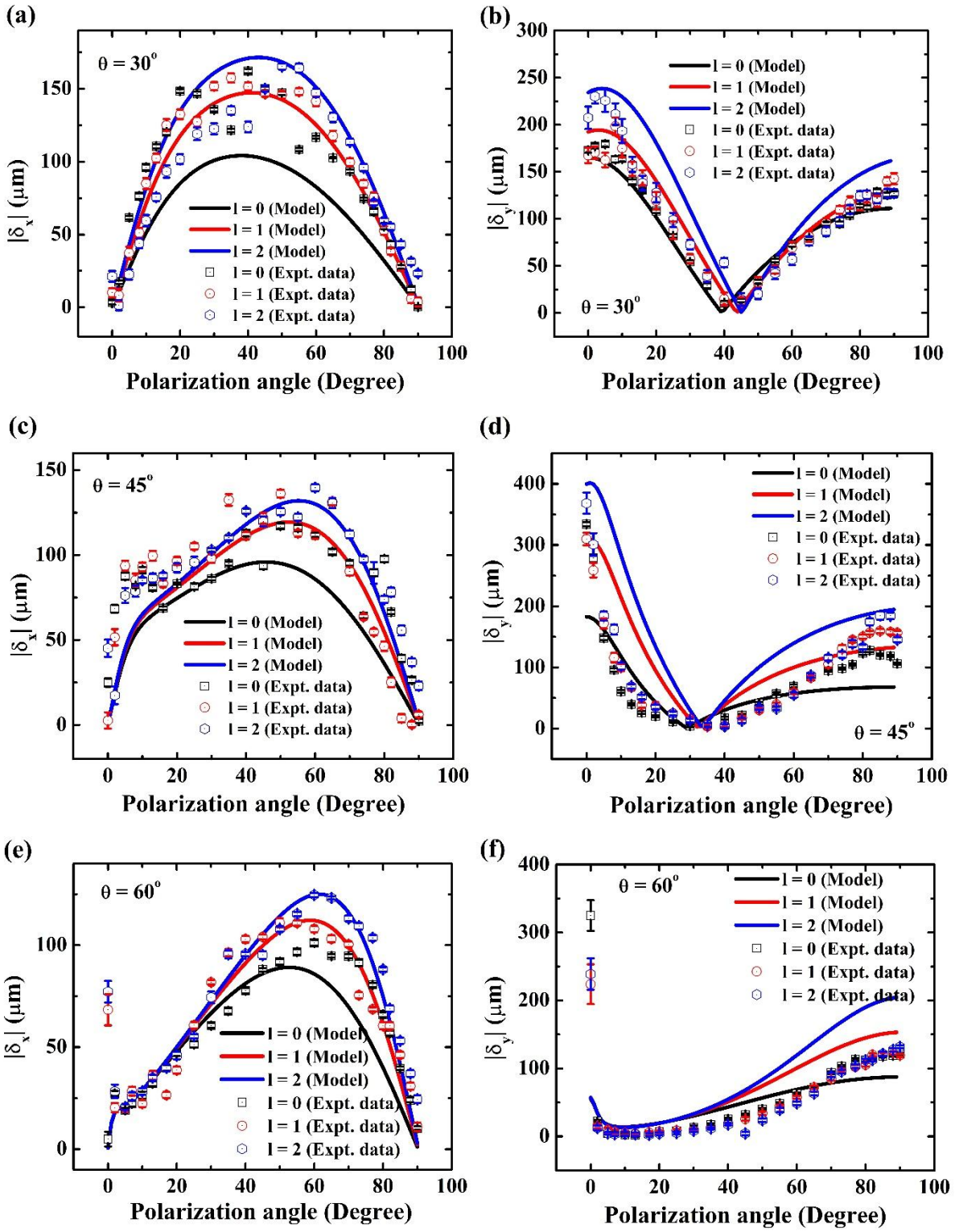

Figure 8.7 The linear polarization angle (α_i) dependence of absolute longitudinal (δ_x) [(a), (c), (e)] and transverse (δ_y) [(b), (d), (f)] shift values for $l = 0$ (black), 1 (red) and 2 (blue) at three different angle of incidences $\theta = 30^{\circ}, 45^{\circ}, 60^{\circ}$. The dot centered square, circle, hexagon denote the experimental data while solid lines represent the theoretical model.

From all the curves presented in Figure 8.5, Figure 8.6, and Figure 8.7; it is evident that the trends of the theoretical model and experimental data are in close agreement, indicating that the theoretical formulation remains valid not only far from the strong coupling region but also in its vicinity. Unlike the conventional weak measurement formalism, the present model exhibits a smooth and continuous variation around zero post-selection angles.

However, slight discrepancies between the theoretical predictions and experimental observations are occasionally observed. These deviations can be attributed to the difficulty in accurately determining the exact orthogonal position for arbitrarily linearly polarized light, which arises from the possible deviation of the reflected pre-selected state from perfect linear polarization (as seen in Figure 8.8). Additionally, intensity fluctuations along the circular ring of the vortex beam, caused by modulation errors of the SLM, may also contribute to these differences. The deviation from linear polarization in the reflected light can be mitigated by introducing a quarter-wave plate (QWP) before GLP2 [28].

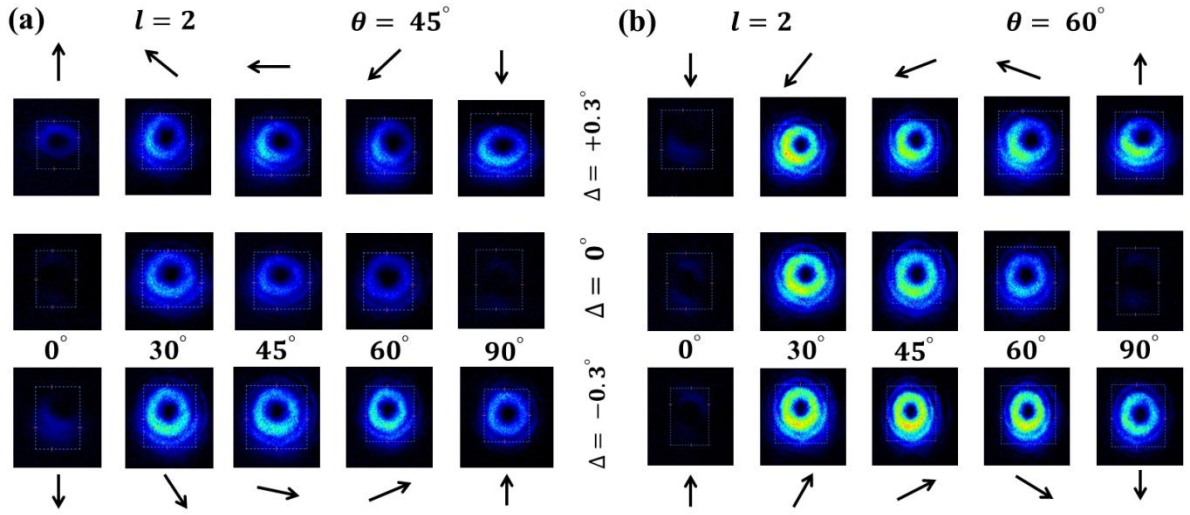

Figure 8.8 Intensity profile of the reflected light beam passing through the GLP2 as a function of incident polarization angle α_i for the angle of incidences $\theta = 45^{\circ}$(a) and 60°(b) considering $l = 2$. The middle row denotes the orthogonal condition while upper and lower row represent $\Delta = \pm 0.3^{\circ}$. The arrows indicate the rotation of polarization axis.

8.5 Concluding remarks

To conclude, the present work provides a comprehensive investigation of photonic spin splitting (PSS) employing arbitrarily linearly polarized orbital angular momentum (OAM) light beams. The experimental results clearly demonstrate that the PSS characteristics can be

effectively tuned by controlling the input beam parameters - such as polarization angle and OAM value - as well as by adjusting the post-selection angle and angle of incidence. By utilizing a higher-order vortex beam instead of the conventional fundamental Gaussian beam ($l = 0$), the maximum measurable shift values are observed to increase by a factor of two to three.

A modified weak measurement model for OAM-carrying light beams has been formulated based on the wave-vector formalism, offering significant improvements over previous models. Specifically, it successfully overcomes the two major limitations of the traditional weak value amplification (WVA) approach: (i) the breakdown under strong interaction regimes and (ii) divergence near the nearly orthogonal post-selection condition. Moreover, the proposed model is applicable to both internal and partial reflections from absorbing and non-absorbing material interfaces, accommodating any higher-order vortex beam with arbitrary coupling strength.

Overall, the findings of this study open new possibilities for exploiting the OAM degree of freedom in diverse photonic applications, including optical beam manipulation, high-resolution imaging, and precision optical sensing, thereby contributing to the broader understanding and control of spin-orbit light-matter interactions.

8.6 Appendix: Calculation of longitudinal and transverse PSS at absorbing material interface

In this Appendix, we provide comprehensive formulas for all of the elements of equations (8.6) and (8.7) presented in Section 8.2, taking into account the absorbing material interface rather than just the air-glass contact. The refractive index will no longer be a completely real quantity, and the reflection coefficients and its first derivatives will be complex in general. As a result, several vital extra terms will occur, as can be seen in the following equations:

$$\begin{aligned}\xi_{xp}^{l} = 2R_p cos^2\alpha_i \Bigg[\Big\{ &\left(\rho_p z_r - \varphi_p z_R\right) cos\,\phi_p + \left(\rho_p z_R + \varphi_p z_r\right) sin\,\phi_p \\ &- \frac{|l|}{(|l|+1)} \left(\rho_p \sin\phi_p - \varphi_p \cos\phi_p\right) z_R \Big\} cot^2\alpha_p \\ &- \frac{|l|}{(|l|+1)} \left\{R_p + R_s \cos\left(\phi_p - \phi_s\right)\right\} z_R \cot\alpha_p \cot\theta \Bigg]\end{aligned} \tag{8.17}$$

$$\xi_{xs}^{l} = 2R_s sin^2\alpha_i \left[\left\{(\rho_s z_r - \varphi_s z_R)\, cos\, \phi_s + (\rho_s z_R + \varphi_s z_r)\, sin\, \phi_s - \frac{|l|}{(|l|+1)}(\rho_s \sin\phi_s - \varphi_s \cos\phi_s) z_R\right\} + \frac{|l|}{(|l|+1)}\{R_s + R_p \cos(\phi_p - \phi_s)\} z_R \cot\alpha_p \cot\theta\right] \tag{8.18}$$

$$\xi_{xps}^{l} = \sin 2\alpha_i \left[\left(\{(\rho_s z_r - \varphi_s z_R) R_p\, cos\, \phi_p + (\rho_s z_R + \varphi_s z_r)\, R_p sin\, \phi_p + (\rho_p z_r - \varphi_p z_R) R_s\, cos\, \phi_s + (\rho_p z_R + \varphi_p z_r)\, R_s sin\, \phi_s\} + \frac{|l| z_R}{(|l|+1)}\{(\varphi_s \cos\phi_p - \rho_s \sin\phi_p) R_p + (\varphi_p \cos\phi_s - \rho_p \sin\phi_s) R_s\}\right) \cot\alpha_p - \frac{|l| z_R}{(|l|+1)}\{(1 - cot^2\alpha_p) R_p R_s \cos(\phi_p - \phi_s) + R_s^2 - R_p^2 cot^2\alpha_p\} \cot\theta\right] \tag{8.19}$$

$$\psi_{yp}^{l} = 2R_p cos^2\alpha_i \left[\left\{z_r R_p + z_r R_s\, cos(\phi_p - \phi_s) + z_R R_s\, sin(\phi_p - \phi_s) - \frac{|l|}{(|l|+1)} z_R R_s\, sin(\phi_p - \phi_s)\right\} \cot\theta \cot\alpha_p + \frac{|l|}{(|l|+1)} z_R (\rho_p \cos\phi_p + \varphi_p \sin\phi_p) cot^2\alpha_p\right] \tag{8.20}$$

$$\psi_{ys}^{l} = 2R_s sin^2\alpha_i \left[\left\{-z_r R_s - z_r R_p\, cos(\phi_p - \phi_s) + z_R R_p\, sin(\phi_p - \phi_s) - \frac{|l|}{(|l|+1)} z_R R_p\, sin(\phi_p - \phi_s)\right\} \cot\theta \cot\alpha_p + \frac{|l|}{(|l|+1)} z_R (\rho_s \cos\phi_s + \varphi_s \sin\phi_s)\right] \tag{8.21}$$

$$\psi_{yps}^{l} = sin\, 2\alpha_i \left[\left\{z_r(R_s^2 - R_p^2 cot^2\alpha_p) + R_p R_s \left\{z_r(1 - cot^2\alpha_p)\cos(\phi_p - \phi_s) - \frac{z_R cosec^2\alpha_p \sin(\phi_p - \phi_s)}{(|l|+1)}\right\}\right\} \cot\theta + \frac{|l|}{(|l|+1)} z_R\{(\rho_s \cos\phi_p + \varphi_s \sin\phi_p) R_p + (\rho_p \cos\phi_s + \varphi_p \sin\phi_s) R_s\} \cot\alpha_p\right] \tag{8.22}$$

$$\chi_p^l = -cos^2\alpha_i \left[\left\{\frac{2R_p^2 k z_R}{(|l|+1)} + \left(\rho_p^2+\varphi_p^2\right)\left(1+\frac{2|l|z_R^2(1-k)}{(|l|+1)(z_r^2+z_R^2)}\right)\right\}cot^2\alpha_p + \left\{R_p^2+R_s^2+2R_pR_s\,cos\left(\phi_p-\phi_s\right)\right\}cot^2\theta\right] \tag{8.23}$$

$$\chi_s^l = -sin^2\alpha_i \left[\left\{\frac{2R_s^2 k z_R}{(|l|+1)} + \left(\rho_s^2+\varphi_s^2\right)\left(1+\frac{2|l|z_R^2(1-k)}{(|l|+1)(z_r^2+z_R^2)}\right)\right\} + \left\{R_p^2+R_s^2+2R_pR_s\,cos\left(\phi_p-\phi_s\right)\right\}cot^2\alpha_p cot^2\theta\right] \tag{8.24}$$

$$\chi_{ps}^l = sin\,2\alpha_i\,cot\,\alpha_p \left[\left\{R_p^2+R_s^2+2R_pR_s\,cos\left(\phi_p-\phi_s\right)\right\}cot^2\theta - \frac{2kZ_R}{(|l|+1)}R_pR_s\cos\left(\phi_p-\phi_s\right) - \left(\rho_p\rho_s+\varphi_p\varphi_s\right)\left\{1+\frac{2|l|z_R^2}{(z_r^2+z_R^2)}\left(\frac{(|l|-1)!-|l|!}{(|l|+1)!}\right)\right\}\right] \tag{8.25}$$

with $r_{p,s} = R_{p,s}exp\,(i\phi_{p,s})$, $\rho_{p,s} = Re\left(\frac{\partial r_{p,s}}{\partial\theta}\right)$ and $\varphi_{p,s} = Im\left(\frac{\partial r_{p,s}}{\partial\theta}\right)$. Re and Im represent the real and imaginary part of a complex number, respectively. Although we believe these generic formulations will work well for arbitrary material interaction, substantial experimental confirmation is still required.

References

1. S. Liu, S. Chen, S. Wen and H. Luo, Opto. Electron. Sci. **1,** 220007-1(2022).
2. K. Y. Bliokh and A. Aiello, J. Opt. **15,** 014001 (2013).
3. A. Aiello, M. Merano and J. P. Woerdman, Phys. Rev. A **80,** 061801 (2009).
4. K.Y. Bliokh, F. J. Rodríguez-Fortuño, F. Nori and A. V. Zayats, Nat. Photonics **9,** 796-808 (2015).
5. K. Y. Bliokh and Y. P. Bliokh, Phys. Rev. Lett. **96,** 073903 (2006).
6. J. B. Götte, W. Löffler and M. R. Dennis, Phys. Rev. Lett. **112,** 233901(2014).
7. S. Mandal, A. Das and M. Pradhan JOSA B, **41,** 750-755 (2024).
8. M. R. Dennis and J. B. Götte, New J. Phys. **14,** 073013(2012).
9. A. Aiello, New J. Phys. **14,** 013058 (2012).
10. A. Das and M. Pradhan, Opt. Commun. **437,** 312-320 (2019).
11. M. Cheng, R. Chen and S. Feng, EPJD, **50,** 81-85 (2008).
12. M. Shah, Opt. Mater. **12,** 421-435 (2022).

13. W. J. Kort-Kamp, F. J. Culchac, R. B. Capaz and F. A. Pinheiro, Phys. Rev. B **98,** 195431(2018).
14. G. Sui, L. Cheng and L. Chen, Opt. Commun. **284,** 1553-1556 (2011).
15. M. J. Padgett, Opt. Express **25,** 11265-11274 (2017).
16. S. Parkin, G. Knüner, T. A. Nieminen, N. R. Heckenberg and H. Rubinsztein-Dunlop, Opt. Express, **14,** 6963-6970 (2006).
17. J. Zeng, Y. Dong, Y. Wang, J. Zhang and J. Wang, JLT, **41,** 2025-2040 (2022).
18. M. Li, S. Yan, Y. Zhang, Y. Zhou and B. Yao, J. Opt. **24,** 114001 (2022).
19. R. Fickler, R. Lapkiewicz, M. Huber, M. P. Lavery, M. J. Padgett and A. Zeilinger, Nat. commun. **5,** 4502 (2014).
20. K. Y. Bliokh, I. V. Shadrivov and Y. S. Kivshar, Opt. Lett. **34,** 389-391 (2009).
21. M. Merano, N. Hermosa, J. P. Woerdman and A. Aiello Phys. Rev. A **82,** 023817 (2010).
22. V. G. Fedoseyev. J. Phys. A: Math. Theor. **41,** 505202 (2008).
23. H. Okuda and H. Sasada, JOSA A **25,** 881-890 (2008).
24. C.Prajapati and N. K. Viswanathan, J. Opt. **21**, 084002 (2019).
25. M. Sato and H. Sasada, J. of Opt. **15,** 014018 (2013).
26. O. J. Santana and L. E. de Araujo, JOSA B **38,** 300-305 (2021).
27. G. Puentes, N. Hermosa and J. P. Torres, Phys. Rev. Lett. **109,** 040401 (2012).
28. W. Long, J. Pan, X. Guo, X. Liu, H. Lin, H. Zheng, J. Yu, H. Guan, H. Lu, Y. Zhong and S. Fu, Photonics Res.**7,**1273-1278 (2019).
29. S. Xie, J. Zhu, A. Wang, Y. Wang, Y. Huang and Z. Zhang, Opt. Express, **32,** 11794-11800 (2024).
30. Z. Chen, H. Zhang, X. Zhang, H. Li, W. Zhang and L. Xi, Opt. Express, **28,** 8308-8323 (2020).
31. Z. Chen, H. Zhang, X. Zhang, H. Li, J. Yang, W. Zhang, L. Xi and X. Tang, Opt. Express, **28,** 29529-29539 (2020).
32. Y. Aharonov, D. Z. Albert, and L. Vaidman, Phys. Rev. Lett. **60,** 1351 (1988)
33. I. M. Duck, P. M. Stevenson, and E.C.G. Sudarshan, Phys. Rev.D **40,** 2112 (1989)
34. N. W. M. Ritchie, J. G. Story, and R. G. Hulet, Phys. Rev. Lett. **66,** 1107 (1991)
35. L. Zhang, A. Datta, I. A. Walmsley, Phys. Rev. Lett. **114,** 210801 (2015)
36. C.Ferrie and J. Combes, Phys Rev. Lett. **112,** 040406 (2014.).
37. Y. Aharonov, A. Botero, S. Popescu, B. Reznik and J. Tollaksen, Phys. Lett. A **301,**130-138 (2002).

38. M. J. Hall, A. K. Pati and J. Wu, Phys. Rev. A, **93,** 052118 (2016).
39. Y. Gao, W. Luo, Q. Yang, J. Liu, Z. Zheng and H. Luo, Opt. Express, **33,** 8557-8568 (2025).
40. Z. H.Liu, W. W. Pan, X. Y. Xu, M. Yang, J. Zhou, Z. Y. Luo, K. Sun, J. L. Chen, J. S. Xu, C. F. Li, and G. C. Guo, Nat.Commun. **11,** 3006 (2020).
41. O. Hosten and P. Kwiat, Science, **319,** 787-790 (2008).
42. J. H. Huang, J. S. Lundeen, K. M. Jordan, A. C. Dada, G. J. Wang and X. Y. Hu, Phys. Rev. A, **108,** 033724 (2023).
43. C. Ren, J. Qiu, J. Chen and H. Shi, Opt. Commun. **425,** 19-23 (2018).
44. X. Qiu, L. Xie, X. Liu, L. Luo, Z. Li, Z. Zhang and J. Du, Appl. Phys. Lett. **110,** (2017).
45. W. Liu, Y. Wang and H. Luo, Phys. Rev. A **108,** 052606 (2023).
46. R. Dhara, N. Modak, S. Guchhait and N. Ghosh, Adv. Phys. Res. 2400136 (2024).
47. S. Chen, X. Zhou, C. Mi, H. Luo and S. Wen, Phys. Rev. A, **91,** 062105 (2015).
48. S. Lin, J. Hong, Z. Chen, Y. Chen and X. Zhou, Opt. Express, **30,** 4096-4105 (2022).
49. Z. Qin, R. Zhang, L. Zhang, L. Ren, P. Zhang, R. Qi, Q. Zhang, C. Wang and L. Jiang, Opt. Commun. **557,** 130283 (2024).
50. S. Mandal, A. Das and M. Pradhan, J. Appl. Phys. **135,** (2024).
51. Z. Qin, Q. Liu, C. Yue and X. Zhou, J. Phys. D Appl. Phys. **52,** 495106 (2019).
52. Z. Cui, Y. Hui, W. Ma, W. Zhao, and Y. Han, JOSA B, **37**, 3730-3740 (2020).
53. S. Goswami, M. Pal, and A. Nandi et al., Opt. Lett. **39**, 6229–6232 (2014).

9 Overall Summary and Future Prospects

In the following, we provide a summary of the key conclusions drawn from this thesis and explore potential pathways for future research that can be built upon the current work.

9.1 Overall Summary

In this thesis, we aim to explore how optical beam shifts at dielectric and other material interfaces can be controlled through different beam profiles, such as Gaussian, Laguerre–Gaussian (LG), and Hermite–Gaussian (HG) modes. To achieve this, we have developed comprehensive theoretical frameworks and carried out experimental measurements of these subtle effects. Our findings not only deepen the understanding of beam shifts but also pave the way for future applications in optical sensing and wavefront manipulation.

Chapter 1 begins with a discussion of Maxwell's equations and their solutions in various coordinate systems, including Cartesian (plane wave), spherical, and cylindrical frames. The focus then shifts to beam-like solutions, particularly Gaussian, Hermite-Gaussian, and Laguerre-Gaussian beams, emphasizing their key properties and diverse applications in nano-photonics. The chapter also provides a brief overview of several techniques for generating higher-order beams using different optical elements, with special attention to the role of spatial light modulators (SLMs) and their associated advantages and limitations. Finally, the chapter concludes with a discussion on the concept of vector beams.

Chapter 2 explores the interaction of plane waves and optical beams with standard optical interfaces, leading to the concept of optical beam shifts. It presents a comprehensive overview of the historical development of both spatial and angular longitudinal (Goos–Hänchen) and transverse (Imbert–Fedorov) shifts of the beam centroid. A unified framework for analyzing beam shifts using arbitrarily shaped beams is also discussed. The chapter concludes by highlighting the fundamental parameters that influence beam shifts and their significance in various precision optical measurement applications.

Chapter 3 provides an overview of the several experimental techniques developed to date for measuring spatial and angular Goos–Hänchen (GH) and Imbert–Fedorov (IF) shifts. The challenges associated with these measurements are discussed in detail, along with the respective advantages and limitations of each technique. This *chapter* offers a comprehensive perspective on the current state of experimental approaches and highlights their effectiveness in different scenarios.

Chapter 4 investigates the polarization-controlled Goos–Hänchen (GH) shift near the critical angle under total internal reflection conditions. A general theoretical model based on Jones matrix formalism is developed to describe the reflection of a Gaussian light beam. In

addition to polarization dependence, the variation of the GH shift with the angle of incidence is analyzed for arbitrary linear polarization states. The *chapter* also explores potential applications of tunable GH shifts in biosensing and polarization-controlled optical devices.

Chapter 5 focuses on the surface-dependent variation of Goos–Hänchen (GH) shifts. When an incident light beam interacts with a monolayer (ML) of tungsten di-selenide (WSe_2) deposited on a SiO_2/Si substrate, the critical angle undergoes a significant shift compared to that of a conventional glass–air interface. This *chapter* experimentally elaborates on the variation of small GH shift values with respect to the angle of incidence, post-selection angle, and linear polarization state. Theoretical modeling is carried out using the transfer matrix method (TMM) to calculate the reflection coefficients, which are then applied within the weak-value amplification framework. Finally, a comparative analysis with previous studies highlights the advantages of employing the ML WSe_2/SiO_2–Si structure in combination with weak-value amplification, demonstrating its superiority over conventional approaches.

Chapter 6 investigates the influence of beam shape on the magnitude of optical beam shifts near the critical angle of incidence. To this end, two orthogonal first-order Hermite–Gaussian (HG) modes, HG_{10} and HG_{01}, are generated using a phase-only spatial light modulator (SLM), with corresponding upgrades made to the experimental setup. The experimental results reveal the angular dependence of GH shifts in the total internal reflection region for both modes. A direct comparison with the fundamental Gaussian mode (TEM_{00}) demonstrates the advantages of employing higher-order beams over simple Gaussian beams. Furthermore, the manipulation of beam shape under orthogonal conditions is discussed, supported by a theoretical model describing light propagation through different optical elements.

In *Chapter* 7, a study of photonic spin splitting (PSS) in both transverse and longitudinal directions using p- and s-polarized Gaussian light beams is presented. The investigation is carried out near the Brewster angle of incidence during partial reflection at a ML WSe_2/SiO_2–Si interface. Distinct features of PSS as functions of the incident angle, polarization state, and post-selection angle are examined. To support the experimental observations of amplified PSS in both transverse and longitudinal directions, an improved weak measurement model based on wave-vector formalism is developed.

Chapter 8 presents a comprehensive study of generalized photonic spin splitting (PSS) using arbitrarily linearly polarized orbital angular momentum (OAM) beams incident on an

air–glass interface. The tunability of PSS is systematically investigated with respect to the post-selection angle, polarization angle, incident angle, and the topological charge of the incident beam. A generalized theoretical model, developed using the angular spectrum representation, is shown to be valid for both external and internal reflections from absorptive material interfaces, regardless of coupling strength. The optimum overlap of pre- and post-selection states for achieving maximum amplified PSS is also analyzed. Experimental results validate the theoretical model across strong-coupling (incident angles near the Brewster angle) and weak-coupling (far from Brewster incidence) regimes, as well as in conditions involving nearly orthogonal pre- and post-selection states.

9.2 Future Prospects

In this field of research, many questions remain unanswered. While we have taken the initial steps, a vast portion of the area is still unexplored. In the following, I summarize several proposals that warrant immediate attention.

Throughout this thesis, we have primarily focused on the manipulation of optical beam shifts using different beam profiles at dielectric and 2D material interfaces. Since beam shifts are highly sensitive to the refractive index of the interacting medium, this phenomenon can be directly applied to detect concentrations or monitor chemical reaction rates in liquid samples, with potential applications in both chemical and biological sensing. Furthermore, employing higher-order light beams may significantly enhance detection sensitivity, offering the possibility of multiple-fold improvement over conventional approaches.

In the last work (*Chapter* 8) of this thesis, we have investigated photonic spin splitting using higher-order vortex light beams at the air–glass interface and developed a generalized, improved weak measurement model. However, experimental verification of this model on absorbing or other exotic materials remains unexplored. Additionally, future studies could examine the conservation of total angular momentum throughout the entire interaction process, including both reflection and transmission at arbitrary material interfaces, which promises to be a particularly interesting avenue of research.

Another significant non-specular phenomenon involving higher-order vortex light beams arises from the Goos–Hänchen (GH) and Imbert–Fedorov (IF) shifts, known as orbital angular momentum (OAM) sideband generation. The intensity of these OAM sidebands can be tuned by various parameters of the incident light as well as the interaction medium. Notably,

low-intensity OAM sidebands are advantageous for optical communications, while higher-intensity sidebands can be exploited for optical beam manipulation. Both theoretical and experimental studies on OAM sidebands and strategies for their modulation represent promising directions for future research.

Finally, exploring applications such as imaging, wave function reconstruction, edge detection, and optical parameter measurement by combining weak value amplification with optical beam shifts would be a highly promising direction for future research.